High-Resolution Multi-Proxy Reconstruction of Holocene Climate Variability Over Interior of West Asia Based on Terrestrial Records from Iran

Sharifi, Orash

UNIVERSITY OF MIAMI

HIGH-RESOLUTION MULTI-PROXY RECONSTRUCTION OF HOLOCENE CLIMATE VARIABILITY OVER INTERIOR OF WEST ASIA BASED ON TERRESTRIAL RECORDS FROM IRAN

By

Orash Sharifi

A DISSERTATION

Submitted to the Faculty
of the University of Miami
in partial fulfillment of the requirements for
the degree of Doctor of Philosophy

Coral Gables, Florida

December 2017

UNIVERSITY OF MIAMI

A dissertation submitted in partial fulfillment of
the requirements for the degree of
Doctor of Philosophy

HIGH-RESOLUTION MULTI-PROXY RECONSTRUCTION OF HOLOCENE CLIMATE VARIABILITY OVER INTERIOR OF WEST ASIA BASED ON TERRESTRIAL RECORDS FROM IRAN

Orash Sharifi

Approved:

_____ Ali Pourmand, Ph.D. Associate Professor of Marine Geosciences	_____ Peter K. Swart, Ph.D. Professor of Marine Geosciences
_____ Larry C. Peterson, Ph.D. Professor of Marine Geosciences	_____ Amy C. Clement, Ph.D. Professor of Atmospheric Sciences
_____ Elizabeth A. Canuel, Ph.D. Professor of Marine Science Virginia Institute of Marine Science	_____ Guillermo Prado, Ph.D. Dean of the Graduate School

SHARIFI, ORASH (Ph.D., Marine Geology and Geophysics)
High-resolution Multi-proxy Reconstruction of Holocene Climate Variability over Interior of West Asia Based on Terrestrial Records from Iran (December 2017)

Abstract of a dissertation at the University of Miami.

Dissertation supervised by Associate Professor Ali Pourmand.
No. of pages in text. (243)

The regional climate over West Asia, extending between Iran and the Arabian Peninsula to the eastern Mediterranean Sea, is governed by interactions between three major synoptic systems; mid-latitude Westerlies, the Siberian Anticyclone and the Indian Ocean Summer Monsoon. In recent years, a number of paleoclimate studies have drawn potential links between episodes of abrupt climate change during the Holocene, and the rise and fall of human civilizations across the "Fertile Crescent" (also known as the Cradle of Civilization) of West Asia. The paucity of high-resolution palaeoclimate data from the "Cradle of Civilization" in West Asia, however, has limited our ability to evaluate the potential role of Holocene climate variability on early societies. The current research is the first study which presents a high-resolution, multi-proxy reconstruction of aeolian input and palaeoenvironmental conditions based on records of ombrotrophic (rain fed) peat and from Neor Lake and sediment record from hypersaline Urmia Lake in Northwest Iran. Multi-proxy record from Neor peat record suggest dry and dusty conditions prevailed during the Younger Dryas, and a substantial increase in atmospheric dust loading and decrease in moisture availability occurred between the early and late Holocene. This result further supported by palaeohydrological reconstructions and multi-proxy record from

Urmia Lake, which suggest wet condition prevailed during the early Holocene and drier condition with increased aeolian input was dominated during mid- to late Holocene.

Variations in radiogenic Sr-Nd-Hf isotopic composition and REE anomalies in samples from Neor peat core indicate dust particles deposited during the low-flux, early Holocene period (11,700-6,000 yr BP) is distinctly different from times of high dust fluxes during the Younger Dryas and the mid-late Holocene (6,000-present). This indicates that the composition of mineral dust deposited at the study site changed as a function of prevailing atmospheric circulation regimes and land exposure. Simulations of atmospheric circulation over the region show the Northern Hemisphere Summer Westerly Jet was displaced poleward across the study area during the early Holocene when solar insolation was higher. This shift, coupled with lower dust emissions simulated based on greening of the Afro-Asian Dust Belt during the early Holocene likely led to potential sources in Central Asia dominating dust export to West Asia during this period, in contrast to the dominant western and southwest Asian and Eastern African sources that prevail during the modern period.

Time-series analysis of aeolian input to NE Iran reveals periodicities that correspond with solar variability and internal climate feedbacks identified in other records of Holocene climate change from the northern hemisphere. Paleoclimate reconstructions from Neor and Lake Urmia suggest an atmospheric teleconnection existed between North Atlantic climate and West Asia during the last glacial termination and the Holocene.

Transitions in major Mesopotamian and Persian civilizations, including the collapse of the Akkadian empire, the fall of the Ur III Empire, the fall of Elam Empire and the demise of the Achaemenids overlap with major climate events from this study.

DEDICATION

Once a wise man said “The journey of thousand miles begins with one step”, now I would like to add to this phrase “The journey of a thousand miles will end if you have a right companion”.

To my life companion Maryam Hooshvar,

who walked with me no matter what path I chose.

ACKNOWLEDGEMENTS

This dissertation would not be nearly what it is without the collaboration and support of a great network of colleagues. First and foremost, I would like to thank my advisor, Ali Pourmand, who took me under his wing, fostered in me a deeper appreciation for the analytical geochemistry, encouraged and pushed me when I needed it most and above all offered me 25 years of limitless friendship. The opportunity which Ali granted me to pursue research with almost no limitation helped me to achieve more than I thought and become the scientist I am today. With his guidance and support, I was able to assemble an interdisciplinary committee from the pillars of the geochemistry and climate science to whom I owe a debt of gratitude. Elizabeth A. Canuel introduced me to the world of biogeochemistry and put everything on hold in her busy lab for many months to provide me a superb condition to work on biomarkers. Her training exceeds beyond the technical skills and helped me to understand how to build and lead a strong research team. Larry C. Peterson provided me with the opportunity to utilize the analytical facilities available at Club Mud. He supported all of my ambitious ideas on unconventional techniques. He not only helped me to have a better understanding about earth system and climate-human interactions but also showed me how one can be a fantastic teacher. When your research needed to utilize stable isotopes and to interpret complex data sets, there is no one better than Peter K. Swart to turn into. He opened his lab to me and gave me all the freedom that I needed to analyze thousands of samples using countless number of instruments. He showed me how to read between the numbers and how to make a dialogue with the data. He also went above and beyond to support me during difficult times. Amy C. Clement helped me to better understand the climate as a system and provided invaluable perspective

to the climate modeling. She also thought me how to think critically and how to have multi-dimensional approach toward the Earth's climate machine.

This work could not have been conducted without the help from many others. I would like to start by thanking Morteza Djamali who initially introduced us to the Neor Lake and provided preliminary data and samples. We shared thoughts and had many discussions on the vegetation coverage during the Holocene in NW Iran and the onset of agropastoral activities in the region. My colleagues and friends at Iranian National Institute for Oceanography and Atmospheric Science (INIOAS), especially Hmiad Alizadeh and Majid Naderi arranged the field campaign and provided scientific support, thank you. Many thanks to Mohammadali Hamzeh and Majid Pourkermanfor, INIOAS scientific staff, and Naser Ghasemi and Asadollah Taheri, INIOAS logistic team, for their tremendous support in the field. I owe sincere thanks to my ropemates and caver friends Payam Banihashemi and Mohammad Nabikhani, whom their selfless support granted us an access to the very valuable set of samples from Iran. I couldn't thank enough my colleagues at Virginia Institute of Marine Science (VIMS), namely Erin Ferer-Tylor, Christina Pondell and Paul Littreal for training and helping me with biomarker extraction and analysis.

I would also like to thank my fellow MMGers for their support over the last six years, especially the geochem-paleo comrades Monica Arienzo, Amanda Oehlert-Piggot, Quinn Devlin-Wakshinsky, Sean Murray, Sharmila Giri, Sevag Mehterian, Chris Kaiser, and Cory Schroeder. Kelly Jackson-Nurse, thank you for training me with the MSCL and for being my big sister during the comprehensive exam. Kelly Gibson, thank you for showing me how not to set the XRF scanner on fire and also for being fantastic neighbor. I would also like to thank my officemate, David Weinstein, for inspiring me to work harder. I

cannot thank enough the SIL and CSL key members, Greta McKenzie, Amel Saied and Karen Neher for providing me with their technical and emotional support. I would like to thank Don McNeill for giving me the opportunity to teach and interact with students. I like to express my appreciation to Shimon Wdowinski, who thought me how to think mathematically while being a geologist.

Lisa Murphy conducted numerous climate simulations for this project and patiently listened to my ideas about pairing paleoclimate data and climate simulations. Thank you for adding a new perspective to my research. I would also like to thank Joe Prospero and Adeyemi Adebeyi for showing me how to chase dust in the atmosphere. Thank you Mehdi Mirsaeidi and Golnaz Ebrahimi for your unconditional friendship and also for giving me the opportunity to extend my research and explore the practical field of human health.

Finally, I would like to thank my parents Manouchehr and Mandan Sharifi and my brother, Arta, for supporting my pursuits during the past four decades of my life. I would also like to thank my extended family Yazdan Hooshvar and Khoobchehr Keshavarzi as well as Mani and Sanam Hooshvar who have been an excellent voice of reason. Last but not the least, I cannot express my gratefulness to my wife, Maryam Hooshvar, who sacrificed a lot so I can pursue my dreams. I cannot ask for a better partner, great voice of wisdom and best friend and confidant; thank you my love.

Funding for this project was provided mainly by National Science Foundation grants EAR-1003639 to A. Pourmand and EAR-1003529 to E. Canuel. NSF P2C2 as well as Rosenstiel Fellowship. The field campaign was supported by INIOAS project No 391-012-01. Other sources of funding includes the Geological Society of America Student Research Grant and INIOAS-Urmia Lake -381-2-04 research grant awarded to Orash Sharifi.

Table of Contents

List of Figures

List of Tables

CHAPTER 1

Introduction

West Asia extends from southwestern Iran and the Arabian Peninsula to the eastern and southeastern Mediterranean Sea and is one of the most climatically dynamic regions in the northern hemisphere. The climate over this region is governed by complex interactions between major Eurasian synoptic systems (Fig. 1-1); the northern hemisphere subtropical westerly jet (NH WJ), the Siberian anticyclone (SA) and the southwest Indian Ocean summer monsoon (IOSM). The convergence of these systems and their response to external (solar insolation) and internal climate oscillations as well as to anthropogenic forcings, make this region highly susceptible to abrupt shifts in climate boundary conditions (Fig. 1-1).

A broad swath of land across NE Africa and west Asia, which is also known as the "Cradle of Civilization" and the "fertile Crescent", has witnessed the birth of agriculture and development of some of the earliest human societies since the beginning of the Neolithic Era (Leick, 2010; Mellaart, 1975; Riehl et al., 2013). Evidence is mounting that abrupt climate change during the Holocene epoch (11,700 before present, BP) may have played a transformative role in the growth and deterioration of human civilizations in this region (Brooks, 2006; Cullen et al., 2000; deMenocal, 2001; Riehl, 2009). Although the amplitude of climate variability was reduced during the Holocene relative to the last glacial period (Grootes et al., 1993), episodes of abrupt climatic change have been documented in marine and terrestrial records throughout the Holocene in both hemispheres (see review by Mayewski et al., 2004).

In recent years, a number of paleoclimate studies have drawn potential links between episodes of abrupt climate change and the rise and fall of civilizations across the "Fertile Crescent" (Cullen et al., 2000; Staubwasser and Weiss, 2006). Nevertheless, high-

resolution, terrestrial archives of climate variability with robust age models are scarce from this region (see the latest review in Nicoll and Küçükuysal, 2013). Such records are needed in order to address the uncertainty regarding the timing and regional significance of climatic transitions and their potential influence on early human societies. Climate reconstructions based on pollen and ostracod assemblages from lakes in Turkey, Iran and Georgia suggest that continental (dry and seasonally variable) climate dominated over the interior of West Asia during early to middle Holocene (Connor and Kvavadze, 2008; El-Moslimany, 1982; Griffiths et al., 2001; Wasylikowa, 2005). In contrast, $\delta^{18}O$ records from carbonates formed in land-locked lakes of western Iran have been interpreted to indicate prevalence of relatively wet conditions during this period (Lora R Stevens et al., 2006; Stevens et al., 2001; Wasylikowa et al., 2006). These apparently contradictory conclusions have been attributed to a number of factors, namely changes in the seasonality of precipitation, underestimating human impact on vegetation during the early Holocene, and the delayed reaction of biomes to postglacial climate change (M. Djamali et al., 2010; Roberts, 2002; Stevens et al., 2001). Available records of changes in palaeovegetation fall short of disentangling human *versus* climate impact (Djamali et al., 2009a), indicating the need for high-resolution palaeoclimate reconstructions that are independent of vegetation types that may have been influenced by agriculture as well as climate change (Roberts et al., 2011).

In modern times, changes in the Atlantic Meridional Overturning Circulation (AMOC) and the north Atlantic Oscillations (NAO) in climate significantly impacts sub-decadal variability in temperature and precipitation over Europe and West Asia (Frankignoul et al., 2013; Hurrell, 1995; Hurrell and VanLoon, 1997). Previous studies

indicate that poleward shifts in the position of North Atlantic storm tracks enforces contrasting precipitation patterns across Europe and the Middle East (eastern Mediterranean Sea) during the modern time as well as the Holocene; interannual northward shifts in the storm tracks resulted in wet seasons in southern Europe and dry spells over the Middle East (Bengtsson et al., 2006; Black, 2009; Black et al., 2010; Evans, 2010, 2009; Kitoh et al., 2008). It is also evident that the climate and the hydrology of the tropical Indian Ocean during Heinrich stadials and the Younger Dry is controlled by the slowdown in AMOC due to reorganization of the Hadley circulation (Mohtadi et al., 2014). Studies of the marine paleoclimate archives from the Arabian Sea, an area significantly impacted by the IOSM, indicate a strong atmospheric telecommunication between the North Atlantic and North Indian Ocean on millennial timescales during the last glacial period (Altabet et al., 2002; Pourmand et al., 2007, 2004; Schulz et al., 1998). The influence of north Atlantic Climate oscillations have also been documented on changes on the hydrology of the "Fertile Crescent" (Cullen et al., 2002).

1-Previous studies

The onset of paleoclimate investigations in Iran goes back to late 50s and early 60s, when investigators started paying attention to geomorphology of the Quaternary systems in Iran (*e.g.* Bobek, 1963; Vita-Finzi, 1968). The systematic cyclostratigraphy of the quaternary sediment with special emphasis on climate variability started when the first sediment cores collected in early 60s from the lake Zarivar in west of Iran (Hutchinson and Cowgill, 1963; Van Zeist and H . E . Wright, 1963). The age-depth model for this core was constructed by only two radiocarbon dates, which puts the beginning of the Zarivar record back to 14,800 years before present (BP). Based on the pollen assemblage, geochemical

data, and down-core mineralogy the authors concluded that dry condition prevailed during the late glacial and early Holocene. The dominance of the dry climate condition during the Last Glacial Maximum (LGM) further confirmed by high eolian deposition along the Caspian lowland in northern Iran (Frechen et al., 2009). Early study on Lake Zarivar sediments paved the way for further paleoclimate investigations in Iran.

A 4.5-meter long sediment core collected from the Lake Urumia in NW of Iran provided another record of climate variability covering the late-glacial and Holocene. The age-depth model on Urmia core is based on two un-calibrated radiocarbon dates on shrimp fecal pellets, which extrapolate the base of the core back to 13,200 year BP (Kelts and Shahrabi, 1986). Sedimentological study conducted on the Urmia core along with the pollen analysis (Bottema, 1986) suggested since the beginning of the record till about 9,000 year BP, lake was experiencing a playa like condition due to prolong dry condition. From 9,000 to 7,300 year BP high energy facies in the sediment suggests higher lake levels during the wet condition. Climate condition became similar to the present day since 7,300 BP. The Urmia Lake climate record is out of phase with other lake records from the Middle East and North Africa due to the age model discrepancies as noted by the authors. A longer sediment record from Uremia Lake was emerged when a 100-meter long core was drilled in 2000. Two radiocarbon date on bulk sediment 8- and 18.5-meter returned calibrated ages of 12,212 and 29,150 cal year BP respectively (Djamali et al., 2008). These ages made the second Urmia pollen data set the longest paleoclimate record from Iran. In the absence of absolute age determinations prior to 29,150 cal yr BP, the chronology was established by temporal correlation of the Urmia record with other well-dated records from the region pushing the Urmia record back to 200,000 years BP. Based on this record, Djamali et al.

(2008) concluded that during the last glaciation the upland vegetation consisted of Artemisia dominant steppe suggesting warm and moist climate condition during this period. The Holocene reported as slightly colder and dryer. Study of aeolian sand ramps in Iran also suggested dry condition during the LGM which extended into the Holocene (Thomas et al., 1997). Study of the alluvial fans in SE Iran (Hormuz Strait) revealed three-^{10}Be surface abandonment ages centered at 5,600, 12,800 and 21,000 ^{10}Be years (Regard et al., 2006). These ages refer to the periods with dry condition in which deposition of alluvial fans either stopped or reduced to minimum. All three-^{10}Be surface abandonment ages coincide with major climatic transitions; the offset of the mid-Holocene humid period (5,600 ^{10}Be yr), the onset of the dry Younger Dryas episode (12,800 ^{10}Be yr), and the end of LGM at 21,000 ^{10}Be yr.

The greatest contribution to the Holocene paleoclimate reconstruction of Iran is largely come from the study of two shallow lakes in western Iran. Being only 300 kilometer apart, Lake Mirabad and Lake Zarivar provided a set of precipitation and vegetation reconstructions based on pollen and plankton assemblages, limnology, sedimentary stratigraphy, stable isotopes, and mineralogy (El-Moslimany, 1982; Griffiths et al., 2001; Snyder et al., 2001; Lora R. Stevens et al., 2006; Stevens et al., 2001; Van Zeist and Bottema, 1977; Van Zeist and H . E . Wright, 1963; Wasylikowa, 2005; Wasylikowa et al., 2006).

The first set of $\delta^{18}O$ proxy records for Lake Zarivar was introduced by Stevens et al., (2001). In her study, the chronology was stablished based on previously dated cores collected by Wasylikowa in 70s, without correcting for the reservoir carbon. The significantly high $\delta^{18}O$ values of bulk sediment at the onset of early Holocene indicating

the dominance of dry condition during this period. The $\delta^{18}O$ values remain relatively low during early- to mid-Holocene until around 5,600 cal year BP suggesting a prolong wet period during this time. Through the remainder of the record the $\delta^{18}O$ values remain slightly higher with an exception during the small wet period between 3,000-4,000 cal year BP. These findings are in good agreement with $\delta^{18}O$ records from Lake Mirabad (Lora R. Stevens et al., 2006). Geochemical data from eastern Mediterranean lakes (Roberts, 2002; Roberts et al., 2008) also suggests generally wet conditions during early Holocene, followed by expansion of drier, more modern-like climate from mid-Holocene to the present in West Asia.

2-Background

2.1- Dominant synoptic regimes over Iran

Today, Mediterranean climate with cool and wet winters and dry summers dominates most inland regions of West Asia (Roberts and Wright, 1993; Lora R Stevens et al., 2006). Located between 25-35°N and 44-62°E, Iran borders the Caspian Sea in the north and the Persian Gulf and the Oman Sea in the south (Fig. 1-1). Except for the coastal regions with open access to humid air masses or mountainous areas of high elevation, the climate over Iran is predominantly arid and semi-arid (Alijani and Harman, 1985) with a wide range of seasonal variations in temperature and precipitation. Average annual precipitation over central and eastern part of Iran is around 120 mm with maximum precipitation of up to 2000 mm in the north along the Caspian Sea and the northern Alborz and in the NW-SE Zagros mountain ranges (Fig. 1-1). Temperature varies within a broad range from 50°C in central Iran and along the Persian Gulf to -20°C in NW (Abbaspour et al., 2009). On a

regional scale, precipitation and temperature regimes over Iran are governed through the interplay between three atmospheric circulation patterns:

2.1.1- The Siberian anticyclone (SA)

The Siberian high pressure system is centered over eastern Siberia in winter and greatly influences the climate of mid to high latitudes across Eurasia. Several studies have reported coupling between the SA and other synoptic systems in the northern hemisphere such as the Arctic Oscillation (AO), NAO and the Indian Ocean summer and winter monsoons (Gong and Ho, 2002; Gong et al., 2001; Han et al., 2008; Vandenberghe et al., 2006; Wu and Wang, 2002). In East Asia, expansion of the SA to lower latitudes results in intensification of the northeast winter monsoon. Southeastward displacement of the SA to lower latitudes over West Asia brings dry and cold surface air masses across northern Iran and impacts the intensity and position of the mid-latitude westerly storms during winter (Alijani and Harman, 1985).

2.1.2- The westerlies

The mid-latitude westerlies are the main source of annual precipitation to the region between the eastern Mediterranean Sea and northern Persian Gulf. The position of the main axis of the jet and intensity of the westerlies over Iran during winter and early spring largely depend on the pressure systems over the Azores and Greenland in the North Atlantic, and the position of the cold and dry SA over West Asia. Studies of modern (Cullen, 2000) and late Holocene (Jones et al., 2006) climate have found a close link between the NAO and precipitation in the eastern Mediterranean Sea. Negative NAO is associated with enhanced zonal penetration of moisture-bearing westerly depressions across the Mediterranean Sea

to the Near East and Iran. Conversely, during positive NAO, the westerlies are shifted to northern Europe and dry and cold winter conditions befall West Asia as the SA spreads to lower latitudes (Hurrell, 1995; Hurrell and VanLoon, 1997). In western Iran, regional modeling results have shown that a combination of topographic effect and the NAO best explains the interannual variability in precipitation over northwest Zagros Mountains (Evans et al., 2004). However, regional modeling (Evans and Smith, 2006) and analysis of gauge data over the last four decades (Raziei et al., 2013a, 2012) have led to the suggestion that "southern" water bodies such as the Red Sea, the Persian Gulf and Northern Indian Ocean may play a more significant role in providing moisture to West Asia during winter months than previously thought.

2.1.3- The Indian Ocean summer monsoon (IOSM)

The IOSM is part of the Asian-African monsoon system and is responsible for most of the annual precipitation to south Asia during the summer. The convective gradient, which forms between warm air over the Asian Plateau and cooler northern Indian Ocean, is responsible for the formation of low-level jets that transport moisture from southern subtropical Indian Ocean to Southeast Asia and the Himalayas (Clemens et al., 1991). The intensity of the IOSM has varied during the Holocene as the latitudinal position of the Intertropical Convergence Zone (ITCZ) migrated in response to changes in the insolation difference between southern and northern Hemispheres (Fleitmann et al., 2007, 2003; Zonneveld et al., 1997). Indeed, there is evidence that changes in the intensity of the Indian Ocean and Asian monsoons coincided with major cooling events in North Atlantic during the Holocene (Bond et al., 2001; Hong et al., 2003; Wang et al., 2005). High precipitation resulting from the IOSM, however, does not reach Iran's Persian Gulf and Oman Sea coasts

during the summer due to the current position of the ITCZ (Fig. 1-1). Northward displacement of the ITCZ during early Holocene may have resulted in higher levels of precipitation along the southern coasts of Iran but there are no studies from this region to confirm this possibility. While the influence of changes in the IOSM may have been inconsequential over Western Iran, the large scale of this circulation and its established modern and paleo relationship with north Atlantic climate variability require that we consider the monsoon system to better understand Holocene climate variability in West Asia.

2.2- Modern climatology of precipitation regime over Iran

Iran is divided into six climatic regions based on daily observations of precipitation during a 5-year span at 40 synoptic station (Alijani and Harman, 1985) (Fig. 1-2A). Mean annual precipitation days (PDs) over this time period revealed two north-south gradients across the country (Fig. 1-2B). The W-NW gradient begins around 100-90 PDs in the NW and diminishes to 20-10 PDs toward S-SE. The second gradient from the NE scales with 70-60 PDs and reduces to 20-10 PDs in the south. The northern flanks of the Alborz Mountains (Fig. 1-1) and the Caspian Sea coastal region is under the influence of Marine climate from the Caspian Sea and does not count as part of these two major gradients.

Mean monthly precipitation of longer time series data (30-55 years) for north-west, west, south and central part of Iran (Fig. 1-3) indicates that the majority of precipitation occurs during the rainy season from October to May. By utilizing high resolution regional climate model (RegCM2) and high density data set (available from FAO) for the Middle East region, the same pattern has been generated (Fig 1-4) for the Mediterranean Sea, the

Fertile Crescent and Zagros Mountains (Evans et al., 2004). The regional climate model indicates that in general, the northern region (Tehran for northern and Amman for NW stations) receives rainfall during winter and spring associated with Mediterranean low pressure passing over the region where precipitation over the southern region (Sanaa station for SW) is mainly governed by the monsoon convection, cross equatorial flow and the remnants of the low pressure system associated with the summer monsoon. The areas between the northern and southern regions (Riyadh station for central part) receive rainfall during the winter due to the Mediterranean cyclone systems and during the summer due to the summer monsoon. Importantly, the rain fall pattern over the central parts does not show any consistency (Babu et al., 2011). The northwest, southwest and southeast parts of the Middle East region receive more annual rainfall compare to other regions (Fig. 1-4). Egypt, Jordan and southern part of Saudi Arabia are the region with least received annual rainfall.

Both the frequency and amount of precipitation over Iran are largely governed by westerly disturbances (mostly upper-level) that dominate the northern part of the country and become more seasonal by moving toward the south (Alijani and Harman, 1985). However, other studies mentioned the significant role of El Niño/Southern Oscillation (ENSO) in controlling (Nazemosadat et al., 2006; Nazemosadat and Cordery, 2000; Sabziparvar et al., 2010) interannual variation in rainfall over Iran. Evans et al., (2004) found that surface disturbances show almost the same temporal and spatial pattern as the upper level disturbances however; their effect on precipitation is smaller. Marine effect and surface heating of the Caspian Sea are considered the second most important source of precipitation in that region. Positive correlations between interannual variation in fall and winter precipitation and ENSO is also observed by Pourasghar et al., (2012).

2.3- Dust over West Asia

Atmospheric dust plays an important role in controlling global radiation budget, which in turn, affects climate (Choobari et al., 2014; Lambert et al., 2008; Miller and Tegen, 1998; Tegen and Lacis, 1996). The vast arid and semi-arid areas in the Middle East, stretching from Syria to the Arabian Peninsula and Iran, are part of the African-Asian "dust belt" and a major contributor to global atmospheric dust content (Prospero et al., 2002). The Arabian Peninsula, Iraq and Syria are considered as major sources of dust with up to 20% contribution to global dust emissions (Hamidi et al., 2013). Large amounts of dust are delivered from these regions to the Persian Gulf, the Red Sea and northern Indian Ocean (Goudie and Middleton, 2006; Littmann, 1991; Middleton, 1986; Pourmand et al., 2004; Prospero et al., 2002; Sirocko et al., 2000).

Aside from local disturbances at the surface and circulation regimes near large bodies of water in the north and the south, two annual wind regimes can be identified over West Asia. During the summer, a gradient is established between the high pressure over the Arabian Peninsula and south and central Iranian Plateau, and the low pressure system over higher latitudes of Eurasia This gradient drives north-northwesterly winds along the Persian Gulf and over the Arabian Peninsula towards northern Indian Ocean. The dominating winds during winter and early spring are the mid-latitude westerlies that penetrate eastward from the North Atlantic and East Mediterranean with sustained westerly-northwesterly directions (Fig. 1-1).

Several dust-bearing wind systems also occur at regional scale across Iran; the winter and summer "Shamal" (north) are north-northwesterly winds that deliver dust to the

Persian Gulf and the Oman Sea from February to July (Figure 1). The "Garmsil" are warm, highly dust-prone winds active during the summer in northeast Iran. In southeast and central regions "Winds of the 120 days" prevail during the summer (Hossenzadeh, 1997; Middleton, 1986). Dust storms generated in east and central Iran, however, do not affect western Iran due to the strong westerly winds and the Alborz and Zagros topographic barriers. Generally, seasonal distribution of dust storm activity in West Asia (Fig. 1-5) is higher during spring and summer months (Goudie and Middleton, 2006; Kutiel and Furman, 2003; Prospero et al., 2002). Total Ozone Mapping Spectrometry (TOMS) of atmospheric dust content shows areas between the Tigris-Euphrates basin and the Arabian Peninsula as the main sources of modern dust to west and northwestern Iran (Prospero et al., 2002).

Although the origin of most dust storms is from within West Asia, occasional winter and spring outbreaks of Saharan dust storms, induced by southeast penetration of the westerlies over the Mediterranean Sea, have been also observed in recent years with the potential to deliver large amounts of dust to West Asia (Goudie and Middleton, 2006; Littmann, 1991).

2.4- Existing reconstructions of Holocene paleoclimate from Iran

Iran's strategic geographic location with respect the SA, IOSM and the westerlies provides a unique opportunity to investigate possible atmospheric teleconnections between West Asia, the north Atlantic and the African-Asian monsoon system during the Holocene. Nevertheless, multi-proxy paleoclimate records with robust chronological constraints are rare from this region and climate variability during the Holocene, in particular, is poorly

documented from terrestrial records in the region (Kehl, 2009; Nicoll and Küçükuysal, 2013).

The bulk of existing Holocene studies have focused on reconstructing past precipitation and vegetation based on pollen and plankton assemblages, limnology, and sedimentary stratigraphy of two shallow-water lakes in western Iran. Depending on what proxy record is used, however, different images emerge. Pollen records (El-Moslimany, 1982; Van Zeist and Bottema, 1977; Van Zeist and H . E . Wright, 1963) and plankton assemblages (Griffiths et al., 2001; Wasylikowa and Witkowski, 2008; Wasylikowa, 2005) from Lake Zeribar and Lake Mirabad located about 300 km apart in the northern section of the Zagros Mountains suggest that dry conditions prevailed during early to middle Holocene. A similar conclusion is drawn based on pollen assemblages from lakes in central and eastern Turkey and southern Caucasus (Connor and Kvavadze, 2008; Roberts and Wright, 1993; Wick et al., 2003). In contrast, (negative) oxygen isotope values ($\delta^{18}O$) from Lake Mirabad and Zaribar (Stevens et al., 2001; Stevens et al., 2006), generally associated with enhanced precipitation, do not support the existence of dry climate during early Holocene as suggested by paleo-vegetation proxies. Stevens et al. (2006) postulated a shift in the seasonal timing of precipitation from spring (rain) to winter (snow), rather than changes in total water balance, as a possible mechanism for explaining negative $\delta^{18}O$ values during early Holocene. Nevertheless, they interpreted positive $\delta^{18}O$ at ca. 5,400, 1,500 and 500 cal yr B.P. from the same records to indicate drought periods. Geochemical data from eastern Mediterranean lakes (Roberts, 2002; Roberts et al., 2008) also suggests generally wet conditions during early Holocene, followed by expansion of drier, more modern-like climate from mid-Holocene to the present in West Asia.

While a delayed response of vegetation to climate may have been conducive to the divergence between pollen and geochemical reconstruction of Holocene climate in west Asia (Roberts et al., 2001), employing pollen assemblages as a climate indicator *sensu stricto* should be exercised with care. Specifically, the importance of anthropogenic influence on expansion of paleo-vegetation in a region of high human activity since 9,500 BP should not be underestimated (Djamali et al., 2009b; Roberts, 2002). In northwestern Iran, for example, Djamali et al. (2009b) identified several intervals of agricultural activities based on pollen assemblages in a 3700-yr ombrotrophic peat record. Ramezani et al. (2008) also documented three episodes of changes in forest vegetation over the last millennium in the central Alborz Mountains along the Caspian Sea, which may be related to increase in human activities as well as climate change. Pollen records from Lake Maharlou in SE Zagros Mountains also show a strong human signature across this region over the last 5700 years (Djamali et al., 2009a). Furthermore, interpretation of geochemical data from carbonate-dominated drainage basins, which are characteristic of most mountain lakes in Iran, is complicated by the presence of hard-water and significant reservoir effects (Djamali et al., 2009a; Geyh et al., 1998; Stevens et al., 2001).

Terrestrial records of climate change from other parts of Iran are exceedingly sparse. Morphological and sedimentological evidence remain difficult to interpret due to poor chronological constrains and the influence of processes other than climate change (Diester-Haass, 1973; Vita-Finzi, 1968). The early-Holocene discrepancies between palynological records and geochemical proxies in West Asia remain unresolved (Eastwood et al., 2007; Stevens et al., 2001). Establishing high-resolution records of inorganic and organic multi-proxies, which represent changes in atmospheric circulation pattern and hydrological

cycles, will provide a much needed independent approach for resolving the conflicting records of early Holocene climate in West Asia.

3-Ombrotrophic (rain fed) peat as an alternative terrestrial climate archive

Finding continuous and well-preserved archives of atmospheric circulation and climate variability in terrestrial environments is a challenge. A rare exception comes from ombrotrophic peat mires, which receive their mineral and water content exclusively from the atmosphere (Barber and Langdon, 2007; Chambers and Charman, 2004; Mauquoy and Barber, 2002). Accumulation of peat is owed to the fact that organic matter production exceeds its geochemical and microbial degradation. Most peat mires in temperate regions and higher latitudes of northern hemisphere began to form as glaciers retracted at the onset of warmer Holocene climate.

There are numerous advantages in using ombrotrophic peat profiles to reconstruct the climate of the Holocene: **a)** while reservoir effects pose complications in radiocarbon dating of lake and cave deposits, carbon dates of ombrotrophic peat are not biased by allochthonous carbon, **b)** exposure to the atmosphere as the sole source of lithogenic (dust) and organic (pollen) particles makes peat mires the closest terrestrial analogues to ice sheets in direct sampling of the atmosphere aerosol content, **c)** organic matter produced in situ is well preserved under anoxic conditions, allowing the use of remnant plants and pollen, insect fossils and molecular biomarkers as tracers of past climate change, **d)** the low-oxygen conditions minimize bioturbation, which is a common problem in climate records from lake and marine sediments, and **e)** continuous mass accumulation rates at about 1-2 mm y^{-1} effectively archive interannual variability in atmospheric dust deposition.

3.1- Lithogenic major and transition elements, rare earth elements and radiogenic isotopes of Sr, Nd and Hf in peats as a proxy for eolian input and provenance

The geochemistry of major and trace elements and their natural and anthropogenic variability in peat mires (bogs) have been studied extensively (Muller et al., 2008; Shotyk et al., 2002; Steinmann et al., 2006; Zaccone et al., 2010, 2008). The concentrations of refractory lithogenic elements (*e.g.* Ti, Zr, Al) solely depend on atmospheric input to the surface of ombrotrophic mires. Down-core variations in the concentration (flux) of these elements have been effectively used to reconstruct changes in past atmospheric fluxes (Bao et al., 2012; Eiss et al., 2002; Zdanowicz et al., 2006). In contrast, groundwater intrusion under mineralotrophic conditions can potentially alter the atmospheric profiles of mobile and redox-sensitive elements, while the conservative lithogenic elements remain unaffected (Novak et al., 1999; Novak and Pacherova, 2008; Orru and Orru, 2006; Rausch et al., 2005), unless fluvial contribution is significant. A deviation from the relationship between down-core profiles of refractory and mobile/redox sensitive elements can therefore be used to test whether ombrotrophic conditions were sustained throughout the record (Shotyk et al., 2001).

In addition to lithogenic major and transition metals, rare earth elements and radiogenic isotopes (Sr-Nd-Hf) have also been extensively employed as tracers of eolian input (Biscaye et al., 1997; Grousset et al., 1988a; Grousset and Biscaye, 2005; Yang et al., 2013). The concentrations of REEs have been shown to closely correlate with refractory trace elements in many peat bogs (Akagi et al., 2002; Aubert et al., 2006; Krachler et al., 2003). Indeed, due to their high resistance to post-depositional processes and conservative

behavior (with the exception of Ce and Eu), the REEs inherit and maintain the composition of their source material (Wedepohl, 1995) and can be additionally utilized to reveal changes in the dust provenance. Previous studies have successfully used REEs as a proxy for eolian input and source origin of eolian deposition in peat bogs from Canada (Zdanowicz et al., 2006), North America (Kamenov et al., 2009) and Western Europe (Aubert et al., 2006). Many studies have shown that radiogenic isotopes are a powerful tool in studying sources of aeolian dust in the receiving sites (*e.g.* Abouchami et al., 2013; Bayon et al., 2009; Borg and Banner, 1996; Frost et al., 2006; Lupker et al., 2010; Pourmand et al., 2014, also see review in Scheuvens et al., 2013).

3.2- Organic proxies for changes in past moisture

Organic compounds ("biomarkers"; biochemical compounds that can be linked to the organisms from which they are synthesized) provide useful tracers for reconstructing changes in climate and offer a complementary tool to inorganic proxies.

3.2.1- Total organic carbon

Plant type and growth vary as a function of changes in effective moisture (precipitation minus evapotranspiration) in peat mires. Total organic carbon concentration (TOC) is a basic indicator of climate conditions; plants generally respond to higher moisture availability (as precipitation in ombrotrophic peats) by increased biomass production (Zhao et al., 2011; Zheng et al., 2007). The TOC-moisture relationship, however, is not straightforward as post-depositional decomposition of organic matter is also accelerated under warm and wet conditions (Meyers and Ishiwatari, 1993). As a result, other proxies must be used to validate inferences drawn from TOC.

3.2.2- Organic biomarkers

Organic biomarkers have been widely used in marine and lacustrine environments to track past climate change (Eglinton and Eglinton, 2008; Holtvoeth et al., 2010; López-Días et al., 2010; Schellekens and Buurman, 2011; Zheng et al., 2007). Specifically, lipid biomarkers offer more reliable constraints on past hydrological regimes in peat mires compared with traditional organic proxies such as the degree of humification (Mauquoy and Yeloff, 2008; Yeloff and Mauquoy, 2006). The geochemical stability of hydrocarbon lipids (*e.g.*, *n*-alkanes) contributes to their usefulness for studying changes in organic matter delivery using sediment core records representing historical and geologic timescales (Nott et al., 2000; Pancost et al., 2002).

High precipitation and low evaporation during cool and wet climate in temperate regions lead to predominance of submerged and floating plant species. Conversely, higher plants that are more resistant to low moisture dominate when dry climate prevails. The abundance of hydrophilic floating and submerged plants (medium chain n-alkanes: C_{23}, C_{25}) relative to terrestrial plants (characterized by long chain n-alkane: C_{29}, C_{31}) can be quantified according to "$P_{aqueous}$" (P_{aq}) ratio employing the equation below (Ficken et al., 2000):

$$P_{aq}=(C_{23}+C_{25})/(C_{23}+C_{25}+C_{29}+C_{31}) \quad (1\text{-}1)$$

where P_{aq} index, used as a proxy for the dominance of submerged vs emergent plants, provides a measure of water availability in peat mires. The effectiveness of these proxies for reconstructing paleo-moisture in bogs has been demonstrated in several peat records from the Holocene (Seki et al., 2009; Zhou et al., 2005, 2002). Long-chain *n*-alkanoic acids

(*e.g.* C_{24}, C_{26}, and C_{28}) are major components of the waxy coatings leaves, flowers, and pollen of higher plants, where shorter chain (C_{12}, C_{14}, and C_{16}) *n*-acids are produced by all plants but are the dominant lipid components of algae, bacteria, and aquatic plants. Short chain *n*-alkanoic acids are widely used to identify the contribution autochthonous sources in lacustrine environments (Meyers, 2003; Muri and Wakeham, 2006). The ratio of terrigenous to aquatic *n*-alkanoic mixture of fatty acids $TAR_{(FA)}$ is a measure for evaluating the relative importance of terrigenous and aquatic sources (Bourbonniere and Meyers, 1996; Waterson and Canuel, 2008) by using the equation below:

$$TAR_{(FA)}=(C_{24}+C_{26}+C_{28})/(C_{14}+C_{16}+C_{18}) \quad (2)$$

Higher values for $TAR_{(FA)}$ may indicate increased watershed sources of lipid matter relative to aquatic sources.

3.2.3- Hydrogen and carbon stable isotopes

The stable hydrogen (δD) and carbon ($\delta^{13}C$) isotopic signatures of organic matter can provide additional information about environmental and climate conditions (Ficken et al., 2000; Seki et al., 2009). Environmental conditions and vegetation types are two major factors controlling the $\delta^{13}C$ values of plants. Since the carbon isotopic compositions of total organic carbon ($\delta^{13}C_{TOC}$) in lake sediments or in peat mires inherit the carbon isotopic compositions of the regional plants (Weiguo et al., 2005), the $\delta^{13}C_{TOC}$ have been widely used to infer temporal variations in vegetation in respond to changes in climate condition (*e.g.* Andersson et al., 2012; Esmeijer-Liu et al., 2012; Jiménez-Moreno and Anderson, 2012; Liu et al., 2005, 2008; Zhang et al., 2003).

Recent studies have shown that leaf wax δD values record the precipitation, modified by the amount of isotope enrichment in the leaf water due to the presence or absence of stomata, and meteorological conditions, such as evapotranspiration, relative humidity and soil moisture (deMenocal and Tierney, 2012; Mügler et al., 2008; Sachse et al., 2006; Tierney et al., 2008).

4-Holocene climate variability and environmental changes in Lake Urmia

Closed-basin brine lakes have been the subject of numerous paleoclimate studies due to their sensitivity to regional and global climate variabilities as well as to anthropogenic (Cohen et al., 2000; Djamali et al., 2008; Morteza Djamali et al., 2010; Fritz, 1996; Kowalewska and Cohen, 1998; Mischke et al., 2005) changes. In these lakes, the balance between water input (mainly precipitation) and output (evaporation) affects lake level and subsequently its chemistry. Records of past abrupt climate change events can be reconstructed with in saline lakes with fewer uncertainties compare to open freshwater systems (Fritz, 1996). Geologic setting, hydrology of the basin, and the degree of evaporative, primarily controls the ionic composition of closed lakes. Changes in mineralogical and ionic concentrations in these environments vary in a predictable fashion (Eugster and Jones, 1979). Depending on the hydrological regime and climate setting, salinity of closed-basin lakes varies from 0.3 up to more than 350 g L^{-1}. In lakes with salinities above 35-45 g L^{-1}, the osmoregulatory stress makes these environments inhospitable to most life forms. However, once a species finds a solution for this physiological problem, it will be able to tolerate a wide range of changes in salinity (Williams et al., 1990). In higher salinity ranges (> 200 g L^{-1}), the number of thriving species abruptly decline and lake dwellers become more susceptible to salinity fluctuations.

Brine shrimp, *Artemia*, is among those species which can tolerate high salinity ranges but its population and cyst production decline substantially in salinities below 100 g L^{-1} and above 300 g L^{-1} (Wurtsbaugh, 1992; Wurtsbaugh and Gliwicz, 2001).

4.1- Sedimentary and hydrological changes in Lake Urmia

The elemental variations in water and sediments of saline lakes have been widely used to study the evolution of brines, hydrology of the watershed area, and impact of anthropogenic activities on the natural environments (Bąbel and Schreiber, 2013; Jirsa et al., 2013; Jones et al., 2009; Shvartsev et al., 2014). While the geology of the watershed area layouts the elemental signature of the lake, the availability of lithogenic elements (*e.g.* Ti, Zr, Al, Ca, Mg, and K) through production and transportation processes controls the concentrations of these elements in lake's water and sediment. Production of lithogenic elements relies on weathering (both chemical and mechanical) while transportation mainly relies on hydrological processes. Variety of indices have been utilized by different investigators to quantify chemical weathering based on depletion of base forming oxides CaO, MgO, Na_2O, and K_2O relative to Al_2O_3 (Nesbitt et al., 1980; Nesbitt and Young, 1982; Nordt and Driese, 2010; Price and Velbel, 2003). Since the weathering process is directly correlated with rainfall amount, an empirical relationship can be establish to estimate mean annual precipitation (MAP) (Myers et al., 2014; Nordt and Driese, 2010; Sheldon et al., 2002).

4.2- Lithogenic major elements, REE's and radiogenic isotopes in lake sediments as proxy for fluvial sediment flux and source of elements in water

The elemental variations in lake's water and sediment have been widely used to study the sources and input mechanisms of dissolved solids and terrigenous material to the lake as well as to fingerprint the effect of anthropogenic activities in the catchment area (D'Haen et al., 2012; Gibbs, 1970; Revel-Rolland et al., 2005; Revel et al., 2014; Rutberg et al., 2005; Saito, 1998; Stichel et al., 2012). Composition of major ions with respect to total dissolved solids (TDS) in the lake's water can be utilized to determine the primary source of elements.

The major cationic end-members of the world's surface waters are Ca and Na for fresh and saline waters, respectively (Gibbs, 1970). Based on the ionic ratios, Na/(Na+Ca) for cations and Cl/(Cl+HCO_3) for anions, and salinity of the water, the world's surface waters can be classified into three major domains with respect to the mechanism that controls the chemical composition and source of the elements. The first group is the rain-dominated river waters, which have low TDS and Na with high contribution from precipitation (%81) and small contribution (%19) from the rocks. Their composition exemplifies the composition of rainwater and most of the rivers in this setting are located in tropical region. The second group, rock-dominated river type, receives 95.2% of its ions from the rock formation of the catchment and they are in partial equilibrium with the rock types in the catchment. Concentrations of the elements in these waters depend on the climate, relief of the catchment, and composition of rock types. Rivers with this water composition are globally distributed. The third end-member is the evaporation-crystallization river type, with water composition extending from medium salinity (Ca-

rich) to high salinity (Na-rich) endmember. Elemental ratios and concentrations vary as a function of distance from the source origin due to water evaporation and precipitation of $CaCO_3$ from solution. The lakes and rivers in this group are usually found in arid and hot regions.

Elemental ratios of the water can also be used to determine the contribution of different rock types in catchment basin. For example, high ratios of total alkali to total dissolved cations, $(Na+K)/TDS^{+}$, along with low ratios of (Ca+Mg)/(Na+K) is an indication for high contribution of aluminosilicate minerals of crystalline rocks through weathering process. On the other hand, high (Ca+Mg)/(Na+K) ratios could be interpreted as contribution of carbonate rock formations (Singh and Hasnain, 1999).

Elemental ratio of major oxides in the lake's sediment is widely used to determine the role of different rock types in providing the weathered material for the sediment load. Contributions of magmatic rocks generally inferred from ratios of Na_2O/Fe_2O_3, where the ratio above (below) 0.3 are referred to higher contribution from plutonic (volcanic) rocks (Saito, 1998). Abundances of quartz, clay and feldspar content in the sediment can be inferred from SiO_2/Al_2O_3 ratios, while chemical maturity (aging) can be determined using Na_2O/K_2O ratios (Das et al., 2006).

Changes in flux of dissolved materials due to climate variability can be inferred from the Rb/Sr rations of the lake sediments, where lower Rb/Sr rations along with higher Ca and Sr concentrations in the sediments can be related to contribution of carbonate formations (Jin et al., 2006, 2003, 2001). Weathering resistance minerals generally contain high concentration of Zr and Ti, which preferentially enriched in different grain size

fractions (Zr enriched in coarse to medium silt and Ti enriched in finer fractions). Sediments with coarser fractions (sand) are enriched in mobile elements such as K (Taboada et al., 2006). Therefore, K/Ti, Zr/Ti, and K/Rb ratios have been used to determine episodes of terrigenous load to the lake or potential changes in land use (Arnaud et al., 2012; D'Haen et al., 2012; Khan, 2013). A robust evidence for terrigenous flux and more clear distinction of different sources comes from isotopic composition of lake sediments by using isotopic ratios of $^{87}Sr/^{86}Sr$ and $^{143}Nd/^{144}Nd$ (εNd) along with REE's (Arnaud et al., 2012; Revel-Rolland et al., 2005). In general, lower fractions of the terrigenous materials resulted in more negative εNd values (Revel-Rolland et al., 2005; Revel et al., 2014).

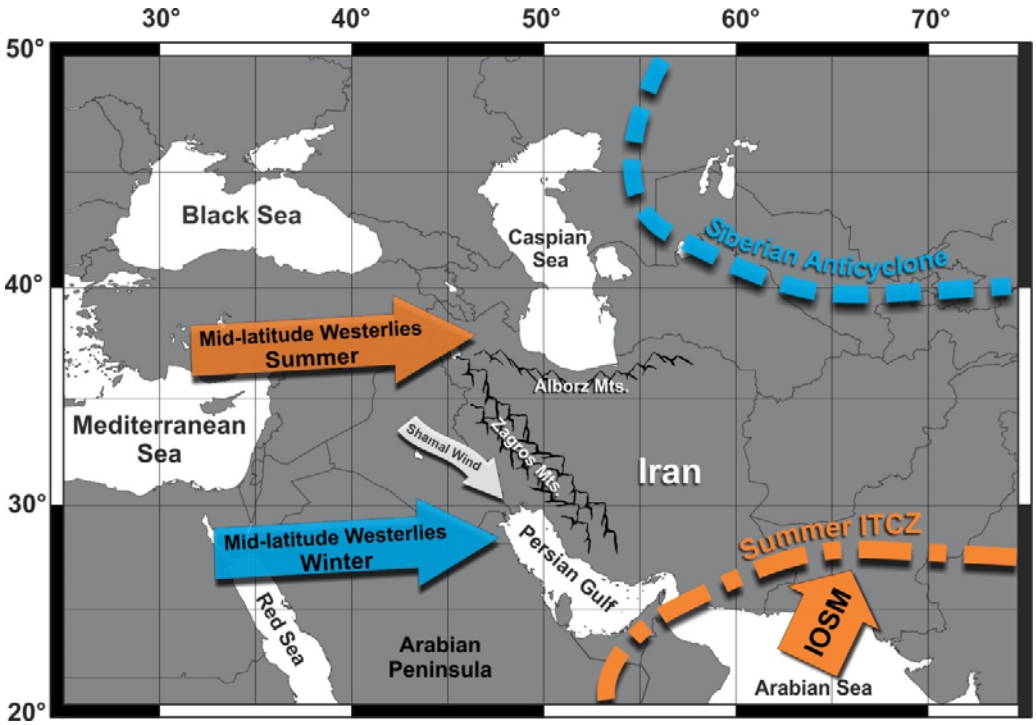

Fig. 1-1. The schematic position of major synoptic systems over West Asia. The Indian Ocean summer monsoon (IOSM) and the approximate summer position of the Inter-tropical Convergence Zone (ITCZ) over West Asia are shown in orange arrow and dashed line respectively. Meridional migration path of the main axis of the northern hemisphere subtropical westerly jet (mid-latitude westerlies) are shown for winter (blue) and summer (orange) after (Schiemann et al., 2009)

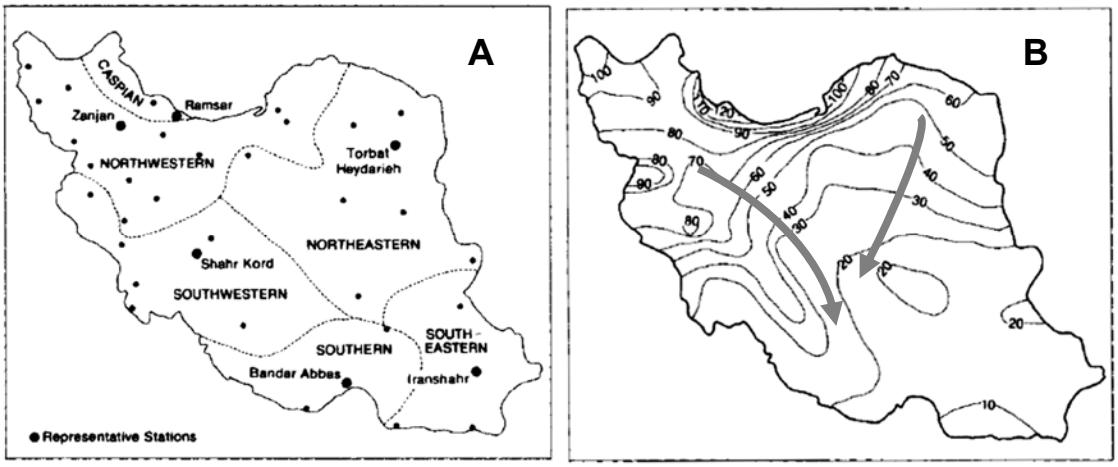

Fig. 1-2. Climate regions and gradients over Iran. (A) Six climatic regions over Iran based on similar predominant uplift mechanism. (B) Mean annual precipitation days (1965-69) showing two major gradients, (Alijani and Harman, 1985).

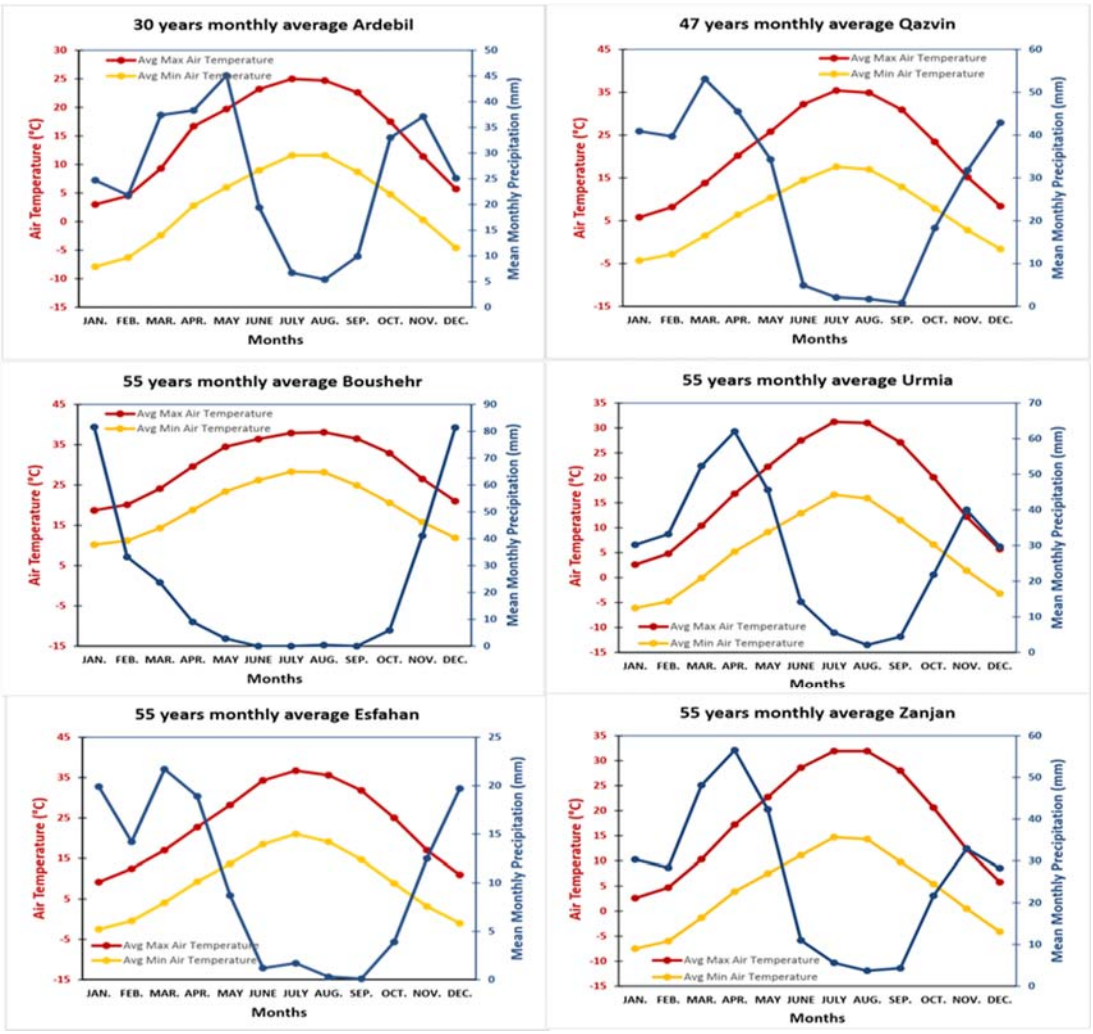

Fig. 1-3. Mean monthly precipitation and air temperature for synoptic stations in Iran over 30 to 55 year time period; Data after IRMO.

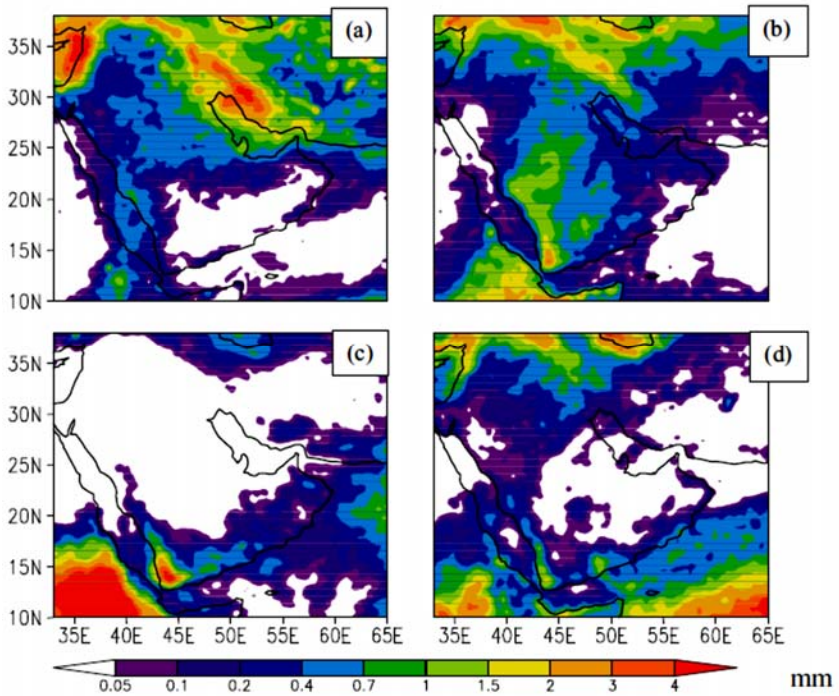

Fig. 1-4. Composite of daily rainfall in mm over the Middle East during January (a), April (b), July (c) and October (d), (Babu et al., 2011).

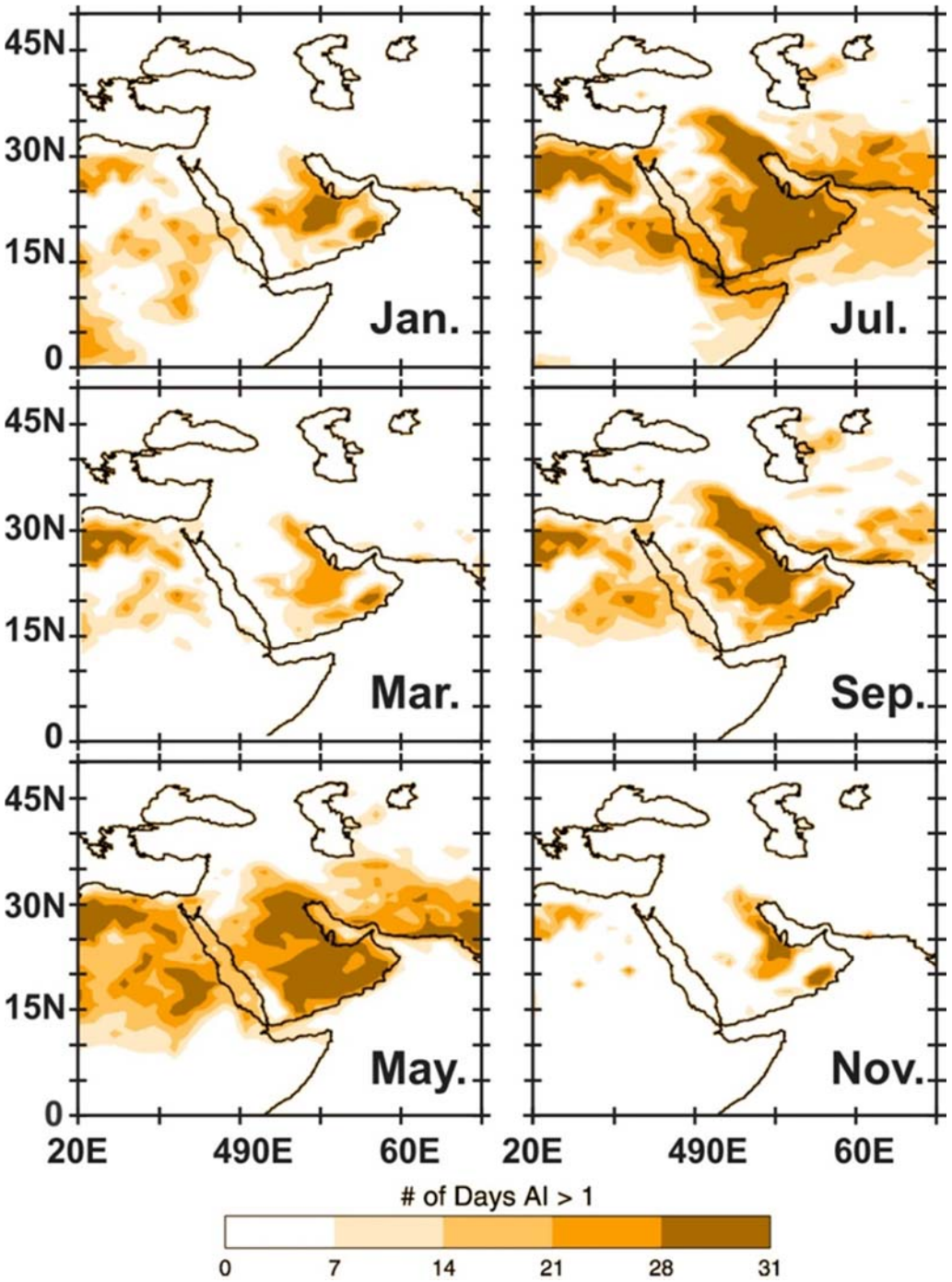

Fig. 1-5. Seasonal variability of dust sources over West Asia based on TOMS during 1980. Color bar represents the number of days in which the aerosol index (AI) was above 1. Modified after Prospero et al., 2002.

CHAPTER 2

Materials and Methods

Summary

The aims of this study were to produce high-resolution, multi-proxy records of climate change with robust chronology through the late Holocene, and to investigate the potential impact of abrupt climate variability on early civilizations in the interior of West Asia. This study uses two complementary approaches using inorganic and organic proxies to reconstruct the climate variability based on peat and lake sediment records from two lakes in Northwest of Iran with two different settings (Fig. 2-1). In this chapter background information about the study areas are provided and sampling methods and analytical techniques are discussed in details.

1- Study area

1.1- Neor Lake

Neor Lake (37°57'37" N, 48°33'19" E) is a seasonally recharged body of water formed over a tectonic depression on the leeward flank of the Talesh (Alborz) Mountains in NW Iran (Fig. 2-2 and Fig 2-3A). The tectonic depression, which formed within an andesitic bedrock as a result of displacements during the Eocene (Madadi et al., 2005) does not receive water from any permanent rivers and has fostered a peripheral peat mire in the southern section of the lake for at least the last 13,000 years. Precipitation in this high-altitude peat mire (~2,500 m above sea level, m.a.s.l.) consists of rain and snow. Water leaves the lake through an incision in the north that has been artificially dammed for the last few decades. The lake surface area is reduced by more than 50% during periods of low precipitation (Fig. 2-3B) (Madadi et al. 2005). Mass accumulation in the peat mire is primarily driven by accretion of decomposing biomass and wet and dry aeolian deposition.

The mean annual precipitation (30-years average) recorded at the nearest meteorological station in Ardebil, located at 1,332 m.a.s.l. and 50 km NE of the lake, exceeds 300 mm. Precipitation is highest in May and November (Fig. 2-3B) and the dry season lasts from July to September. Mean annual temperature at the station is 15.4°C and the mean maximum and minimum temperatures of the warmest and coldest months of the year are 25°C (July) and -7.9°C (January), respectively. As Neor peat mire is 1,200 m higher than the meteorological station, it is not unreasonable to expect higher annual precipitation and lower temperature at Neor relative to the weather station. Vegetation in the lake basin is composed of Irano-Turanian mountain steppe, dominated by thorny-cushions vegetation. Local nomado-pastoral communities exploit both the steppe and the Neor peat mire vegetation.

1.2- Lake Urmia

Prior to the drastic decrease in lake water level and surface area over the last two decades, Urmia Lake (37°29'49"N, 46°00'34"E, 1275 m.a.s.l.) was the second largest hypersaline lake in the world and the largest land-locked body of water in Iran (Fig. 2-4A). The salinity of the lake varies from 140 to more than 220 g L^{-1} on an annual basis. Urmia Lake is formed in a tectonic depression in northwest Iran (Berberian and Arshadi, 1976) and has a catchment area of 52000 km^2 with 13 perennial and seasonal tributaries (Fig. 2-4B). The annual mean river discharge and the mean catchment area of the major rivers are given in table 2-1. The majority of water inflow to the lake is from Zarrineh Rud and Simineh Rud, both of which discharge to the lake from the south (Fig. 2-4B).

The average surface area of the lake varies from 4750 to 6100 km^2 (Eimanifar and Mohebbi, 2007). The Urmia Lake basin is part of the tectonic crush zone between the

colliding Arabian and Eurasian plates (Mckenzie, 1976, 1972). Turkish and Iranian macro-plates are laterally squeezed along a very active strike-slip fault system. Tabriz Fault is one of these fault systems, which crosses along the northern margin of the lake, and is responsible for the actual closure of the drainage basin (Berberian and Arshadi, 1976; Kelts and Shahrabi, 1986). Based on the depth profile, Urmia Lake basin can be divided into two sub-basins; the deep northern basin with an average depth of 10 m and the shallow southern basin with average depth of 2 m (Fig. 2-5, profile A-B).

The geological setting of the lake is quite diverse and its drainage basin is comprised of a variety of rock formations with different ages, ranging from the Precambrian metamorphic complexes to quaternary mud deposits (Fig. 2.6). Volcanic and volcano-sedimentary formations are most dominant in the east and northeast of the catchment basin, while intrusive rocks are mainly found in the south, west and northwest. The distribution of metamorphic rocks are mainly limited to the southern and, to a lesser extent, northwestern part of the basin. Carbonate sedimentary units are mainly found in south and western parts and evaporite sedimentary units are only found in northeast of the watershed area. The Urmia Lake sediments comprise of chemically precipitate aragonite , shrimp fecal pellet sands, detrital clay, thin aragonite crusts, oolites, evaporites such as gypsum and traces of dolomite in peripheral areas (Kelts and Shahrabi, 1986; Shah-Hosseini, 2003; Sharifi, 2002).

The climate of the Urmia region is classified as Mediterranean pluviseasonal–continental (Rivas-Martinez et al., 1999) with mean annual winter temperature reaching below -10°C and summer temperatures of up to 40°C across the watershed area (Fig. 2-4C). Most of the precipitation occurs during winter and spring months with maximum

precipitation in spring from March to May (Fig. 2-4C). Mean annual precipitation recorded at the Urmia meteorological station (west of Urmia Lake at 1313 m.a.s.l) for the last 55 years return an average of 340 mm with evaporation estimated at about 1 m yr^{-1} (Sima et al., 2013), which can increase to 1.5 m yr^{-1} by strong NW-SE seasonal winds (Kelts and Shahrabi, 1986). Mean annual temperature recorded at Urmia meteorological station is 11.2°C with the minimum of −2.5°C in January and maximum of 23.9°C in July. The 25- to 50-year average annual prevailed wind direction over the Urmia Lake watershed area is mainly westerly and southwesterly, however in Tabriz and Maraqeh meteorological stations, both located on the east of Urmia Lake, easterlies are the dominant average annual prevailed wind direction.

2- Core samples

2.1- Peat core

In the summer of 2010, we recovered a 7.5-meter core from the southwest part of the Neor peat mire (Fig. 2-2), as well as two additional cores of about the same length recovered from within 2 meters of the main core. Half-barrel cores were collected in 1-m increments of 7-cm diameter using a Russian Split Corer until the basal bedrock was reached. The final segment of the core included dense, laminated gyttja and a mixture of andesitic gravel from the bedrock. The cores were photographed on site and transferred into PVC core liners, sealed in non-reactive plastic sheets and stored at 4 °C and constant humidity at the core repository of the Rosenstiel School of Marine and Atmospheric Science (RSMAS), the University of Miami. The physical properties of the core segments were logged (see appendix A), and changes in core dimensions were closely monitored

throughout the course of the study as peat water content tended to vary with time. Each core segment was transferred into an especially-designed polymethyl methacrylate core holder and PVC liner with scale bars for reference. The cores were subsequently imaged using a Geotek Multi-Sensor Core Logger (GeotekMSCL) at the Department of Marine Geosciences (MGS), RSMAS and the images were calibrated for cross-core resolution, light intensity and white balance. The position of each sample taken for discrete organic and inorganic geochemical analyses was determined based on comparing down-core XRF elemental intensities and core images. Samples were taken from areas of high terrigenous input, which correspond to high XRF intensities, areas of high organic content with low XRF intensities as well as midpoints in order to capture the entire range of variability and minimize the effect of aliasing. The sampling resolutions are specific to each proxy (see the following sections). Sub-samples were taken for organic and inorganic geochemical analyses using a pre-cleaned ceramic knife and the samples were dried at 45 °C over 5 days. The water content was measured for each sample gravimetrically based on sample masses before and after evaporation.

2.2- Short and long lake sediment cores

In the spring of 2002, nineteen short (50-cm long) core samples were collected from inside the lake (Fig. 2-7) using KC gravity corer and preserved in acid rinsed polyethylene tubes at 4°C until they were split-opened and photographed in the lab. Sub-samples were taken with 2 cm intervals from the cores using a pre-cleaned plastic knife. The upper most sub-samples from the cores are treated as surface sediment samples. Sub-samples were oven-dried at 50°C for three days. Approximately 5 grams of dried sample was used to extract the detrital silicate fraction of the sediments. The soluble salt content of the samples

was removed by multiple sequential stages of 30-minutes agitation, 30-second sonication and 20-minutes of centrifuging at 3500 rpm using the MQ water (Millipore, resistivity > 18 MΩ). After removing the supernatant solution, organic content as well as biogenic and detrital carbonate of the samples were removed using 30% H_2O_2 and 3% HCl solutions respectively. Subsequently, the samples were oven dried at 60°C and a representative portion was used for grain size analysis. A second portion was finely powdered in pre-cleaned agate mortar and used for bulk chemical analysis. All samples were processed at the marine geology laboratory of the Iranian National Institute of Oceanography and Atmospheric Science (INIOAS) in 2002.

In the summer of 2012, we recovered a 5-m core (U-6) and a duplicate core (U-7) from the east coast of the Urmia Lake as well as two additional 2-m cores from southwest and south parts of the lake (U-1 and U-4 respectively)(Fig. 2-7). Half-barrel cores were collected in 1-m increments of 7-cm diameter using a Russian Split Corer. All cores were photographed on site and transferred into pre-cleaned PVC core liners, sealed in non-reactive plastic sheets and stored at 4 °C. The physical properties of the core segments were logged (see appendix A), and changes in core dimensions were closely monitored throughout the course of the study at the Rosenstiel School of Marine and Atmospheric Science (RSMAS), the University of Miami. Individual core segments were transferred into an especially-designed polymethyl methacrylate core holder and PVC liner with scale bars. The cores were subsequently imaged using a Geotek Multi-Sensor Core Logger (GeotekMSCL) at the Department of Marine Geosciences (MGS), RSMAS. Calibration for white balance, light intensity and cross-core resolution was conducted prior imaging. Down-core XRF elemental intensities and core images were used to determine the position

of each sample taken for discrete geochemical analyses. In order to minimize the effect of aliasing and to capture the entire range of variability, samples were taken from areas of high and low XRF intensities as well as midpoints. Sub-samples were taken using a pre-cleaned ceramic knife and the samples were dried at 45 °C over 5 days. The water content was measured gravimetrically using sample masses before and after evaporation.

3- Water samples

Water samples were collected from 34 locations across the lake at various depths, ranging from 0.5m up to 4.8m by the Azarbaidjan Regional Mining Cooperation (Fig. 2-7) during May and October 1987. The samples were analyzed for major ions at the chemistry department of Tabriz University, Iran (ARMC-Azarbaidjan Regional Mining Cooperation, 1995). To our knowledge, these samples are the only available seasonal hydrochemical data for the Urmia Lake (Tolouei, 1995). We used these data to study the Hydrochemistry of the major ions inside the Urmia Lake. We also compare this dataset with other available hydrochemical data from Urmia Lake, its peripheral ponds and major tributaries (Karbassi et al., 2010; Kelts and Shahrabi, 1986; Mohajer Bavaghar, 1997; Shahrabi, 1994; Tolouei, 1995). See Table SI-1 in supplementary data file (appendix B) for compilation of the hydrochemical data.

4- Major and trace element analysis by XRF scanning

High-resolution measurements of the relative abundances of trace and major elements were performed on an AVAATECH XRF-core scanner in the Palaeoclimatology Lab at RSMAS-MGS. All core sections were scanned twice (10kV, 1000μA, no filter; 30kV, 1000μA, Pd filter) to acquire the range of elements reported here. For all

measurements, the surface area was irradiated for 20 seconds of integration time at 2-mm intervals (average resolution of 3.5 yr, see section 5 for chronology) using a window 2-mm high by 12-mm wide for the peat core and at 1-mm intervals (an average sampling resolution of 2.5 yr, see section 5 for chronology) using a window 1-mm high by 12-mm wide for the lake sediment cores. The raw XRF spectra were then processed using the Canberra WinAxil software with standard software settings and spectrum-fit models, and abundances are reported as the intensity of each element in counts per second (cps). The JR-1 standard (Geological Survey of Japan) was used for calibration, and calibrated data were compared with previous measurements to check for discrepancies.

The XRF elemental abundances along the peat core is interpreted as a qualitative proxy for changes in atmospheric dust input throughout the core. In addition, the aeolian fluxes is calculated based on discrete analysis of Ti concentrations from a sub-set of 60 samples that corresponded to intervals of high, intermediate and low Ti intensities from XRF measurements and the bulk dry density of the peat core as described below. As for the lake sediments, the down core XRF elemental abundances is interpreted as a qualitative proxy for changes in sediment load to the lake throughout the core.

5- Age model

5.1- Neor Lake

Based on variations in the intensity of lithogenic elements measured by XRF (see section 4), 19 sub-samples were submitted for ^{14}C dating to the National Ocean Sciences Accelerator Mass Spectrometry Facility (NOSAMS), Woods Hole Oceanographic Institution. At NOSAMS, samples were pretreated using acid-only or acid-base-acid

protocols prior to graphitization based on their organic contents. Ages were based on ^{14}C analysis and associated uncertainties were calibrated using CALIB 6.0 program (Stuiver et al., 1998) by utilizing IntCal13 calibration dataset (Reimer et al., 2013). Ages are reported as calibrated year before present (cal. yr BP). The age model based on 19 calibrated radiocarbon dates is shown in Fig. 2-8, and the data are presented in Table 2-2. The average sedimentation rate (SR) calculated based on the age-depth model was 0.9±0.6 (SD) mm yr^{-1}, with the lowest rates dominating the early to mid-Holocene and the highest rates occurring after 1,500 cal. yr BP to the present (Fig. 2-8).

5.2- Lake Urmia

As discussed previously, the effect of reservoir carbon on radiocarbon dates are substantial in Urmia Lake and must be characterized in order to establish a robust chronology for paleoclimate reconstructions. To measure the effect of old carbon on calibrated radiocarbon dates, we compared the radiocarbon dates of shrimp fecal pellets, organic matter from shrimp cysts and bulk sediment from homogenized sediments. Approximately 20 mg of intact fecal pallets (Shah-Hosseini, 2003) and shrimp cyst were collected from two 15-cm intervals at 0.65 and 5.4 meter of the sediment core. Samples were rinsed in 1 mL of 0.01 M HCl solution followed by 5 mL of MQ water to remove potential carbonate contamination and were dried in the oven at 40°C for 4 hours. A homogenized bulk samples were also collected from the same intervals. These samples along with 8 other bulk sub-samples from core U-6 (Fig. 2-9 and 2-10) were submitted for ^{14}C dating to Beta Analytic Co. Ltd., Miami. Bulk samples were pretreated using acid-only protocol prior to graphitization. No further treatment was conducted on shrimp cysts and fecal pellets. Ages were based on ^{14}C analysis and associated errors were calibrated using

CALIB 6.0 program (Stuiver et al., 1998) by utilizing IntCal13 calibration dataset (Reimer et al., 2013). Since the shrimp cysts contained the most pristine organic content in the Urmia Lake sediment (Morteza Djamali et al., 2010; Manaffar et al., 2011), the age difference between the radiocarbon dates driven from shrimp cyst and the ones from the bulk or fecal pellet samples collected from the same interval are considered to be the best representation of the "reservoir effect". Subsequently, all radiocarbon dates were corrected for the reservoir effect and reported as calibrated year before present (cal. yr BP).

Comparative calibrated radiocarbon ages from bulk sediment, shrimp fecal pellet and shrimp cyst extracted from 0.65 and 5.4 meter intervals of the long core from the NE margin of the lake are shown in Fig. 2-9 and the data are presented in Table 2-3. Among the collected samples, shrimp cyst returned the youngest age. By averaging the age difference between shrimp cyst calibrated radiocarbon dates and the ones from bulk sediment and fecal pellet samples at 0.65 and 5.4 meter intervals, we considered a 560- and 719-year correction on bulk sediment and fecal pellets radiocarbon dates, respectively to account for the Urmia Lake's reservoir effect. The age model based on 8 calibrated radiocarbon dates is shown in Fig. 19 (see Table 2-3 for the data). The minimum and maximum sedimentation rates (SR) calculated based on the age-depth model were 0.05 to 1.45 mm yr^{-1} respectively, with the overall decreasing trend from the early Holocene to the late Holocene.

6- Bulk density

Bulk density of peat material is required for quantifying atmospheric deposition. However, accurate measurement of bulk density in peat and poorly consolidated sediment

is challenging. As a result, bulk density of sediments is often assumed to be constant in the sedimentary record or is measured on discrete samples using destructive gravimetric and volumetric techniques (Boelter, 1966; Chambers et al., 2011; Janssens, 1983). In addition to sample loss, this approach is not suitable for organic-rich sediments with high porosity.

I utilized a novel, alternative approach using Gamma Ray Attenuation Porosity Evaluator (GRAPE) data (Evans, 1965). The bulk density based on gamma ray attenuation measurements as part of the GEOTEK-MSCL is calculated from the following equation:

$$\rho = \frac{1}{\mu d} \, ln \frac{I_0}{I} \qquad \text{(eq. 2-1)}$$

where "ρ" is sediment bulk density, "μ" is the Compton attenuation coefficient, "d" is the sediment thickness and "I_0" and "I" are the gamma intensity of the source and measured through the sample, respectively. To generate high quality density data, corrections must be implemented for experimental factors such as water content, beam spreading and attenuation through the PVC core liner. We took an empirical approach to calibrating the gamma density measurements by using half-cylinder aluminum calibration tubes of varying thicknesses that resembled the split peat cores (Fig. 2-11). Gamma counts were measured for 100 seconds along the calibration tubes that were encased in PVC core liners and filled with water. The average densities at different thicknesses were calculated using the following equation:

$$\rho_{av} = \left(\frac{d_i}{D}\right) * \rho_{Al} + \frac{(D - d_i)}{D} * \rho_{water} \qquad \text{(eq. 2-2)}$$

where "ρ_{av}" is the average density, "d_i" is the thickness of the aluminum calibration tube, "D" is total thickness and "ρ_{Al}" and "ρ_{water}" are the density of aluminum and water, respectively. The natural log of gamma intensities was then plotted against the average

density of aluminum and water for various tube thicknesses ($\rho_{av} \times d$ vs. *ln (cps)*). The best-fit line through the measured values deviated from the theoretical line (Fig. 2-12) as a function of the variables mentioned above. The multi-sensor was calibrated for measuring wet bulk density using the following empirically-derived equation and the Gamma ray attenuation counts from the Neor peat core at increments of 1 cm and 10 seconds of integration time:

$$y = -0.07x + 8.8991 \quad \text{(eq. 2-3)}$$

where $y = ln(cps)$ and $x = \rho \times d$. Parameter d is the core thickness. Measurements of wet bulk density were performed on an adjacent core and transferred to the main core using the near-identical profiles of lithogenic elements. The dry bulk densities were calculated using the equation below and the water content of sub-samples extracted from the main core:

$$\rho_{dry} = (1 - \frac{Water\,\%}{100}) \times \rho_{wet} \quad \text{(eq. 2-4)}$$

where "ρ_{dry}" and "ρ_{wet}" are the dry and wet bulk densities respectively.

7- Geochemical Discrete Analysis

7.1- Total organic carbon (TOC), total nitrogen (TN) and stable isotope composition of organic carbon ($\delta^{13}C_{TOC}$, $\delta^{15}N_{TOC}$)

Based on elemental variations identified using the XRF data, 400 sub-samples (average resolution of 30 yr) were collected for TOC, TN and $\delta^{13}C$ and $\delta^{15}N$ analyses. Between 0.002-0.015 g were sampled from 0.5-1.5 g of dried and homogenized peat material. Samples were transferred into pre-cleaned tin cups and treated with 10% HCl to remove inorganic carbon according to the procedure described in Hedges and Stern (1984).

Total organic carbon was measured with a Thermo Scientific® Flash 2000 CHN analyzer at the Virginia Institute of Marine Science (VIMS). Quality control and data reproducibility procedures included analyzing duplicate samples and multiple acetanilide standards and use of an acetanilide standard curve with a correlation coefficient (R^2) > 0.99. The $\delta^{13}C$ and $\delta^{15}N$ were determined at the RSMAS stable isotope laboratory (SIL) using a Costech elemental combustion system interfaced with a Thermo Scientific® Delta V Advantage continuous flow isotope ratio mass spectrometer. Reproducibility (<0.01‰) was assessed from repeated analysis of acetanilide and glycine standards.

Total organic carbon in samples from Urmia Lake was gravimetrically established by removing the organic content from bulk sediment. Approximately 0.5 g dried and homogenized sample was transferred to a 250 mL glass beaker and 50 mL of 10% hydrogen peroxide (H_2O_2) was introduced to the sample while stirring. Additional H_2O_2 was added until no fizzing was observed. Samples were oven dried at 70°C for several days.

7.2- Stable carbon and oxygen isotope analysis

Stable carbon and oxygen isotope measurements were conducted on shrimp fecal pellets samples. Approximately 0.002-0.005 g of intact fecal pellets were collected from 12 intervals along the core from 9,100 to 10,500 cal. yr BP. Samples were rinsed with MQ water and dried in the oven at 40°C. The $\delta^{18}O$ and $\delta^{13}C$ measurements were conducted at the RSMAS stable isotope laboratory (SIL) using a Kiel III interfaced with a Thermo-Finnigan Delta Plus Mass Spectrometer. All data have been corrected for inferences at mass 45 and 46 and reported relative to Vienna Pee Dee Belemnite (VPDB). The precision

of the $\delta^{18}O$ and $\delta^{13}C$ values (<0.01‰) was assessed from repeated analysis of from repeated measurements of an internal standard.

7.3- Elemental analysis

An assessment of elemental distribution patterns in Urmia Lake surface sediments was conducted by analyzing 19 homogenized and carbonate-free core top samples for major oxides and trace elements. Approximately 0.2 g of carbonate-free sediment was fused with 0.9 g of lithium metaborate/lithium tetraborate flux at 1000°C. The resulting melt was dissolved in 100 mL of 4% HNO_3:2% HCl acid mixture. This solution was analyzed by direct dilution by ICP-AES for major elements and by ICP-MS for trace element concentrations and the results were corrected for spectral inter-element interferences. Concentration of major elements were calculated from the determined elemental concentrations and reported as concentration of oxide in percent (%), where concentrations of trace elements were reported in part per million (ppm; µg/g). Loss on Ignition (L.O.I.) values were gravimetrically calculated by heating 1.0 g of sample at 1000°C for one hour. Analytical accuracy was assessed by analyzing certified reference material CRM277 and MAG-2 and results were within 1% to 2% of literature compilations for various elements. Bulk elemental analysis of surface samples and short cores were conducted at the ALS Chemex in Vancouver, Canada.

In order to quantify the XRF results and to calculate variation in weathering indices over the last 11,600 years, 68 samples (average sampling resolution of ~185 yr) were collected for analysis of major oxides. Approximately 1 g of dried and homogenized sample was transferred to 50 mL centrifuge tube and rinsed with MQ water following

sequential stages of 30-minutes agitation, 30-second sonication and 20-minutes centrifuging at 3500 rpm. The supernatant solution was transferred into a 50 mL centrifuge vial and saved for further analysis (see section 7-5). Dried sample was transferred to capped, high-purity quartz crucibles and ashed in a muffle furnace at 750 °C for one hour to remove organic materials. A 20 mL solution of 1 M NaAc in 25% HAc (final pH = 4) was added to the organic-free sample in a 50 mL centrifuge vial and continuously agitated for 2 hours at room temperature to remove the carbonate content. Sample was centrifuged at 5000 rpm for 15 min and the supernatant solution was discarded. This stage was repeated until no fizzing/bubbling was visible. The sample was rinsed with MQ water twice and oven dried at 60°C overnight. Approximately 0.01-0.02 g of organic and carbonate free sample was transferred to a pre-cleaned 6-ml PFA Savillex vial and dissolved in 5 mL of concentrated HNO_3-HCl-HF mixture (2:2:1, volumetric ratios) following the method described by Sharifi et al, 2015. After complete digestion was achieved, about 0.1 g of the solution was diluted in 40 g of 0.45 mol L^{-1} HNO_3 and elemental concentrations was measured against a multi-elemental standard solution (Spex CertiPrep) of known concentration (±5 ‰) by sample-standard-sample bracketing technique on the multi-collector inductively coupled plasma mass spectrometer (MC-ICPMS) at the Neptune Isotope Laboratory (NIL), RSMAS. Elemental concentrations were reported as percent of oxides. The accuracy and precision of measurements were evaluated by comparing analyses of USGS certified reference material BHVO-2 with literature compilations (GEOREM, http://georem.mpch-mainz.gwdg.de/). Results for reference materials agreed well with literature values within analytical uncertainties (Fig. 2-12). Contributions from the procedural blank were negligible (smaller than 0.1 %).

7.4- Ti concentration and aeolian flux

In order to quantify the flux of dust to Neor peat mire over the last 13,000 years, 60 samples (average resolution of ~220 yr) were collected to be analyzed for Ti concentration. Approximately 0.2 g of peat material was transferred to capped, high-purity quartz crucibles and ashed in a muffle furnace at 750 °C for one hour. Approximately 0.01-0.02 g of the ashed residue was transferred to a pre-cleaned 6-ml PFA Savillex vial and dissolved in 5 mL of concentrated HNO_3-HCl-HF mixture (2:2:1, volumetric ratios). The vials were placed in an ultrasonic bath for 2 hours at 80 °C and then heated at 220 °C on a hotplate overnight. After complete digestion was achieved, about 0.1 g of the solution was diluted in 40 g of 0.45 mol L^{-1} HNO_3 and Ti concentration was measured against a mono-elemental standard solution (Spex CertiPrep) of known concentration (±5 ‰) by sample-standard-sample bracketing technique on the multi-collector inductively coupled plasma mass spectrometer (MC-ICPMS) at the Neptune Isotope Laboratory (NIL), RSMAS. Concentrations calculated based on ^{48}Ti, ^{49}Ti and ^{50}Ti isotopes were identical within uncertainties. The accuracy and precision of Ti measurements were evaluated by comparing three replicate analyses of USGS certified reference materials BCR-2 and BHVO-2 with 16 and 26 literature compilations (GEOREM, http://georem.mpch-mainz.gwdg.de/), respectively. Results for both reference materials agreed well with literature values within analytical uncertainties (Fig. 2-14). Contributions from the procedural blank were negligible (smaller than 0.1 %). Nevertheless, corrections were applied to all measurements prior to calculating Ti concentrations.

Aeolian fluxes were calculated based on Ti concentrations in peat ash residues (Ti_{ash}) and assuming an average Ti concentration of 0.40% (4010 μg g^{-1}) in continental crust (Wedepohl, 1995) through the following equations (Bao et al., 2012):

$$Ti_{ash}\ (\mu g\ g^{-1}) = Ti(\mu g\ g^{-1}) \times (\frac{Ash(\%)}{100})/(0.4) \quad \text{(eq. 2-5)}$$

$$Aeolian\ Flux\ (\mu g\ cm^{-2}y^{-1}) = Ti_{ash}(\mu g\ g^{-1}) \times \rho_{dry}(g\ cm^{-3}) \times r(cm\ y^{-1}) \quad \text{(eq. 2-6)}$$

where "r": is the average accumulation rate (mm y^{-1}) and "ρ_{dry}" is the dry bulk density (g cm^{-3}) measured as described above.

7.5- Radiogenic Sr isotope analysis

In order to assess if changes occurred in source rock contributions to lake water chemistry through time, we measured radiogenic Sr ($^{87}Sr/^{86}Sr$) isotopic composition on four bulk samples, four shrimp fecal pellets and 10 pore water/soluble salt samples along an interval from 9,100 to 10,500 cal. yr BP that showed large variations in Al abundances of XRF measurements. Approximately 0.015 g of intact fecal pellet was digested in 5 mL of 0.45 M HNO_3. This solution was directly measured by MC-ICPMS. Approximately 0.035 g of bulk sample was fused with $LiBO_2$ alkali flux following the method by Pourmand and Dauphas, (2010). Sr was separated from the matrix through a three-stage extraction chromatography scheme following the method by Pourmand et al. (2014) and analyzed by MC-ICPMS. The pore water/soluble salt samples collected in section 3.5.1 was diluted by factor of two in 5 mL of 0.45 M HNO_3 solution and analyzed by MC-ICPMS without any further processing. All measurements were conducted at the Neptune Isotope Laboratory (NIL), RSMAS.

7.6- Radiogenic Sr-Nd-Hf isotope and REE analysis

In order to investigate the changes in sources of dust to Neor peat mire over the last 13,000 years, 41 samples (average resolution of ~330 yr) of about 1 gram were taken from high and low dust intervals based on XRF elemental profiles of a 7.5 m core from Neor Lake's peripheral peat complex. Dried samples were homogenized in an agate mortar and ashed at 750 °C for one hour. Approximately 0.015 to 0.035 g was fused with $LiBO_2$ alkali flux in a high-purity graphite crucible at 1170 ℃ for 12 minutes to ensure complete dissolution of refractory minerals (Pourmand et al., 2012; Pourmand and Dauphas, 2010). Sr, Nd, Hf and the REEs were separated from the matrix through a three-stage extraction chromatography scheme previously developed for aerosol analysis (Pourmand et al., 2014). Measurements were conducted on a ThermoFisher Scientific Neptune Plus multi-collector inductively coupled plasma mass spectrometer at the Neptune Isotope Lab. The measured $^{143}Nd/^{144}Nd$ and $^{177}Hf/^{177}Hf$ ratios are reported in " ε " notation relative to the Chondritic Uniform Reservoir (CHUR) values of 0.512638± 25 and 0.282785 ± 11, respectively (Bouvier et al., 2008). Model Sm-Nd ages for source rocks were calculated based on assuming $^{143}Nd/^{144}Nd$ = 0.51315 for depleted mantle and a simple evolution leading to modern $^{147}Sm/^{144}Nd$ = 0.2137 (Goldstein et al., 1984; Grousset et al., 1988a) using the equation below:

$$T_{CHUR} = \frac{1}{\lambda} * ln\left[\frac{\left(^{143}Nd/^{144}Nd\right)_{Sample,today} - \left(^{143}Nd/^{144}Nd\right)_{CHUR,today}}{\left(^{147}Sm/^{144}Nd\right)_{Sample,today} - \left(^{147}Sm/^{144}Nd\right)_{CHUR,today}} + 1\right] \qquad \text{(eq. 2-5)}$$

where the T_{CHUR} is the model Sm-Nd age and λ is the decay constant (6.25×10^{-12} y^{-1}). As a result, relative changes in model ages are more meaningful than the absolute ages. See

appendix C for details of extraction chromatography scheme for aerosol analysis and instrumental setting for isotope measurements.

7.7- Compound-specific hydrogen isotope analysis

Alkanoic acids were separated from the total lipid extract of 39 samples (average resolution of ~340 yr) fron Neor peat core using column chromatography (5 cm × 40 mm Pasteur pipette, NH2 sepra bulk packing, 60 Å). Separation was achieved by eluting with 2:1 DCM:isopropanol, followed by 4% formic acid in diethylether, yielding neutral and acid fractions, respectively. The acid fraction was esterified with 5% HCl and 95% methanol of known isotopic composition at 70 °C for 12 h to yield corresponding fatty acid methyl esters (FAMEs). FAMEs were obtained by liquid-liquid-extraction using hexane as a non-polar solvent, and traces of water picked up during sample processing were removed by passing the sample through a column of anhydrous Na_2SO_4. FAMEs were further purified using column chromatography (5 cm × 40 mm Pasteur pipette, 5% water-deactivated silica gel, 100–200 mesh), eluting with hexane, followed by FAMEs eluted with DCM.

Compound specific hydrogen isotopic values were obtained using gas chromatography isotope ratio mass spectrometry (GC-IRMS). We used a Thermo Scientific® Trace gas chromatograph equipped with a Rxi-5ms column (30 m × 0.25 mm, film thickness 1μm) and a programmable temperature vaporizing (PTV) injector operated in solvent split mode with an evaporation temperature of 60 °C. The GC was connected via a GC Isolink with a pyrolysis furnace (at 1,400 °C) via a Conflo IV interface to a DeltaVPlus isotope ratio mass spectrometer. The H_3^+-factor was determined daily to test

linearity and accounted for 6.1 ppm mV^{-1} on average. Reference peaks of H_2 were co-injected between *n*-alkanoic acid peaks during the course of a GC-IRMS run; two of these peaks were used for standardization of the isotopic analysis, while the remainders were treated as unknowns to assess precision. Except for the case of co-elution, precision of these replicates was better than 0.6‰. The data were normalized to the VSMOW/SLAP hydrogen isotopic scale by comparing with an external standard containing 15 *n*-alkane compounds (C_{16} to C_{30}) with known δD values obtained from A. Schimmelmann, Indiana University, Bloomington. The RMS error of replicate measurements of the standard across the course of analyses was 4.62 ± 0.83‰. We further monitored for instrument drift by measuring the δD values of a C_{34} *n*-alkane internal standard co-injected with the sample (240.6 ± 3.0‰; n = 105). The isotopic composition of H added during methylation of alkanoic acids was estimated by methylating and analyzing phthalic acid as a dimethyl ester (isotopic standard from A. Schimmelmann, University of Indiana) yielding $\delta D_{methanol}$ = –198.3‰ ± 3.9 (n = 7). Correction for H added by methylation was then made by way of mass balance.

7.8- Calcimetry

Carbonate content ($CaCO_3$+$MgCO_3$) of the bulk sediment was measured based on the volumetric analysis of the carbon dioxide (CO_2) (Hulseman, 1966) using Bernard calcimeter. Under constant pressure and temperature, approximately 0.5 g of dried and homogenized bulk sample was evolved with 10 mL of 4M HCl in closed vessel and the volume of CO_2 was measured by means of a burette filled with $CaCl_2$ buffer solution. The calibration was conducted by reacting 0.2 g pure calcium carbonate as standard with 10 mL of 4M HCl. The carbonate content is calculated using the equation below:

$$Carbonate\ Content\ (\%) = \frac{m_2 \times V_1}{m_1 \times V_2} \times 100 \qquad \text{(eq. 2-7)}$$

Where m_1 and m_2 are the masses of sample and standard respectively. The V_1 and V_2 are the CO_2 volume produced by sample and standard after reacting with HCl.

8- Measurement of carbon accumulation rate

Changes in the Long Term Rate of Carbon Accumulation (LORCA), which is a function of carbon production and preservation, were calculated based on 71 samples following the method described in Tolonen and Turunen (1996) and using the following equation (Page et al., 2004):

$$LORCA\ (g\ C\ m^{-2}\ y^{-1}) = r \times 10000 \times \rho_{dry} \times c \qquad \text{(eq. 2-8)}$$

where "r" is the average accumulation rate (mm y^{-1}), "ρ_{dry}" is dry bulk dry density (g cm^3) and "c" is carbon content (g C g^{-1} dry weight).

9- Lipid extraction and n-alkane separation

Total lipids were extracted from approximately 1 g of 97 dried and homogenized peat samples (average resolution of ~140 yr) with a solution of 2:1 dichlorometane:methanol (DCM/MeOH) using an Accelerated Solvent Extractor (Dionex ASE-200). The lipid extracts were partitioned into the organic phase following addition of methanol and NaCl-saturated water. Samples were concentrated to 1 ml using a Turbo-vap system under N_2 gas and half of the sample was used to separate *n*-alkanes from the remaining lipids through column chemistry. Samples were blown to "just dry" under N_2 and re-dissolved in hexane. Columns were packed with 5% water-deactivated silica gel (100–200 mesh) using hexane. Samples were eluted by three solvents, 10 mL of hexane,

10 mL of 25% toluene in hexane and 10mL of MeOH. The first fraction was reduced to 0.5 mL under N_2 using the Turbo-vap. Concentrations of all *n*-alkanes present in the sample were identified using gas chromatography mass spectrometry (GC-MS) and individual *n*-alkanes were quantified relative to an internal standard (5α-cholestane). The abundance of hydrophilic floating and submerged plants (medium chain *n*-alkanes: C_{23}, C_{25}) relative to terrestrial plants (characterized by long chain *n*-alkane: C_{29}, C_{31}) was quantified according to "$P_{aqueous}$" (P_{aq}) ratio employing the equation below (Ficken et al., 2000):

$$P_{aq}=(C_{23}+C_{25})/(C_{23}+C_{25}+C_{29}+C_{31}) \quad \text{(eq. 2-9)}$$

10- Grain size analysis

10.1- Neor Lake

A total of 23 samples were taken from high and low dust intervals along the core and dried overnight at 105°C. The organic component was oxidized using a solution of 30% hydrogen peroxide (H_2O_2) at 200°C. The remaining fraction was then resuspended in a 0.3% Hexametaphosphate solution and sub-sampled under stirring. The grain-size distribution was measured using a Beckman Coulter LS 13320 laser granulometer with a range of 0.04 to 2000 μm at Aix-Marseille Université , Centre de Recherche et d'Enseignement de Géosciences de l'Environnement (CEREGE, France).

The particle size calculation model was performed in accordance with the Fraunhöfer and Mie theory, in which water was used as the medium (Refractive Index = 1.33 at 20 °C). A refractive index in the range of kaolinite was utilized for the solid phase (RI = 1.56) along with absorption coefficients of 0.15 for the 780-nm laser wavelength, and 0.2 for the

polarized wavelengths (Buurman et al., 1996). Sample size reproducibility based on independent replicate measurements of the same sample did not exceed 2% (Psomiadis et al., 2014). Additionally, measurements of the SRM 1003C NIST standard, certified at a D50 of 32.1 ±1 μm based on SEM analysis, returned a D50 of 31.99 μm, which is within the analytical uncertainty.

10.2-Lake Urmia

To examine changes in sedimentary regime and anthropogenic remobilization of sediments within the lake basin as a result of the construction of Kalantari Causeway, grain size analysis was conducted on detrital silicate fraction of the Urmia Lake core top samples as well as samples along the short cores using FRITCH Laser Particle Sizer (Analysette 22, Comfort). The organic component was oxidized using a solution of 18% hydrogen peroxide (H_2O_2) at room temperature for several days. The remaining fraction was then reacted with 2% HCl to remove detrital and autogenic carbonate fraction. To prevent sample from coagulation, 5% sodium hexametaphosphate ($Na_6(PO_3)_6$) solution was added to the samples prior to measurement. Samples were introduced to the laser particle sizer via a wet dispersion unit and sonication mode was active during the measurement. Each sample was measured four times within the 1.25 mm to 0.163 μm size range and number of scans was set at 30. The accuracy of measurement was assessed (<0.5%) by analyzing FRITCH 10-100 μm reference material.

11- Wavelet analysis

In order to track the degree of coherence between elemental pairs from the XRF measurements as a function of time, wavelet semblance analyses were performed following

the continuous wavelet transform method (Cooper and Cowan, 2008) and using a modified MATLAB script. To identify the major periodicities within the time series, downcore variations of Ti abundances was decomposed into their major components using the complete ensemble empirical mode decomposition (CEEMD) approach (Torres et al., 2011). Subsequently, wavelet power spectrum analyses were performed on each individual component using the Morlet wave (Torrence and Compo, 1995) and a modified MATLAB script. We report notable periodicities according to the wavelet power spectra of each component, with global power spectra that exceed 1σ confidence level considered as significant periodicities. Prior to the analysis, each time series was detrended and linearly interpolated at a constant 3.5-year time step. To detrend the time series, the least-square best-fit line was subtracted from the original data by using the built-in MATLAB command. The 3.5-year time step closely approximates the average temporal sampling resolution of the XRF elemental data.

12- Climate simulations

The simulations analyzed and performed using two versions of the National Center for Atmospheric Research (NCAR) Community Climate System Model (CCSM). The Transient Climate Evolution of the last 21 ka (TraCE), which used CCSM version 3 (CCSM3) (He et al., 2013; Liu et al., 2009) was analyzed. Trace was forced with time-varying changes in orbital parameters, greenhouse gases, ice-sheet orography and extent, solar forcing, freshwater forcing, and interactive vegetation dynamics. This simulation is used to examine how the large-scale circulation varies through time in response to these changing conditions. However, aerosols were prescribed at pre-industrial (PI) conditions and held constant in time.

To examine the role of the greening of North Africa on dust emissions three time slice experiments was performed using CCSM version 4 (CCSM4; Gent et al., 2011) coupled to a slab ocean model (SOM) and interactive dust aerosol model (Albani et al., 2014) (Table 2-4). CCSM4 consists of atmosphere, ocean, land, and sea ice components that are linked through a coupler that exchanges state information and fluxes between the components. The atmospheric model is the Community Atmosphere Model version 4 (CAM4), which uses the Lin-Rood finite volume core with a 1.25°x0.9° uniform resolution, and 26 levels in the vertical. The land model is the Community Land Model version 4 (CLM4) (Lawrence et al., 2011), which uses the same horizontal resolution as CAM4. In SOM, ocean heat transport convergence is prescribed as a Q-flux, which maintains the climatological sea surface temperatures based on the fully coupled version of CCSM4 (with the dynamic ocean model) (Bitz et al., 2012). Q-flux is calculated using output from the last 20 years of the 1300 year-long fully coupled mid-Holocene (6ka) simulation and is used in all our SOM experiments performed here. This is done so that we can focus on the atmospheric changes associated with the surface boundary conditions, though it has been argued that ocean dynamics can provide a modest positive feedback to changes over Africa (Braconnot et al., 2007; Kutzbach and Liu, 1997). We initialized our SOM experiments from their equilibrated 6ka (Otto-Bliesner et al., 2009) and Preindustrial (1850 A.D, PI) fully coupled climate model simulations that were performed for the Paleoclimate Modeling Intercomparison Project phase 3 (PMIP3) and Coupled Modeling Intercomparison Project phase 5 (CMIP5), respectively, and integrated for 50 years, which is sufficient for the slab model to reach equilibrium. The last 20 years of each slab model simulation is used to calculate the seasonal and annual means. Summer means are based

on the climatological June-July-August (JJA) average and spring means are based on the climatological March-April-May (MAM) average.

The interactive dust model includes an active emission scheme, dust transport, and wet and dry deposition processes. Dust emission is a function of wind speed, vegetation and snow cover, soil moisture, and soil erodibility. Soil erodibility accounts for differences in soils' susceptibility to erosion, and is applied as a spatially varying scale factor for dust emissions, which were constrained by particle size-resolved dust mass accumulation rates data and provenance fingerprinting for the 6ka and PI (see Albani et al., 2015, 2014). Consequently, dust source regions in the PI experiment are different from the mid-Holocene experiments.

Two model simulations of the mid-Holocene- 6ka and 6ka+greening- were performed. These experiments have the same continental configuration, ice sheets, and topography as the PI experiment, however, greenhouse gases and orbital forcing follow the PMIP3 protocol, and dust source regions differ. Our 6ka experiment uses the same vegetation cover as the PI experiment. To take into account the "greening" of North Africa in the early Holocene an additional simulation (6ka+greening) was performed, where the same 6ka orbital forcing is used, but modify the PI vegetation cover to include the early Holocene North African lake and wetland distribution based on Hoelzmann et al., (1998), and account for the conversion of desert to savanna biomes by replacing bare ground over the North Africa and the Arabian Peninsula (10ºN-31ºN, 20ºW-55ºE) with 70% C3 grasses, 10% broadleaf deciduous tropical tree, and 20% broadleaf deciduous temperate shrub (Castañeda et al., 2009; Jolly et al., 1998). The dust sources were removed by setting the soil erodibility to zero where the vegetation was modified. In CLM4, the soil color is

spatially fixed and derived based on the current vegetation distribution. The albedo effect has been shown to increase the precipitation-vegetation feedback (Levis et al., 2004) and alter the sign of the dust-climate feedback (Tegen and Lacis, 1996). Since the bright Saharan desert was replaced with darker savanna, the soil color was darkened in a spatially uniform way, by setting it to values similar to the nearby Sahel. To facilitate comparisons with previous mid-Holocene climate simulations performed for PMIP3, we use 6ka orbital conditions in all simulations presented here. Although our 6ka+greening is meant to represent conditions in the early rather than the mid-Holocene (6ka), additional simulations using 9ka orbital conditions are needed.

13- HYSPLIT back-trajectory climate simulations

Three-day air mass back-trajectory ensemble plots at 1000-5000 m starting altitudes were computed for representative winter, spring and summer days using the on-line web version of HYSPLIT model (Stein et al., 2016). These windows were chosen to approximately correspond with periods of dust sampling at Abadan and Sar Pol Zahab meteorological stations, as well as times of minimum precipitation during winter and summer seasons at Neor Lake (Fig. 2-3) (Sharifi et al., 2015). The starting altitude range for the HYSPLIT model was chosen at 1000-5000 m to provide maximum coverage for the aerosol bearing air masses that reach Neor Lake, which is located at an average altitude of 2500 m.a.s.l. We used the Global Data Assimilation System (GDAS) to provide a comprehensive meteorological dataset for the HYSPLIT models. The GDAS incorporates diverse instrumental data (*e.g.,* surface observations, balloon data, wind profiler data, radar observations, etc.) into gridded, 3-D model space.

14- Spatial distribution pattern reconstructions

To visualize the spatial distribution pattern of various parameters measured at sampling stations in Urmia Lake, a grid of 100×70 lines was made by means of Surfer version 9.3.451 (Golden Software, Inc. 1993-2009) using point type Kriging method and linear variogram model (Slope=1, Anisotropy=1.0). The filled contour map was generated using the medium smoothing method.

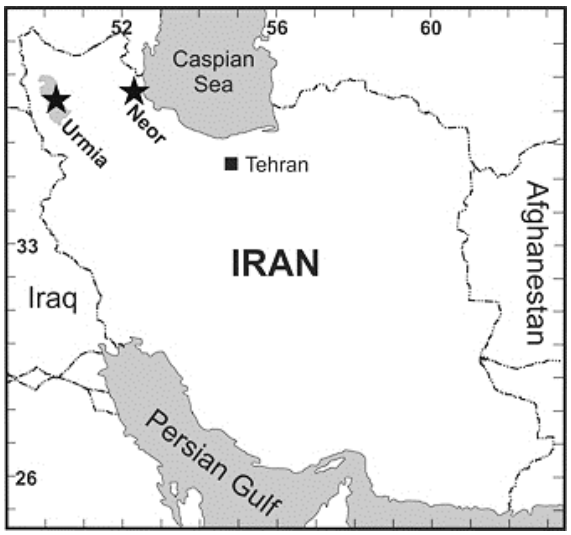

Fig. 2-1. Location of Neor Lake and Lake Urmia in NW Iran.

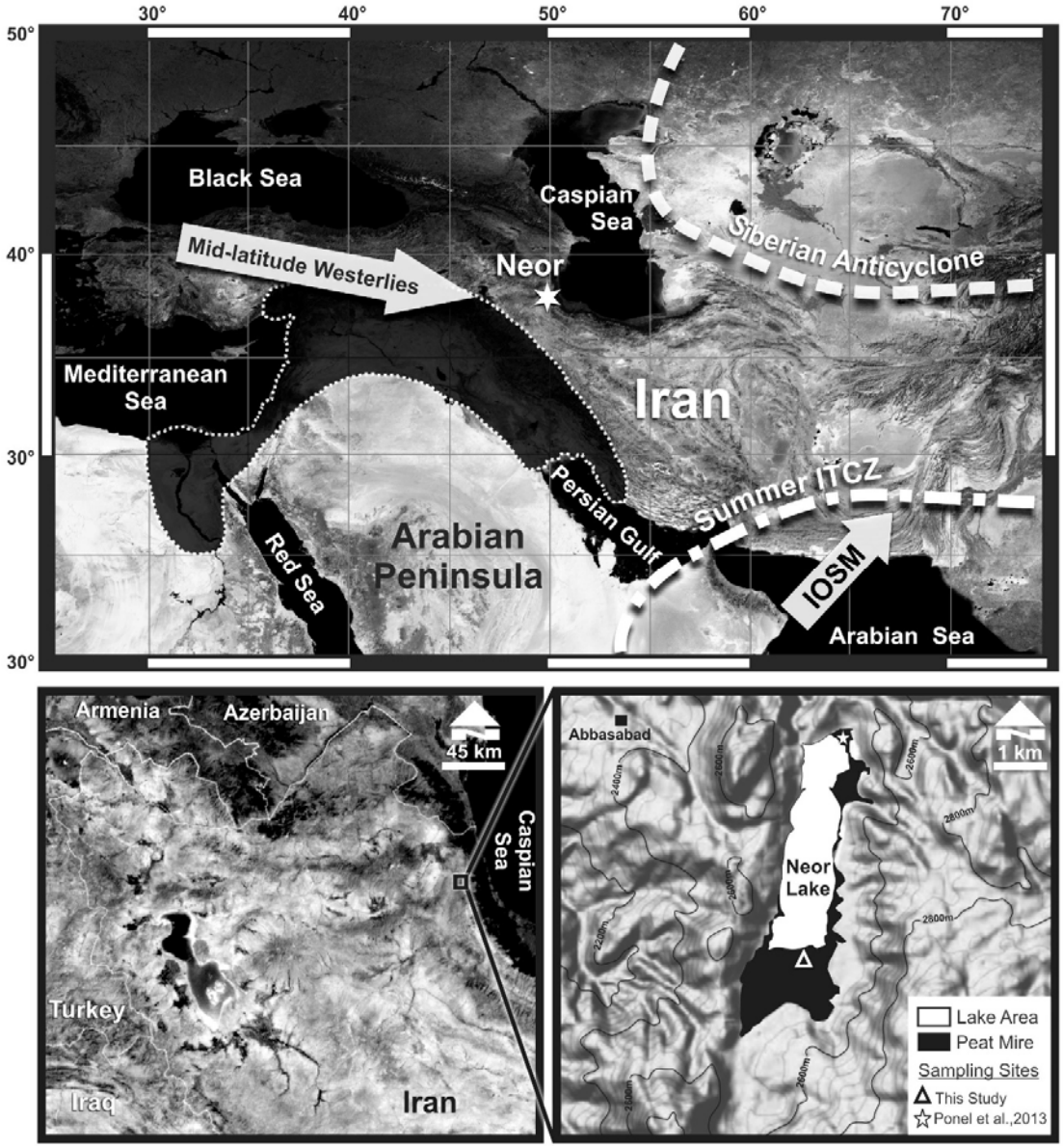

Fig. 2-2. Schematic position of major synoptic systems over West Asia and the location of Neor peat mire (star). Shaded area marks the region known as the "Fertile Crescent". The approximate current location of the Intertropical Convergence Zone (ITCZ) is also shown. IOSM refers to Indian Ocean Summer Monsoon. The Neor Lake's catchment basin and peripheral peat mire are shown in the bottom panel. Open triangle denotes the location of the peat core for this study.

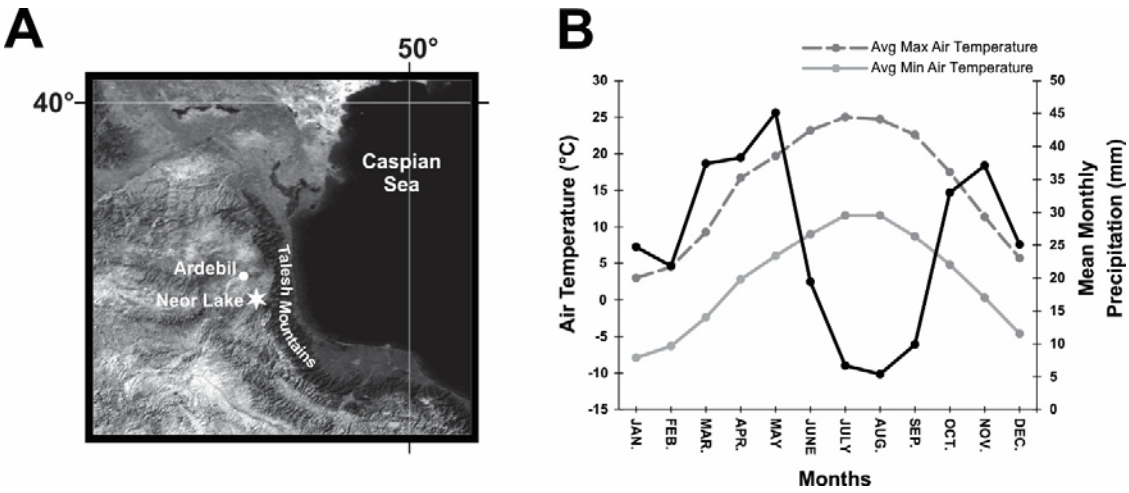

Fig. 2-3. Climate data for Neor Lake. A) Location of Neor peat mire with respect to Talysh (Alborz) Mountains. B) 30-year average of minimum and maximum monthly mean air temperature (dark red and yellow lines) and mean monthly precipitation (blue line) as recorded in Ardebil meteorological station.

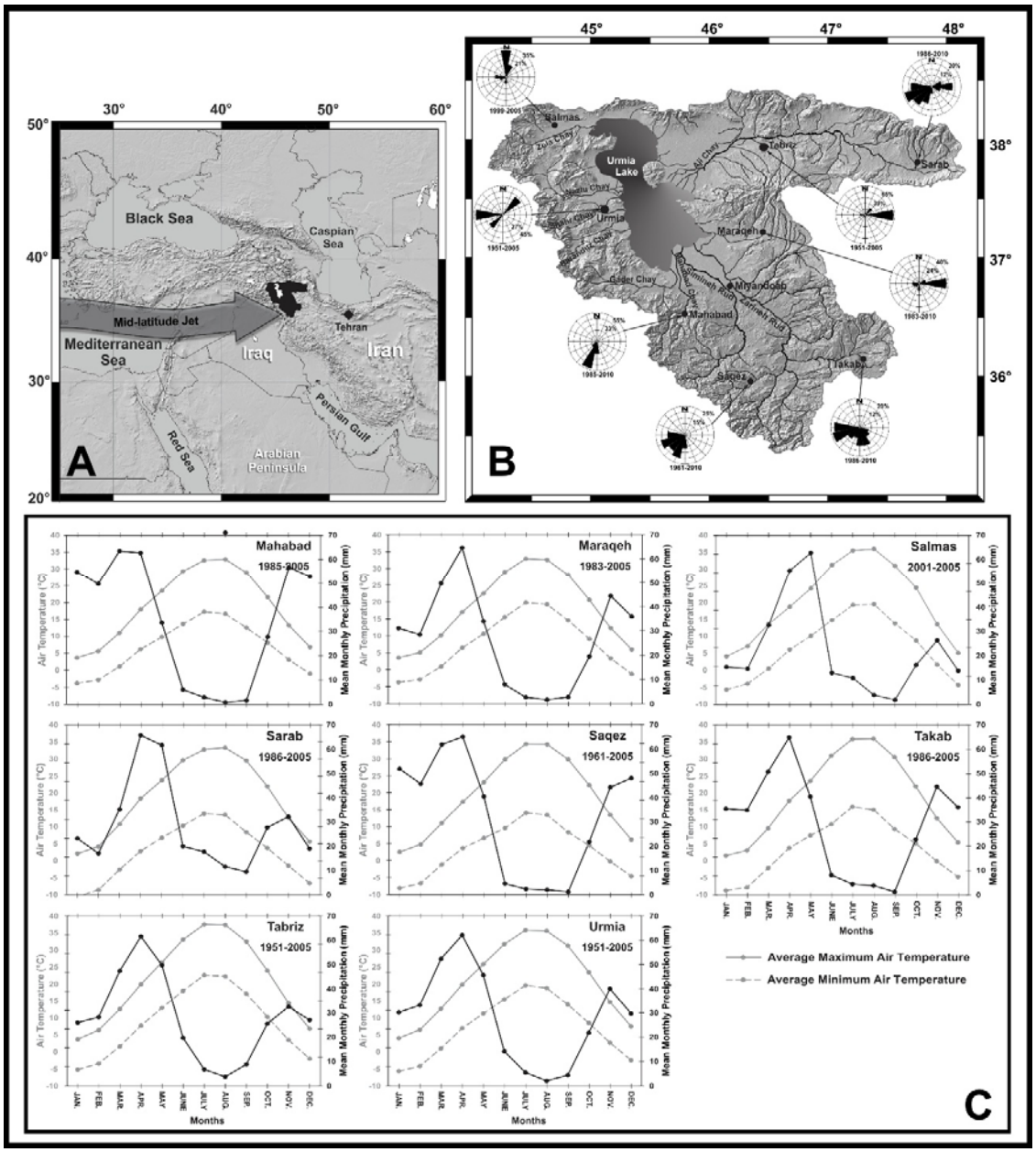

Fig. 2-4. A) Schematic position of mid-latitude jet and location of Urmia Lake and its watershed area. B) Urmia Lake watershed area and major perennial and seasonal tributaries. Rose diagrams denote the long-term average annual prevailed wind speed recorded at major meteorological stations. C) Climate diagrams of the regional meteorological stations (data from the Iran Meteorological Organization, www.imo.ir).

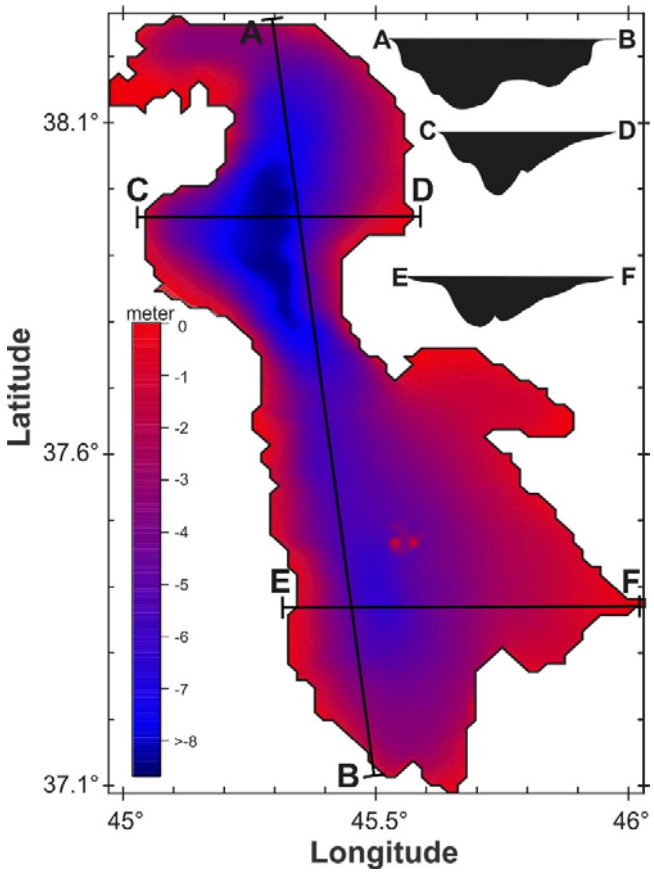

Fig. 2-5. Bathymetry of Urmia Lake. Depths are below 1275 meter above sea level (0=1275 m.a.s.l.), Depth profiles are not to scale.

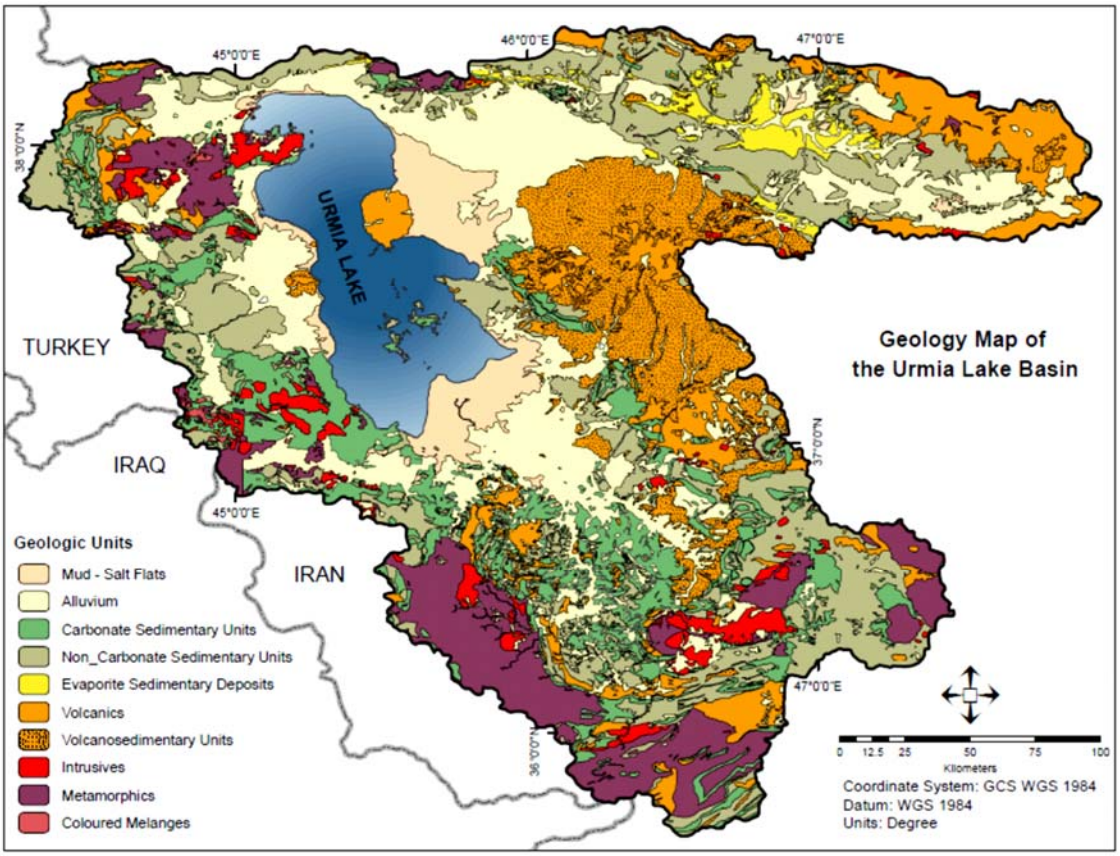

Fig. 2-6-Simplified geology map of the Urmia Lake watershed area.

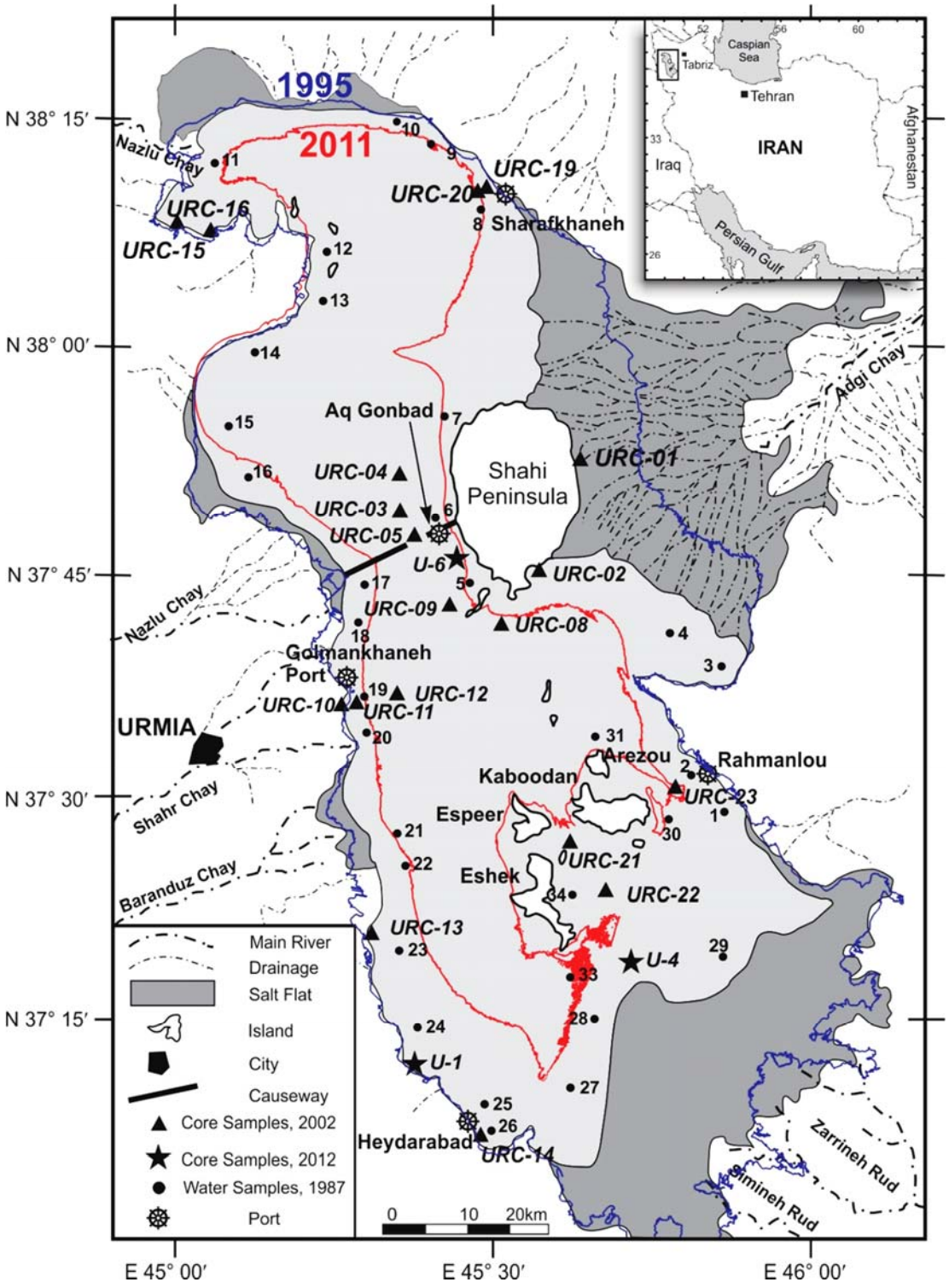

Fig. 2-7- Location of sediment cores and water samples in Urmia Lake. The solid line denotes the location of Kalantari causeway across the narrow part of the lake. Blue and red contours denote lake's shoreline in 1995 and 2011 respectively.

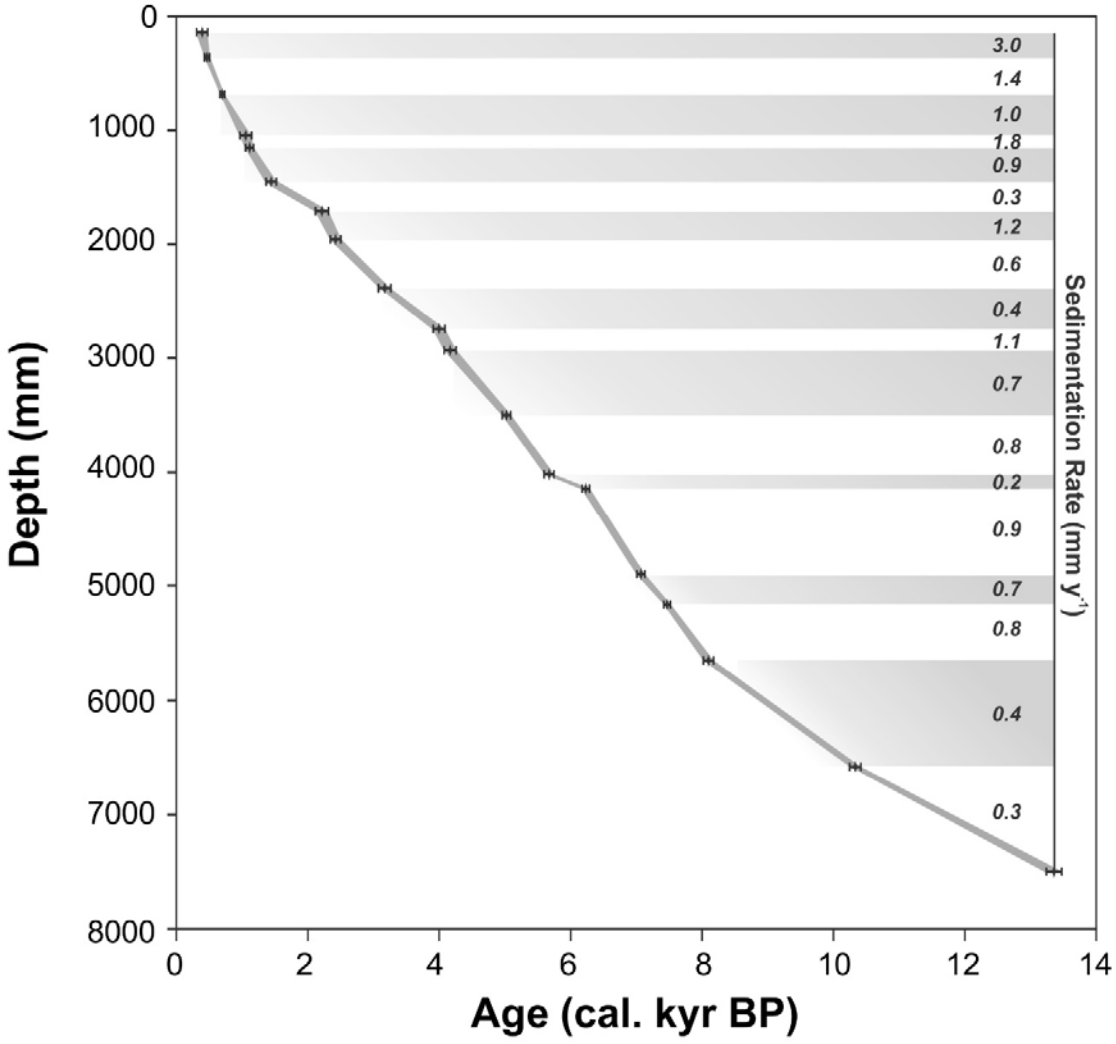

Fig. 2-8- The age model for the Neor peat core based on 19 calibrated AMS radiocarbon dates is shown. The narrow gray area between tie points refers to the 2σ uncertainty. Sedimentation rates (SR) between paired tie points are shown on the right axis. Sedimentation rates were calculated based on midpoint, calibrated ages; see Table 1 for details.

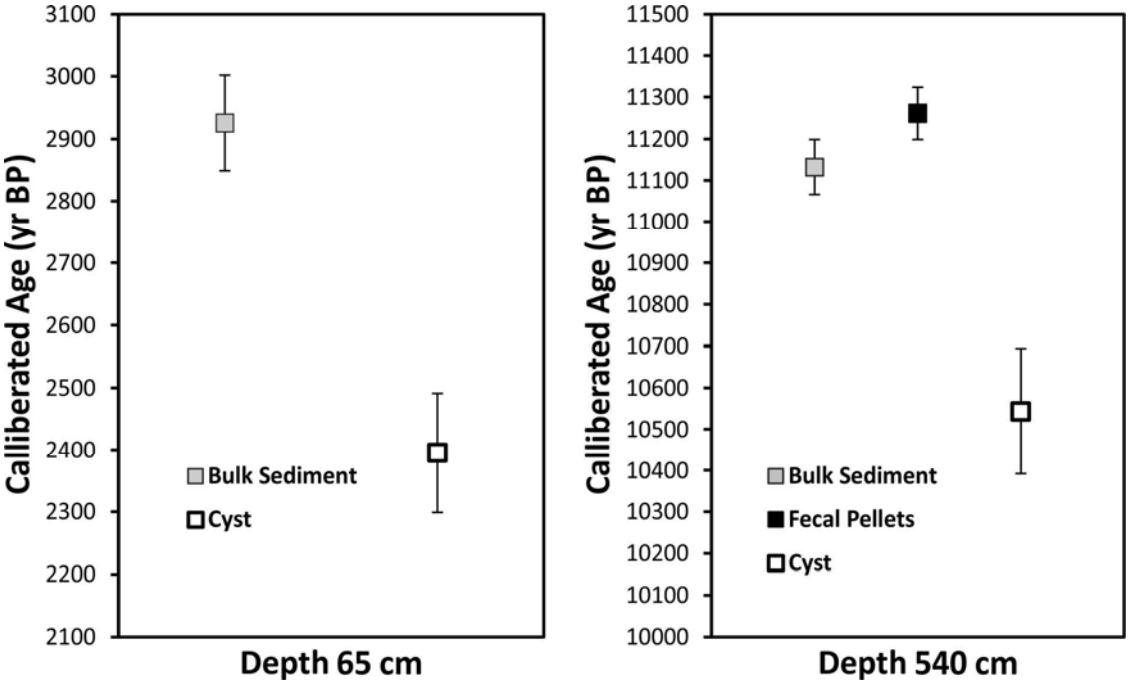

Fig. 2-9- Comparative calibrated AMS radiocarbon ages measured on bulk sediment, shrimp fecal pellets and shrimp cyst at two different depths form Urmia Lake. The average age offset between bulk sample and cyst is considered as the reservoir effect correction factor, see text for details.

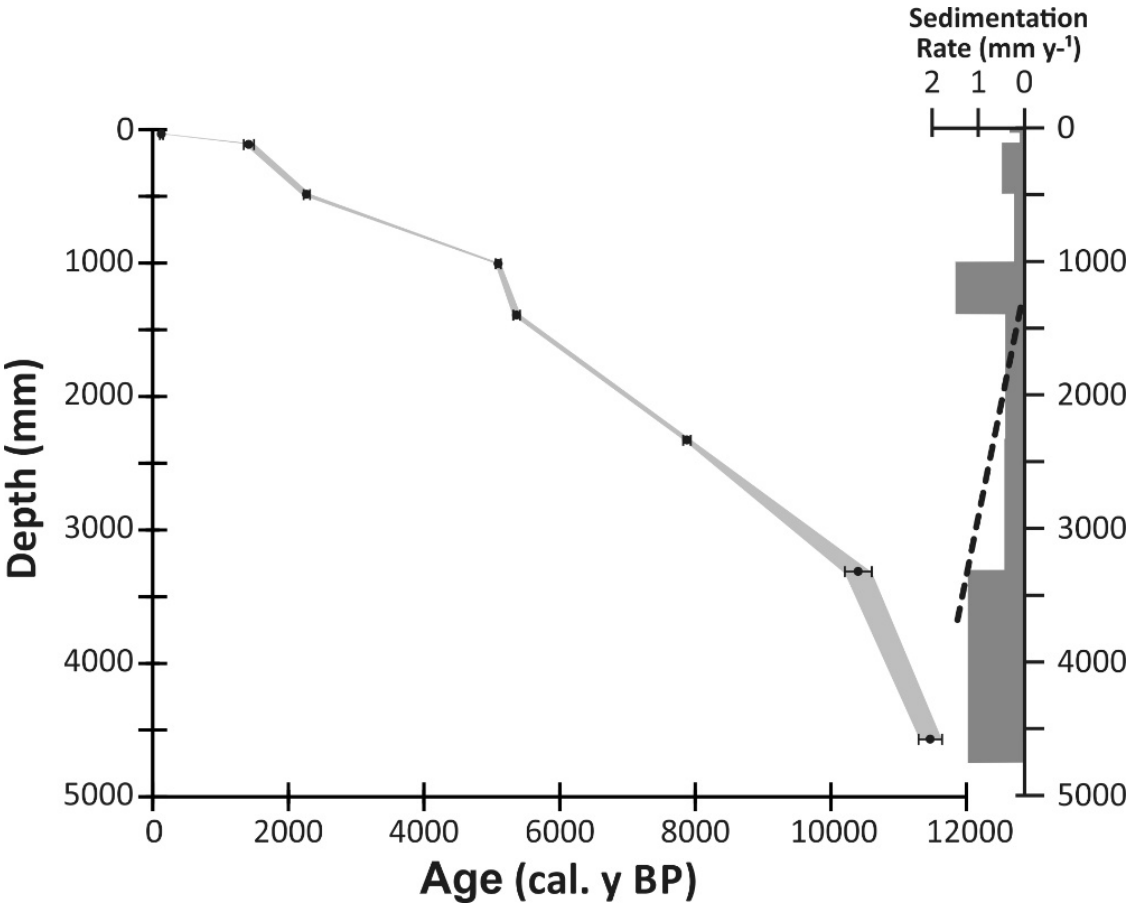

Fig. 2-10- The age model for the Urmia Lake sediment core based on 8 calibrated AMS radiocarbon dates is shown. The narrow gray area between tie points refers to the 2σ uncertainty. Sedimentation rates (SR) between paired tie points are shown on the right axis. Sedimentation rates were calculated based on midpoint, calibrated ages; see Table 2-3 for details. Dashed black line denotes the overall SR trend since the beginning of the record at 11,620 cal. y BP. All ages are corrected for reservoir effect.

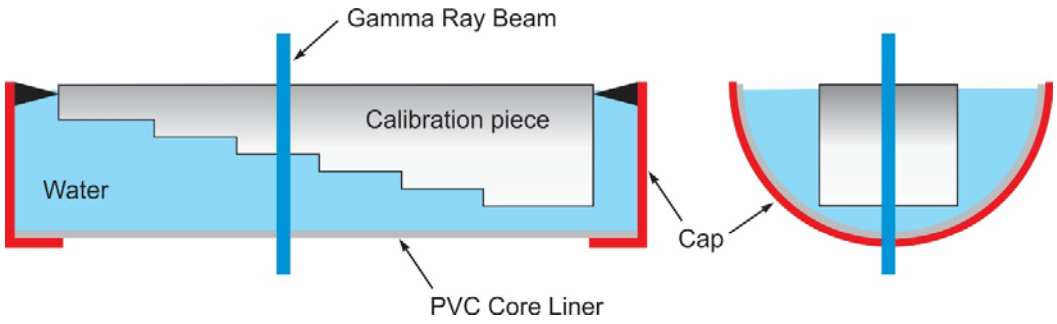

Fig. 2-11- Schematic view of Gamma calibration piece placed in half cylinder core liner with water.

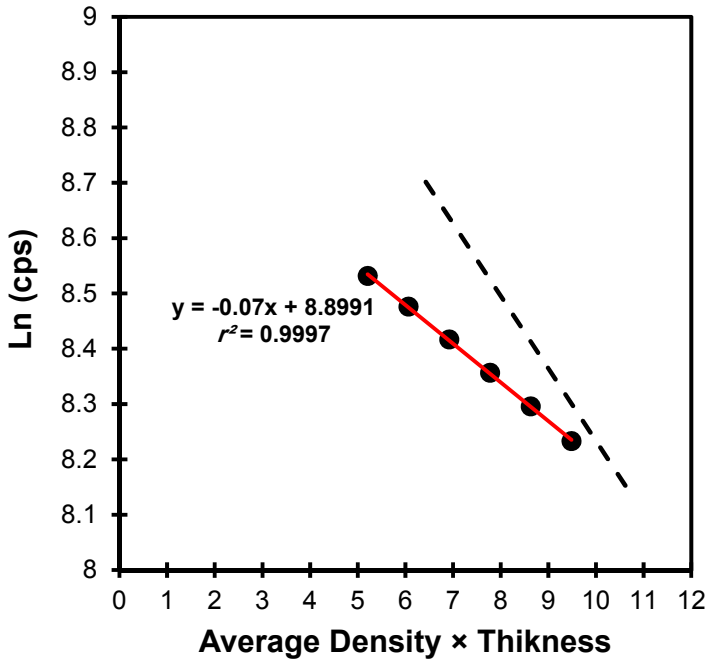

Fig. 2-12- Gamma density calibration curve. The black dotted line represents the theoretical values.

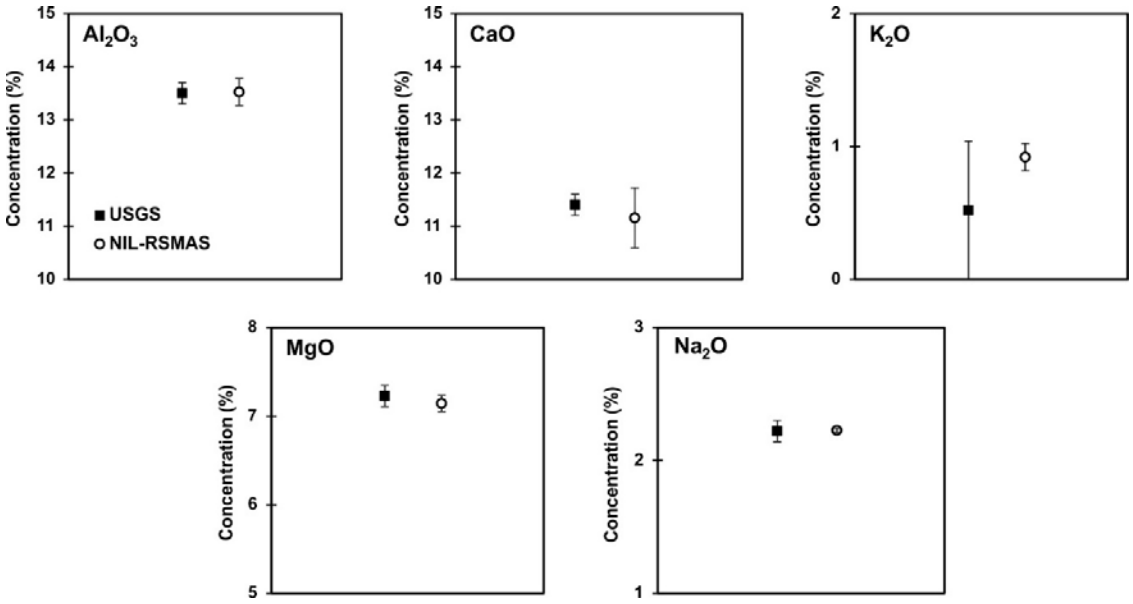

Fig. 2-13- Replicate measurements of major oxide concentrations (%) for USGS CRMs BHVO-2 at the Neptune Isotope Lab (NIL-RSMAS, open circle) are comparable within uncertainties to the mean values from literature compilation (USGS, solid square), data from GEOREM, http://georem.mpch-mainz.gwdg.de/. Uncertainties are reported as the relative standard deviation.

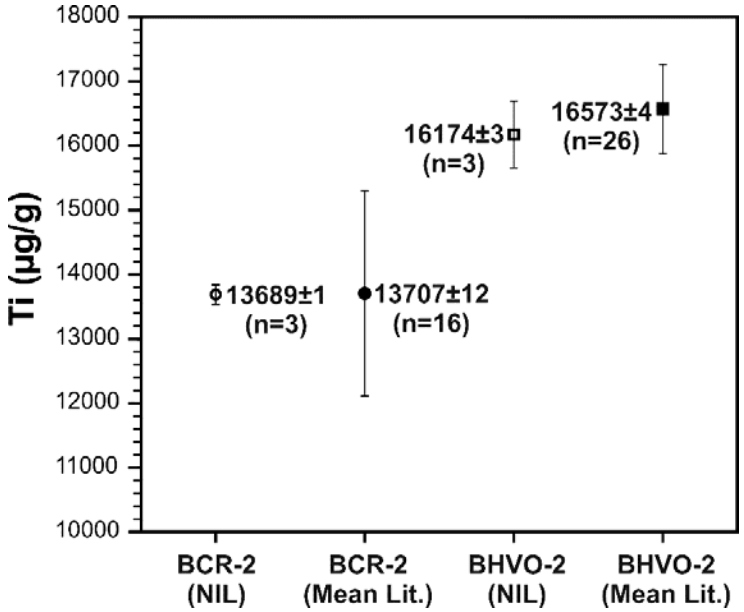

Fig. 2-14- Replicate measurements of Ti concentrations (µg g^{-1}) for replicates of USGS CRMs BCR-2 and BHVO-2 at the Neptune Isotope Lab (NIL) are comparable within uncertainties to the mean values from literature compilation (Mean Lit.), data from GEOREM, http://georem.mpch-mainz.gwdg.de/. Uncertainties are reported as the relative standard deviation.

Table 2-1- Annual mean river discharge and the mean catchment area of the main rivers in the Urmia lake watershed (After Shah-Hoseini, 2003).

River's Name	Mean Discharge (Ls^{-1})	Catchment Area (km^2)
Zarrineh Rud	48.52	11400
Simineh Rud	10.31	2421
Nazlu Chay	7.95	1715
Aji Chay	6.65	7525
Barandooz Chay	6.63	637
Zola Chay	5.26	819
Shahr Chay	3.75	369

Table 2-2. Radiocarbon dates and calibrated ages for peat core from Neor Lake.

Sample No.	Depth ±5 mm*	Conventional Age (RCYBP) ±Reported Error**	Midpoint Calibrated Age (year BP) ±2σ Error	Midpoint Calibrated Age (Calendar year) ±2σ Error
NES3-1-21	138	335±30	393±84	1557±84 AD
NES3-1-2	361	385±25	467±39	1483±39 AD
NES3-1-3	683	760±35	699±36	1251±36 AD
NES3-2-4	1044	1140±35	1055±89	895±89 AD
NES3-2-22	1150	1180±25	1114±61	836±61 AD
NES3-2-5	1449	1540±30	1443±78	510±78 AD
NES3-2-6	1710	2180±30	2215±99	266±99 AD
NES3-3-7	1956	2400±35	2422±79	473±79 BC
NES3-3-8	2384	2990±30	3170±95	1221±95 BC
NES3-3-9	2740	3670±30	3997±90	2048±90 BC
NES3-4-24	2930	3780±35	4166±90	2217±90 BC
NES3-4-10	3497	4450±30	5024±64	3075±64 BC
NES3-5-26	4017	4950±40	5672.5±75.5	3724±75.5 BC
NES3-5-12	4143	5390±35	6230±56	4281±56 BC
NES3-6-13	4900	6220±35	7070±60	5121±60 BC
NES3-6-14	5166	6550±40	7468±50	5519±50 BC
NES3-6-15	5653	7290±35	8098±77	6149±77 BC
NES3-7-17	6583	9180±70	10331±85	8423±85 BC
NES3-8-20	7500	11500±50	13356±116	11407±116 BC

* Indicates the error on depth measurement.

** RCYP=Radiocarbon year before present, for error calculation please refer to the National Ocean Sciences Accelerator Mass Spectrometry Facility (NOSAMS) radiocarbon data and calculation protocol at http://www.whoi.edu/nosams.

Table 2-3. Radiocarbon dates and calibrated ages corrected for reservoir effect.

Sample No.	Depth ±5 mm*	Sample Type	Conventional Age (RCYBP) ±Reported Error**	Midpoint Calibrated Age (year BP) ±2σ Error	Midpoint Calibrated Age (BP) Corrected for Reservoir Effect ±2σ Error***
U7-2B	640	Bulk Sediment	2820±30	2926±77	-
U7-2C	640	Cyst	2330±50	2395±96	-
U7-2f	5400	Fecal Pellets	9850±40	11262±63	-
U7-2c	5400	Cyst	9330±50	10543±151	-
U7-2b	5400	Bulk Sediment	9660±40	11133±67	-
U6-1-3	35	Bulk Sediment	680±30	657±23	129±23
U6-1-2BK	111	Bulk Sediment	1860±30	1946±76	1418±76
U6-1-1BK	487	Bulk Sediment	2690±30	2801±48	2273±48
U6-2-3	1005	Bulk Sediment	4890±30	5624±37	5096±37
U6-2-2BK	1390	Bulk Sediment	5130±40	5894±50	5366±50
U6-3-3BK	2328	Bulk Sediment	7610±40	8406±56	7878±56
U6-4-4BK	3312	Bulk Sediment	9580±50	10934±200	10406±200
U6-5-5BK	4571	Bulk Sediment	10270±40	11995±174	11467±174

* Indicates the error on depth measurement.

** RCYP=Radiocarbon year before present, for error calculation please refer to the information provided by Beta Analytic Co. on radiocarbon data and calculation protocol at http://www.radiocarbon.com.

*** Calibrated ages were corrected for the reservoir effect by 590 years, the age difference between comparative bulk sediment and shrimp cyst. All corrected ages recalculated for present time being 2012.

Table 2-4. Details of the three model experiments performed with CCSM4 coupled to the SOM and interactive dust model. The columns describe simulation name, orbital configuration, greenhouse gas concentrations (GHC), prescribed vegetation, and soil erodibility map used to scale dust emissions.

Simulation	Orbital	GHG	Vegetation	Soil Erodibility
6ka Mid-Holocene	6ka	6ka	PI	6ka
6ka+greening Early Holocene	6ka	6ka	modified North Africa/Arabian Peninsula (10°-31°N, 20°W-55°E)	6ka with modified North Africa/Arabian Peninsula (10°-31°N, 20°W-55°E)

CHAPTER 3

Abrupt climate variability since the last deglaciation based on a high-resolution, multi-proxy peat record from NW Iran: The hand that rocked the Cradle of Civilization?[1]

[1] This chapter was published in Quaternary Science Review (2015):
Sharifi, A., Ali Pourmand, Elizabeth A. Canuel, Erin Ferer-Tyler, Larry C. Peterson, Bernhard Aichner, Sarah J. Feakins, Touraj Daryaee, Morteza Djamali, Abdolmajid Naderi Beni, Hamid A.K. Lahijani, Peter K. Swart, 2015: Abrupt climate variability since the last deglaciation based on a high-resolution, multi-proxy peat record from NW Iran: The hand that rocked the Cradle of Civilization? *Quaternary Science Reviews*, Volume 123, pp. 215-230. DOI: 10.1016/j.quascirev.2015.07.006

Summary

In this chapter a high-resolution (sub-decadal to centennial), multi-proxy reconstruction of aeolian input and changes in palaeohydrological conditions based on a 13,000 yr record from Neor Lake's peripheral peat in NW Iran was presented. Variations in relative abundances of refractory (Al, Zr, Ti, and Si), redox sensitive (Fe) and mobile (K and Rb) elements, total organic carbon (TOC), $\delta^{13}C_{TOC}$, compound-specific leaf wax hydrogen isotopes (δD), carbon accumulation rates and dust fluxes presented here fill a large gap in the existing terrestrial paleoclimate records from the interior of West Asia. These results suggest that a transition occurred from dry and dusty conditions during the Younger Dryas (YD) to a relatively wetter period with higher carbon accumulation rates and low aeolian input during the early Holocene (9,000-6000 yr BP). This period was followed by relatively drier and dustier conditions during middle to late Holocene, which is consistent with orbital changes in insolation that affected much of the northern hemisphere. Numerous episodes of high aeolian input spanning a few decades to millennia are prevalent during the middle to late Holocene. Wavelet analysis of variations in Ti abundances as a proxy for aeolian input revealed notable periodicities at 230, 320, and 470 years with significant periodicities centered around 820, 1,550, and 3,110 years over the last 13,000 years. Comparison with palaeoclimate archives from West Asia, the North Atlantic and African lakes point to a teleconnection between North Atlantic climate and the interior of West Asia during the last glacial termination and the Holocene epoch.

Furthermore, the potential role of abrupt climate change on early human societies was assessed by comparing current record of palaeoclimate variability with historical, geological and archaeological archives from this region. The terrestrial record from this

study confirms previous evidence from marine sediments of the Arabian Sea that suggested climate change influenced the termination of the Akkadian empire. In addition, nearly all observed episodes of enhanced dust deposition during the middle to late Holocene coincided with times of drought, famine, and power transitions across the Iranian Plateau, Mesopotamia and the eastern Mediterranean region. These findings indicate that while socio-economic factors are traditionally considered to shape ancient human societies in this region, the influence of abrupt climate change should not be underestimated.

1- Overview

Since the beginning of the Neolithic Era, the area in West Asia that extends from southwestern Iran and the Arabian Peninsula to the eastern and southeastern Mediterranean Sea, also referred to as the "Cradle of Civilization" and the "Fertile Crescent", has witnessed the birth of agriculture and development of some of the earliest human societies (Leick, 2010; Mellaart, 1975; Riehl et al., 2013). Evidence is mounting that abrupt climate change during the Holocene epoch (beginning 11,700 before present, BP) may have played a transformative role in the growth and deterioration of human civilizations (Brooks, 2006; Cullen et al., 2000; deMenocal, 2001; Riehl, 2009). Although the amplitude of climate variability was reduced during the Holocene relative to the last glacial period (Grootes et al., 1993), episodes of abrupt climatic change have been documented in marine and terrestrial records throughout the Holocene in both hemispheres (see review by Mayewski et al., 2004).

On a regional scale, the climate of West Asia is governed by complex interactions between the mid-latitude Westerlies, the Siberian Anticyclone and the Indian Ocean

Summer Monsoon (Fig. 2-2). While a number of paleoclimate studies have drawn potential links between abrupt climate change and the rise and fall of civilizations across the Fertile Crescent (Cullen et al., 2000; Staubwasser and Weiss, 2006), high-resolution (sub-decadal to centennial) terrestrial archives of climate variability with well-constrained age models are scarce from this region (Nicoll and Küçükuysal, 2013). Such records are needed in order to address the uncertainty regarding the timing and regional significance of climatic transitions and their potential influence on early human societies, and the extent to which anthropogenic activities may have influenced the climate of the last deglacial period. Interpreting the available proxy reconstructions of Holocene climate variability in the interior of West Asia is not straightforward. For example, Stevens et al. (2001) found disagreement between relatively lower $\delta^{18}O$ values from Lake Zeribar during the early Holocene, which are generally interpreted to represent wetter conditions (Roberts et al., 2008), and pollen and macrofossil data for this period from Lake Zeribar, which were interpreted to indicate drier conditions during this period. They concluded that lower $\delta^{18}O$ values may have been due to a shift in the timing of precipitation (i.e., protracted summers). Other explanations that have been suggested for this discrepancy include underestimating human impact on vegetation during the early Holocene, and the delayed reaction of biomes to postglacial climate change (Djamali et al., 2010; Roberts, 2002). Stevens et al. (2006) further examined geochemical and biological evidences from Lake Mirabad in western Iran during this period and concluded that the early Holocene was dry. Based on microfossil assemblages and pollen data, Wasylikowa et al. (2006) concluded that Zeribar lake levels were variable during the early Holocene. Pollen and ostracod assemblages from lakes in Turkey, Iran and Georgia suggest that continental (dry and variable) climate dominated

over the interior of West Asia during the early to middle Holocene (Connor and Kvavadze, 2008; El-Moslimany, 1982; Griffiths et al., 2001; Wasylikowa, 2005). Available records of palaeo-vegetation changes, however, fall short of disentangling human *versus* climate impact (Djamali et al., 2009a), indicating the need for high-resolution palaeoclimate reconstructions that are independent of vegetation types that may have been influenced by agriculture as well as climate (Roberts et al., 2011).

In the following sections, the inorganic and organic proxy reconstruction of aeolian input and palaeohydrological changes over the last 13,000 yr from an ombrotrophic (rain fed) peat mire located at the periphery of Neor Lake in NW Iran will be presented. Additionally, the possibility of an atmospheric teleconnection during the last glacial termination and the Holocene by comparing our results with records from the North Atlantic, African lakes and eastern Mediterranean will be examined. Furthermore, the potential influence of abrupt climate change on major early human societies from West Asia will be investigated by comparing our findings with historical and archaeological records from this region.

2- Materials and methods

Neor Lake (37°57'37" N, 48°33'19" E) is a seasonally recharged body of water formed over a tectonic depression on the leeward flank of the Talesh (Alborz) Mountains in NW Iran (Fig. 2-2 and Fig 2-3A). A 775-cm long split-core (Fig 3-1 A) was collected from the SW edge of the Neor peat complex. The core chronology was established by 19 radiocarbon dates (Fig. 3-1, Fig. 2-8 and Table SI-2). The relative abundances of refractory and redox-sensitive elements were measured with an Avaatech XRF-core scanner. Sub-

samples were analyzed for TOC by high-temperature combustion using a Fisons CHN analyzer. Stable carbon isotope analyses of TOC ($\delta^{13}C_{TOC}$) and stable Nitrogen isotope analyses of TOC ($\delta^{15}N_{TOC}$) were performed using a Costech elemental combustion system interfaced to a Thermo Scientific Delta V Advantage continuous flow isotope ratio mass spectrometer (IRMS). Lipids were extracted using a Dionex ASE-200 Accelerated Solvent Extractor and alkanoic acids were pre-concentrated using silica column chromatography. Compound-specific hydrogen isotopic values were obtained by gas chromatography IRMS. Wavelet semblance analyses were performed following the continuous wavelet transform method (Cooper and Cowan, 2008) and using a modified MATLAB script. Downcore variations of Ti abundances time series was decomposed using the complete ensemble empirical mode decomposition (CEEMD) approach (Torres et al., 2011). Subsequently, wavelet power spectrum analyses were performed on each individual component using the Morlet wave (Torrence and Compo, 1995) and a modified MATLAB script. Details of the sampling and analytical methodology are provided in the chapter 2.

3- Results and discussion

3.1- The climate of the last deglaciation and Holocene

3.1.1- Inorganic proxy record

The age model based on 19 calibrated radiocarbon dates is shown in Fig. 2-8, and the data are presented in Table 2-2. The average sedimentation rate (SR) calculated based on the age-depth model was 0.9±0.6 (SD) mm yr^{-1}, with the lowest rates dominating the early to mid-Holocene and the highest rates occurring after 1,500 cal. yr BP to the present (Fig. 2-8). Down-core abundances of Al, Zr, Ti, Si, Fe, K, and Rb measured by XRF-scanning

at an average resolution of 3.5 yr are shown in Fig. 3-1 along with a composite image of the 7.5 m peat core (see Table SI-2a for results). The light bands represent periods of high lithogenic (aeolian) input, while dark bands contain higher contents of decomposed organic matter. In general, the light bands dominated prior to the onset of the Holocene during the late Allerød and Younger Dryas periods. With the exception of several light bands that are evident between 8,500-6,500 cal. yr BP, the period encompassing the early Holocene (*ca* 9,000-6,000 yr BP) is dominated by dark organic matter. In contrast, the upper half of the core from around 6,000 cal. yr BP is marked with numerous and distinct bands of lithogenic material. It is evident from Fig. 3-1 that the relative abundances of refractory (Al, Zr, Ti, and Si), redox-sensitive (Fe) and mobile (K and Rb) elements covary throughout the entire record, with highest intensities corresponding to the light bands that contain high lithogenic content. Discrepancies are expected in the geochemical behavior of immobile elements compared with redox-sensitive and mobile elements if post-depositional mobilization and groundwater hydrochemistry affected the abundances of these elements during their depositional history. We observe significant correlations between the intensities of representative immobile (Ti), redox sensitive (Fe) and mobile (Rb) elements (Fe vs.Ti, R^2=0.81; Rb vs Ti, R^2=0.84, Fig. 3-2 A and B). Additional confirmation comes from wavelet semblance analyses that show significant correlations among refractory conservative elements and both mobile and redox sensitive elements as a function of time, indicating that mineral dust particles have not been mobilized since deposition, and the ombrotrophic nature of the peat has been sustained throughout the record (Fig. 3-2 C-H). Taken together along with the absence of any significant riverine input to this high-altitude

peat mire, we attribute elevated intensities of lithogenic elements to enhanced aeolian input of mineral dust to the study area.

The record of lithogenic input as represented by Ti intensities (Fig. 3-3 A) captures at least eleven abrupt episodes of enhanced aeolian deposition that lasted from several decades to millennia. Six of these events correspond to major Holocene rapid climate change (HRCC) periods associated with changes in the chemistry of the Greenland Ice Sheet ice core (GISP2) that were correlated to the record of globally distributed glacier fluctuations during the Holocene (Fig. 3-3 A and J) (see Mayewski et al., 2004 and references therein). As noted by Meyewski et al., (2004), however, the HRCC events are not necessarily limited to these six episodes but rather these periods provide an overarching framework against which Holocene palaeoclimate records can be placed in regional and hemispheric context.

Strong evidence for an atmospheric teleconnection between the climate of the North Atlantic and the interior of West Asia comes from the agreement between the dust record from Neor and the expansion of the Siberian Anticyclone inferred from elevated K^+ ion concentrations in the GISP2 ice core (Mayewski et al., 1997) (Fig. 3-3 I), as well as Holocene ice rafted debris (IRD) events from North Atlantic sediments (arrows 1-9 in Fig. 3-3 A) (Bond et al., 1997), which are also associated with intervals of reduced solar irradiance (Bond et al., 2001). Shifts to more arid conditions found in records from the eastern Mediterranean Sea (Kaniewski et al., 2010; Migowski et al., 2006; B. Schilman et al., 2001) are also coincident with episodes of enhanced aeolian input from our record, and further indicate a climate coupling with the northern hemisphere (Fig. 3-3 J).

Changes in the intensities of lithogenic elements measured by XRF provide a qualitative account of aeolian input. The flux of dust over the entire record was quantified by measuring down-core concentrations of Ti in discrete samples at an average resolution of ~220 yr/sample (Table SI-2b). The relative changes in Ti intensities measured by XRF at high resolution and dust fluxes based on the Ti concentrations of discrete samples are in good agreement throughout the record (Fig 3-3 A-B). Higher abundances of Ti coincide with increases in dust flux by one to more than two orders of magnitude (Fig. 3-3 B, Table SI-2c). The maximum dust fluxes observed in the record were 510 and 545 μg $cm^{-3}y^{-1}$ centered at 12,230 and 5,200 cal. yr BP, respectively and the minimum value was 3 μg cm^{-3} y^{-1} centered at 3,450 cal. yr BP. From the beginning of the record at 13,356 cal. yr BP up to 10,340 cal. yr BP, dust fluxes ranged between 510 to 100 μg $cm^{-3}y^{-1}$. Dust fluxes are low during most of early Holocene with an episodic high input of 290 μg $cm^{-3}y^{-1}$ around 8,000 cal. yr BP. The mid-late Holocene is highlighted by several dust events with fluxes ranging from 10 to 545 μg cm^{-3} y^{-1}, with the highest flux around 5,200 cal. yr BP.

Elemental variations in the Neor peat core (Fig. 3-1 and 3-3 A-B) indicate that the most recent period of deglaciation is marked by a gradual increase in the intensities of lithogenic elements and aeolian fluxes from the Allerød period to the Younger Dryas, followed by a decline in aeolian input until around 10,200 cal. yr BP. We note that dust fluxes declined by nearly fivefold from the highest values during the Younger Dryas to the early Holocene (Fig. 3-3 B). With the exception of two episodes of elevated dust from 8,350-7,900 and 7,650-7,400 cal. yr BP, less dust was deposited prior to and during the early Holocene relative to the last deglacial period and mid-late Holocene. Episodes of enhanced dust deposition from 8,500 to 6,300 cal. yr BP (Fig. 3-3 A-B) coincide with times

of reduced rainfall and strong solar minima as recorded in stalagmites from the Hoti cave, Oman (Neff et al., 2001). The prolonged period of dust deposition from 6,300 to 5,000 cal. yr BP is in good agreement with the termination of the African Humid Period in subtropical Africa between 6,000 to 5,000 cal. yr BP (deMenocal et al., 2000; Gasse and Van Campo, 1994). Episodes of low dust input during the mid-Holocene around 5,700 and 6,000 cal. yr BP also coincide with wet periods in eastern Mediterranean as recorded in stalagmites from Soreq Cave in Israel (Bar-Matthews and Ayalon, 2011).

Enhanced aeolian input is more frequent as summer solar insolation at 60 °N declines (Fig. 3-3 A) after around 6,000 cal. yr BP to the present. These episodes are also coincident with drier conditions as recorded in palaeoclimate archives from Lake Tecer in Turkey (Kuzucuoglu et al., 2011) and Maharlou and Zeribar Lakes in Iran (Djamali et al., 2009; Griffiths et al., 2001; Wasylikowa and Witkowski, 2008; see Fig. 3-3 J). Our results support the findings of a recent compilation of aeolian fluxes from 43 palaeodust records over the last 12,000 yr that suggest minimum mineral dust deposition during the early to mid-Holocene (Albani et al., 2015).

3.1.2- Organic proxy records and dust source variability

The picture that emerges from the lithogenic input to Neor peat mire is corroborated by variations in TOC content and $\delta^{13}C$ of bulk organic matter. At a resolution of 30 yr/sample, the $\delta^{13}C_{TOC}$ range from -28.7 to -25.3 ‰, with more negative values corresponding with lower TOC and higher abundances of Ti since 9,800 cal. yr BP (Fig. 3-3 A and C-D). This suggests that drier conditions coincided with lower production and/or lower preservation of organic matter during dustier periods. Although variations in sedimentation rate can potentially influence TOC, a strong covariation is observed between

TOC, $\delta^{13}C_{TOC}$ and the relative abundances of Ti, which suggests that the TOC record is not significantly biased by changes in accumulation rates. It is notable that the relationship between $\delta^{13}C_{TOC}$ and TOC is less evident between 11,500 to 8,000 cal. yr BP, and apparently becomes decoupled from XRF intensities of Ti prior to 11,500 cal. yr BP. While we cannot offer a straightforward explanation for this decoupling, it is likely due to a change in plant assemblage/species and the hydrological regime during the transition from glacial to interglacial conditions. The dominant plant species in the Neor peat mire is *Drepanocladus sp.* moss (*D. aduncus – polygamous*), a highly polymorphic species typical of periodically flooded bogs that are subjected to environmental modifications (Harald Kürschner, Freir Universität Berlin, Institut für Biologie, Systematische Botanik und Pflanzengeographie, unpublished data).

Additional evidence for changes in the hydrological regime during the deglacial period and Holocene comes from the hydrogen isotopic composition (δD) of C_{28} *n*-alkanoic acid (Fig. 3-3 E). The average monthly δD of precipitation in the interior of West Asia is correlated with average monthly precipitation at two meteorological stations located 1,365 km to the west and 390 km to the east of the Neor peat mire at the same latitude (Fig. 3-4). Changes in δD measured on 39 samples (340 yr/sample resolution, Table SI-2d) range from -225 to -185‰ with the most positive values observed during the Younger Dryas (-195 to -186 ‰), a time period also represented by the highest input of lithogenic elements in the entire record as seen in the XRF-Ti profile and aeolian fluxes (Fig. 3-3 A-B). In contrast, the most negative δD values are observed during the early Holocene, followed by a gradual increase around 8,000-7,000 cal. yr BP to a plateau for the rest of the record (Fig. 3-3 E). This agrees with reconstructions of water availability based on chironomid assemblages in

Neor peat mire during the Younger Dryas and the early Holocene (Aubert, 2013), as well as some of the records (particularly oxygen isotopes) from Lake Zeribar (Stevens et al., 2001) in west Iran that documented a wet early Holocene period followed by drier conditions (Fig. 3-3 J). A similar shift from enriched $\delta^{18}O$ values during Younger Dryas to more negative values during early Holocene is observed in most of the records from Mediterranean lakes (Roberts et al., 2008), indicating wet conditions prevailed in the region during early Holocene. These records are consistent with the influence of high solar insolation (Fig. 3-3 A) during the early Holocene.

Transition from the most positive δD values during the Younger Dryas to the most negative δD values during the early Holocene, followed by a return to more positive values during the middle to late Holocene indicate that moisture availability, moisture source, or most likely a combination of both varied between these time periods, with the wettest interval during the early Holocene. This observation is further supported by the maximum in carbon accumulation rates of up to 13 g C m^{-3} y^{-1} (Fig. 3-3 A, E and G). The lowest carbon accumulation rates are observed during the Younger Dryas and other periods of high dust input, while higher carbon accumulation rates are associated with periods of low dust input throughout the record. Although absolute values differ as would be expected between climatic regions, a similar trend of δD-enrichment across the Holocene is also observed in leaf wax δD composition measured in sediments of Lake Victoria (Berke et al., 2012), Lake Tanganika (Tierney et al., 2008) in East Africa (Fig. 3-3 H), as well as in other records of hydrological changes in the African Tropics (Gasse, 2000). Moisture delivery to northwest Iran and eastern Africa during the early Holocene likely occurred through different synoptic systems; enhanced summer monsoon over east Africa and the

position of the subtropical westerly jet and westerly disturbances over NW Iran. Expansion of moisture from the Caspian Sea is another possibility. Neor peat mire, however, is located on the leeward side of the Alborz Mountain Range, a natural barrier that retains moist air masses from the Caspian Sea (Fig. 2-2). Nevertheless, the similarities in δD records of leaf wax between Neor peat mire and East African Lakes, especially Lake Victoria, are indicative of a hemispheric forcing mechanism, most likely changes in solar insolation that influenced the climate of tropical and subtropical Africa and Eurasia.(deMenocal et al., 2000; deMenocal and Tierney, 2012).

In addition to carbon accumulation rates and δD records, the P*aq* index, used as a proxy for the dominance of submerged *vs* emergent plants, provide a measure of water availability in peat mires (Seki et al., 2009; Zhou et al., 2005, 2002). Although the P*aq* index (Fig. 3-3 F, Table SI-2e) are highly variable from sample to sample (not shown) and do not show a wide range, the highest mean value for P*aq* was observed during the early Holocene (Fig. 3-3 F). In comparison, the average P*aq* during the middle and late Holocene were progressively lower, suggesting the declining dominance of submerged plants, most likely due to diminishing moisture availability as solar insolation declined. While carbon accumulation rates, the P*aq* index and compound-specific δD point to substantial changes in moisture availability and/or shifts in the hydrological regime during the last 13,000 years over the study area, they do not allow us to differentiate between potential changes in the path/source of moisture brought from the Mediterranean Sea via subtropical westerlies and westerly disturbances (Alijani, 2002; Alijani and Harman, 1985) the Caspian Sea , and the Persian Gulf, Arabian and the Red Sea regions (Evans and Smith, 2006; Raziei et al., 2013b, 2012), especially during the early Holocene.

The potential change in source is not limited to water. The clustering of lithogenic elements (Ca, Al, Si) into three distinct groups (Fig. 3-5) raises the possibility of shifts in the source(s) of aeolian material during the late Termination to early and mid-late Holocene. Indeed, the results of geochemical fingerprinting with radiogenic Sr-Nd-Hf isotope systematics and rare earth element anomalies measured in mineral dust from Neor peat, paired with simulations of atmospheric circulation can shed light on the shifts in dust source provenances during these periods and provide better understanding of changes in atmospheric circulation related to the meridional migration of the main axis of the subtropical Westerly jet over the study area as a result of changes in solar insolation over the northern Hemisphere, see chapter 4.

3.1.3- Wavelet analysis and periodicities in aeolian input

Wavelet power spectrum analysis conducted on major components of the Ti intensity time series for the entire record (13,356 years, Fig. 3-6) reveal six centennial to millennial periodicities. Peaks centered on the power spectra of ~230, ~320 and ~470 years are notable but not significant (global power spectrum below 1σ). These periodicities are close to the de Vries cycle of solar excursions (~ 210 yr ; Steinhilber et al., 2012) and ~520 yr (un-named cycle). Significant periodicities over the entire record are centered at~820, ~1,550, and ~3,110 years and are similar to a 1,000 yr (Eddy cycles; Abreu et al., 2010) cycle based on ^{14}C in tree-rings and solar activity records (Stuiver and Braziunas, 1991), and the 1,500 and 3,000 years cycles in solar irradiance (Bond et al., 2001, 1997). Given the length of the entire record, however, the 3,000 year periodicity should be treated with caution.

Previous studies in the Arabian Sea, an area significantly impacted by the Indian Ocean Summer Monsoon, have shown a strong atmospheric teleconnection between the North Atlantic and northern Indian Ocean on millennial timescales during the last glacial period (Altabet et al., 2002; Pourmand et al., 2007a, 2004, 2005; Schulz et al., 1998). Taken together, the correlations between our multi-proxy records and other archives from the eastern Mediterranean Sea, African lakes, Greenland (GISP2) (deMenocal et al., 2000; deMenocal and Tierney, 2012; Turner et al., 2008), and the results from wavelet analysis of aeolian input to Neor peat mire point to changes in solar irradiance and insolation on Holocene climate variability, and suggest an atmospheric teleconnection between the North Atlantic and the interior of West Asia during the last glacial termination and the present interglacial period.

3.2- Climate change and human societies in West Asia during the mid-late Holocene

Archaeological and historical records from West Asia have documented rise and fall of human societies across the eastern Mediterranean, Mesopotamia and northern Persian Gulf (*e.g.* Brooks, 2006; Cullen et al., 2000; deMenocal, 2001; Riehl, 2009). Nevertheless, little is known about the influence of rapid climate change on human societies due to the scarcity of high-resolution palaeoclimate reconstructions with robust age models, and the gaps in the historical and archaeological records, which are also prone to uncertainties. As a step towards a better understanding of the potential relationship between rapid climate change and human responses in this region, we compare our findings with a compilation of historical and archaeological records of drought, famine, socio-economic and cultural transitions over the Iranian Plateau (Iran), Mesopotamia (MSP), and eastern Mediterranean

(EM) regions along with palaeoclimate records of dry/wet periods for West Asia (see Table 3-1 and 3-2).

The rugged terrain of the Iranian Plateau was likely not as hospitable to societal development compared to epicenters of development across the Fertile Crescent where sociocultural developments evolved within river valleys (e.g. Egypt). Interpretation of archaeological records across the Iranian Plateau is challenging because unequal attention has been paid to different locations and even different historical periods (Abdi, 2011). Although some artifacts of early settlements and the onset of agriculture in the region date back to ~12,000 yr BP (Riehl et al., 2013) and despite the fact that the early villages in Iran were existed as early as 9,000 yr BP (7,000 BC), the nomadic-sedentary dichotomy did not appear till the early Bronze Age (ca. 3,200 to 2,200 BC) (Abdi, 2011). Transition from food procurement to food production societies in Mesopotamia took place around 5000 BP, when irrigated cultivation yielded surpluses that led to increased population and formation of the first city-units, the central entity in the rise of early Near Eastern civilizations (Childe, 1950; Redman, 1978). Middle Bronze Age (ca. 2,200 to 1,600 BC) in the Iranian Plateau is highlighted by florescence of urbanism (Abdi, 2011). As a result, we compare these records with the high-resolution aeolian input from Neor between 5,000 cal. yr BP to present (2010) with considerations for uncertainties in our age model (Fig. 3-7). Note that we do not incorporate the age uncertainties that are inherent in the historical and archaeological records but are not reported or often difficult to establish.

With these caveats in mind, we note eight episodes of high aeolian input that mostly coincided with dry conditions in other regional palaeoclimate records (Fig. 3-7 A and F). These episodes also coincided with accounts of drought, famine, socio-economic and

cultural transitions over Iran, MSP, and EM regions. Most notably, we confirm evidence from a marine core that suggested the fall of the Akkadian Empire at 4,200 yr BP was coincident with an episode of exceptionally high aeolian input to the Arabian Sea (Cullen et al., 2000). Further, transitions in major Mesopotamian and Iranian civilizations, including the collapse of the Ur III empire at 3,955 yr BP (Leick, 2010), the fall of the Elam empire at 2,800 yr BP, and the Medes empire at 2,500 yr BP, as well as the demise of the Achaemenids around 2,280 BP, the Partians around 1,730 yr BP, the Sasanians at 1,300 yr BP, and the Safavids at 290 yr BP (Daryaee, 2011), overlapped with major dust events from this study (Fig. 3-7 F and G). Periods of prolonged drought from 4,550 to 2,800 cal. yr BP and several short droughts from 2,100 to 100 cal. yr BP in Iran, MSP and EM are also coincided with episodes of enhanced dust deposition from our record (Fig. 3-7 B, C, and F). Drought events during the period of 1,800-1,500 cal. yr BP in Iran were followed by famine (Fig. 3-7 B, and C) and other famine events in Iran after 1,300 cal. yr BP, which have been associated with war, political tensions and resource crisis (Table 3-23), also coincided with high levels of atmospheric dust deposition (Fig. 3-7 C, and F) at Neor. Consecutive drought events from 1770 to 1930 AD recorded in central Anatolia also coincided with the latest major dust event from our record (200 BP to present).

The author emphasize, however, that historical and archaeological accounts of societal change are lacking during some periods of elevated atmospheric dust (Fig. 3-7). This suggests that either climate change did not significantly impact the human societies in the region during those periods, or the communities were better equipped to adjust to abrupt changes. Alternatively, it is possible that accounts of these events were not recorded or are missing from historical and archaeological archives due to the power transition

between ruling governments. Nevertheless, given that agriculture, livestock and timber production dominated the economies of early civilizations in this region (Zohary and Hopf, 2000), climate change can be expected to have played a significant role in the development of human societies and in power transitions. While we made every effort to compile notable historical and archaeological archives, some records may be missing from this compilation and should be further considered in future comparisons.

As a final remark, the author note that while abrupt climate change may have influenced human societies across the region, it is reasonable to expect that increasing human activities in the form of deforestation and agropastoral land use may have, in turn, contributed to elevated eolian content of the atmosphere as these activities are known to expose soil material to erosion and transport by wind (Eastwood et al., 1999; Vermoere et al., 2002). A recent study on the fossil pollen and insect remains from a peripheral peat core in NE part of the lake (Fig. 2-2) suggest that pastoralism was likely practiced in the high elevation surroundings of Neor in Talysh Mountains ~6,000 yr BP (Ponel et al., 2013). The authors also conclude that on a regional scale, agropastoral activities intensified after about 2,000 yr BP. In another study, Djamali (2009b) identified several phases of intensified human activities based on pollen records of the last 3,500 years from a crater peat record located about 175 km SW of our study area.

Major dust events of the last 5,000 years in Neor broadly covary with the intensity of the Siberian anticyclone, and the peaks of high eolian input are followed by a shift in $\delta^{13}C_{TOC}$ and TOC (Fig. 3-7 D and E, see also Fig. 3-3 C, D and I). These proxies are independent of human activities and suggest drier conditions prevailed during the episodes of enhanced dust input. Indeed, the δD data during the last 3,000 years are relatively

constant, indicating little or no change in moisture availability during these high-dust input events. This observation suggests that although human activity may have contributed to additional dust during the last 3,000 years, as implied by numerous high –frequency events over this period (Fig. 3-3), this most likely happened in the broader context of abrupt climate change that was already underway. It is worth mentioning that based on satellite observations of dust optical depth from MODIS measurements (Ginoux et al., 2012), anthropogenic sources in modern times account for up to %25 of global dust emission, with significant spatial variability. Dust emissions due to human activities were likely lower during late Holocene than they are today. The contribution from natural *vs* anthropogenically-introduced aeolian sources and the extent to which human activities affected climate change in the region cannot be fully addressed with the current dataset and additional high-resolution proxy reconstructions that can be linked to specific human activities based on historical and archeological records in the region are needed to assess this hypothesis.

4- Conclusions

In this chapter a high-resolution reconstruction of aeolian input and changes in palaeoenvironmental conditions from a 13,000 year peat record from NW Iran was presented. Variation in elemental abundances, TOC, $\delta^{13}C_{TOC}$, compound-specific leaf wax hydrogen isotopes (δD), carbon accumulation rates and aeolian fluxes revealed that dry and dusty conditions prevailed during the late glacial termination. These conditions were followed by a wetter and less dusty interval during the early Holocene over the interior of West Asia. Subsequently, the middle-late Holocene became drier and is marked by higher frequency intervals of aeolian input to the study area. It is notable that the multi-proxy

dataset presented in this study supports the traditional interpretation that low $\delta^{18}O$ values from lakes in western Iran correspond to wetter conditions during the early Holocene.

Comparison with regional records and wavelet analysis of aeolian input to Neor peat mire suggest changes in solar insolation (and possibly irradiance) most likely played a key role in controlling water availability and aeolian input to the studied region. Our data also suggest an atmospheric teleconnection existed between North Atlantic climate and West Asia during the last glacial termination and the Holocene. Nearly all episodes of enhanced deposition of lithogenic material in our record corresponded with episodes of drought and famine in the region as well as with transitions in major Mesopotamian and Iranian civilizations. This includes the fall of the Akkadian empire around 4,200 yr BP as was previously suggested from marine sediments of the Arabian Sea. Our findings indicate that ancient human societies from West Asia were likely highly susceptible to abrupt climate variability during the current interglacial period. The extent to which human activities across the region influenced soil erosion and created new sources of eolian material for proximal and distant transport during the last 3,000 years remains to be constrained as more high-resolution reconstructions become available from West Asia.

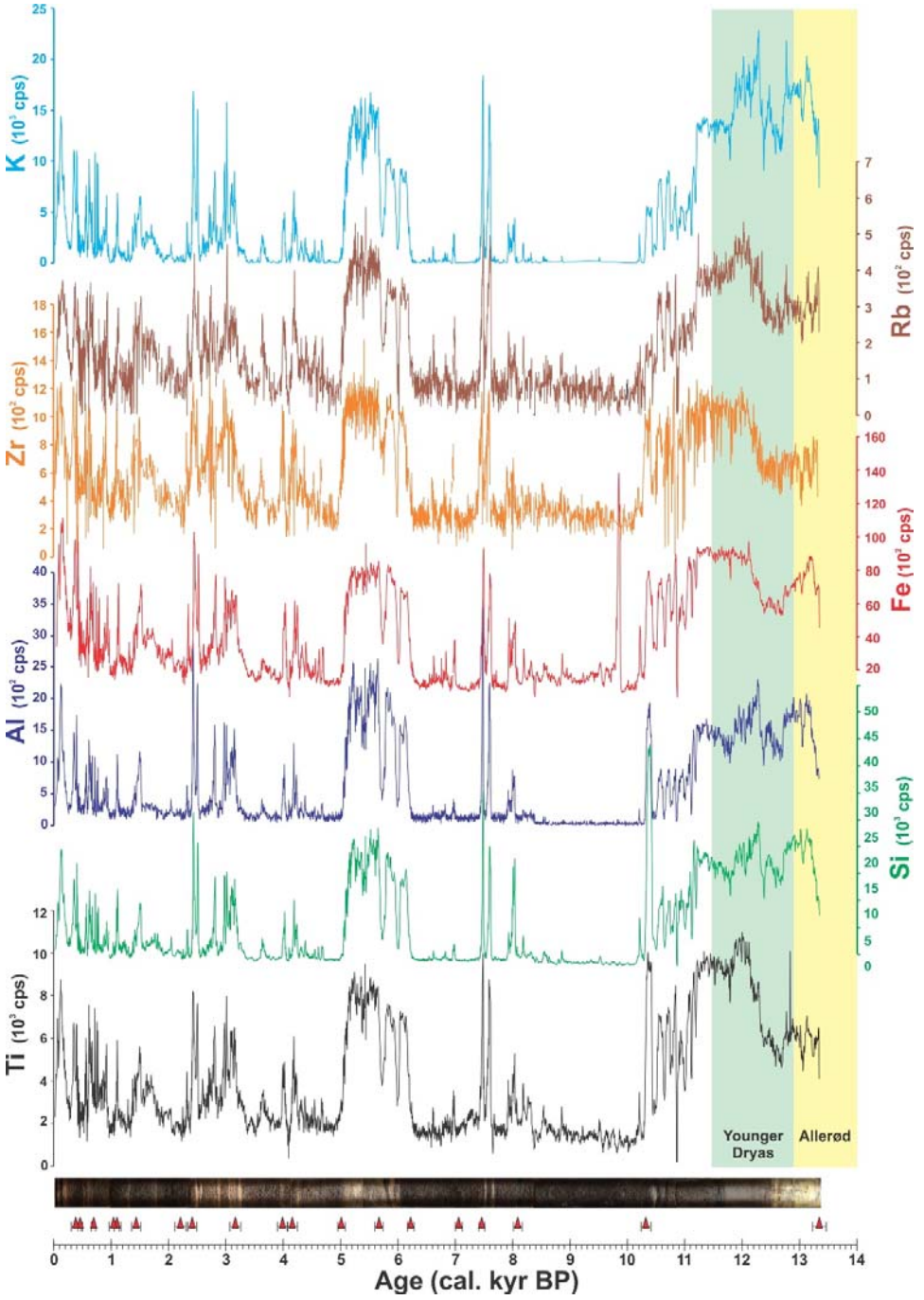

Fig. 3-1- Downcore XRF profiles of elemental abundances in Neor peat core. Downcore profiles of elemental abundances for refractory lithogenic (Al, Zr, Ti, and Si) and redox sensitive (Fe) and mobile (K and Rb) elements in counts per second (cps) associated with major dust intervals (light bands) over the last 13,356 cal. yr BP at Neor peat mire. The red triangles denote the stratigraphic position of calibrated radiocarbon dates measured on bulk samples. Light bands in the core image correspond with peaks of lithogenic elements. Dark bands are mainly comprised of decomposed organic matter with low intensities of lithogenic elements.

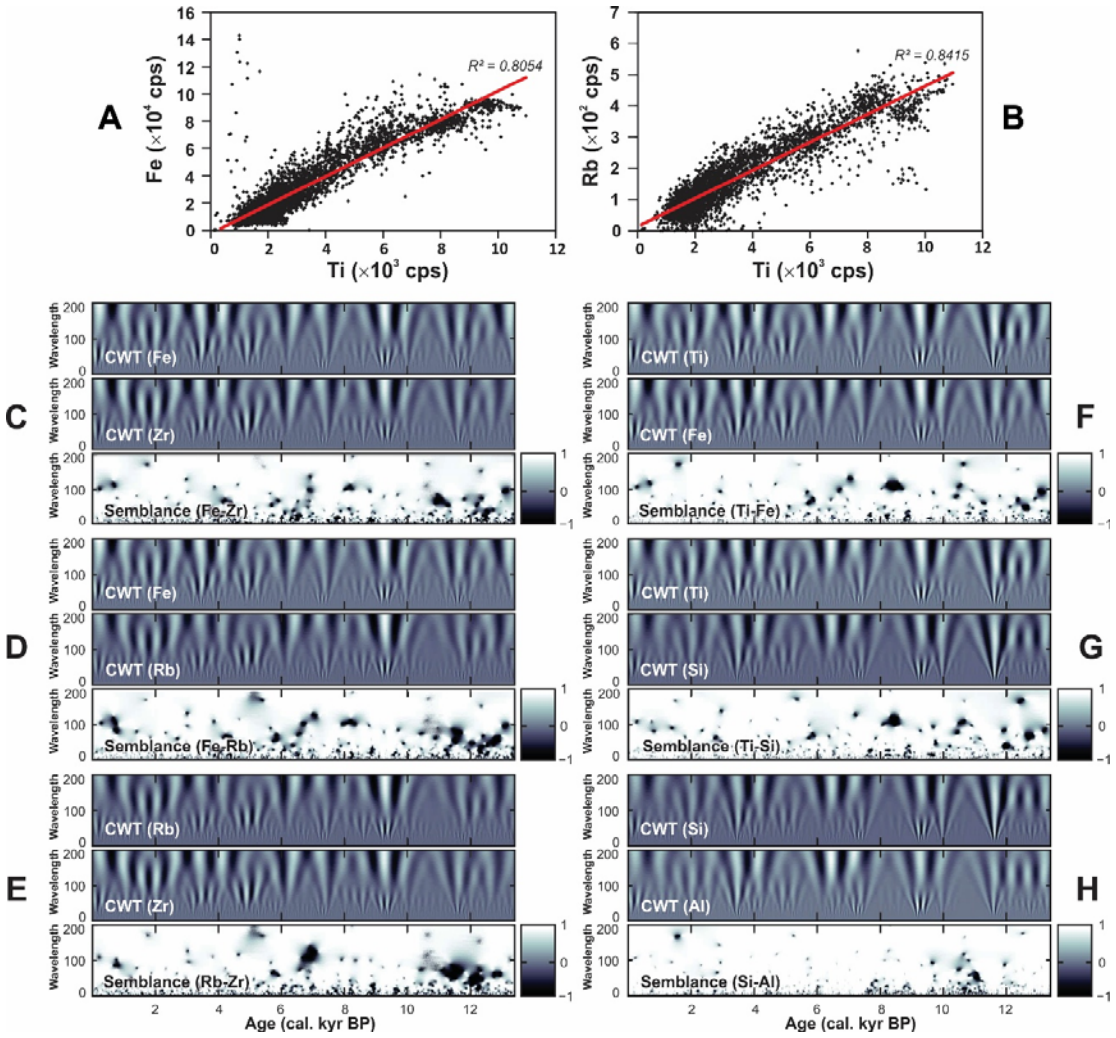

Fig. 3-2- Correlation between elemental pairs in Neor peat core. Variation of Fe (A) and Rb (B) with respect to Ti. Cross-wavelet transform (CWT) for elemental pairs (C-H) and their corresponding semblance wavelet analysis capture covariations of elemental abundances as a function of time. White areas in CWT panels indicate positive amplitude where black indicates negative amplitude. In the panels referring to semblance analysis, the degree of correlation between relative abundances of two elements are shown in white, corresponding to a semblance of +1 (positive correlation), 50% grey to a semblance of zero, and black to a semblance of -1 (negative or inverse correlation). For most of the record, the relative abundances of refractory and mobile elements show significant agreement (+1) and attest to the ombrotrophic nature of the entire record with respect to atmospheric dust input.

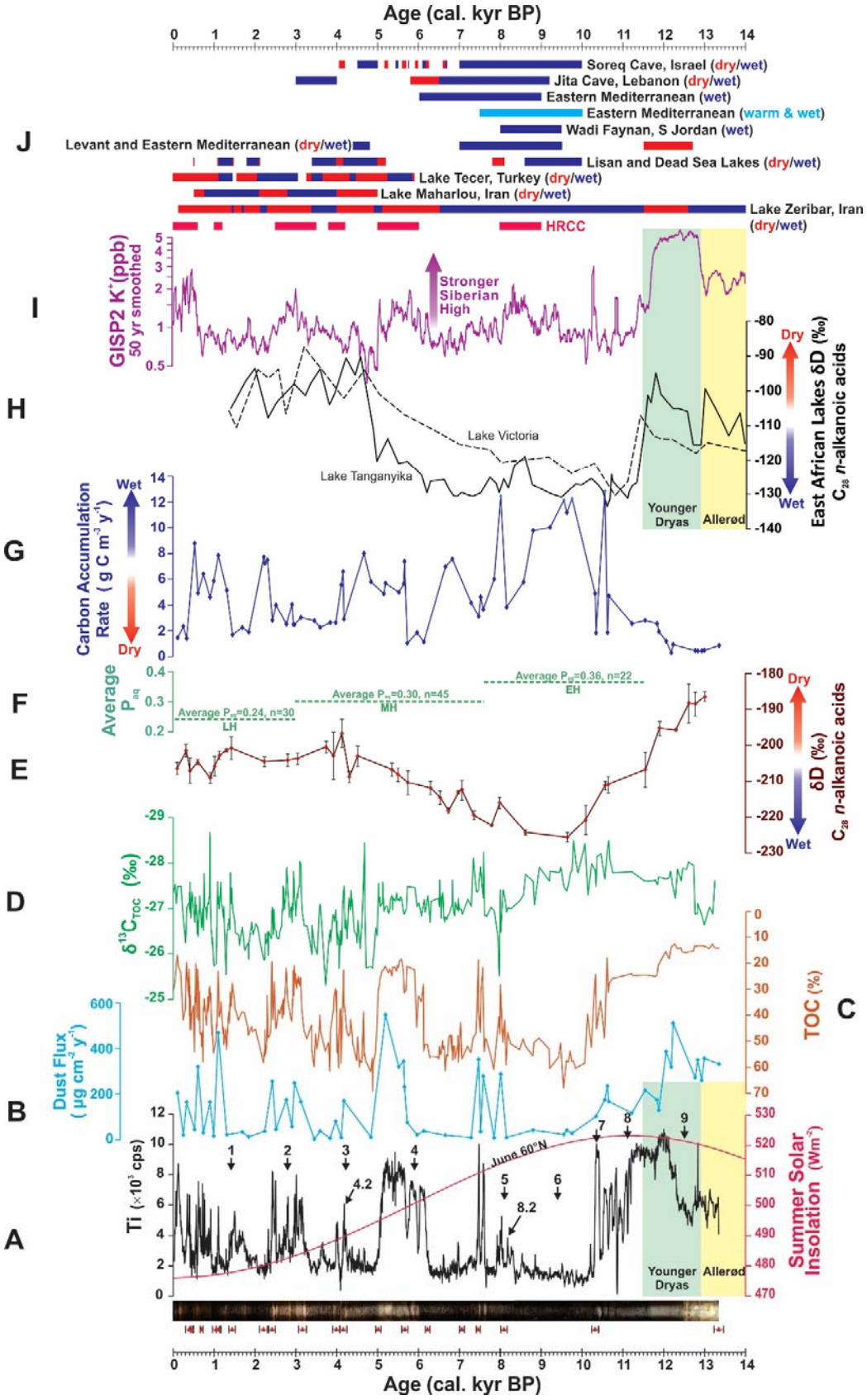
Age (cal. kyr BP)
Soreq Cave, Israel (dry/wet)
Jita Cave, Lebanon (dry/wet)
Eastern Mediterranean (wet)
Eastern Mediterranean (warm & wet)
Wadi Faynan, S Jordan (wet)
Levant and Eastern Mediterranean (dry/wet)
Lisan and Dead Sea Lakes (dry/wet)
Lake Tecer, Turkey (dry/wet)
Lake Maharlou, Iran (dry/wet)
Lake Zeribar, Iran (dry/wet)
HRCC
GISP2 K+ (ppb) 50 yr smoothed
Stronger Siberian High
Lake Victoria
Lake Tanganyika
East African Lakes δD (‰) C28 n-alkanoic acids
Dry
Wet
Younger Dryas
Allerød
Carbon Accumulation Rate (g C m-2 y-1)
Average Paq
Average Paq=0.24, n=30
LH
Average Paq=0.30, n=45
MH
Average Paq=0.36, n=22
EH
δ13CTOC (‰)
TOC (%)
Dust Flux (µg cm-2 y-1)
Ti (×10³ cps)
June 60°N
Summer Solar Insolation (Wm-2)
4.2
8.2
A
B
C
D
E
F
G
H
I
J

Fig. 3-3- Multi-proxy sediment record in Neor peat from NW Iran. A) Core image (750-cm), 19 radiocarbon dates and Ti ($\times 10^3$ cps) intensity profile measured by XRF are shown along with summer solar insolation (Wm^{-2}) at 60°N (red line), North Atlantic Holocene Ice Rafted Debris (IRD) 1-9 (Bond et al., 1997), and 4.2, 8.2 cooling events (Bond et al., 1997). B) Dust flux based on Ti concentration ($\times 10$ μg cm^{-3} y^{-1}). C) Total organic carbon (TOC) %. D) Bulk $\delta^{13}C$ of TOC, TOC and $\delta^{13}C_{TOC}$ are plotted in reverse scale. E) Compound-specific δD (‰). F) The average of Paq index during early (EH), middle (MH) and late Holocene (LH). G) Carbon accumulation rate (g C cm^{-3} y^{-1}). (H) Compound-specific δD (‰) values for Lake Tanganyika (solid line) (Tierney et al., 2008) and Lake Victoria (Berke et al., 2012) (dashed line) in East Africa. I) Variations in K^+ ion concentration from GISP2 ice core as a proxy for changes in the strength of the Siberian Anticyclone (Mayewski et al., 1997) and (J) Compilation of Mesopotamian and Mediterranean palaeoclimate records. Bars associated with pink bands denote Holocene rapid climate change events (HRCC) (Mayewski et al., 2004); see text and Table 3-1 for details.

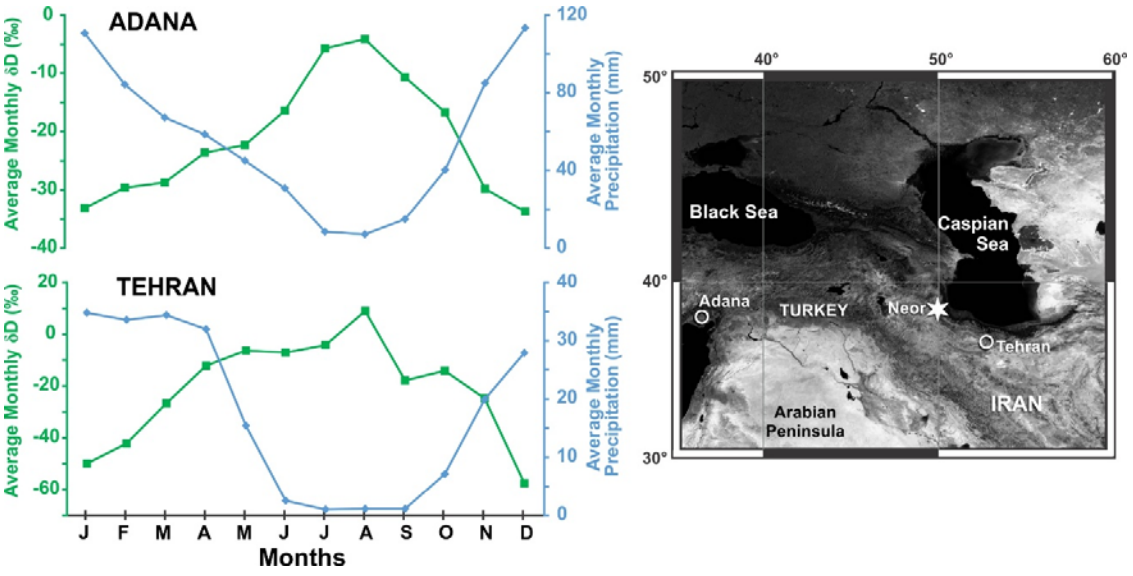

Fig. 3-4- Correlation between δD and precipitation in the region. Average monthly δD is highly correlated with monthly precipitation at the two synoptic station in Turkey (Adana, 36-year average) and Iran (Tehran, 44-year average) ($R^2_{Iran,Jan-Aug}$= 0.66; R^2_{Turkey}= 0.93) . Source: Global Network of Isotopes in Precipitation (GNIP), http://www.univie.ac.at/cartography/project/wiser/

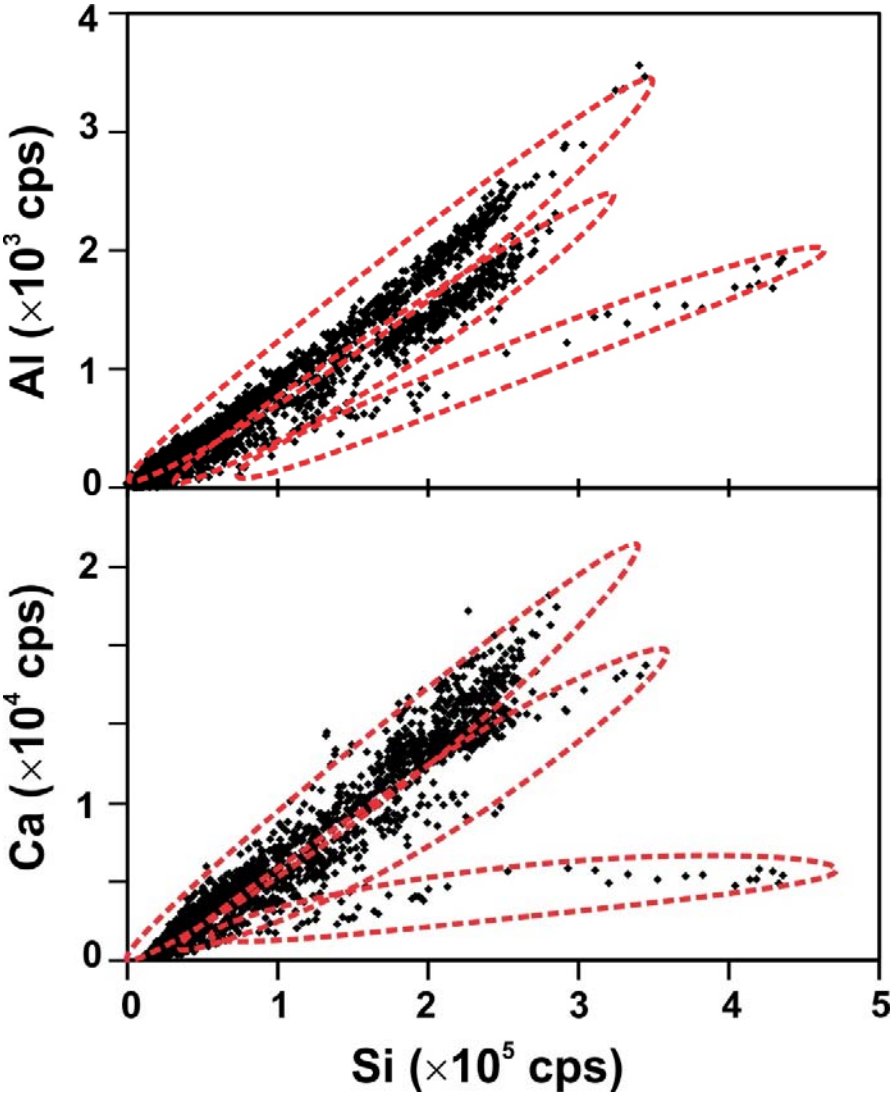

Fig. 3-5- XRF-abundances of Al (×10^3 cps) and Ca (×10^4 cps) with respect to Si (×10^5 cps) in Neor peat core. Areas identified with dotted line denote major clustering groups of potentially different source provenances.

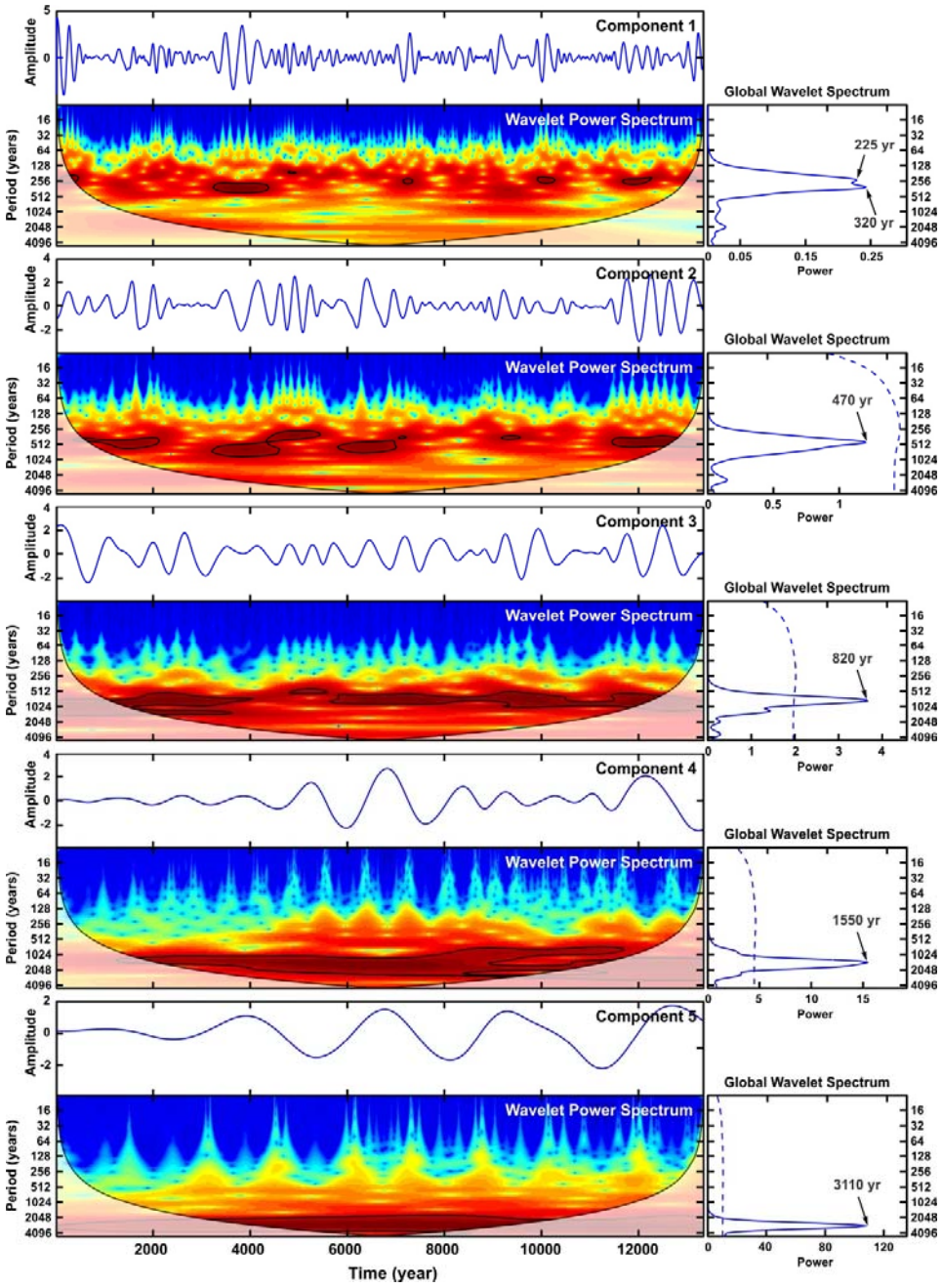

Fig. 3-6- Wavelet power spectrum of the major components of detrended time series of Ti intensities using the Morlet wavelet (Torrence and Compo, 1995) and complete ensemble empirical mode decomposition (CEEMD) approach (Torres et al., 2011). White areas denote the cone of influence and black boundaries mark 1σ confidence level. The color bar refers to the wavelet power values from dark blue (low values), to dark red (high values).The global power spectrum with the most significant peaks of spectral power is shown on the right panel, dashed lines are refer to 1σ confidence level.

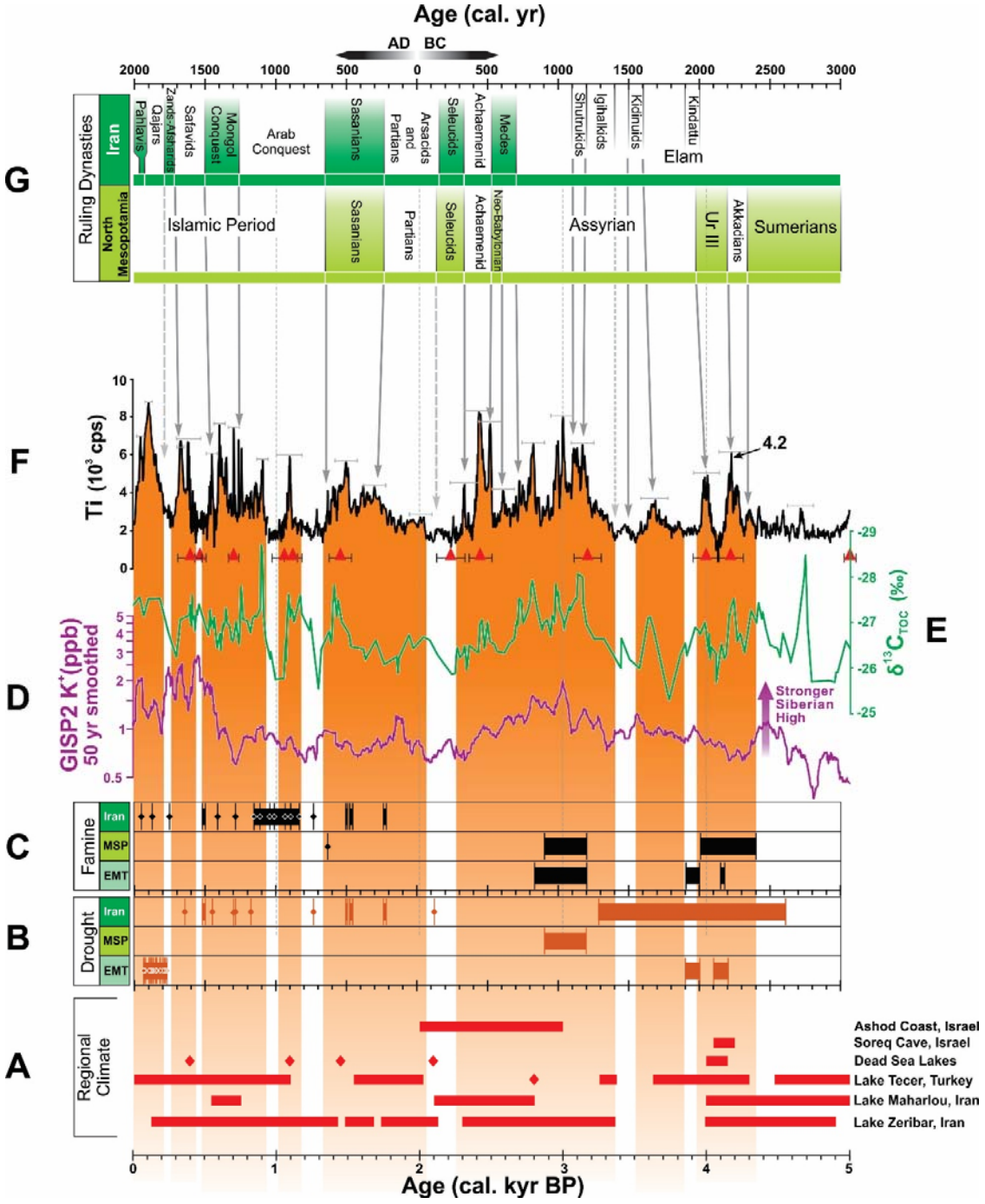
Age (cal. yr)
AD BC
2000 1500 1000 500 0 500 1000 1500 2000 2500 3000
G
Ruling Dynasties
Iran
North Mesopotamia
Pahlavis
Qajars
Zands-Afsharids
Safavids
Mongol Conquest
Arab Conquest
Sasanians
Arsacids and Parthians
Seleucids
Achaemenid
Medes
Shutrukids
Igihalkids
Kidinuids
Kindattu
Elam
Islamic Period
Sasanians
Parthians
Seleucids
Achaemenid
Neo-Babylonian
Assyrian
Ur III
Akkadians
Sumerians
F
Ti (10³ cps)
4.2
D
GISP2 K⁺(ppb) 50 yr smoothed
Stronger Siberian High
E
δ¹³C_TOC (‰)
C
Famine
Iran
MSP
EMT
B
Drought
Iran
MSP
EMT
A
Regional Climate
Ashod Coast, Israel
Soreq Cave, Israel
Dead Sea Lakes
Lake Tecer, Turkey
Lake Maharlou, Iran
Lake Zeribar, Iran
Age (cal. kyr BP)

Fig. 3-7- Periods of enhanced aeolian deposition from Neor peat core compared with cultural transitions and historical and archaeological accounts of climate change in West Asia over the last 5,000 yr. A) Episodes of dry conditions as recorded in regional palaeoclimate data are from Ashod Coast, Israel; Soreq Cave, Israel; Lisan and Dead Sea Lakes; Lake Tecer, Turkey; Lake Maharlou, Iran, and Lake Zeribar, Iran. B) Drought records from Iran, MSP and EM since 3,000 BC . C) Historical records of prolonged (bars) and single (diamonds) famine events from Iran, MSP and EM since 3,000 BC; bars and diamonds refer to prolonged and single drought events, respectively. For data on panels A through C see Tables 3-1 and 3-2. D) Variations in K+ ion concentration from GISP2 ice core as a proxy for changes in the strength of the Siberian Anticyclone. E) Bulk $\delta^{13}C_{TOC}$ plotted in reverse scale. F) Ti intensity (cps) over the last 5,000 yr. Data for panels D through F are presented in Table SI-2.The error bars on major peaks approximate the uncertainties associated with the age model in this study interpolated from two adjacent age tie points. Red triangles are calibrated radiocarbon dates and Orange areas denote major episodes of dust deposition since 5,000 cal. yr BP. The 4.2 kyr event coinciding with the Collapse of the Akkadian Empire is also shown. (G) Ruling dynasties in Iran (top) and Mesopotamia (bottom) since 3,000 BC (~5,000 BP). Gray arrows denote power transitions.

Table 3-1- Records of climate variability inferred from paleoclimate archives and available literature (Year BP).

Date	Event*	Record's Location	Evidence	Reference
200 BP-Today	Dry and arid			
200-800 BP	Warm Condition, Hot summers			
800-1100 BP	Dry Condition			
1450-1100 BP	Wet Condition			
1540-1640 BP	Dry Condition, Drought			
1640-2020 BP	Dry and warm Condition			
2020-3050 BP	Wet Condition			
3250-3380 BP	Dry Condition	Lake Tecer, Turkey	Sedimentological evidences	(Kuzucuoglu et al., 2011)
3380-3630 BP	Wet Condition			
3630-4300 BP	Dry Condition			
4300-4480 BP	Wet Condition			
4480-4950 BP	Dry Condition			
4950-5250 BP	Dry Condition, Drought			
5250-5850 BP	Humid and Wet Condition			
5850-5900 BP	Dry Condition			
4048 BP	Wet Condition			
4048-6505 BP	Dry Condition	Lake Mirabad, Iran	Ostracod	(Griffiths et al., 2001)
6505-9265 BP	Warm Condition			
550-750 BP	Dry Condition			
2100-2800 BP	Dry Condition, Drought			
2800-4000 BP	Wet Condition	Lake Maharlou, Iran	Pollen	(Djamali et al., 2009a)
4000-5100 BP	Dry Condition			
5100-5500 BP	Wet Condition			
Before 5500 BP	Dry Condition			
3250-4540 BP	Drought	Central Iran	Pollen	(Schmidt et al., 2011)
4200 BP	Arid conditions, Akkadian Collapse	Mesopotamia	Eolian Input, Marine Geochemical Proxies	(Cullen et al., 2000)

Table 3-1- *Continued*

Date	Event	Record's Location	Evidence	Reference
7000 BP	Wet Condition	Eastern Mediterranean	$\delta^{18}O$, $\delta^{13}C$, Pollen Records Speleothem $\delta^{18}O$	(Cheddadi et al., 1991) (Goodfriend, 1999)
3000 BP	Intense Drying			
8000 BP	Progressive Drying	Jerusalem, Israel	Speleothem $\delta^{13}C$	(Frumkin et al., 2000)
11000-13000 BP	High Temperature and Precipitation			
4500-5000 BP	Wet Condition			(Bar-matthews, 1997)
7000-8500 BP	Deluge Period	Soreq Cave, Israel	Speleothem $\delta^{18}O$, $\delta^{13}C$	(Bar-Matthews et al., 1999)
7000-10000 BP	Extremely Wet Condition			(Bar-matthews, 1997)
400 BP	Lake Level Drop, Dry Condition			
800 BP	Lake Level Rise, Wet Condition			
1100 BP	Lake Level Drop, Dry Condition			
1100-1450 BP	Lake Level Rise, Wet Condition			
1450 BP	Lake Level Drop, Dry Condition			
1800-2100 BP	Lake Level Rise, Wet Condition			
2100 BP	Lake Level Drop, Dry Condition			
3200 BP	Lake Level Drop, Dry Condition	Lisan and Dead Sea Lakes	Lake Level Records from palaeoshorelines and lithological variations	(Migowski et al., 2006)
3400-4000 BP	Lake Level Rise, Wet Condition			
4000-4150 BP	Lake Level Drop, Dry Condition			
4150-5000 BP	Lake Level Rise, Wet Condition			
5000-5200 BP	Lake Level Drop, Dry Condition			
7800-8100 BP	Lake Level Drop, Dry Condition			
8200 BP	Lake Level Drop, Dry Condition			
9000 BP	Lake Level Rise, Wet Condition			
9150 BP	Lake Level Drop, Dry Condition			
9200-10000 BP	Lake Level Rise, Wet Condition			
4500-4800 BP	Wet Condition			
7000-9500 BP	Wet Condition	Levant and Eastern Mediterranean	Review of Multiple Datasets	(Robinson et al., 2006)
11500-12700 BP	Extremely Dry and Cold, Younger Dryas			

Table 3-1- *Continued*

Date	Event	Record's Location	Evidence	Reference
5500BP 8000-9500 BP	Dry Condition Wet Condition	Wadi Faynan, S Jordan	Active Aeolian deposition Paleogeomorphology	(McLaren et al., 2004)
7000 BP	Wet Condition	Soreq and Peqiin Caves, Israel and Eastern Mediterranean Sea	Speleothem and Foraminiferal $\delta^{18}O$, $\delta^{13}C$ and Calculated Paleorainfall	(Bar-Matthews et al., 2003)
9000-6000 BP	Wet Condition	Eastern Mediterranean	Pollen Records	(Rossignol-Strick, 1995) (Rossignol-Strick, 1999)
3000-4000 BP 5800-6500BP 6500-9200 BP	Wet Condition Dry Condition Wet Condition	Jeita Cave, Lebanon	Speleothem $\delta^{18}O$, $\delta^{13}C$	(Verheyden et al., 2008)
4050-4200 BP 4700-4800 BP 5170-5250 BP 5450-5500 BP 5600-5700 BP 5740-5760 BP 6100-6170 BP 6180-6250 BP 6550-6450 BP 6600-6650 BP 6680-6700 BP	Dry Condition Wet Condition Dry Condition Wet Condition Dry Condition Wet Condition Wet Condition Dry Condition Wet Condition Dry Condition Wet Condition	Soreq Cave, Israel	Speleothem $\delta^{18}O$	(Bar-Matthews and Ayalon, 2011)
1400 BP 2000-3000 BP 3200 BP	Wet Condition Arid Condition Wet Condition	Ashdod Coast, Israel	$\delta^{18}O$, $\delta^{13}C$, Geochemical Proxies	(B. Y. Schilman et al., 2001)

Table 3-1- *Continued*

Date	Event	Record's Location	Evidence	Reference
100-1450BP	Dry Condition	Lake Zeribar, Iran	$\delta^{18}O$, Ostracod, and Pollen Records,	(Wasylikowa and Witkowski, 2008) (Stevens et al., 2008)
1450-1500 BP	Wet Condition			
1500-1700 BP	Dry Condition			
1700-1750 BP	Wet Condition			
1750-2100 BP	Dry Condition			
2100-2300 BP	Wet Condition			
2300-3350 BP	Dry Condition			
3350-4000 BP	Wet Condition			
4000-4900 BP	Dry Condition			
4900-5100 BP	Wet Condition			
5100-6500 BP	Dry Condition			
6500-11500 BP	Wet Condition			
11500-12600 BP	Dry Condition			
12600-14000 BP	Wet Condition			

* As noted by others (M. Djamali et al., 2010; Jones et al., 2013; Jones and Neil Roberts, 2008; Lora R Stevens et al., 2006), threshold and sensitivity to moisture and temperature varies between different climate proxies at different locations and evaluation of relative wet and dry conditions is not straightforward. However, the following interpretations of climate proxies are commonly accepted: High lake level or lake level rise=wet; Low lake level or lake level drop=dry; Frequent flood events=wet; More negative $\delta^{18}O$ of speleothem and ostracod= wet; More positive $\delta^{13}C$ of speleothem=dry; High percentage of oak pollen=wet; High percentage of artemisia pollen=dry; Aeolian layers in lacustrine and marine sedimentary profile=dry; Aeolian layers in archaeological profile=dry. Majority of climate conditions/events presented under the event column are interpretations provided by the original authors. In some occasions where direct interpretation was not available from the original authors, we used the above mentioned criteria to interpret the data.

Table 3-2- Climate related events in Southwest Asia inferred from available literature (Calendar Year).

Date	Event	Record's Location	Evidence	Reference
1927-1930 AD				
1916-1918 AD				
1898-1900 AD				
1894 AD				
1890-1892 AD				
1882 AD				
1873-1874 AD				
1853 AD	Severe Drought	Central Anatolia (Turkey)	Historical, Dendroclimatological and Meteorological Records	(Erinç, 1978)
1845 AD				
1819-1822 AD				
1799-1803 AD				
1792 AD				
1779-1782 AD				
1770-1773 AD				
1957 AD	Countrywide Famine			
1870-1872 AD	Countrywide Famine			
1863-1864 AD	Lack of Winter Rain in Fars			
1752 AD	Famine in Isfahan			
1640 AD	Simoom in Tabas			
1410 AD	Famine in Kerman			
1284-1286 AD	Drought and Famine in Fars	Iran		
1299 AD	Drought in Fars			
1180 AD	Drought in Kerman		Historical Survey	(Ketabi, 2005; Melville, 1984)
1153-1154 AD	Famine in Bayhaq			
1110 AD	Famine in Qaznein			
1033 AD	Countrywide Famine			
1010 AD	Famine in Sistan			
935 AD	Famine in Khorasan			
893-894 AD	Famine in Tehran and Rey			
835 AD	Famine in Sistan	Mesopotamia		
733 AD	Drought and Famine in Khorasan	Iran		
495-502 AD	Drought and Famine			

Table 3-2- *Continued*

Date	Event	Record's Location	Evidence	Reference
499 AD	Famine			(Frye, 1983)
459-484 AD	Drought and Famine			(Daryaee, 2013)
628 BC	Famine			
224–241 AD	Severe Drought and Famine			(Ketabi, 2005)
954 BC 940 BC	Famine	Mesopotamia	Textual evidence	(Alpert and Neumann, 1989)
800 BC	Desertion of Sussia in South Judaea	Levant and Dead Sea Region	Archeological Surveys	(Issar and Zohar, 2007)
1007 BC	Famine			
1050-1007 BC	Drought	Mesopotamia	Textual evidence	(Alpert and Neumann, 1989)
1080 BC	Famine			
1150-950 BC	*minima* in the Tigris and Euphrates river discharge	Ashdod Coast, Israel	$\delta^{18}O$, $\delta^{13}C$, Geochemical Proxies	(Schilman et al., 2001)
1150-950 BC	*minima* in the Tigris and Euphrates river discharge	Mesopotamia	Historical Survey	(Alpert and Neumann, 1989)
1150-950 BC			Pollen, $\delta^{18}O$, Population, Lake Level	(Kay and Johnson, 1981)
1150-950 BC			Textual and nontextual evidence	(Neumann and Parpola, 1987)
1200-825 BC	Dark Age	East Crete, Greece	Archeological Survey	(Haggis, 1993)
1200-825 BC	Dark Age	Eastern Mediterranean	Historical Survey	(Weiss, 1982)
1200-825 BC	Drought,	Gibala-Tell Tweini, Syria	Pollen	(Kaniewski et al., 2010)
1200-900 BC	Decline in Babylonian and Babylonian, Crop Failures, Famine	Mesopotamia	Textual and nontextual evidence	(Neumann and Parpola, 1987)
1200 BC	Extreme Heat and Dryness	Ugarit near the modern city of Latakia, Syria	Archeological Excavation	(Alpert and Neumann, 1989)
2000-1900 BC 2180-2150 BC	Severe Drought and Catastrophic Famine, Civilization Collapse	Upper Egypt and Mediterranean	Archeological Surveys	(Bell, 1971)

Table 3-2- *Continued*

Date	Event	Record's Location	Evidence	Reference
2200 BC	Abandon of Tell Leilan by Akkadian, Arid phase	Tell Leilan, Abu Hgeira2 and Abu Hafur- Syria	Volcanic glass and fine sand	(Weiss et al., 1993)
2300-2200 BC	Serious Drought	Palestine	Archeological Surveys, Sudden Desertion of Cities with no sign of voiolence	(Issar and Zohar, 2007)
2400-2000 BC	General Crisis	Near East	Pollen, $\delta^{18}O$	(Issar and Zohar, 2007)
2900-2350 BC	Termination of Wet Period	Egypt	Indirect Archeological Evidences	
3000 BC	Aridity during Uruk Period	Tell Nasran1- Syria		
4500 BC	Aridity during Ubaid Period	Tell Nasran2- Syria	Windblown Calcitic Dust	(Weiss et al., 1993)
5900 BC	Aridity during Halaf Period	Tell Bager- Syria		

CHAPTER 4

Early Holocene greening of the Afro-Asian dust belt changed sources of mineral dust in West Asia[2]

[2] This chapter was published in Earth and Planetary Science Letters:
Arash Sharifi, Lisa N. Murphy , Ali Pourmand, Amy C. Clement, Elizabeth A. Canuel, Abdolmajid Naderi Beni, Hamid A. K. Lahijani, Doriane Delanghe , Hesam Ahmady-Birgani, 2018: Early-Holocene greening of the Afro-Asian dust belt changed sources of mineral dust in West Asia *Earth and Planetary Science Letters*, Volume 481, pp.30–40. DOI: https://doi.org/10.1016/j.epsl.2017.10.001

Summary

Production, transport and deposition of mineral dust have significant impacts on different components of the Earth systems through time and space. In modern times, dust plumes are associated with their source region(s) using satellite and land-based measurements and trajectory analysis of air masses through time. Reconstruction of past changes in the sources of mineral dust as related to changes in climate, however, must rely on the knowledge of the geochemical and mineralogical composition of modern and paleo-dust, and that of their potential source origins. In this contribution, we present a 13,000-year record of variations in radiogenic Sr-Nd-Hf isotopes and Rare Earth Element (REE) anomalies as well as dust grain size from an ombrotrophic (rain fed) peat core in NW Iran as proxies of past changes in the sources of dust over the interior of West Asia. Our data shows that although the grain size of dust varies in a narrow range through the entire record, the geochemical fingerprint of dust particles deposited during the low-flux, early Holocene period (11,700-6,000 yr BP) is distinctly different from aerosols deposited during high dust flux periods of the Younger Dryas and the mid-late Holocene (6,000-present). Our findings indicate that the composition of mineral dust deposited at the study site changed as a function of prevailing atmospheric circulation regimes and land exposure throughout the last deglacial period and the Holocene. Simulations of atmospheric circulation over the region show the Northern Hemisphere Summer Westerly Jet was displaced poleward across the study area during the early Holocene when Northern Hemisphere insolation was higher

due to the Earth's orbital configuration. This shift, coupled with lower dust emissions simulated based on greening of the Afro-Asian Dust Belt during the early Holocene likely led to potential sources in Central Asia dominating dust export to West Asia during this period. In contrast, the dominant western and southwest Asian and Eastern African sources have prevailed during the mid-Holocene to modern times.

1- Overview

West Asia (also referred to as the Middle East) is a climatically sensitive region that extends across the eastern Mediterranean Sea, Syria, Iraq, Iran and the Arabian Peninsula. Major Eurasian synoptic systems dominate over this region, including the Siberian anticyclone (SA), the Indian Ocean Summer Monsoon (IOSM) and the Northern Hemisphere Summer Westerly Jet (NHSWJ) (Fig. 4-1). The convergence of these systems over West Asia and their interaction with external forcing such as solar irradiance and insolation, internal climate oscillations and anthropogenic forcing mechanisms make this region highly susceptible to abrupt shifts in climate regimes (*e.g.,* Liu et al., 2015; McGee et al., 2014; Nagashima et al., 2011; Sharifi et al., 2015) .

Mineral dust is an actively changing component of the biogeochemical (Moore et al., 2002) and hydrological cycles (Arimoto, 2001) and significantly influences the global radiation budget (Choobari et al., 2014; Miller and Tegen, 1998; Tegen and Lacis, 1996). The vast, arid and semi-arid areas across West Asia are part of the Afro-Asian "dust belt" and a major contributor to global atmospheric dust emissions (Prospero et al., 2002), with the Arabian Peninsula, Iraq and Syria contributing up to 20% (Hamidi et al., 2013) in modern times. Large amounts of dust are delivered from these regions to the Persian Gulf,

the Red Sea and the northern Indian Ocean (Goudie and Middleton, 2006; Littmann, 1991; Middleton, 1986; Pourmand et al., 2004; Prospero et al., 2002; Sirocko et al., 2000).

Paleo-dust records in lacustrine/marine sediments and ice cores suggest a strong link between mineral dust and the climate state. These records also indicate systematic variations in dust emission and transport in the past, changes in the amount of dust, dust typology and shifts in the source areas (Shao et al., 2011). The controlling mechanisms on atmospheric circulation and dust emission during the Holocene and the effect of climate variability on introducing new dust source regions in West Asia are poorly investigated. In this chapter, by taking a novel approach of combining the results from paleo-dust grain size analysis with geochemical fingerprinting of modern and paleo-mineral dust using radiogenic Sr-Nd-Hf isotopes and Rare Earth Element (REE) anomalies measured in samples from Neor Lake peat complex an attempt was made to examine the influence of dominant atmospheric circulation regimes as a function of abrupt climate change on the availability of potential source areas to mineral dust transport and deposition across the interior of West Asia. Climate simulation experiments were also utilized to examine how variations in Holocene insolation influenced the dominant atmospheric circulation regimes over the region.

2- Materials and methods

Paleo-dust samples from high and low dust intervals were taken from a 7.5 m peat core based on XRF elemental profiles. Modern dust samples were collected at two meteorological stations (Fig. 4-1) from December 2011 to May. Radiogenic Sr-Nd-Hf isotope and REE analysis were conducted based on method by Pourmand et al., (2014)

using three-stage extraction chromatography scheme and multi-collector inductively coupled plasma mass spectrometer. A total of 23 samples were taken from high and low dust intervals along the core and the grain-size distribution was measured using a Beckman Coulter LS 13320 laser granulometer with a range of 0.04 to 2000 μm. Three-day air mass back-trajectory simulated using HYSPLIT model (Stein et al., 2016). Additionally, the impact of insolation changes from early to late-Holocene on climate was examined in a transient fully coupled climate model simulation of the last 21 ka (TraCE) using the National Center for Atmospheric Research (NCAR) Community Climate System Model version 3 (CCSM3). TraCE was forced with time-varying changes in orbital parameters, greenhouse gases, ice-sheet orography and extent, solar forcing, freshwater forcing, and interactive vegetation dynamics. To examine the role of the greening of North Africa on dust emissions, three time slice experiments using CCSM version 4 coupled to a slab ocean model (SOM) and interactive dust aerosol model were performed. The SOM experiments were initialized from their equilibrated 6ka and Preindustrial (1850 A.D, PI) fully coupled climate model simulations that were performed for the Paleoclimate Modeling Intercomparison Project phase 3 (PMIP3) and Coupled Modeling Intercomparison Project phase 5 (CMIP5), respectively, and integrated for 50 years. Two model simulations of the mid-Holocene- 6ka and 6ka+greening- were performed using the same continental configuration, ice sheets, and topography as the PI experiment, however, greenhouse gases and orbital forcing follow the PMIP3 protocol, and dust source regions differ. The 6ka experiment uses the same vegetation cover as the PI experiment. To take into account the "greening" of North Africa in the early Holocene an additional simulation (6ka+greening) was performed, where the same 6ka orbital forcing was used, but the PI vegetation cover

was modified to include the early Holocene North African lake and wetland distribution. The dust sources were removed by setting the soil erodibility to zero where the vegetation was modified. Additional details of the analytical methodology are provided in chapter 2.

3- Results and discussion

3.1- Geochemical fingerprinting of paleo-dust from West Asia

A multi-proxy, high-resolution (decadal-centennial) reconstruction of changes in aeolian input and paleoenvironmental conditions at this lake (Fig. 4-2 A and C) has shown that dust fluxes were elevated prior to the onset of the Holocene, dropped significantly and abruptly during the early Holocene (EH, 11,700-6,000 yr BP) but increased again during mid-late Holocene (M-LH, 6,000-present). In a recent study, (Kylander et al., 2016) demonstrated that calculation of the net dust deposition in peat can vary based on the choice of a particular element. While this can potentially influence the absolute flux calculations, the relative changes in dust deposition measured from the input of a specific element (Ti) remains unaffected throughout the record (Sharifi et al., 2015).

As discussed in chapter3, variations in hydrogen isotopic composition (δD) of C_{28} *n*-alkanoic acid (Fig. 4-2E), total organic content (TOC), bulk stable isotope composition of organic carbon ($\delta^{13}C_{TOC}$), *n*-alkane enrichment ratios (P_{aq}), indicate that the early Holocene (EH) was wet in West Asia, consistent with records from Iran (Mehterian et al., 2017), Africa (Berke et al., 2012; Costa et al., 2014; Tierney et al., 2008) and the eastern Mediterranean (Rossignol-Strick, 1999, 1995) region. In contrast, the M-LH was drier and punctuated by at least eight abrupt episodes of elevated dust fluxes, several of which impacted early human civilizations from the Mesopotamia (Sharifi et al., 2015) and

coincide with the ending of the African Humid Period (deMenocal et al., 2000; Gasse, 2000).

In addition to changes in dust fluxes, the elemental composition of paleo-dust from Neor peat suggested that the sources of dust likely changed throughout the record (Sharifi et al., 2015). The mean grain size values of dust measured on the lithogenic fraction of 23 samples (an average resolution of ~600 years per sample), ranged from 3.3 to 7.4 μm throughout the record (Fig. 4-2D). The smallest and largest particle sizes measured in all samples ranged from < 0.1 μm to 11.4 μm (Table SI-3 in appendix E). It is notable that, on average, 86.7 volume % of particles measured in all samples fall below 10 μm with only 13.3 volume % exceeding this threshold (Table SI-3, Fig. 4-11A). The origin of this bimodal distribution (Fig. 4-11B) remains unresolved and we speculate that it may be attributed to contribution from proximal sources, considering the pattern persists throughout the record. These measurements suggest that in spite of significant centennial-millennial scale changes in dust fluxes since the last deglaciation, most part of the dust deposited at Neor Lake was most likely transported from long range sources (Fig. 4-2d).

To further investigate this, 41 dust samples in this record with an average resolution of ~320 years per sample were analyzed for radiogenic Sr ($^{87}Sr/^{86}Sr$), Nd ($^{143}Nd/^{144}Nd$), and Hf ($^{176}Hf/^{177}Hf$) isotopic composition and REE anomalies (La_N/Lu_N, normalized to Post Archaean Australian Shale (Pourmand et al., 2012). These isotope systematics paired with the REE relative abundances and anomalies have proven among the most distinctive geochemical proxies for the source provenance of sediments in modern and ancient deposits (Abouchami et al., 2013; Grousset et al., 1988a; Muhs et al., 2014; Pourmand et al., 2014; Scheuvens et al., 2013).

As shown in Fig. 4-2 F-G and Table SI-3 in appendix E, the onset of the Holocene is marked by a large shift to distinctly less radiogenic εNd and εHf values (isotope ratios reported in ε notation relative to the Chondritic Uniform Reservoir, CHUR (Bouvier et al., 2008). It is notable that this abrupt shift which took place within ~300 years in the geochemical composition of mineral dust was coincident with a large reduction in dust fluxes (Fig. 4-2 C). The $^{87}Sr/^{86}Sr$ isotope ratios become more radiogenic during the same transition from the YD to EH (Fig. 4-2 I). In general, the Sr and Hf isotope ratios show more variability over the entire record and this is likely due to heterogeneity within the source materials and the sensitivity of Rb-Sr and Lu-Hf systematics to changes in grain size (Feng et al., 2009). The Sm-Nd model ages (Fig. 4-2 H), which are based on idealized crustal residence ages of potential source rocks (Goldstein et al., 1984; Grousset et al., 1988a), also suggest that contributions from relatively younger sources of aerosols dominated during the EH compared with the YD and M-LH. By 6,000 years BP, all isotope systematics gradually return to values more akin to pre-Holocene. This transition coincided with a gradual decrease in solar insolation over the northern hemisphere (Fig. 4-2 B).

In order to examine whether the mineral dust in the Neor peat record may have come from local andesitic sources, the geochemical signature of several pieces of gravels recovered from the bedrock at the base of the core and a sample from the Sabalan volcanic complex to the west of the study area was analyzed (Fig. 4-1). The average isotopic composition of mineral dust from Neor during the last deglacial and Mid-late Holocene is close to, albeit distinct from the values measured in the andesitic bedrock and Sahand volcanic complex (Fig. 4-3 and 4-4). Early Holocene Sr-Nd-Hf values, in contrast, are distinctly different in a regime of reduced dust fluxes, indicating the possibility that early

Holocene mineral dust originated from sources with geochemical signatures different from local sources.

It can be argued that the geochemical transitions observed in Fig. 4-2 between the EH and M-late Holocene occurred due to higher soil coverage over the volcanic complex (*i.e.,* proximal sources) during the early Holocene that led to lower dust fluxes and less contribution from these sources. Indeed, the Sr-Nd-Hf isotopes measured in modern dust samples from West Asian sources (Fig. 4-3 and 4-4) are closer to values observed during the early Holocene period than the rest of the record, indicating that sources in West Asia may have contributed to deposition of mineral dust to this site during this time. This argument, however, is compounded by the observation that the geochemical composition of mineral dust at Neor has remained relatively constant from mid Holocene to modern times, even though the export of West Asian sources of mineral dust to the interior of the Middle East presumably emerged as the region got drier and dustier (Sharifi et al., 2015). Modern satellite observations show our study area receives significant amounts of dust from these western and southwestern sources (Goudie and Middleton, 2006; Prospero et al., 2002), indicating that long-range dust transport from West Asian potential sources must have played an important role throughout mid-late Holocene. The observation that mean particle size of mineral dust measured in Neor peat samples (Fig. 4-2d, Table SI-3 and Fig. 4-11) remained below 8 μm throughout the record, irrespective of dust flux and changing geochemical composition, lends strong support to the long range nature of eolian deposition at this location.

3.2-Dominant regimes of dust emission and transport

The circulation regime over the study area during NH summers is dominated by a gradient established between a high-pressure system over the Arabian Peninsula and the Iranian Plateau and a low pressure system over higher latitudes of Eurasia. This gradient drives low-level, north-northwesterly winds along the Persian Gulf and over the Arabian Peninsula towards the northern Indian Ocean. During the summer months, the upper level NHSWJ that extends across the entire continent is at its northernmost position (Schiemann et al., 2009). In contrast, the jet is displaced to lower latitudes with sustained westerly directions (Fig. 4-1) and penetrates eastward from the North Atlantic and across the Mediterranean during winter months. Today, dust storm activities are elevated during spring and summer months across West Asia (Goudie and Middleton, 2006; Kutiel and Furman, 2003; Prospero et al., 2002). Although the origin of most dust storms in the region is from within West Asia, occasional winter and spring outbreaks from NE Africa have also been observed (Goudie and Middleton, 2006; Littmann, 1991) (Fig. 4-5 and 4-6). Total Ozone Mapping Spectrometry (TOMS) of atmospheric dust content and Moderate Resolution Imaging Spectroradiometer Deep Blue Level 2 of dust optical depth (M-DB2 DOD) shows areas between the Tigris-Euphrates basin and the Arabian Peninsula as the main sources of modern dust to the interior of West Asia (Ginoux et al., 2012; Prospero et al., 2002).

While it is clear that a change in the geochemical composition of paleo-dust occurred throughout the YD and the Holocene at our study area, linking the aerosols to specific sources is challenging. A comparison between the Sr-Nd-Hf isotope composition of paleo-dust from Neor and the available data from sources in N. Africa and deserts in Mongolia

and China (Abouchami et al., 2013; Chen et al., 2007; Chen and Li, 2013; Scheuvens et al., 2013) render these areas as unlikely sources (Fig. 4-4). Some overlap is observed between Sr-Nd isotopic composition of the EH samples and sources in Egypt and Sudan. Nevertheless, the geochemical compositions of potential sources in N. Africa are far from being fully constrained (Scheuvens et al., 2013).

A marginal overlap is observed between some of the εNd-εHf values from Neor and those of clay-sized particles (<2.0 μm) from the Central Asian Orogeny Belt in China (Zhao et al., 2014) (Fig. 4-3). However, approximately 3,700 km longitudinal distance and the general trend of the NHSWJ make significant contributions from these distant eastern sources to West Asia unlikely. Nevertheless, the potential for circumpolar, long-range transport of clay-size particles from the Chinese and Mongolian deserts during the early Holocene when dust fluxes were low cannot be ruled out, considering evidence for transport of these particles has been found in the Greenland ice records (Biscaye et al., 1997).

Aerosol and soil samples collected over SW Iran and soil samples from the Abu Zirig wetland in Iraq analyzed in this study plot close to $^{87}Sr/^{86}Sr$-εNd values of the EH samples (Fig. 4-1 and 4-4). A dust sample from Sar Pol Zahab, located 470 Km southwest of Neor (Fig 4-1 and 4-6), also falls within the cluster of samples from the EH with respect to εNd-εHf composition (Fig. 4-3). In contrast, the fractionation of light/heavy REE (La_N/Lu_N) as a function of Sm-Nd model ages (Fig. 4-7) set modern samples distinctly apart from the paleo-dust. The paucity of information on the geochemical and mineralogical composition of potential sources of mineral dust in West Asia make it difficult to establish a definitive linkage between sources and receptor sites.

3.3- Simulations of atmospheric circulation and dust emission and deposition

To help interpret the observed changes in the geochemical composition of paleo-dust from Neor peat, changes in atmospheric circulation and dust emission rates were analyzed in a transient climate model simulation that covers the last 21,000 years (TraCE) and in three time slice simulations of the EH (6ka+greening), MH (6ka), and Late Holocene (PI) (Table 2-4). Orbital-driven changes in insolation can drive shifts in the NHSWJ and thereby impact atmospheric circulation and large-scale precipitation patterns over the eastern Mediterranean region (Brayshaw et al., 2010) , Tibetan Plateau (Schiemann et al., 2009) and East Asia (Chiang et al., 2015; Nagashima et al., 2011). The position of NHSWJ in the TraCE simulation moved equatorward throughout the Holocene, and followed the NH June insolation curve (Fig. 4-2 b and j). Analysis of the maximum in zonal wind at 250-hPa averaged over June-July-August (JJA) indicates a clear poleward (equatorward) shift in the NHSWJ when boreal summer insolation was high (low). Additionally, the YD cold period shows a significant equatorward shift in the JJA NHSWJ, whereas the Bølling-Allerød warm interval indicates a poleward shift in the jet (Fig. 4-2 j). These results highlight the importance of orbital forcing and the Northern Hemisphere temperature on the NH mid-latitude circulation.

The location and high elevation of Neor Lake makes it ideal to record the migration in the NHSWJ from a northernmost position of ~39°N in the EH to a southernmost position of ~37°N in the LH. Previous studies have shown how the migration of the main axis of the NHSWJ from higher latitudes during the summer to lower latitudes in winter modulates air mass circulation and precipitation patterns over West Asia and the Tibetan Plateau (Nagashima et al., 2011; Schiemann et al., 2009). Three-day HYSPLIT back-trajectory

ensembles for selected days (Schiemann et al., 2009) during winter (M-LH analog) and summer (EH analog) over Neor Lake indicate a distinct shift in the direction of air masses due to changes in the position and intensity of the NHSWJ (Fig. 4-8). The shift from N-NW sources in the summer to western sources of air masses during winter months is also supported by records of wind direction (29-year monthly average, 1976-2005) from the nearest meteorological station located 50 km NE of our study area (Fig. 4-8). Together, these results suggest that contributions from the Mesopotamian source regions in Iraq, Syria and the Arabian Peninsula to atmospheric dust deposition over the Neor Lake are higher during the winter, whereas contributions from Central Asian sources such as Qobustan in Azarbaidjan, Atrek delta of Turkmenistan, Turan plain of Uzbekistan, and the region around the Aral Sea (Fig.4-1) become more pronounced during the summer.

This observation is further supported in our equilibrium climate model simulations. The differences in dust emissions between our 6ka and PI simulations are attributed both to differences in climate (due to orbital changes and greenhouse gas forcing), as well as differences in dust source regions (i.e., soil erodibility). Since all boundary conditions are the same in our 6ka and 6ka+greening experiments, except for the land surface characteristics of North Africa and the Arabian Peninsula, changes in dust emissions are due solely to changes in climate driven by the greening.. There is a large reduction in the annual mean atmospheric dust loading over North Africa at 6ka compared to the PI and in the 6ka+greening experiment compared to the 6ka (Fig 4-9). Consistent with the proxy data from Neor Lake, which shows a reduction in dust fluxes at Neor Lake in the early to mid-Holocene compared to the late Holocene, we also find a decrease in annual mean dust deposition in our 6ka+greening and 6ka experiments (37 and 33 g m^{-2} yr^{-1}, respectively)

compared to the PI (40 g m^{-2} yr^{-1}). Compared to the 6ka simulation, the greening of North Africa and the Arabian Peninsula in the early Holocene (6ka+greening) results in a slight increase in the simulated annual mean dust deposition at the study site, that is driven largely by enhanced dust emissions from West and Central Asia in boreal winter (gray box in Fig. 10A). In boreal winter, the greening of North Africa causes a decrease in precipitation minus evaporation over central and Iran (Fig. 4-10B). This enhances aridity and results in more dust mobilization compared to 6ka conditions. The anomalous easterly low level winds in the 6ka+greening experiment exports dust westward towards Neor Lake (Fig. 4-10A). In boreal summer, the greening of North Africa results in wetter conditions (positive precipitation minus evaporation, Fig. 4-10 D) over central Asia and Iran but dust emissions averaged over this region are similar in both the 6ka+greening and 6ka simulations. We hypothesize that the greening of North Africa resulted in greater drying over Central Asia in boreal winter and resulted in these regions dominating dust export to Neor Lake during the African Humid Period. This is consistent with our new proxy records that show the dust deposited during the African Humid Period had a significantly different isotopic and geochemical signature than the dust deposited in the LH (Fig. 4-2 F and E, Fig. 4-3 and 4-4).

4- Conclusions and implications

Geochemical fingerprinting of paleo-dust from Neor Lake peat core with radiogenic Sr-Nd-Hf isotopes and REE anomalies reveal sources of dust were different between the dry Younger Dryas, when dust fluxes were high, and the wet period of the early Holocene when dust fluxes were substantially lower. A poleward shift in the westerly jet axis together with less dust emission from North African sources covered by vegetation hampered the

long-range transport of African dust to western Asia during the early Holocene. At this time, transport from Mesopotamian and Central Asian sources of mineral dust may have dominated atmospheric deposition over NW Iran, albeit contributing at lower fluxes than the late Holocene. The composition of paleo-dust gradually became more similar to the Younger Dryas during the middle-late Holocene. Migration of the main axis of the NHSWJ towards the equator during the drier middle-late Holocene allowed the jets to transport higher fluxes of dust from potential source regions in West Asia as well as the NE African sources. With increased temperatures resulting from global warming, it is expected that the Middle East will become more arid in the next few decades to centuries (IPCC, 2014). This will likely expose new sources of mineral dust available for export from these regions to the interior of West Asia.

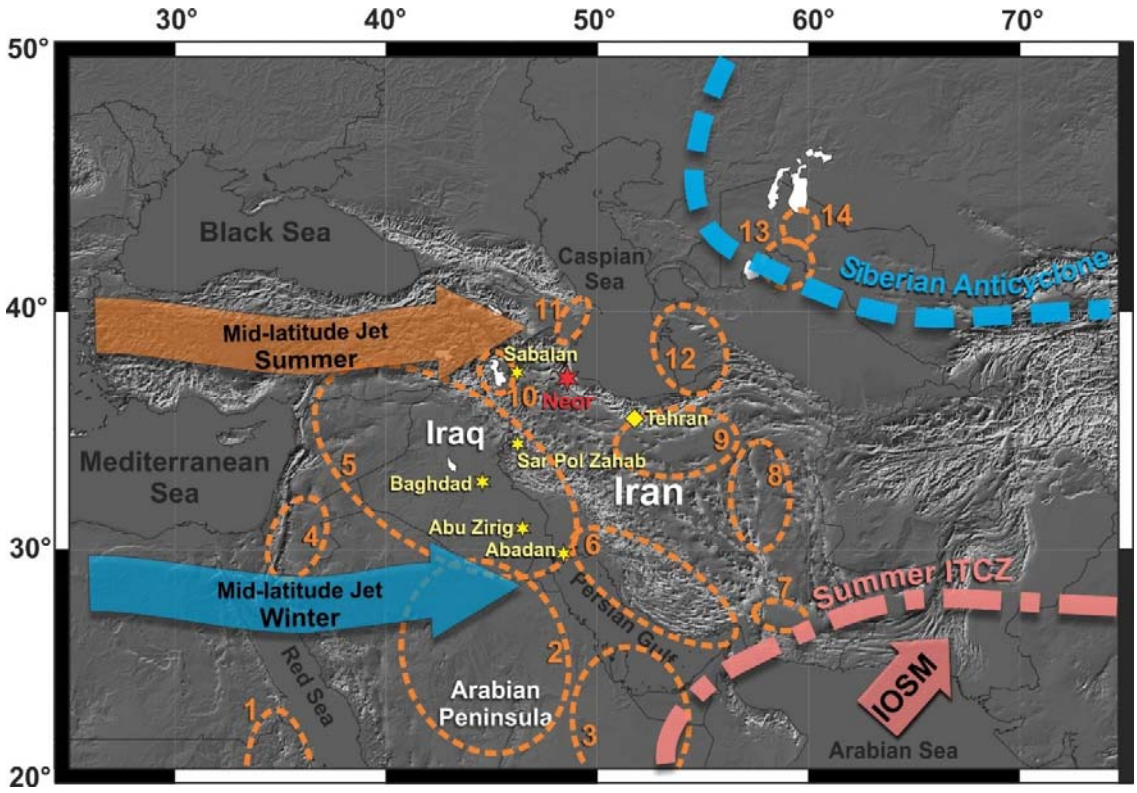

Fig. 4-1- Schematic position of major synoptic systems and dust sources over West Asia. Stars denote the location of Neor peat mire (red) and dust collection sites (yellow). Orange and blue arrows denote the location of the Northern Hemisphere Summer Westerly Jet (NHSWJ) in summer and winter respectively (Schiemann et al., 2009)**. The approximate current location of the Intertropical Convergence Zone (ITCZ) is also shown** (Aguado and Burt, 2012)**. IOSM refers to Indian Ocean Summer Monsoon. Dashed circles in orange denote the major dust sources in the region** (Ginoux et al., 2012) **and are numbered as follow: 1, northeast Sudan; 2, highlands of Saudi Arabia; 3, Empty Quarter (Rob Al Khali); 4, Jordan River Basin of Jordan; 5, Mesopotamia;; 6, coastal desert of Iran; 7, Hamun-i-Mashkel; 8, Dasht-e Lut Desert of Iran; 9, Dasht-e Kavir Desert of Iran; 10, Lake Urmia of Iran; 11, Qobustan in Azarbaidjan; 12, Atrek delta of Turkmenistan; 13, Turan plain of Uzbekistan, and 14, Aral Sea.**

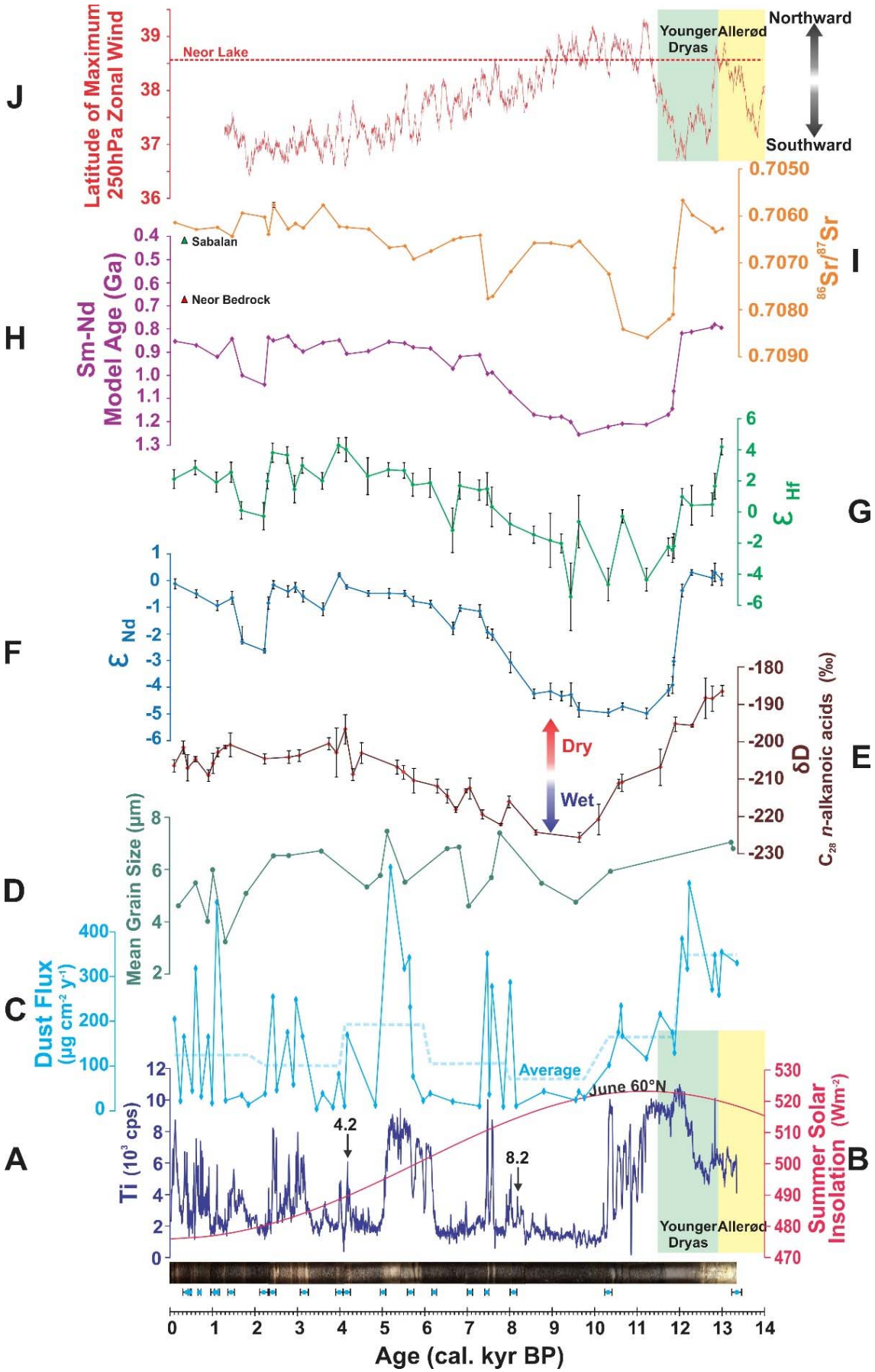
J
Latitude of Maximum 250hPa Zonal Wind
Neor Lake
Younger Dryas
Allerød
Northward
Southward
H
Sm-Nd Model Age (Ga)
Sabalan
Neor Bedrock
I
$^{86}Sr/^{87}Sr$
G
ε_{Hf}
F
ε_{Nd}
Dry
Wet
E
δD
C_{28} n-alkanoic acids (‰)
D
Mean Grain Size (μm)
C
Dust Flux (μg cm^{-2} y^{-1})
Average
A
Ti (10^3 cps)
4.2
8.2
June 60°N
B
Summer Solar Insolation (Wm^{-2})
Younger Dryas
Allerød
Age (cal. kyr BP)

Fig. 4-2- Multi proxy record from Neor peat core. A) Core image (750-cm), 19 radiocarbon dates (cal. kyr BP) and Ti ($\times 10^3$ cps) XRF intensity profile, arrows refer to 4.2 and 8.2 events; B) Summer solar insolation (Wm^{-2}) at 60°N; C) Dust flux based on Ti concentration ($\times 10$ μg cm^{-3} y^{-1}) (solid line) and 2,000 year-averaged flux (dashed line); D) Mean grain size (μm) of major dust intervals; E) Compound-specific leaf wax δD (‰); F,G) downcore variation of Nd and Hf isotopic ratios expressed as εNd and εHf; H) Sm-Nd model age (Ga) for dust intervals, values for Neor bedrock and Sabalan volcano (NW Iran) as the regional volcanic end-members are shown in red and green triangles respectively. I) Downcore variation of $^{87}Sr/^{86}Sr$; J) A Hovmöller plot of the mean June-July-August (JJA) zonal wind maximum at 250 h-Pa (U250_max) averaged longitudinally between 30-60°E in the Trace experiment. The time series of U250_max is smoothed by applying a 121-point running temporal average, the dashed line indicates the latitude of the study site. (A-D adopted from Sharifi et al., 2015).

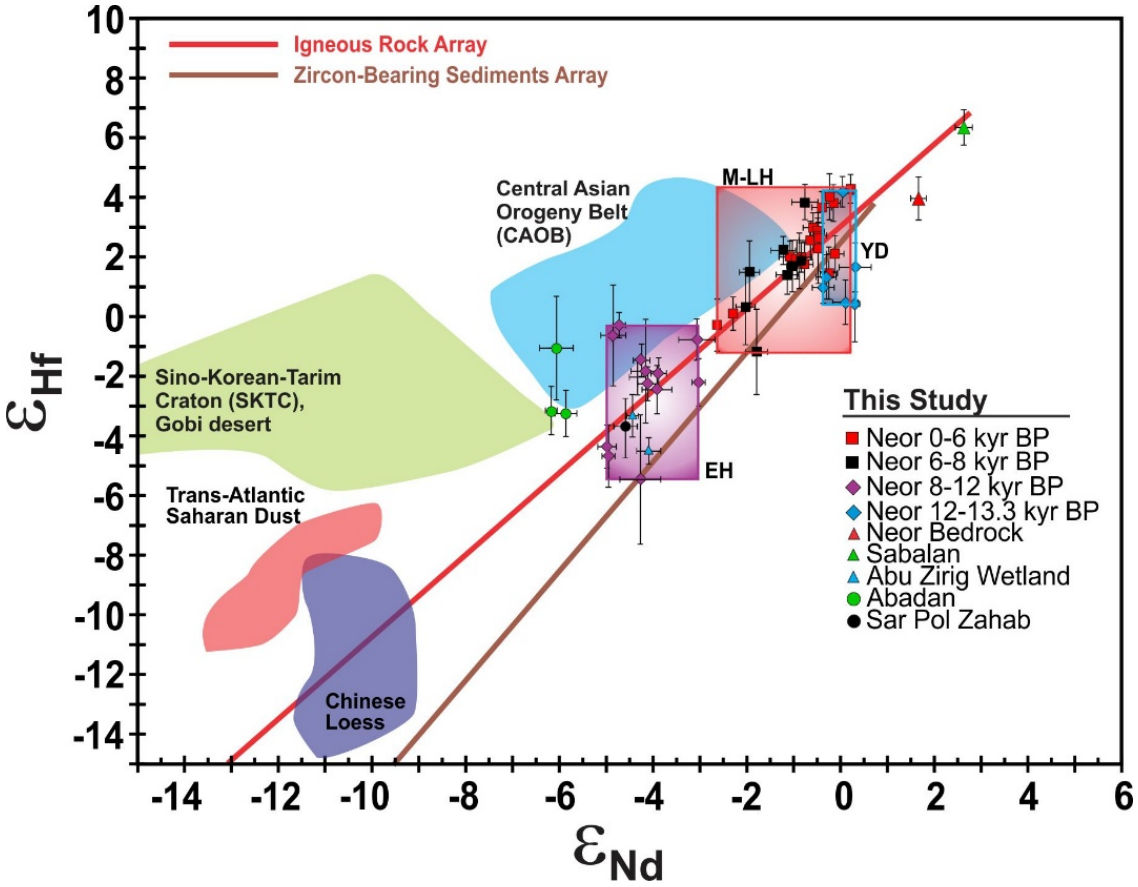

Fig. 4-3- Radiogenic Hf and Nd isotopes in aerosols from Neor compared to African and Asian source regions. Colored boxes represent clusters of Neor paleo-dust samples for the Younger Dryas (YD), early Holocene (EH) and mid-late Holocene (M-LH). Colored lines denote sediment and igneous arrays (Bayon et al., 2009). Areas in red, purple, blue and green represent data for Trans-Atlantic Saharan Dust (Pourmand et al., 2014), Chinese Loess (Chen and Li, 2013), Central Asian Orogeny Belt (SAOB) and Sino-Korean-Tarim Craton (SKTC)/Gobi Desert source regions (Zhao et al., 2014), respectively. Uncertainties from this study are 95% confidence interval. The sample from the Sabalan volcano is courtesy of Dr. Jamshid Hassanzadeh, California Institute of Technology. Samples from Abu Zirig Wetland in Iraq are courtesy of Dr. Ahmed I. Rushdi, King Saud University.

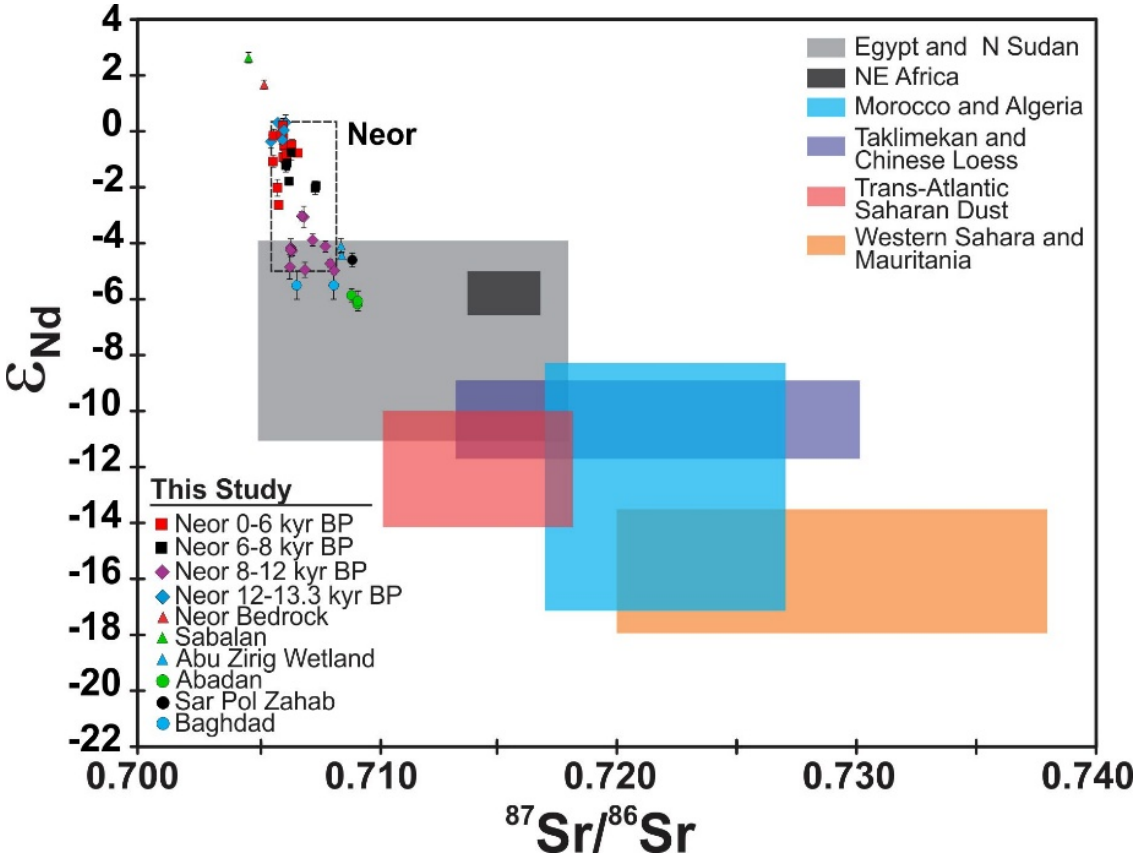

Fig. 4-4- Radiogenic Sr and Nd isotopes in aerosols from Neor compared to the world's source regions. Colored boxes represent ranges of values measured in surficial samples of North Africa and East Asia (Abouchami et al., 2013; Chen et al., 2007; Chen and Li, 2013; Scheuvens et al., 2013). Dashed box denotes the Neor paleo-dust samples. Uncertainties from this study are 95% confidence interval. Sample from Sabalan volcano is courtesy of Dr. Jamshid Hassanzadeh, California Institute of Technology. Samples from Abu Zirig Wetland in Iraq are courtesy of Dr. Ahmed I. Rushdi, King Saud University.

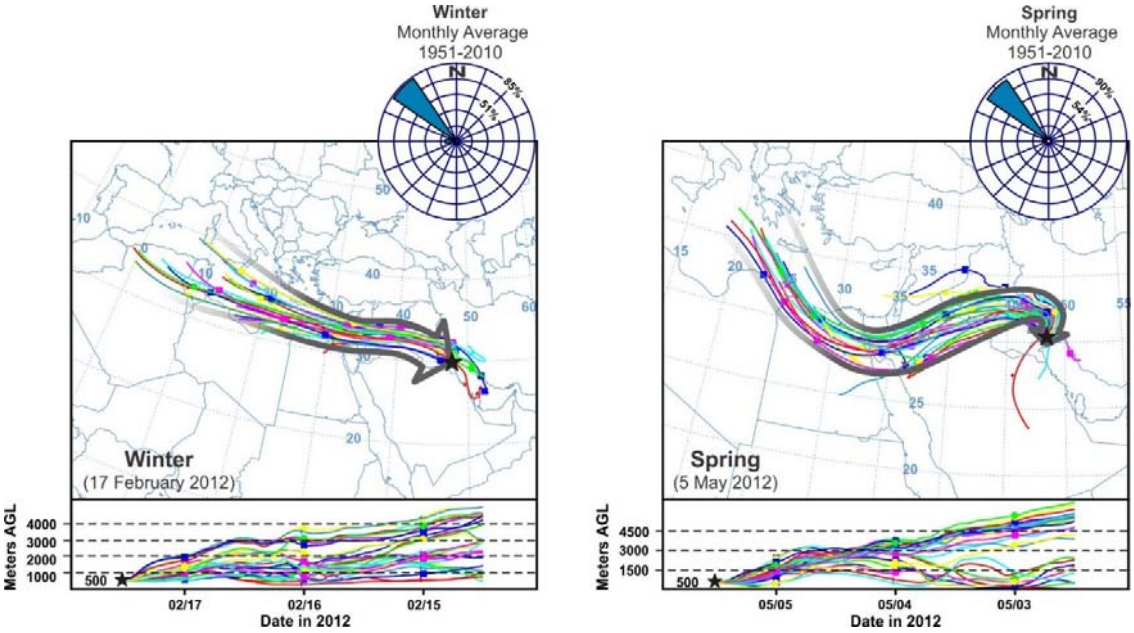

Fig. 4-5- Back-trajectory and general seasonal wind direction over SW Iran. Three-day air mass back-trajectory ensemble plots for the sampling days at Abadan (black star) during winter and spring at different altitudes (1000-4500 meter above ground level). The back-trajectories indicate transport of air parcels from North Africa, NE of Arabian Peninsula, Syria and Iraq to SW Iran. The 59-years (1951-2010) monthly average wind direction (http://www.irimo.ir) for the winter and spring, recorded at Abadan meteorological station, indicates the northwesterly dominant wind regime.

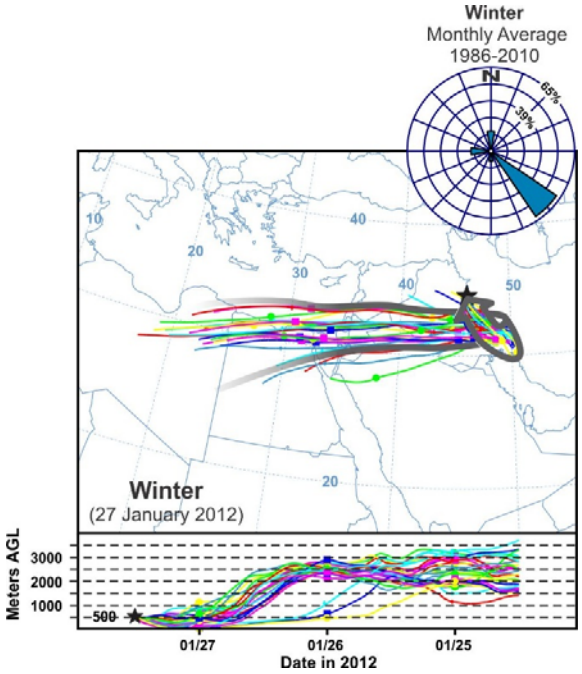

Fig. 4-6- Back-trajectory and general seasonal wind direction over W Iran. Three-day air mass back-trajectory ensemble plots for the sampling days at Sar Pol Zahab (black star) during winter at different altitudes (500-4500 meter above ground level). Based on this back-trajectory, air parcel passes over Jordan, NE of Arabian Peninsula and Iraq through a westerly wind and reaches to Sar Pol Zahab in W Iran via a southwesterly wind. Furthermore, the 24-years (1986-2010) monthly average wind direction (http://www.irimo.ir) for the winter, recorded at Sar Pol Zahab meteorological station, is in good agreement with the model output and indicates that the southeasterly winds are dominant during the winter season.

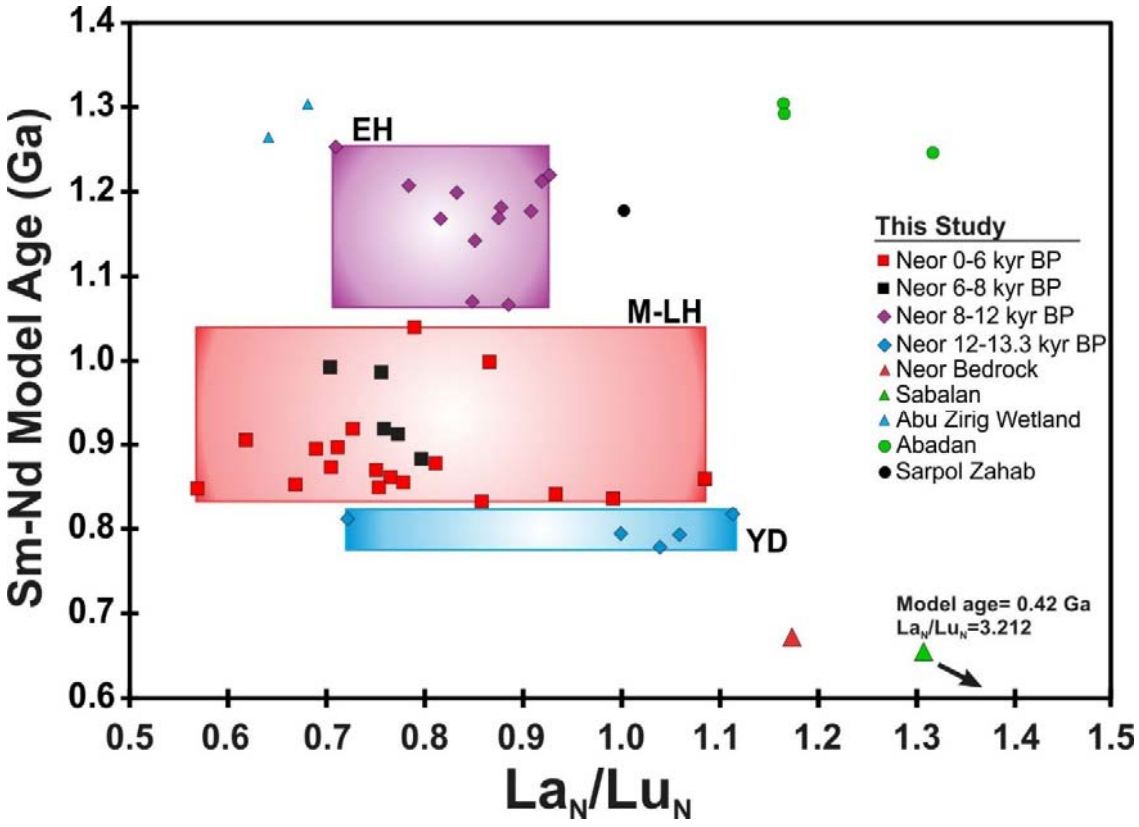

Fig. 4-7- Difference in Sm-Nd model ages compared to normalized La_N/Lu_N ratios. Colored boxes represent clusters of Neor paleo-dust samples for the Younger Dryas (YD), the early Holocene (EH) and the mid-late Holocene (M-LH). Sample from Sabalan volcano is courtesy of Dr. Jamshid Hassanzadeh, California Institute of Technology. Samples from Abu Zirig Wetland in Iraq are courtesy of Dr. Ahmed I. Rushdi, King Saud University.

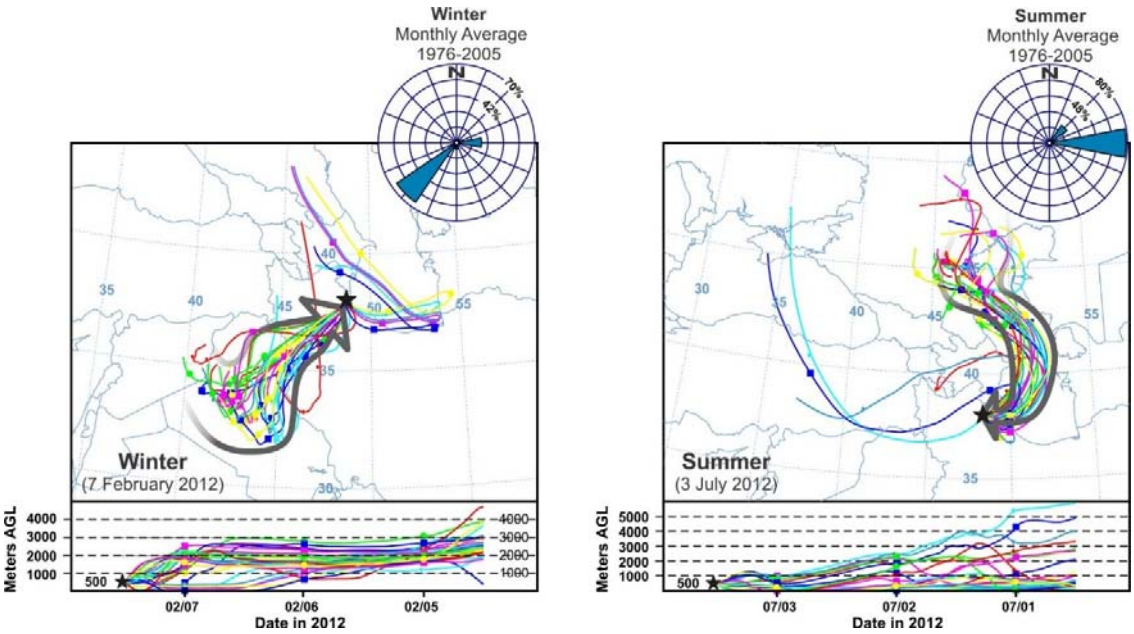

Fig. 4-8- Back-trajectory and general seasonal wind direction over Neor Lake,NW Iran. Three-day air mass back-trajectory ensemble plots for representative (Schiemann et al., 2009) days in winter (left) and summer (right) at Neor Lake (black star). Shift in back-trajectory results from summer to winter follows the 29-years (1975-2005) monthly average prevailed wind direction recorded at Ardabil meteorological station (located 50 km NE of the Neor Lake), see text for discussion.

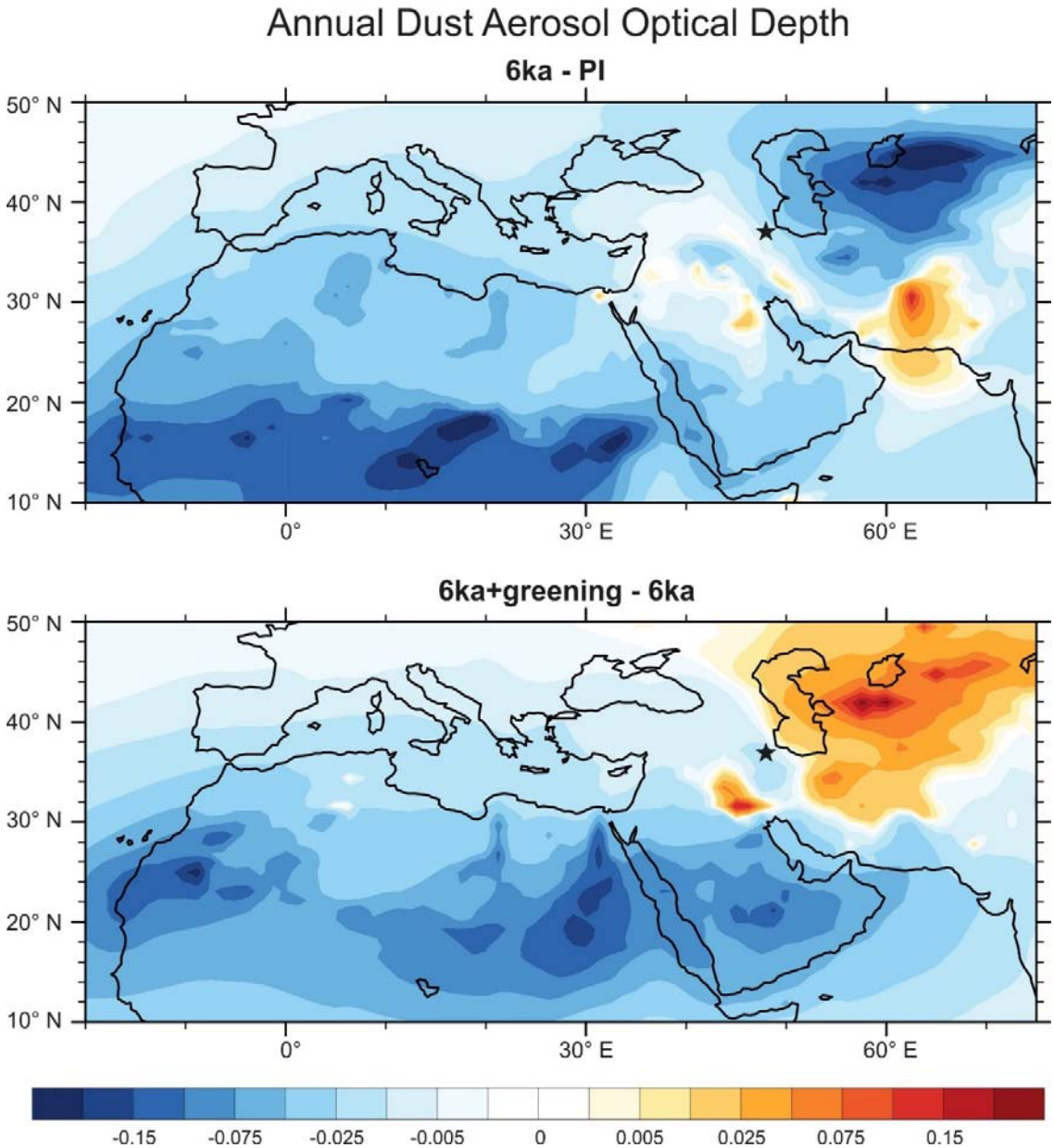

Fig. 4-9- Annual mean dust aerosol optical depth anomalies. The change in annual mean dust aerosol optical depth in our 6ka simulation compared to our PI simulation (top) and our 6ka+greening simulation compared to the 6ka simulation (bottom). Our simulations show a reduction in the annual mean atmospheric dust loading over North Africa and the Arabian Peninsula and at the Neor location. Black star denotes the location of the study site.

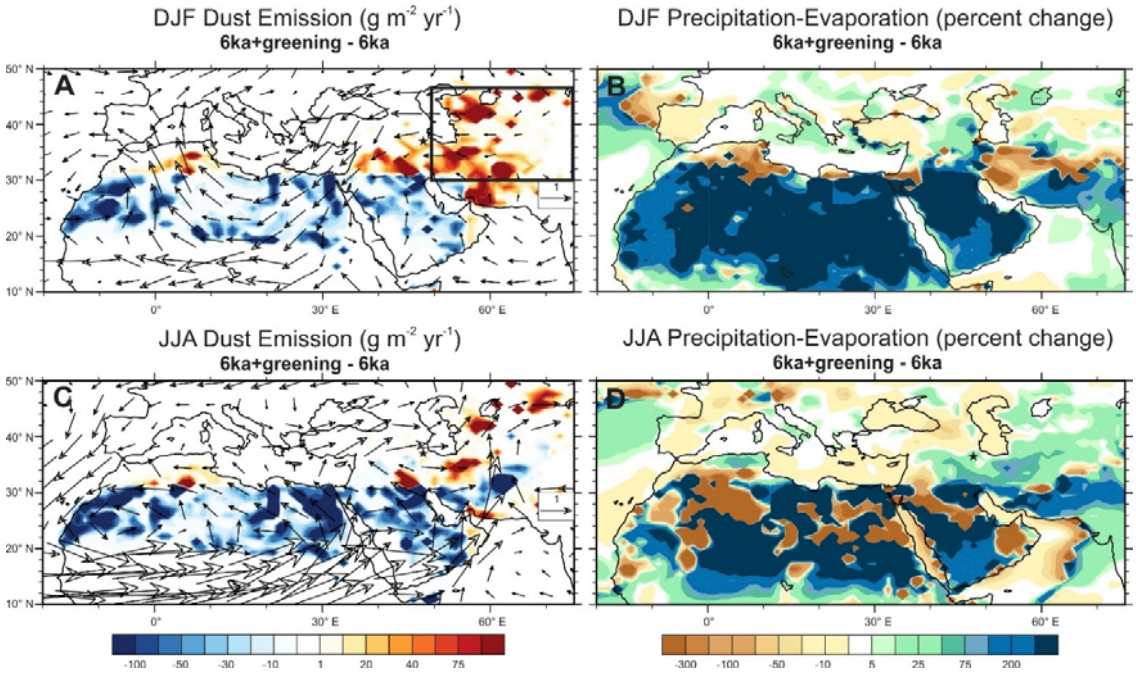

Fig. 4-10- Boreal winter (DJF) and summer (JJA) dust emission anomalies and 800-hPa wind vector anomalies and precipitation minus evaporation. Boreal winter (A.) and summer (C.) dust emission anomalies (6ka+greening – 6ka) in g m^{-2} yr^{-1}. Wind vector anomalies at 800 hPa are overlaid with a reference vector length of 1 m s^{-1}. Black Star denotes the location of the study site. Boreal winter (B.) and summer (D.) precipitation minus evaporation anomalies (given as a percent change). The dark gray box in panel A shows the location of the West Asian box used to calculate the seasonal and annual mean dust emission anomalies.

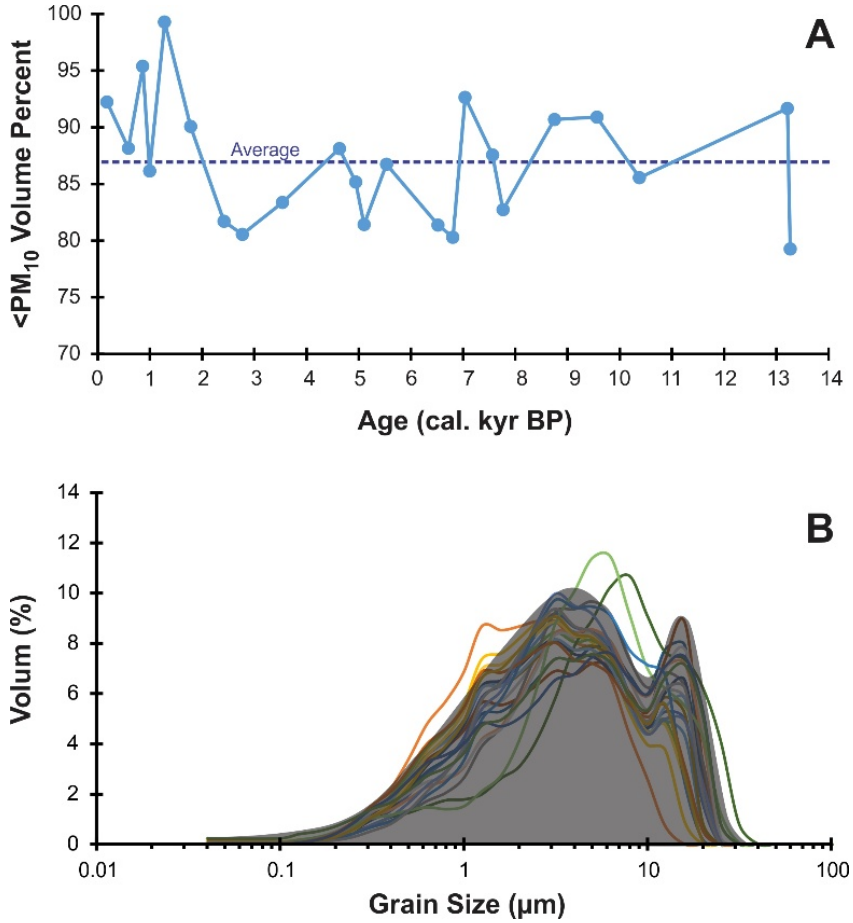

Fig. 4-11- Grain size distribution of high and low dust intervals from Neor Lake. a) Volume percent of lithogenic particles below 10 µm (<PM_{10}), dashed line denotes the average value (86.7 %) measured in all samples; b). Bimodal distribution of lithogenic fraction centered at 4 and 16 µm.

Geochemical perspective of Salt Lake Urmia in Northwest Iran and the human impact on its natural environment

Summary

Urmia Lake is the second largest hypersaline lake in the world and the largest terminal lake in west Asia. It formed in a tectonic depression in northwest Iran with the average catchment area of 52000 km^2 and 13 perennial and seasonal tributaries. The salinity of the lake varies from 140 to more than 220 g L^{-1} and is regulated by the imbalance between water inflow and evaporation. Over the last three decades the lake's water supply has diminished significantly leading to more than 90% reduction in the lake's surface area that has driven the salinity to 380 g L^{-1}. With the paucity of geochemical data from Urmia Lake's sediments and water and lack of a robust decadal to millennial scale archive of climate variability, it is difficult to assess whether the disappearance of this lake is primarily caused by Anthropogenic or natural processes. In this chapter, the geochemical background of water and sediment for the Urmia Lake is provided and role of regional geology in evolution of water and sediment composition is investigated. Grain size analysis of the siliciclastic fractions from core top samples reveal that the majority of the Urmia Lake bottom sediments consist of silt and clay-silt particles. This grain size distribution is changed to sand and silty sand in the NW part of the lake where felsic intrusives and metamorphic rocks are present at the vicinity of the lake. This distribution pattern is mimicked by the variation of lithogenic conservative elements such as Ti and Zr and chemical index of alteration (CIA) potentially due to their associations with weathering resistance heavy minerals. Distribution pattern of conservative elements (*e.g.*, Ti, Si, Al, Ca) as well as redox-sensitive and mobile elements (*e.g.*, Fe, K, Rb, Sr) in the clastic fraction of the lake's sediment indicate the role of regional geology on defining the chemical signature of the Urmia Lake sediment. Concentrations of total organic matter show high

correlation with distribution pattern of clay in the sediment, which may reveals stabilization of organic matter related to the total surface area of the fine grained particles. Prior to significant loss of water, the Urmia Lake brine was initially classified as Na+K-Cl-Mg-SO_4, however the ionic signature of the Urmia brine has changed to Na+K-SO_4-Mg-Cl in 2010 followed by a factor of 2 increase in TDS content.

1- Overview

Closed-basin brine lakes have been the subject of numerous paleoclimate studies due to their sensitivity to regional and global climate variabilities as well as to anthropogenic changes (Cohen et al., 2000; Djamali et al., 2008; Morteza Djamali et al., 2010; Fritz, 1996; Kowalewska and Cohen, 1998; Mischke et al., 2005; Oren, 2009). In these types of lakes, the balance between water input through precipitation in the catchment basin and output as evaporation and occasional run off affects lake level and its chemistry. The ionic composition of brine lakes is primarily controlled by the geologic setting in the catchment basin and basin hydrology driven by precipitation and surface runoff and lake evaporation. Changes in mineralogical and ionic concentrations in these environments that are dominated by water balance in the lake vary in a predictable fashion (Eugster and Jones, 1979). More specifically, the elemental variations in water and sediments of saline lakes have been widely used to study the evolution of brines, hydrology of the watershed area, and impact of anthropogenic activities on the natural environments (Bąbel and Schreiber, 2013; Jirsa et al., 2013; Jones et al., 2009; Shvartsev et al., 2014).

Depending on the hydrological regime and climate setting, salinity of closed-basin lakes range from 2.5 up to more than 300 g L^{-1} (Langbein, 1961). Lakes with salinities

above 35-45 g L^{-1} are generally inhospitable to most life forms due to the osmoregulatory stress. However, once a species finds a solution for this physiological problem, it will be able to tolerate a wide range of changes in salinity (Williams et al., 1990). In higher salinity ranges (> 200 g L^{-1}), the number of thriving species abruptly decline and lake dwellers become more susceptible to salinity fluctuations (Golubkov et al., 2007; Rahaman and Ambikadevi, 2000; Williams, 1998; Williams et al., 1990). Brine shrimp, *Artemia*, is among species that can tolerate high salinity ranges but its population and cyst production decline substantially in salinities below 100 g L^{-1} and above 300 g L^{-1} (Wurtsbaugh, 1992; Wurtsbaugh and Gliwicz, 2001).

Urmia Lake, the world's second largest hypersaline lake, is located in a closed tectonic depression drainage basin in northwest Iran at the elevation ~ 1275 meters above sea level. The lake and its associated islands and wetlands was declared as protected area in 1967 and was incorporated in the Ramsar-1971 Convention on Wetlands of International Importance in 1975. The fragile and unique environment of the lake is home to more than 550 flora and 287 fauna species, including 27 mammals, 212 birds and 48 reptiles and amphibians (DOE, 2009; Scott, 1995) and is the world largest habitat for *Artemia urmiana* (Ahmadi et al., 2011; Vahed et al., 2011). Subsequent to Iran's integrated plan for development since the early 1980s excessive anthropogenic activities inside the lake basin and its watershed area (Ghalibaf and Moussavi, 2014) led to up to 88% loss of lake surface area (AghaKouchak et al., 2015). Fluctuations in lake levels is evidently controlled by the imbalance in the net annual flux from major tributaries that terminate at Urmia Lake. Nevertheless, the primary cause(s) of such a drastic change in lake surface area and water level in a span of three decades remains a matter of considerable debate (UNEP, 2012).

While natural forcing mechanisms of abrupt climate change are favored by local authorities, extensive anthropogenic activities in the catchment basin and within the lake environment in fact appear to have significantly affected the hydrological imbalance that has led to the disappearance of the lake. Specifically, construction of a dike-type structure known as the Kalantari Causeway across a 15-Km passage in the middle of the lake that has disrupted the natural water circulation, construction of 59 dams in the catchment basin since the 1960s and excessive extraction of groundwater from more than 65000 wells across the watershed area (M.Q.C.E., 2013) have had lasting effects on the delicately balanced environment of Urmia Lake over the last few decades.

To answer the question whether natural climate variabilities or anthropogenic activities are responsible for the ongoing deterioration of the lake, regional instrumental climate data and satellite monitoring have been used for nearly 50 years to study the effect of climate variability, drought frequency and hydrological changes in the lake's watershed (see *e.g.,* Abbaspour et al., 2012; Delju et al., 2013; Golian et al., 2014; Shahabfar et al., 2012; Shahabfar and Eitzinger, 2013). Nevertheless, instrumental data covers a short period of time in the history of the lake and provide limited insight regarding the pre-industrial and ancient conditions. Furthermore, scarcity of hydrochemical and sedimentological data from the lake (Eimanifar and Mohebbi, 2007) have made it difficult to characterize the natural hydrochemistry of the lake against which modern changes can be assessed. Paleoclimate reconstructions have the potential to provide such a perspective.

In this chapter, an evaluation of lake water and surface sediment chemistry before drastic loss of water in the last decade is presented to provide a baseline for the

sedimentological and hydrochemical regime of Urmia Lake. Furthermore, the role of regional geology on providing ions as well as detrital materials to the lake is investigated.

2- Materials and methods

Urmia Lake (37°29'49"N, 46°00'34"E, 1275 m.a.s.l.) is the largest land-locked body of water in Iran and formed in a tectonic depression in northwest Iran (Fig. 2-4). In the spring of 2002, nineteen short (50-cm long) core samples were collected from inside the lake (Fig. 2-7) using KC gravity corer. Sub-samples were analyzed for elemental concentrations using ICP-OES and MC-ICPMS. Carbonate content ($CaCO_3$+$MgCO_3$) of the sediment samples was measured based on the volumetric analysis of the carbon dioxide (CO_2) (Hulseman, 1966) using Bernard calcimeter. Total organic carbon was gravimetrically established by removing the organic content from bulk sediment using 10% hydrogen peroxide. Grain size analysis was conducted on detrital silicate fraction of the Urmia Lake core top and down core short sediments using FRITCH Laser Particle Sizer (Analysette 22, Comfort). Hydrochemistry of the lake's water was established by using available hydrochemical data from Urmia Lake, its peripheral ponds and major tributaries (Karbassi et al., 2010; Kelts and Shahrabi, 1986; Mohajer Bavaghar, 1997; Shahrabi, 1994; Tolouei, 1995). Details of the sampling and analytical methodology are provided in the chapter 2.

3- Results

In this section, the results of core top and down core analysis for the short cores and modern water samples are presented to reconstruct the lake's modern hydrochemistry and examine the influence of bedrock composition on lake sediments.

3.1- Grain-size distribution

The distribution patterns of major grain-size classes for the siliciclastic fraction of surficial sediment samples are shown in Fig. 5-1. Accumulation percent of the grain-size reveals that silt is the dominant size fraction of the Urmia Lake's sediment. Sand and sandy silt fractions are mostly found in the northwest (NW) part of the lake, where intrusive formations are adjacent to the lake's shoreline and metamorphic rocks are widely spread (Fig. 2-6). Clay bearing siliciclastics are mainly seen in southern and central part of the lake and to a lesser extent in the northeastern (NE) part. The highest amount of clay (up to 20%) is seen in the narrow middle section of the lake, adjacent to the Kalantari causeway (Fig. 5-2 and Fig. 2-7). Down core grain size variation in cores URC-3 and URC-21 from central and southern parts of the Urmia Lake (Fig. 2-7) reveal that although some intervals of clay and sand layers are present, the dominant size fraction along the core is primarily silt-size particles with a unimodal distribution tailing toward the clay fraction (Fig. 5-2 A and C). However, downcore grain-size variation in core URC-5, collected close to the Kalantari causeway (Fig. 2-7) does not follow the same pattern and bimodal distribution of siliciclastic fraction observed along the most part of the core (Fig. 5-2 B).

3.2- Sediment geochemistry

Spatial distribution of major oxides (%) and trace element concentrations of the siliciclastic fraction (in % and in ppm respectively) are presented in Fig. 5-3. High concentrations of TiO_2, CaO, MnO and Zr are seen in the NW region of the lake, where intrusive formations are in close proximity to the shoreline. This pattern is consistent with the distribution of coarse-grained sediments (Fig. 5-1). Concentration of Na_2O is higher in

the northern sub-basin and along the western shoreline and reaches its maximum (~3%) in NW of the lake. The abundances of K_2O and Rb present the same distribution pattern with higher concentrations in the NE of the lake and around Shahi peninsula, where high potassic volcanic rocks are most abundant (Golafshani, 1995). High concentrations of Sr (~150 ppm) are seen around Shahi peninsula in the eastern shoreline and toward the NW part of the lake while the lowest concentrations (~75 ppm) are seen in the southern part of the lake. Both Fe_2O_3 and MgO show a similar distribution pattern with the highest concentrations in the NW part of the lake.

The concentrations of Ni and Cr are highest (~120 and ~230 ppm respectively) in the siliciclastic fraction of sediments in the southern part of the lake. However, high Ni concentrations are also present in the central section of the lake. P_2O_5 is more abundant in the deep parts (Fig. 2-5) of the southern and northern basins with the highest concentrations of ~0.45 % in the central part of the lake (Fig. 5-3). Al_2O_3 and SiO_2 and to less extent Ba are evenly distributed in the core top sediments of the lake, albeit a hotspot for Ba can be seen in the central part.

While the distribution pattern of the major oxides and trace elements in the Urmia Lake sediments seems to correlate well with grain-size distribution patterns and geological formations within the catchment basin, the anomalous concentrations of some elements (*e.g.,* Ni, Sr, Ba and P_2O_5) in the narrow central part of the lake are likely caused by the anthropogenic impact of Kalantari causeway construction. Al_2O_3 ranges from 10.05% to 16.70% in the surface samples, lower in coarse grain samples from NW part of the lake (Fig. 2-7 and Table SI-4b), and shows an inverse correlation with SiO_2, TiO_2 and Zr (Fig. 5-4). Carbonate content of the surfacial sediments are varied from 0.04% in NW of the lake

to 29.6% in west-central of the lake (Fig. 5-5 and Table SI-4b). In general, distribution pattern of sediments' carbonate content shows higher concentrations in southern basin. Total organic matter in the surfacial sediments varies from 0.07% in NW up to 10.4% in central part of the lake (Table SI-4b). High concentrations of organic matter are mostly seen in southeast and central part of the lake.

3.3- Modern hydrochemistry of Lake Urmia

Spatiotemporal distribution pattern of total dissolved solid (TDS) in the Urmia Lake surface water, constructed from seasonal hydrochemical data for May and October 1987 (ARMC-Azarbaidjan Regional Mining Cooperation, 1995), shows a large TDS gradient (from 0.85 to 21.6 g L^{-1}) in the southern part of the lake (Fig. 5-8) in May, which is attributed to high fluxes of fresh water through the Simineh Rud and Zarrineh Rud rivers due to higher precipitation in the catchment basin during the spring (Fig. 2-4). This gradient is diminished during the October as the water inflow decreases and the TDS shows more homogenous distribution throughout the entire lake with a gradient of ~0.2 g L^{-1}. During the 1977-1987 period where the lake's level was stabled around 1278 m.a.s.l. (Fig. 5-9 A), the average TDS values for the Urmia Lake varied in a relatively narrow range from 219 g L^{-1} in 1977 to 222 g L^{-1} in 1987 (Table SI-1). In 1997, when lake level was high (~1278 m.a.s.l.), the TDS value decreased to 174 g L^{-1}. In contrast, the average TDS in 2010 was as high as 379 g L^{-1}, a factor of 2 increase, while lake level dropped to 1272 m.a.s.l. This drop in lake level coincide with implementation of extensive water management plans in the region (AghaKouchak et al., 2015; Ghalibaf and Moussavi, 2014). A prominent change came with a 60% increase in the number of dams since 1990 (Fig. 5-9 A). To date, there are 59 operational dams and 65000 wells in the 52000 Km^2 of the catchment basin (Fig. 5-

9 B), with average of one dam per 1000 Km^2 and one well per 1 Km^2 regulating water inflow to the lake.

The hydrochemical facies of the Urmia Lake brine and its major tributaries are shown on trilinear piper diagram in Fig. 5-10. The cation distribution indicates that except for Aji Chay River, all tributaries are of Ca-Mg cation type, where samples from Urmia Lake brine and those from Aji Chay River are predominantly of Na-K cation type. In the anion triangle, water samples collected from Zarrineh Rud, Nazlou Chay and Barasndooz Chay are dominated by bicarbonate ions while water samples from other tributaries are mixed. Urmia Lake brine and samples from Aji Chay River fall close to the chlorine corner. It is notable that the Urmia Lake 2010 sample, in contrast, plotclose to the sulphate apex, indicating the dominance of sulfate anion in the brine. All water samples from the major tributaries, except for Zarrineh Rud, fall in the field of mixed Ca-Mg-Cl in the quadrilinear plot of Fig. 5-10. Zarrineh Rud water samples plot in the Ca-HCO_3 region. Water samples from Aji Chay River as well as the ones from Urmia Lake are predominantly Na-Cl type. Taken together, the changes in the ionic composition of Urmia Lake brine since 1977 is presented in the stiff diagram of Fig. 5-11. In spite of variations in salt concentration (TDS) from 1977 to 1997, the water samples from this period are classified as Na+K-Cl-Mg-SO_4. The ionic composition of the Lakes water, in contrast, is changed substantially by 2010 when it became Na+K-SO_4-Mg-Cl. This change in ionic composition is coincide with the increase in TDS and a drastic drop in water supply to the lake, confirm the effect of reduced inflow and continued evaporation on the hydrochemical composition of the Urmia Lake (Vengosh, 2013).

The sources of the dissolved ions in the Urmia Lake brine can be studied through the Gibbs diagram (Gibbs, 1970) where the TDS of the water is measured against specific ionic ratios (*e.g.,* Na/(Na+Ca)). As shown in Fig. 5-12, with the exception of Aji Chay River, all water samples from Urmia Lake tributaries fall in the rock dominance domain. The Aji Chay water samples plot in the evaporation-precipitation domain, close to the world's ocean region. This observation along with the fact that Aji Chay water samples have the same ionic composition as Urmia Lake brine (Fig. 5-10), suggest that although chemical weathering of the rock forming minerals and evaporation may contribute to the chemical composition of the Urmia Lake brine, dissolution of evaporite formations (Fig. 2-6) by Aji Chay River is likely the main source of major ions to the Urmia Lake. The observed increase in TDS values from 1977 to 2010 in both Urmia Lake brine and Aji Chay water samples (Fig. 5-12 and Table SI-1) can be attributed to factors such as reduction in water supply throughout the basin due to natural cycles and anthropogenic activities, increase in evaporation rates due to rise in temperature and reduction in surface area, and increase in sediment load due to anthropogenic activities in the catchment basin. Previous studies have shown that the average temperature for the region has increased by 0.8°C along with a 9.2% decrease in precipitation for the period 1964-2005 (Delju et al., 2013), which ultimately led an increase in evaporation rate of +6.2 mm decade^{-1} (Alizadeh-Choobari et al., 2016). The warming of the lake basin along with reduction in lake's surface area resulted in increase in lake's surface temperature (Kabiri et al., 2012; Sima et al., 2013, 2012). Construction of Kalantari causeway in the middle of the lake proved to play a major role in increasing lake's water salinity by dividing the lake into almost tow closed sub-basins (Zeinoddini et al., 2009).

4- Discussion

The modal distribution of sediments is a function of the energy of sediment transport, depositional processes and hydraulic conditions in lake environments (Håkanson and Jansson, 1983; Sly, 1978; Xiao et al., 2009). Typically, lake shoreline materials are characterized by dominance of sand and low proportions of silt and clay fractions (Håkanson and Jansson, 1983; Sly, 1989a, 1989b, 1978). In general, the offshore zone of lakes lie at lower hydraulic energy compare to nearshore zones and this allows finer particles to be deposited in depositional zones within the lake basin (Adhikari, 2011; Xiao et al., 2009). Hence, variation in the fraction of fine and coarse grain clastic materials potentially reflect lake level fluctuation (Sly, 1989a, 1989b). Down core dominance of silt fraction in cores URC-3 and URC-21 from central and southern parts of the Urmia Lake (Fig. 5-2 A and C) suggest deposition of these sediments in a low energy environment. Grain-size variation and bimodal distribution of siliciclastic fraction observed in core URC-5 (Fig. 5-2 B), which is close to the Kalantary causeway and potentially impacted by significant dredge and dump activities, may be attributed to anthropogenic disturbance of depositional process. Carbonate content distribution pattern shows higher concentrations in the southern basin where most of the carbonate formations are located adjacent to the lake (Fig. 2-6 and 5-5). Variation of total organic content in sediment correlates with distribution of clay size particles (R^2 = 0.65, p-value=3.3×10^{-5}, p<0.01, Fig. 5-13), which may indicate the stabilization of organic matter related to the total surface area of the aluminosilicate minerals (Adams and Bustin, 2001; Hassink, 1997; Mayer, 1994).

Inverse correlation between Al_2O_3 and weathering-resistant elements/minerals (SiO_2, TiO_2 and Zr) (Fig. 5-4) is mainly due to contribution from clay minerals *vis-à-vis* grain size effect (Das and Haake, 2003; Jackson et al., 1948; Jin et al., 2006). The association of Al_2O_3 with fine grain sediments as an end product of incongruent chemical weathering has been assessed by calculating the chemical index of alteration (CIA) (Nesbitt and Young, 1989, 1982) in the siliciclastic fraction of surficial samples using the following equation and molar oxide values:

$$CIA = 100\times[Al_2O_3 / (Al_2O_3+CaO^*+Na_2O+K_2O)] \quad \text{(eq. 5-1)}$$

where CaO* is CaO associated with the silicate fraction of the sample and corrected for carbonate and apatite content. The CIA value provides a useful framework for estimating the degree of chemical weathering in the catchment basin, which is based on the proportion of primary to secondary minerals in samples (Nesbitt et al., 1996). For unweathered feldspars, hornblende and pyroxenes, the CIA values are 50-55, 10-30, and 0-10 respectively; consequently, all felsic rocks (*e.g.,* granite and rhyolite) have the CIA values around 50 while intermediate to mafic rocks (*e.g.,* basalt and andesite) are expected to have CIA values that are typically below 50. The CIA value, however, is equal to 100 for kaolinite, gibbsite and chlorite as the final products of the weathering processes. Accordingly, the CIA=50-60 will indicate early stages of weathering while CIA= 60-80 and >80 indicate moderate to high degrees of weathering, respectively (Nesbitt and Young, 1982).

Variation of CIA in the siliciclastic fraction of Urmia Lake surficial samples mostly range from 63 to 77 throughout the lake with rapid decrease in this index as we approach

the NW part of the lake (CIA= 29-47, Fig. 5-6 and 5-7), where coarse-grained sediments dominate (Fig. 5-1). Based on the geochemical and mineralogical composition of Urmia Lake sediments, Sharifi (2002) suggested that igneous rock formations in the catchment basin are the main sources of weathered siliciclastic material in lake sediments. To further investigate weathering trends in the Urmia Lake sediments, a representative source rock composition (see Table SI-4b) was calculated by averaging the chemical composition of igneous rocks around Urmia Lake as well as in its catchment basin using available geochemical data (Isfahani, F. and Sharifi, 1999). The CIA value for this source rock is 29 and for coarse-grained samples, URC-15 and URC-16, the values are 47 and 29 respectively (Table SI-4b). On a A-CN-K diagram (*i.e.*, molar values of Al_2O_3-($CaO+Na_2O$)-K_2O) (Nesbitt et al., 1996; Nesbitt and Young, 1982), the coarse-grained sample URC-15 is plotted on the feldspar join (line joining plagioclase and K- feldspar compositions), indicating that feldspars are the most abundant aluminous minerals of the sample while coarse-grained sample URC-16 and source rock are plotted below the feldspar joint suggesting the abundance of mafic aluminous minerals in these samples. The silt size siliciclastic fraction of Urmia Lake samples are clustered along the weathering trend parallel to the A-CN join (Fig. 5-7) suggesting these samples experienced a moderate degree of chemical weathering.

5- Conclusions

Lake Urmia was once the second largest brine lake in the world but has been shrinking to less than 90% of its surface area compared to three decades ago due to extensive anthropogenic activity in the lake's catchment and terminal basins. We present a dataset of core top sediments and water composition from the lake and its tributaries.

Based on chemical analysis of conservative lithogenic elements (*e.g.*, Ti, Si, Al, Ca) as well as redox-sensitive elements (*e.g.*, Fe, K, Rb, Sr) in the clastic fraction of the lake's sediment along with the sediment grain size, elemental distributions in the lake sediments and water are reflective of regional geology. The water of the Urmia Lake is classified as Na+K-Cl-Mg-SO_4 based on 1977-1997 hydrochemical data, during which the lake experienced less anthropogenic disturbances. This ionic composition changed substantially by 2010 and became Na+K-SO_4-Mg-Cl followed by a factor of 2 increase in TDS content and 88% reduction in the surface area. These drastic changes coincided with a 60% increase in the number of operative dams since 1990 along with general warming of the watershed area.

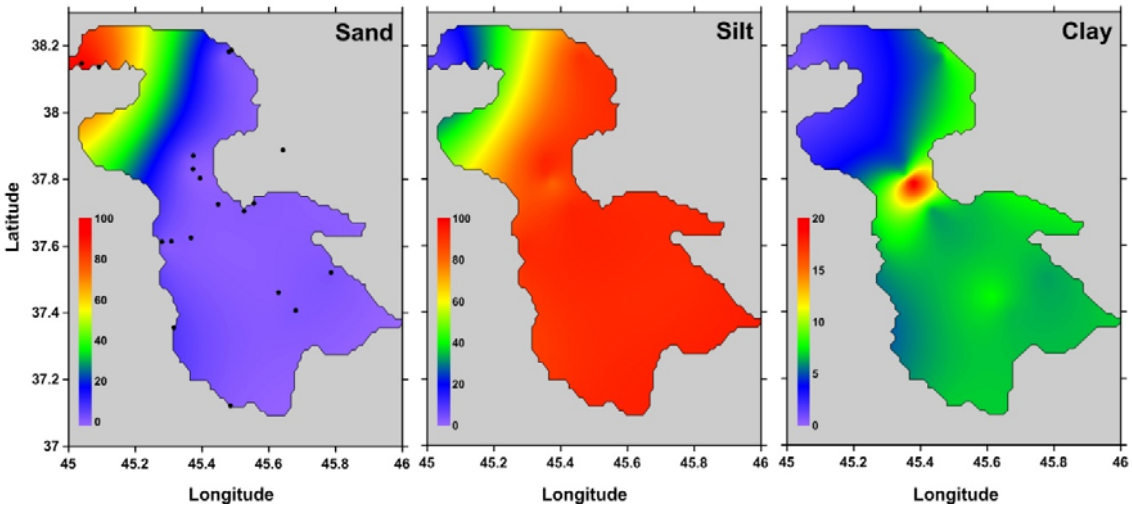

Fig. 5-1- Distribution pattern of three major grain-size classes (accumulation %) in siliciclastic fraction of the Urmia Lake surficial sediments. Filled circles on the left panel indicates the sampling points, see chapter 2 and figure 2-7 for details.

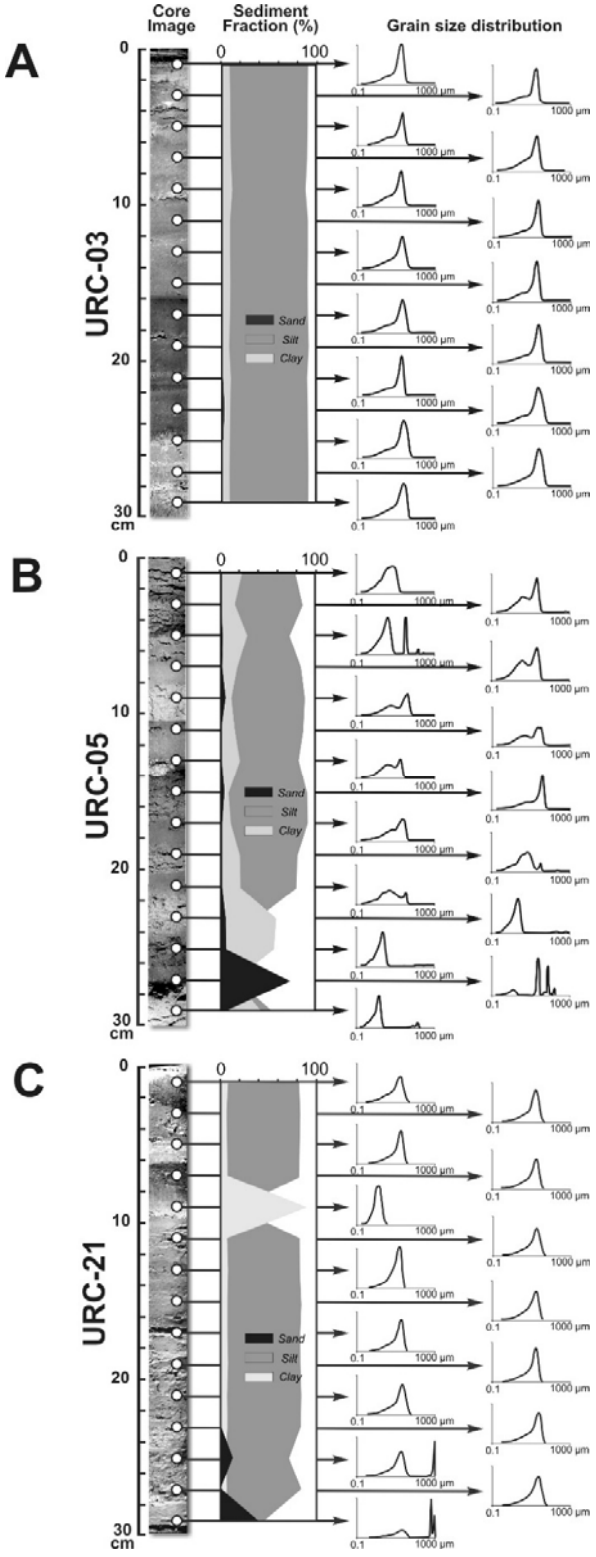

Fig. 5-2- Downcore variation of siliciclastic fractions in 30-cm long cores from central and southern part of the Urmia Lake, see figure 2-7 for sample locations.

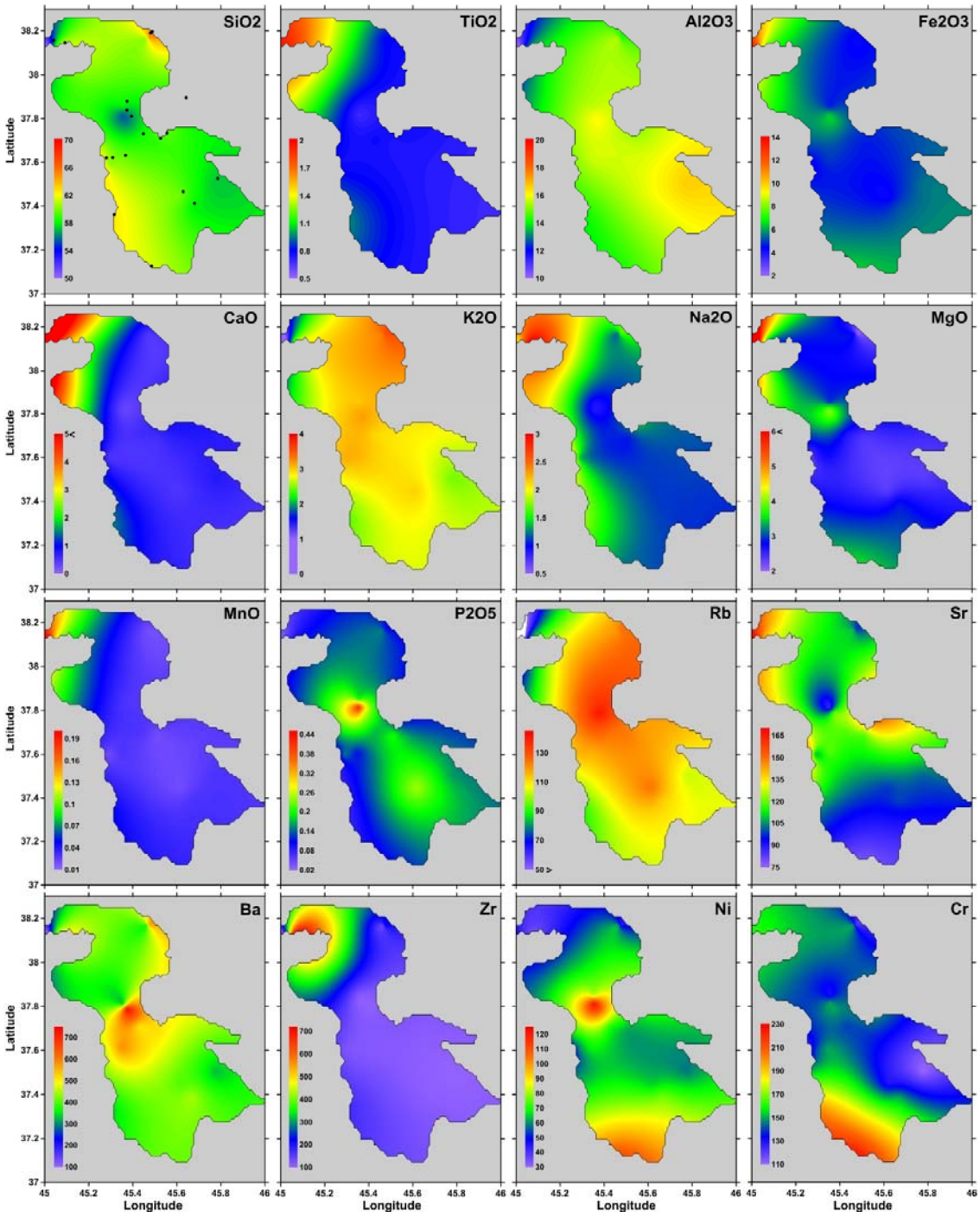

Fig. 5-3- Distribution patterns of major oxides (in %) and trace elements (in ppm) concentrations in siliciclastic portion of Urmia Lake sediments. Filled circles on the SiO_2 panel (top left) indicates the sampling points, see chapter 2 and figure 2-7 for details.

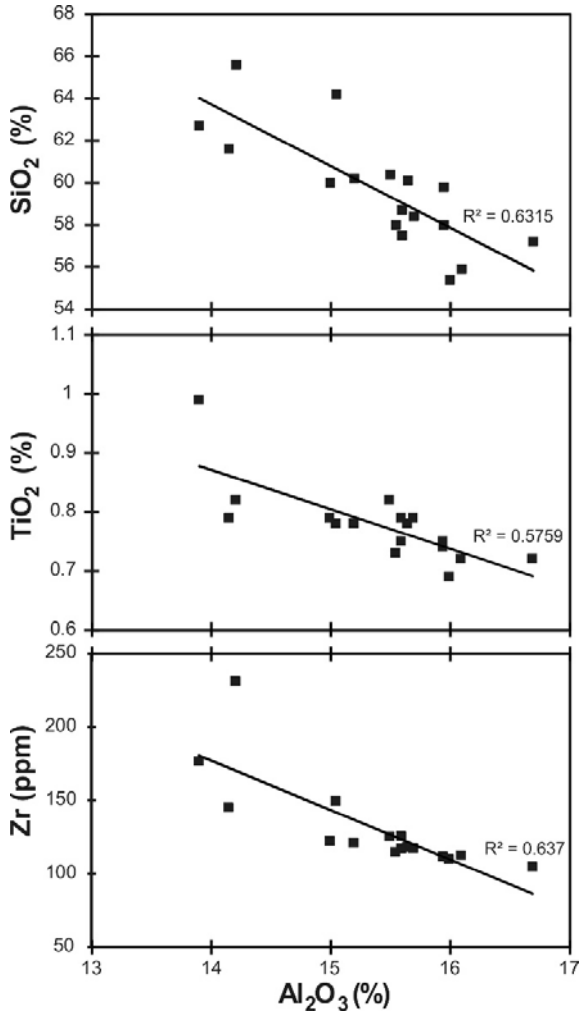

Fig. 5-4- Variation diagrams of SiO_2, TiO_2 and Zr versus Al_2O_3 of the Urmia Lake surface sediments.

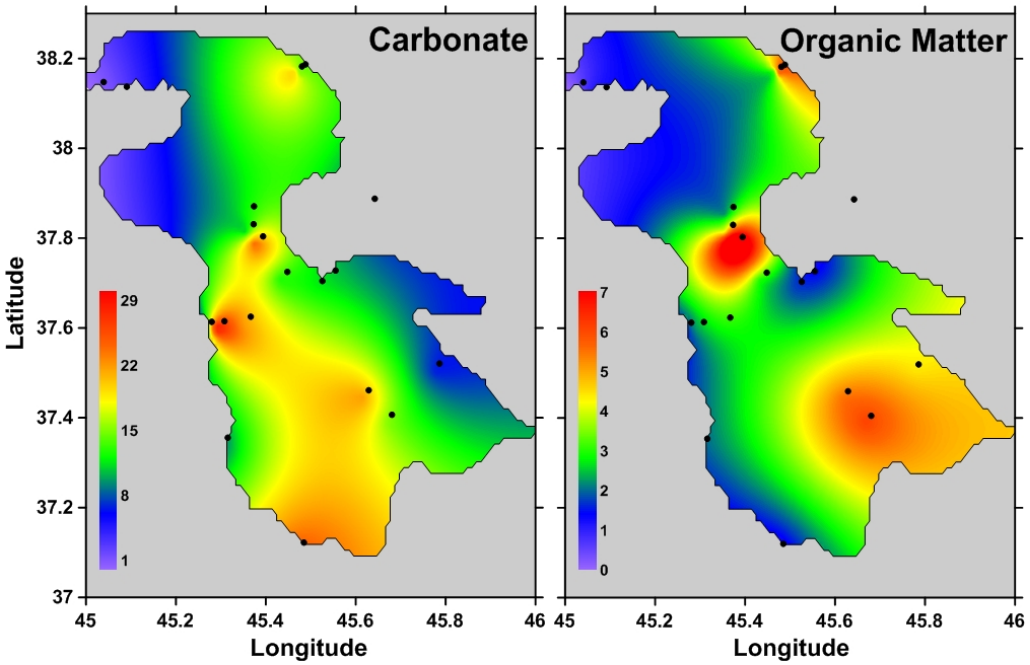

Fig. 5-5- Spatial variation of carbonate content (left) and organic content (right) in Urmia Lake sediments. Filled circles indicates the sampling points, see chapter 2 and figure 2-7 for details.

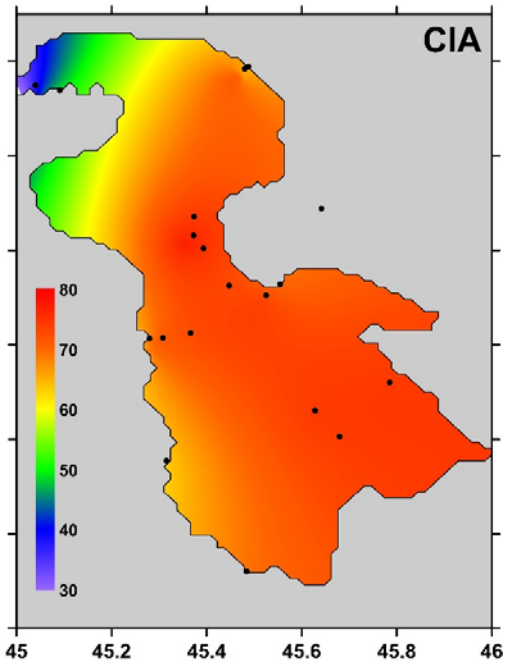

Fig. 5-6- Spatial variation of chemical index of alteration (CIA) in siliciclastic fraction of Urmia Lake sediments. Filled circles indicates the sampling points, see chapter 2 and figure 2-7 for details.

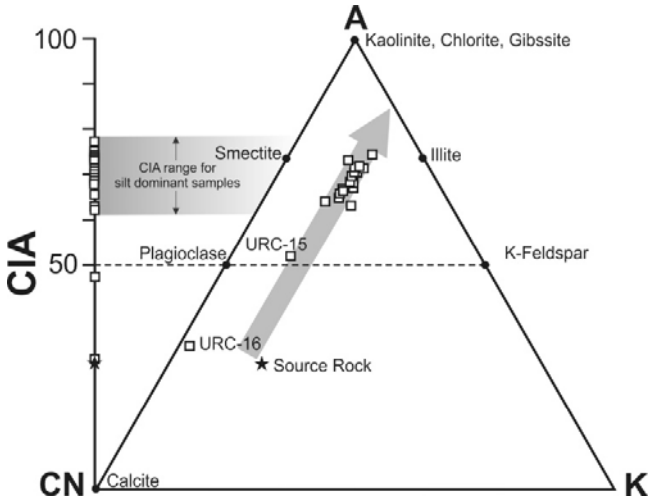

Fig. 5-7- A-CN-K diagram and the weathering trend for the Urmia Lake siliciclastic samples (open quadrangles), solid star denotes the composition of representative source rock. Values for chemical index of alteration (CIA) are plotted on the vertical axis.

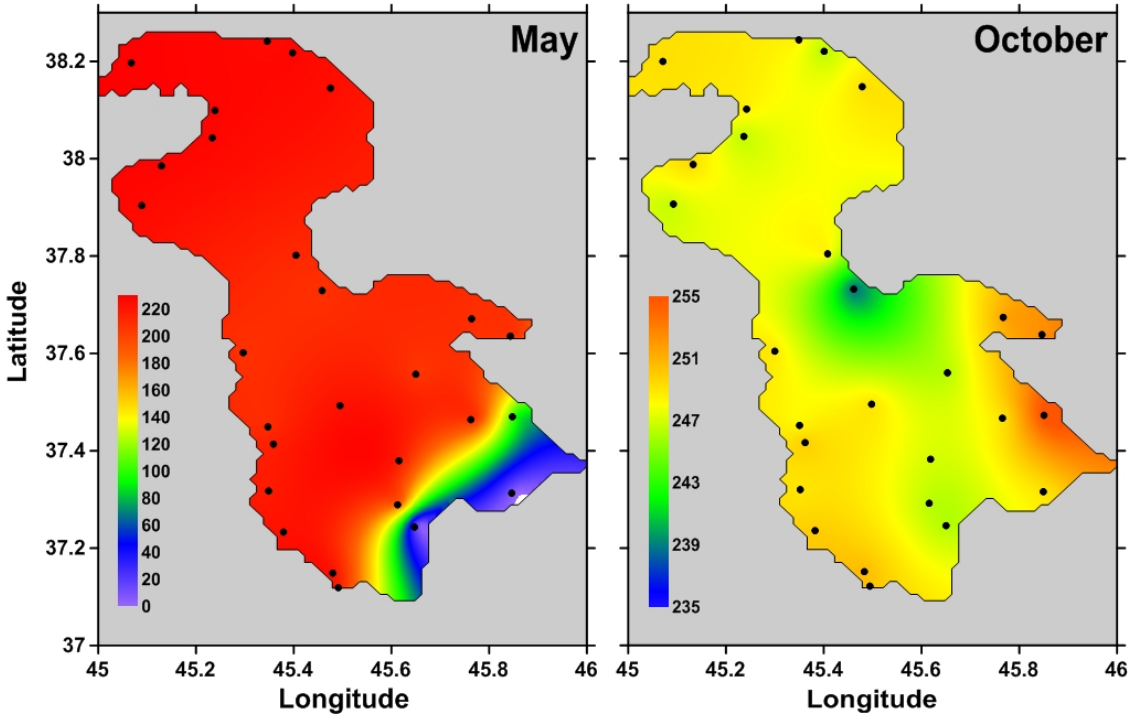

Fig. 5-8- Spatiotemporal distribution pattern of total dissolved solid (TDS) in the Urmia Lake brine in May and October 1987. TDS scales are in gL^{-1}. Filled circles indicates the sampling points, see chapter 2 and figure 2-7 for details.

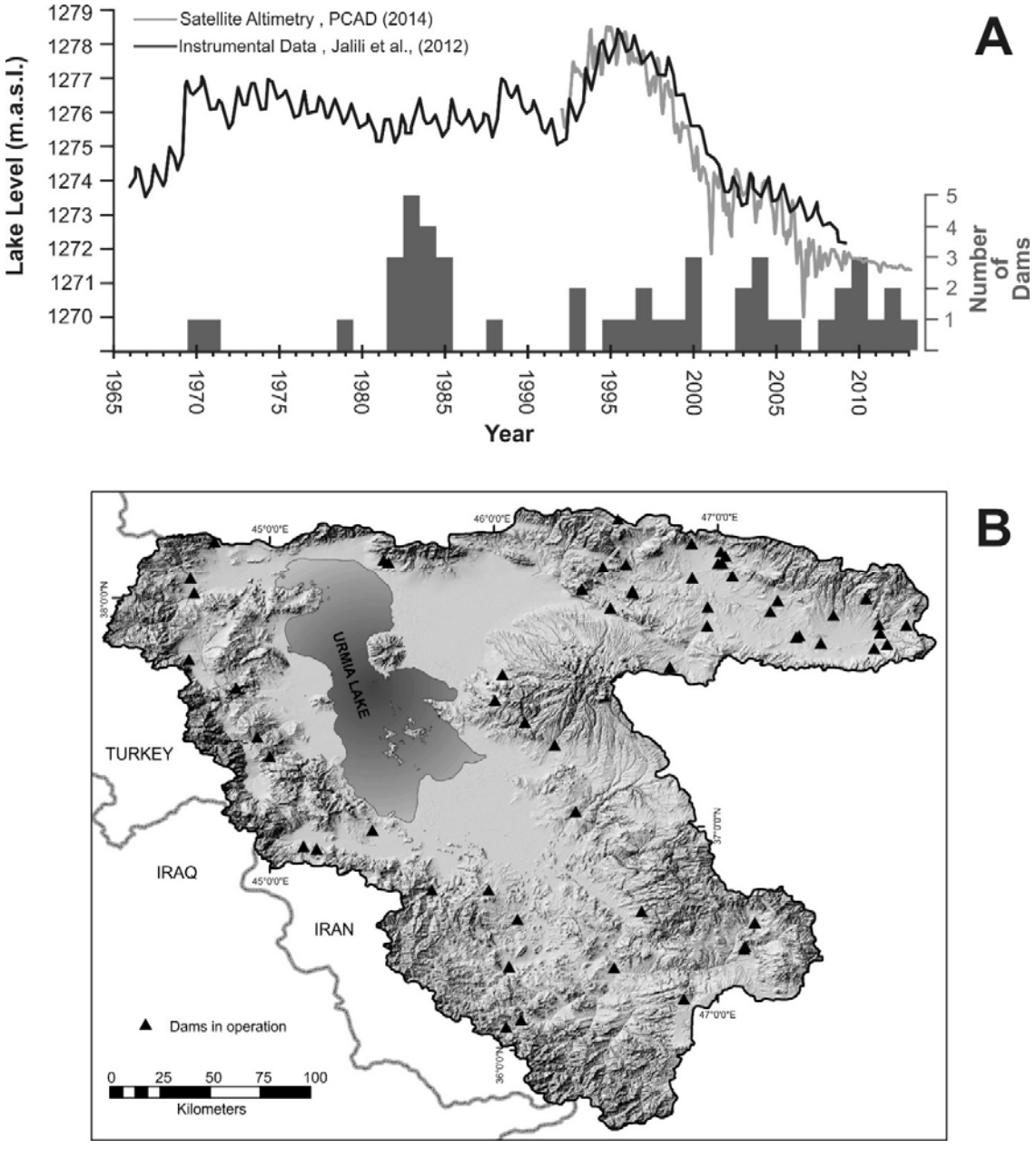

Fig. 5-9- Lake level fluctuation since 1965 and Dam construction over the Urmia Lake watershed area. A) Lake level data above sea level based on the instrumental data (Jalili et al., 2011) and the satellite altimetry computed from TOPEX/Poseidon historical archive and Jason-1/OSTM interim GDR 20hz altimetry (data from http://www.pecad.fas.usda.gov). Number of dams in each year is based on their operation starting date (M.Q.C.E., 2013), only those with available dates are shown. B) Location of dams in operation (total of 59) in the Urmia Lake watershed area.

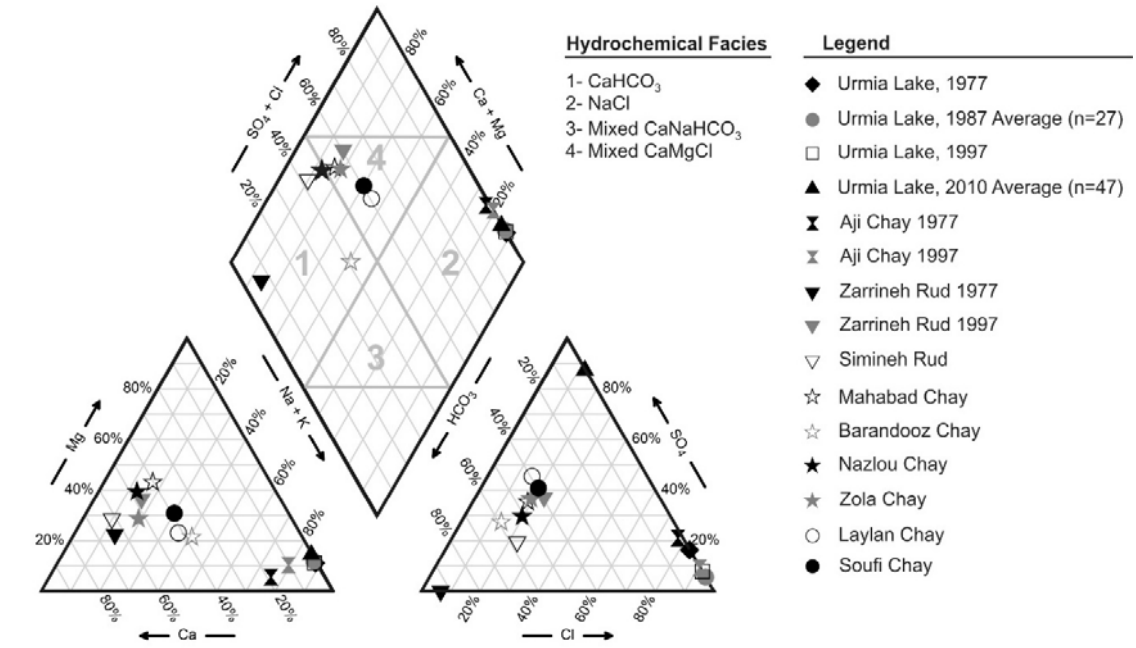

Fig. 5-10- Piper diagram of water samples from the Urmia Lake and its major tributaries.

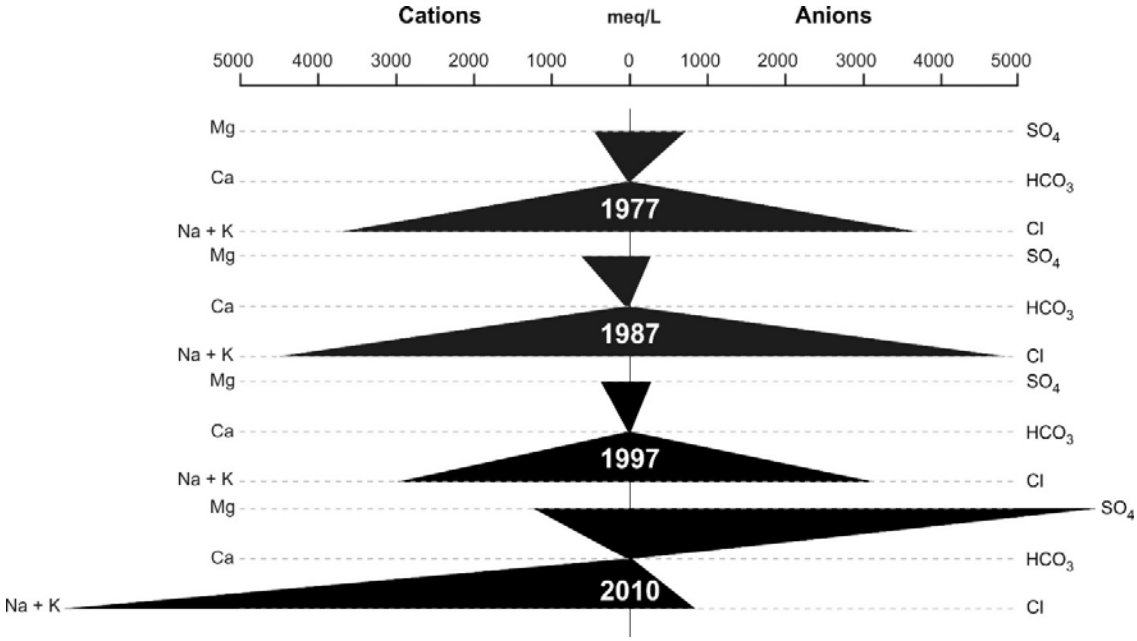

Fig. 5-11- Ionic composition of Urmia Lake brine since 1977.

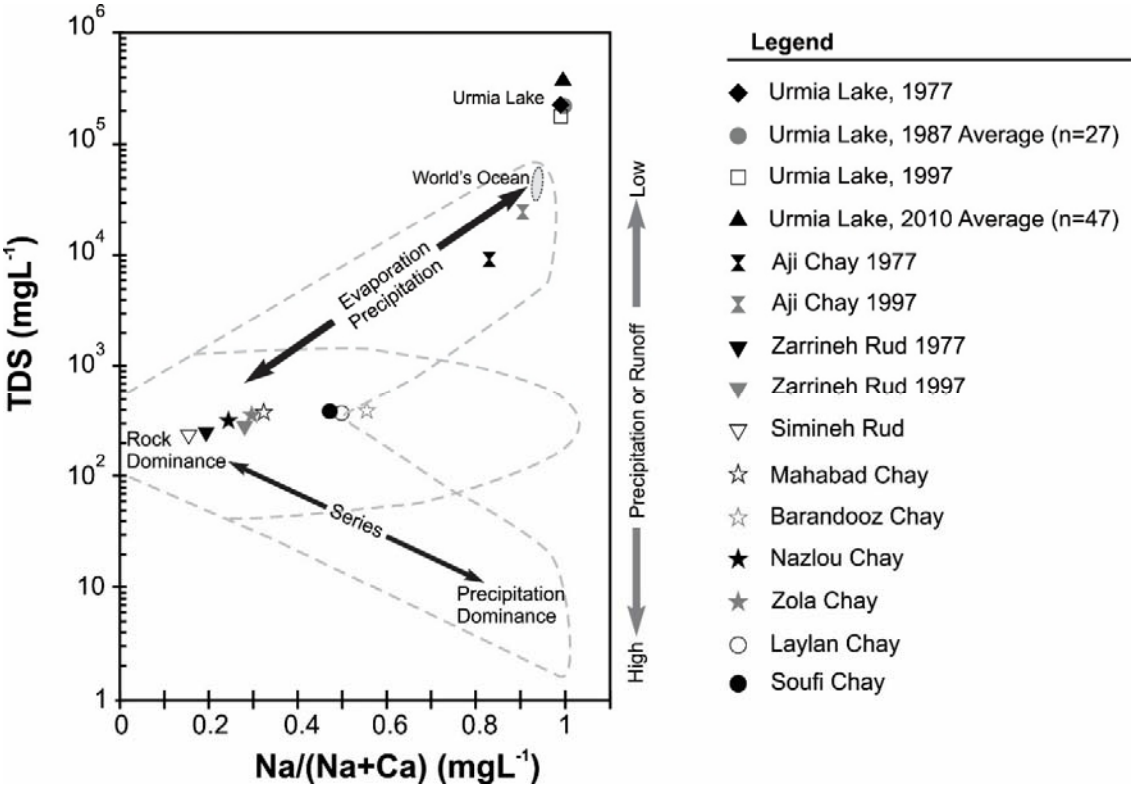

Fig. 5-12- Variation of the Na/(Na+Ca) weight ration as a function of total dissolved solid for the Urmia Lake and its major tributaries.

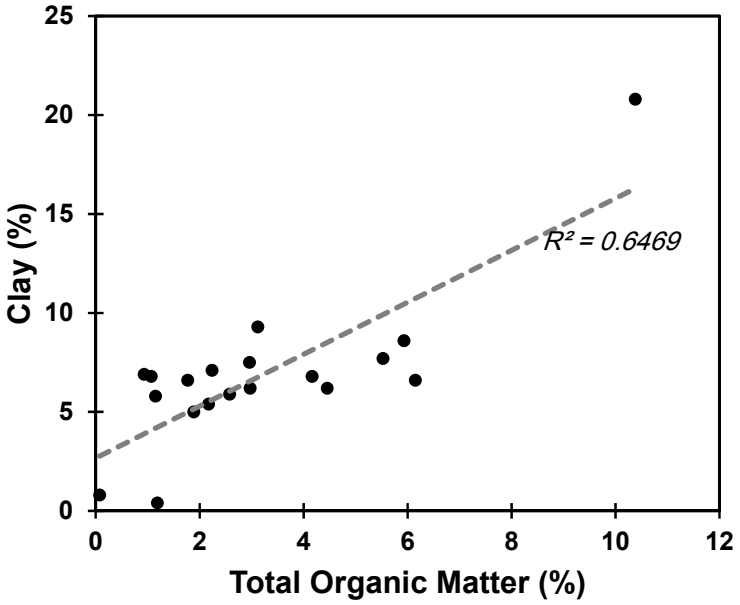

Fig. 5-13- Correlation between total organic content and clay size particle in the surfacial sediments of Urmia Lake.

Holocene palaeohydrology and climate reconstruction of the largest hypersaline lake of the Middle East, Salt Lake Urmia, NW Iran

Summary

Urmia Lake is the largest hypersaline lake in Middle East and the largest terminal lake in Iran with the average catchment area of 52000 km^2. Urmia Lake is facing more than 90% reduction in its surface area during the past 30 years due to decrease in water supply to the lake. With the paucity of robust decadal to millennial scale archive of climate variability, it is difficult to assess whether the disappearance of this lake is primarily caused by anthropogenic or natural processes. In this chapter, a multi-proxy approach is utilized to characterize the geochemical composition of Holocene samples in form of a 5-meter long core from the lake for a high resolution reconstruction of climate and hydrology of the region since 11,600 cal. y BP.

Elemental paleo-dust (Si/Al, Ti/Al and Zr/Al), paleo-hydrology (Rb/K) and paleo-redox (Mn/Al, Fe) proxies suggest several episodes of wet and dry conditions associated with high and low lake levels. Paleo-rainfall reconstruction over the Urmia region suggest wet condition was dominant during the early Holocene and dry condition became more frequent toward the late Holocene. Variation in estimated precipitation along with XRF profile of Al covary closely with the record of North Atlantic ice rafted debris events (IRD) and Holocene reconstruction of sunspots, indicating the influence of climate forcings on the hydrological condition of the Urmia Lake's watershed as well as teleconnection between the North Atlantic climate and the interior of the West Asia. Our findings suggest the contribution of natural climate cycles as observed throughout the Holocene may have less influence on water availability to the lake than extensive anthropogenic activities over the last few decades.

1- Overview

Records of past abrupt climate change events can be reconstructed within saline lakes with fewer uncertainties compare to open freshwater systems due to their sensitivity to climate forcings and also to lack of bioturbidation (Fritz, 1996). Although such opportunity is provided by Salt Lake Urmia, but biogeochemical precipitation of calcium carbonate inside the lake and contribution of older geological formations in the watershed area to the lake's carbon budget seems to be the main reasons behind the lack of robust and well calibrated age model (Stevens et al., 2012; Talebi et al., 2016). The first paleoclimate records from Urmia Lake cover the past 13,200 years and are based on sedimentological (Kelts and Shahrabi, 1986) and pollen (Bottema, 1986) data of a 4.5-m sediment core with a chronology based on extrapolation of two un-calibrated radiocarbon dates on shrimp fecal pellets. These studies suggested low lake levels since the beginning of the record till about 9,000 year BP, high lake levels from 9,000 to 7,300 year BP and dominance of "modern conditions" since 7,300 BP. These attempts to reconstruct Holocene paleoenvironmental conditions at the lake are out of phase with other lake records from the Turkey (Degens et al., 1984) and North Africa (Street-Perrott and Roberts, 1983), mainly due to caveats in the chronology of sediment core as noted by the authors (Kelts and Shahrabi, 1986).

The longest available record for this lake is from a 200,000-years climate reconstruction based on pollen and $\delta^{18}O$ data of a 100-m sediment core (Djamali et al., 2008) at low resolution (average sampling resolution of 2000 yr). The core chronology was established by temporal correlation of the Urmia record with other well-dated records from the region and extrapolation of two calibrated radiocarbon dates on bulk samples at 8 and 18.5 m, which returned calibrated ages of 12,212 and 29,150 cal year BP, respectively.

Based on this record, Djamali et al. (2008) concluded that warm and moist climate conditions prevailed during the last glaciation transition, while the Holocene interglacial was relatively colder and dryer.

Difficulties in establishing a robust chronology and low resolution assessments of limited proxies have made it difficult to decipher the existing paleoclimate records from Urmia Lake during the last deglacial period that is most pertinent to understanding natural and anthropogenic causes of changes in lake hydrochemistry. In this chapter, the first high-resolution, sub-decadal multi-proxy reconstruction of palaeohydrological changes in Urmia Lake is provided for the past 11,600 years from a 5-meter long sediment core in north eastern part of the lake. The geochemical proxies are interpreted in the context of a robust, well-calibrated chronology by measuring the effect of reservoir carbon on the radiocarbon ages obtained from bulk sediments, shrimp cyst and shrimp fecal pallets. We further examine the potential atmospheric teleconnection during the Holocene by comparing our results with records from the eastern Mediterranean Sea and the North Atlantic.

2- Materials and methods

In the summer of 2012, a 5-m split-core and a 5.5-m duplicate core from the east coast of the Urmia Lake as well as two additional 2-m cores from southwest and south parts of the lake was recovered (Fig. 2-7). The core chronology was established by 8 radiocarbon dates. The effect of reservoir carbon on radiocarbon dates was established by taking bulk samples, shrimp fecal pellets and shrimp cyst from two 15-cm intervals at 0.65 and 5.4 meter of the sediment core. The age difference between the radiocarbon dates

driven from shrimp cyst and the ones from the bulk or fecal pellet samples collected from the same interval are considered to be the best representation of the “reservoir effect”, see section 5-2 in chapter 2 for more details (Fig. 2-10 and Table 2-3). The relative abundances of refractory and redox-sensitive elements were measured at 1-mm intervals with an Avaatech XRF-core scanner. Stable carbon and oxygen isotope measurements were conducted on shrimp fecal pellets samples using Kiel III interfaced with a Thermo-Finnigan Delta Plus Mass Spectrometer. Elemental and radiogenic isotope analyses were conducted using MC-ICPMS. Details of the sampling and analytical methodology are provided in the chapter 2.

3- Results

In this section the results of Holocene climate variability and precipitation reconstruction are presented to contrast natural and anthropogenically induced changes on Urmia Lake’s sedimentary and hydrochemical regimes on modern and ancient times. Comparative calibrated radiocarbon ages from bulk sediment, shrimp fecal pellet and shrimp cyst extracted from two intervals along the 5.5-meter long core from the NE margin of the lake are shown in Fig. 2-9 and the data are presented in Table 2-3. Among the analyzed samples, shrimp cyst returned the youngest age. The average age difference between shrimp cyst calibrated radiocarbon dates and the ones from bulk sediment and fecal pellet samples through the record, suggest a 560- and 719-year correction on bulk sediment and fecal pellets radiocarbon dates respectively to account for the Urmia Lake’s reservoir effect, see chapter 2 section 5-2 for details. The age model based on 8 calibrated radiocarbon dates is shown in Fig. 2-10 (see Table 2-3 for the data). The minimum and

maximum sedimentation rates (SR) were 0.05 to 1.45 mm yr^{-1} respectively, with the overall decreasing trend from the early Holocene to the late Holocene.

Down-core abundances of conservative lithogenic, redox sensitive and mobile elements measured by XRF-scanning at an average resolution of 2.5 yr are shown in Fig. 6-1 along with the 8 radiocarbon age controlling points (see Table SI-4a for results). Downcore elemental variation of Al and Si suggested at least 10 periods of high abundances since the beginning of the record at 11620 BP (Fig. 6-1 A and B). Al-normalized ratio of conservative lithogenic elements as proxy for aeolian input (Si/Al, Ti/Al and Zr/Al) (Calvert and Pedersen, 2007; Govin et al., 2012; Jiménez-Espejo et al., 2014; Nieto-Moreno et al., 2011) are used to reconstruct the aeolian input (Fig. 6-1 D-F). It is evident from Fig. 6-1 D-F that the Si/Al, Ti/Al and Zr/Al ratios covary throughout the entire record, with high frequencies and abundances during the Late Holocene. As K is more readily mobilized than Rb during chemical weathering (Brown, 2011; Muhs et al., 2001), the extent of chemical weathering and the riverine supply was assessed by studying the of Rb/K ratios in the sediment (Fig. 6-1 G). The ratio of Mn as a redox-sensitive trace metal to Al (Mn/Al) and variations of Fe abundances in the sediment are used (Fig. 6-2 H and I) to demonstrate the fluctuation of water oxygen content at the time of sediment deposition (Calvert and Pedersen, 2007; Martinez-Ruiz et al., 2015; Rodrigo-Gámiz et al., 2014). High Rb/K ratios are coincide with the episodes of higher Mn/Al ratios and lower abundances of Fe (Fig. 6-2 G-I).

4- Discussion

High contents of Zr and Ti are carried by heavy minerals and due to higher density, they are usually transported within the coarse-grained particles (Grousset et al., 1988b).

Since enhanced concentration of aeolian particles in lake sediment can potentially increase the concentration of Si, Ti and Zr, the high Al-normalized values (Si/Al, Ti/Al and Zr/Al) can be related to changes in the supply of wind-blown dust (Martinez-Ruiz et al., 2015). In general, supply of aeolian input into the marine and lake environments increases during dry periods (Harrison et al., 2001). Study of dust emission and transport in the west Asia during the Holocene (Sharifi et al., 2015) as well as in modern era (Middleton, 1986; Prospero et al., 2002) further confirm higher dust transport and deposition to West Asia where the lake is located during dry periods.

Deposition of dark-colored sand has been interpreted as a signature of shoreline regression (Mohajer Bavaghar, 1997; Sharifi, 2002; Tolouei, 1995). We observe similar intervals that are accompanied with high Ti/Al ratios and low Si abundances in the U-1, U-4 and U-6 cores (Fig. 6-2) collected from southeast, south and east part of the lake respectively (Fig. 2-7). While we have not established the chronology for U-1 and U-4, the occurrence of these intervals in the top one meter across the lake basin can be interpreted as representing the same intervals of low lake levels, shoreline erosion and potentially higher aeolian deposition.

The most compelling evidence for high Si/Al, Ti/Al and Zr/Al ratios in the Urmia Lake sediment cores to represent dry periods of erosion and enhanced eolian input is the observation that these periods coincide with high times of low abundances in Al intensities. More support for this interpretation comes from the fact that chemically weathered material are characterized by high Rb/K ratios as this process preferentially mobilizes K from minerals such as feldspars and micas. During dry periods, chemical weathering outpaces physical removal of weathered material on land and resulted in high Rb/K ratios in the

sediment deposited during the dry period (Brown, 2011). By transition from transport-limited, dry condition to weathering-limited denudation during humid periods, the weathered materials are washed off from the lanscape exposing fresh rocks with low Rb/K ratios to more chemical weathering (Stallard, 1985). Nearly all episodes of high Rb/K ratios in Urmia Lake U-6 core coincide with high Si/Al, Ti/Al and Zr/Al ratios (Fig. 6-1 D-G), supporting lower riverine supply and low lake level during dry periods.

Under oxic conditions, Mn forms highly insoluble Mn(III) or Mn(IV) oxi-hydroxides that are rapidly deposited in particulate form. Conversely, under anoxic conditions, Mn is reduced to Mn(II) and forms soluble Mn^{2+} or $MnCl^{+}$ cations and diffuses out of the sediment or from the sediment-water interface into the water column (Algeo and Maynard, 2004; Calvert and Pedersen, 1993). This behavior of Mn is expected to result in high (low) Mn/Al ratios during oxic (suboxic-anoxic) condition (Martinez-Ruiz et al., 2015; Rodrigo-Gámiz et al., 2014). Down core variations of Mn/Al ratios in the Urmia Lake's sediment core (Fig. 6-1 H) indicate several episodes of high ratios, indicative of oxic conditions. These periods are also associated with low Fe abundances along the core (Fig. 6-1 I). Association of sediment Mn and Fe contents with oxic-anoxic conditions is not always straight forward and factors such as water column sulfur content, total organic content, biomineralization of Mn- and Fe-bearing minerals, stratification of water column with respect to oxygen and circulation of lake bottom water play a major role in final concentration of these redox sensitive elements in the sediment (Miot et al., 2016). In lack of such information for Urmia Lake environment, we speculate that the high Fe abundances associated with low Mn/Al and Rb/K ratios may represent higher lake levels shown qualitatively in Fig. 6-1 H with the dashed gray lines. It is worth mentioning that during

the early Holocene and beginning of the mid-Holocene, when solar insolation was higher (Fig. 6-1 C), high lakes levels were sustained for longer periods. However, the periods of high lake level became shorter and the frequency of dry periods became higher as solar insolation reduces from mid- to late Holocene (Fig 6-1 C and H). This observation correlates well with the multi-proxy records from Lake Van (Wick et al., 2003) and Neor Lake (Sharifi et al., 2015), ~230 Km west and ~290 Km east of Urmia Lake respectively, where both suggested higher moisture availability during the early and mid-Holocene and prevailed dry condition during late Holocene. At the Urmia lake, the onset of late Holocene at 3,000 BP is marked by high fluxes of aeolian input (high Ti/Al, Si/Al and Zr/Al ratios) and low lake levels (high Mn/Al ratio), which is also in good agreement with episodes of enhanced aeolian input to the Neor Lake and increase in aridity at Lake Van (Sharifi et al., 2015; Wick et al., 2003).

The hydrological regime of terminal lakes such as Urmia and its catchment basin can also be potentially assessed by measuring the stable oxygen and carbon isotope values of the lake's autogenic carbonates (Cohen, 2004; Cohen et al., 2000; Ingram et al., 1996; Kowalewska and Cohen, 1998). The oxygen isotope composition of waters and precipitating carbonates ($\delta^{18}O_w$ and $\delta^{18}O_c$) are mainly controlled by the balance between evaporation and precipitation (E-P), temperature, seasonality and source of precipitation, and mineral composition of carbonate fraction (Angert et al., 2008; Çağatay et al., 2014; Cole et al., 1999; Stevens et al., 2001). The stable carbon isotope values however, mainly depend on $\delta^{13}C$ value of the carbonate rocks in the watershed, organic productivity and water balance. The Sr isotopic composition ($^{87}Sr/^{86}Sr$) of autogenic carbonates in lake environments (*e.g.* mollusks, foraminifera and ostracod shell) is also widely used for

paleosalinity reconstructions of marine and lacustrine environments (Ingram and Sloan, 1992; Kemp et al., 2012; McCulloch et al., 1989; Reinhardt et al., 1998). A comparison between different paleohydrology proxies for the Urmia Lake sediment in a time frame ranging from 9,100 to 10,500 cal. y BP was made in comparison with downcore abundances of Al as the final product of incongruent weathering transported into the lake (Fig. 6-3 A-E). The variations in $\delta^{13}C$ and $\delta^{18}O$ values of shrimp fecal pellets somewhat mirror each other but no significant covariation is observed with Al abundances (Fig. 6-3 A, B and E). The Sr isotopic composition ($^{87}Sr/^{86}Sr$) of bulk sediment, shrimp fecal pellets and pore water do not demonstrate any meaningful trend (Fig. 6-3 C), indicating these proxies are apparently unaffected in Lake Urmia by environmental changes and source rock composition.

Variation in weathering indices as proxies for the supply of weathered material to marine and lacustrine environments have also been employed to study changes in hydrological regime of depositional basins (Harmon et al., 2016; Myers et al., 2014; Sheldon et al., 2002). A widely utilized weathering indices to estimates rainfall is CIA-K, which is similar to the chemical index of alteration (CIA) (Nesbitt and Young, 1989, 1982) minus potassium to account for the potential effect of illitization (Myers et al., 2014). The CIA-K is calculated based on molar values of oxides and expressed as follow:

$$CIA = 100\times[Al_2O_3 / (Al_2O_3+CaO^*+Na_2O)] \qquad \text{(eq. 6-1)}$$

where CaO* is CaO associated with the silicate fraction of the sample. An alternative CIA-K index was introduced by Myers et al. (2014) and is known as CALMAG, where Na_2O is substituted by MgO:

$$CALMAG = 100\times[Al_2O_3 / (Al_2O_3+CaO+MgO)] \quad \text{(eq. 6-2)}$$

In contrast to stable oxygen and carbon and radiogenic Sr isotopes, down core variation of weathering indices, CIA-K and CALMAG, covary closely with Al abundances, suggesting the potential link between chemical weathering and Al input to the lake (Fig. D and E).

Several studies have shown a correlation between the amount of rainfall and degree of weathering (Myers et al., 2014; Nordt and Driese, 2010; Sheldon et al., 2002), therefore the weathering indices can be used to estimate mean annual precipitation (MAP) using a variety of empirical equations. The MAP estimates based on CIA-K weathering index is widely used for soil types with various clay content (vertic and non-vertic soils) using equations 6-3 (Sheldon et al., 2002) and 6-4 (Nordt and Driese, 2010):

$$MAP\ (mm\ y^{-1}) = (14.3\times CIA\text{-}K) - 37.6\ ,\ R^2=0.73 \quad \text{(eq. 6-3)}$$

$$MAP\ (mm\ y^{-1}) = (18.64\times CIA\text{-}K) - 350.4,\ R^2=0.73 \quad \text{(eq. 6-4)}$$

Since the above empirical equation is subjected to local environmental setting such as clay content of the climosequence, range of MAP, vegetation coverage and topography of the study area, an attempt was made to develop a new MAP tailored for the Urmia Lake watershed area and precipitation range by comparing the 1951-2005 mean annual precipitation data recorded at Urmia synoptic station with down core variation of Al for the top 70 mm of the core U-6 (Fig. 6-4) based on extrapolation of the age model. The peak-matching between regional precipitation record and down core Al abundances suggests a significant correlation, which may indicate the potential link between moisture

availability and supply of weathered material to the lake. Based on these observations and by comparing four discrete analyses from the top 70 mm of the core with the Urmia's mean annual precipitation, a CIA-K - MAP correlation with R^2=0.83 was established for the Urmia Lake region (Fig. 6-5) and the equation 6-3 was modified as follow:

$$\text{MAP (mm y}^{-1}) = (3.7442 \times \text{CIA-K}) + 148.86 \quad , R^2=0.83 \qquad \text{(eq. 6-5)}$$

Admittedly, this calibration is based on small dataset and is subject to improvement as more data from the lake becomes available. To date, this represents the best available calibration. It is important to note that while using other calibrations will affect the absolute estimates of precipitation, the pattern change in precipitation rate should remain valid regardless of what calibration is used. The CIA-K index was calculated based on 68 samples (average resolution of ~185 yr) and was used to reconstruct the paleo-rainfall (MAP_{paleo}) for the Urmia Lake basin (solid black line in Fig. 6-6). As it can be seen in Fig. 6-6, regardless the offset in reconstructed absolute MAP_{paleo} values using equation 6-3 (upper limit) and equation 6-4 (lower limit), there is a good agreement between the mean precipitation patterns throughout the record. The equation 6-5 returned the minimum and maximum MAP_{paleo} estimates of 180 mm y^{-1} and 370 mm y^{-1} respectively. The average estimated rainfall for the Holocene shows a decreasing trend from early to late Holocene (Fig. 6-7 A) following the decline in summer solar insolation (Fig. 6-1 C), which is in good agreement with down core abundances of Al (Fig. 6-7 B) and other proxies for redox, aeolian input and riverine supply (Fig. 6-1). The observed trend in rainfall estimates is also in good agreement with the multi-proxy record from Neor Lake where Sharifi et al. (2015) reconstructed the Holocene moisture availability based on δD values of C_{28} *n*-alkanoic acid and variation in P_{aq} biomarker. This reduction in precipitation from the early to late

Holocene is also noted in Holocene record from Lake Van (Wick et al., 2003). A transition toward more arid conditions from early to late Holocene is also observed in records from the eastern Mediterranean Sea (Kaniewski et al., 2010; Migowski et al., 2006; B. Y. Schilman et al., 2001).

Down core abundances of Al (Fig. 6-7 B) from U-6 sediment core covary closely with the Holocene ice rafted debris (IRD) events from North Atlantic sediments (Bond et al., 1997) and intervals of reduced solar irradiance (Bond et al., 2001; Solanki et al., 2004). This suggests Urmia Lake watershed is highly sensitive to both internal and external climate forcings and further indicates the atmospheric teleconnection between the North Atlantic climate and the interior of West Asia during the present interglacial period. This teleconnection on millennial timescales during the last glacial period was previously observed between the North Atlantic, interior of West Asia and northern Indian Ocean (Altabet et al., 2002; Pourmand et al., 2007b, 2005; Schulz et al., 1998; Sharifi et al., 2015). Further support for such teleconnection between Urmia climate and that of the North Atlantic also comes from the time series study of modern climate data from NW Iran (Alizadeh-Choobari et al., 2016; Jalili et al., 2011; Zoljoodi and Didevarasl, 2014).

5- Conclusions

High resolution multi proxy reconstruction of climate and hydrological condition over Urmia Lake suggested several lake level fluctuations since the Early Holocene. More frequent low lake levels during the mid- and late Holocene are coincide with episodes of enhanced aeolian input and low riverine input to the lake. The agreement between paleoclimate proxies from Urmia lake, high-altitude peat from NW Iran and the Eastern

Mediterranean Sea records in one hand, and the correlation between Urmia Lake's record with the variation in the North Atlantic climate and changes in solar irradiance on the other suggest the sensitivity of the Urmia Lake environment to internal and external forcings which controls the climate of the northern hemisphere as well as an atmospheric teleconnection between the North Atlantic and the interior of West Asia during the last deglacial period.

Although the moisture availability has changed since the beginning of the Holocene, paleo-rainfall reconstruction for the Urmia Lake's watershed seems to have fluctuated within the range comparable to modern times. This suggests the contribution of natural climate cycles may have less influence on water availability to the lake than extensive anthropogenic activities over the last few decades.

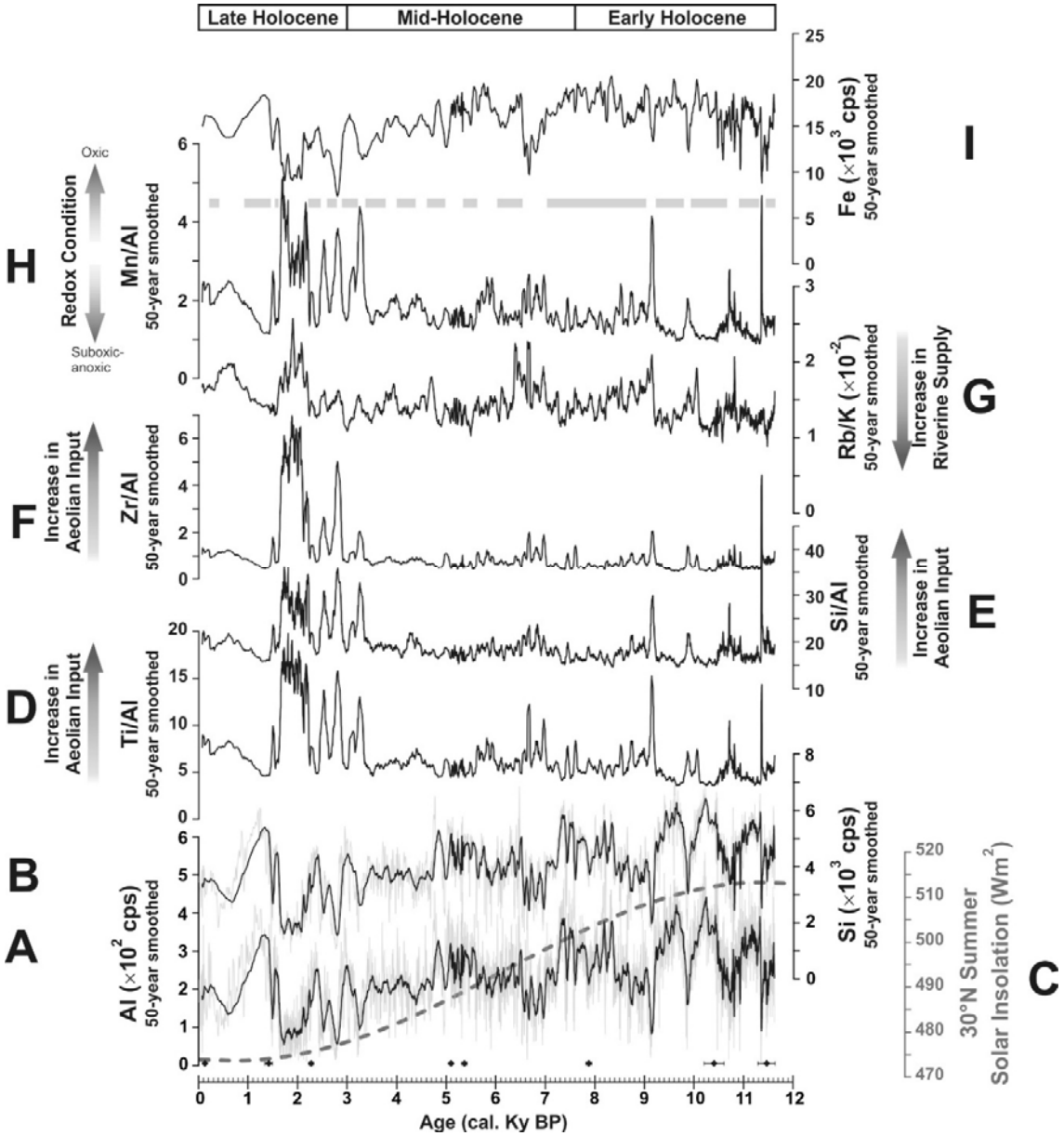

Fig. 6-1- Multi proxy sediment record in Urmia Lake from NW Iran. A and B) 50-years smoothed scanning XRF intensity profile for Al ($\times 10^2$cps) and Si ($\times 10^3$cps) respectively, original data are shown in grey, 8 radiocarbon dates (filled diamonds) and their associated uncertainties (2σ) are plotted along the age axis. C) Summer solar insolation (Wm^{-2}) at 30°N. D-F) Downcore profiles of the Al-normalized abundances of lithogenic (Ti, Si, Zr) elements used as aeolian input proxies. G) Rb/K ratio ($\times 10^{-2}$) as proxy for riverine input and weathering. H-I) Al-normalized abundances of Mn as well as downcore XRF intensity profile of Fe ($\times 10^3$cps) as paleoredox proxies. The thick gray lines denotes the periods of high lake level.

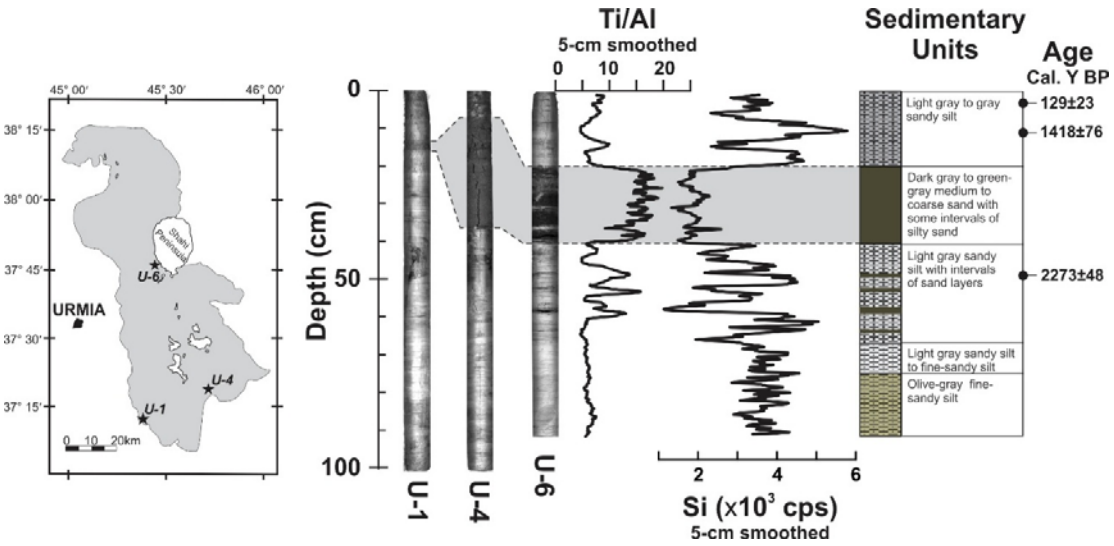

Fig. 6-2- Correlation of dark colored sand layer in top one meter of U-1, U-4 and U-6 sediment cores. Down-core variations of Ti/Al ratios and Si abundances (in count per second) along with sedimentary units and radiocarbon age controlling points for core U-6 are shown on the right.

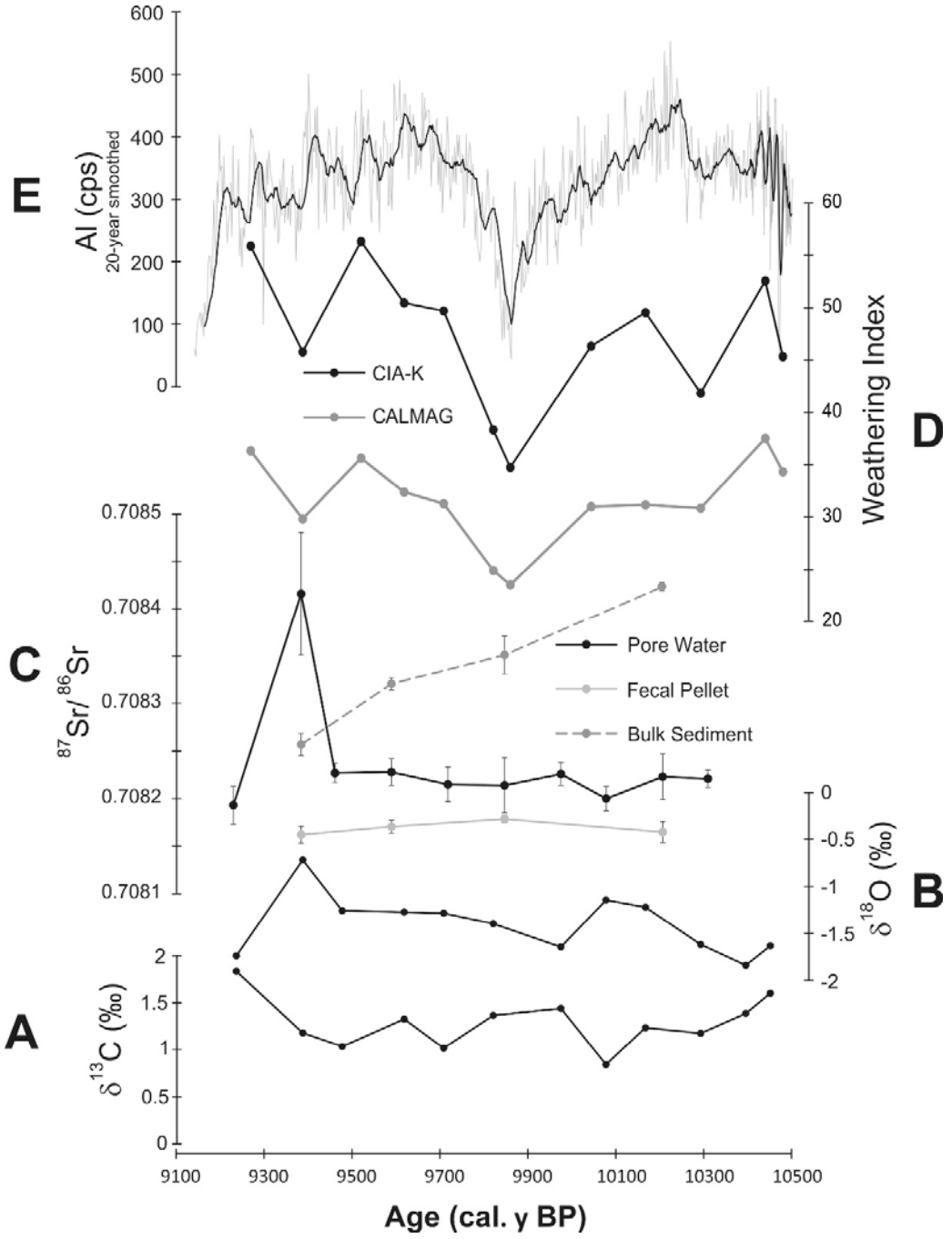

Fig. 6-3- Comparison between different paleohydrology proxies in the Urmia Lake sediments. A and B) $\delta^{13}C$ and $\delta^{18}O$ values of shrimp fecal pellets. C) Sr isotopic composition of bulk sediment (dashed line in grey), fecal pellet (light grey) and pore water (black). D) CALMAG (grey) and CIA-K (black) weathering indices calculated based on concentration of major elements in siliciclastic fraction of sediment, see text for detail. E) Downcore variation in Al abundances (cps) (light grey), the 20-year smoothed data is shown in black.

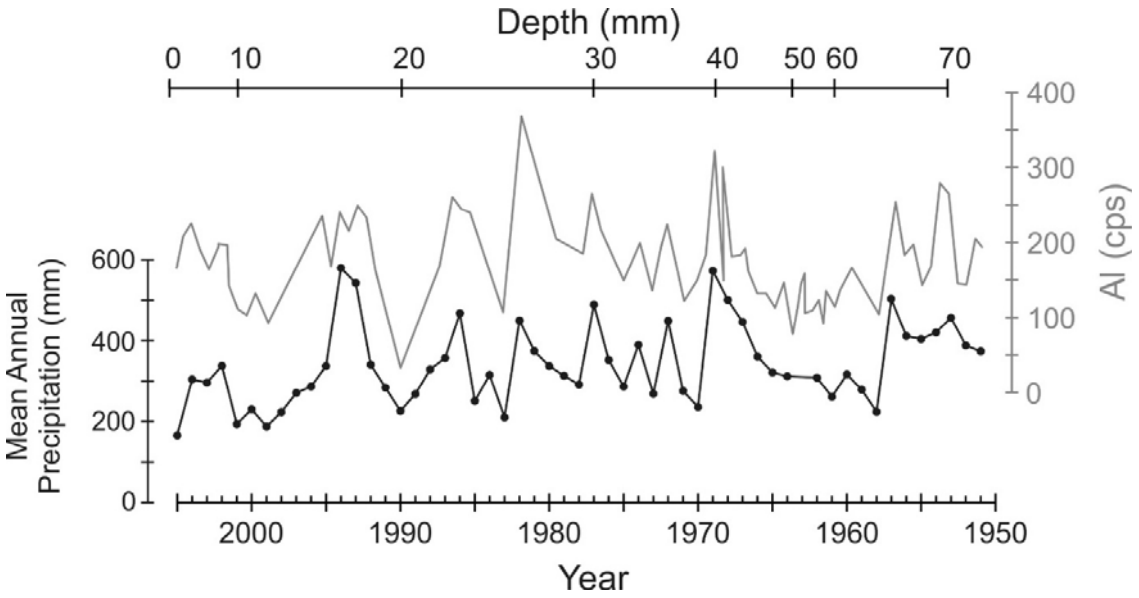

Fig. 6-4- Downcore variation of Al abundances (cps, grey line) with respect to mean annual precipitation (mm) recorded at Urmia synoptic station. Correlation was made by means of wiggle matching.

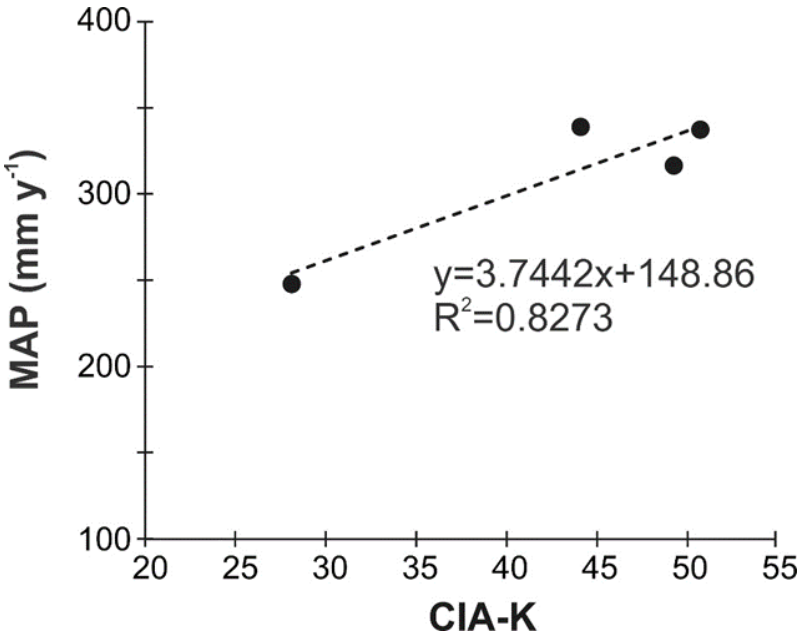

Fig. 6-5- Relationship between mean annual precipitation (MAP) and CIA-K in samples from Urmia Lake.

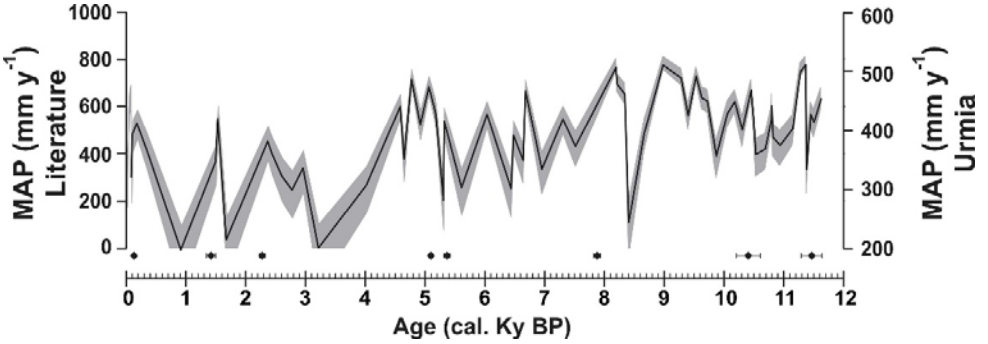

Fig. 6-6- Paleo-rainfall reconstruction based on CIA-K weathering index using different equations for mean annual precipitation (MAP). Solid black line shows MAP_{paleo} reconstruction based on 1951-2005 mean annual precipitation data recorded at Urmia synoptic station. The grey area denotes the MAP_{paleo} reconstruction based on equation suggested by Sheldon et al, 2002 (upper limit) and Nordt and Driese, 2010 (lower limit). Radiocarbon dates (filled diamonds) and their associated uncertainties (2σ) are plotted along the age axis.

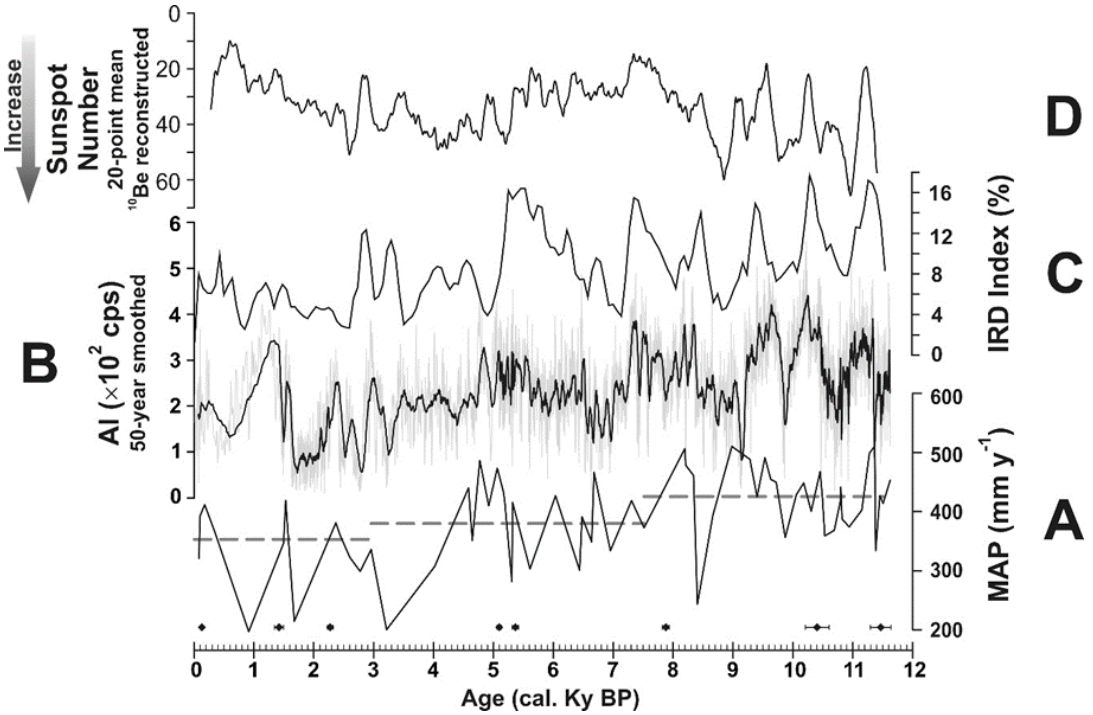

Fig. 6-7- Paleo-rainfall reconstruction over Urmia Lake's region. A) Mean annual precipitation estimates (mm y^{-1}) based on CIA-K weathering index, dashed gray lines denote the average estimated rainfall for the early, mid- and late Holocene. The age controlling tie points are the same as Fig. 6-1 A. B) 50-years smoothed scanning XRF intensity profile for Al (×10^2cps), same as Fig. 6-1 A. C) North Atlantic Holocene Ice Rafted Debris (IRD) events (Bond et al., 2001, 1997). D) 11 Ka reconstruction of sunspot numbers based on ^{10}Be, note the vertical axis is in reverse order (Solanki et al., 2004).

CHAPTER 7

Epilogue; Holocene climate variability over interior of West Asia based on terrestrial records from Iran

West Asia, which extends from Iran and the Arabian Peninsula to eastern Mediterranean Sea, is one of the most climatically dynamic regions in the northern hemisphere. The interactions between the mid-latitude Westerlies, the Siberian Anticyclone (SA) and the Indian Ocean Summer Monsoon (IOSM) control precipitation and atmospheric dust content across West Asia. There is mounting evidence that rise and fall of some of the earliest human societies in the "Fertile Crescent" may be related to periods of abrupt climate change during the Holocene. Nevertheless, high-resolution records of climate variability are scarce from this region and the existing archives are, in part, contradictory. In this dissertation, over 13,000 years of paleoclimate change, as recorded in the sediment records of Neor and Urmia Lakes in NW Iran, were examined for the occurrence and patterns of suborbital scale variability. Neor and Urmia Lakes are 280 kilometer apart and providing two different morpho-hydro-geological settings. Neor is high altitude (~2500 m.a.sl.) lake sitting on andesitic basement with 4500 km^2 watershed area and no riverine input, which has fostered a peripheral peat mire. In contrast, Urmia Lake, at the approximate elevation of 1275 m.a.s.l., is the largest hypersaline lake in Middle East with the average catchment area of 52000 km^2 and diverse geological setting. Water supply to the lake is provided by 13 perennial and seasonal tributaries which are passing through various geological units with different ages.

Multi-proxy reconstruction of climate variability and hydrology of the region based on peat core from the Neor Lake as well as sediment core from the Lake Urmia have provided the first sets of high-resolution paleoclimate record for the West Asia with robust chronology. The high resolution nature of these records as well as rich historical background of the study area provided a unique opportunity to investigate the impact of

climate variability on early civilizations over the Iranian Plateau and Mesopotamia. The novel approach of geochemical fingerprinting of paleo-dust using Sr-Nd-Hf radiogenic isotopes pair with climate simulations resulted in better understanding of atmospheric circulation over the interior of West Asia during the Holocene. Paleo-hydrology reconstructions over the Urmia Lake's watershed area has provided an insight about the effect of anthropogenic activities on the water availability in the region. The results of the current study has led us to the following conclusions:

1-Climate variability since last deglaciation

Transition from glacial to inter-glacial period over the interior of the West Asia is marked by abrupt shift from dry and dusty condition during the late glacial termination to wetter condition with lower dust fluxes and higher lake levels during the early Holocene. Low lake levels and drier conditions with frequent aeolian input to the study area prevailed during mid-late Holocene. These observations are consistent with the records from Eastern Mediterranean and North Africa.

2-Changes in atmospheric circulation as told by shift in dust sources

Geochemical fingerprinting of paleo-dust revealed a shift in Sr-Nd-Hf as well as in rare earth elements values from the Younger Dryas to the early Holocene and from the early Holocene to the mid-late Holocene suggesting changes in dust source(s) during these time periods. The shift in dust sources are consistent with the polar/equatorial shift in the position of the Northern Hemisphere Summer Westerly Jet axis during the early Holocene/mid-late Holocene following the solar insulation curve. Climate simulations revealed that lower dust emission during the early Holocene coincided with higher

moisture availability and high vegetation coverage over the North Africa and the Middle East resulted in contribution of potential sources in Mesopotamian and Central Asia. Equatorial migration of the Northern Hemisphere Summer Westerly Jet axis during the mid-late Holocene coincide with higher dust fluxes from potential sources in NE Africa and the Middle East.

3-Climate forcings

Wavelet analysis of aeolian input to Neor Lake as well as covariation of Urmia Lake's multi-proxy record with changes in solar irradiance suggest that water availability and aeolian input to the studied region may have been controlled by variation in solar insolation (and possibly irradiance) as an external forcing. The multi-proxy records from NW Iran also suggest an atmospheric teleconnection between North Atlantic climate and West Asia during the last deglacial termination and the Holocene.

4-Climate impact on human societies

High-resolution multi-proxy record from Neor Lake indicates that, since 5000 B.P., nearly all power transitions in the Eastern Mediterranean, Mesopotamia and Iran as well as periods of prolonged drought and famine occurred during the episodes of enhanced aeolian input to the region. This observation may suggest that the ancient human societies from West Asia were highly susceptible to the abrupt climate change.

5-Detecting anthropogenic activities using paleoclimate reconstructions

Paleoclimate and paleohydrology reconstructions for the Urmia Lake suggested several episodes of high and low lake levels since 11,600 years PB. Sedimentological

facieses as well as geochemical data reveal that although the Urmia Lake had many fluctuations since the beginning of the Holocene era, but never experienced its current status. The paleo-rainfall reconstructions for the past 11,600 years, when there was almost no anthropogenic activities in the watershed area, suggest that the Urmia Lake has maintained its ecological balance with a minimum of 180 mm mean annual precipitation. The modern meteorological data indicates that the 55-year mean annual precipitation recorded for the Urmia Lake is 340 mm, almost a factor of two higher. If there is a revival plan for the Urmia Lake, the amount of renewable water produced in the watershed area by 180 mm y^{-1} precipitation should be considered as the minimum requirement for water inflow to the lake.

REFERENCES

Abbaspour, K.C., Faramarzi, M., Ghasemi, S.S., Yang, H., 2009. Assessing the impact of climate change on water resources in Iran. Water Resour. Res. 45, 1–16. doi:10.1029/2008WR007615

Abbaspour, M., Javid, a. H., Mirbagheri, S. a., Givi, F.A., Moghimi, P., 2012. Investigation of lake drying attributed to climate change. Int. J. Environ. Sci. Technol. 9, 257–266. doi:10.1007/s13762-012-0031-0

Abdi, K., 2011. The Iranian plateau From paleolithic times To the rise of the Achaemenid empire, in: Daryaee, T. (Ed.), The Oxford Handbook of Iranian History. Oxford University Press Inc., p. 400.

Abouchami, W., Näthe, K., Kumar, A., Galer, S.J.G., Jochum, K.P., Williams, E., Horbe, A.M.C., Rosa, J.W.C., Balsam, W., Adams, D., Mezger, K., Andreae, M.O., 2013. Geochemical and isotopic characterization of the bodélé depression dust source and implications for transatlantic dust transport to the Amazon basin. Earth Planet. Sci. Lett. 380, 112–123. doi:10.1016/j.epsl.2013.08.028

Abreu, J.A., Beer, J., Ferriz-Mas, A., 2010. Past and Future Solar Activity from Cosmogenic Radionuclides. SOHO-23 Work. Underst. a Peculiar Sol. Minim. 428, 287–295.

Adams, R.S., Bustin, R.M., 2001. The effects of surface area, grain size and mineralogy on organic matter sedimentation and preservation across the modern Squamish Delta, Bristish Columbia: The potential role of sediment surface area in the formation of petroleum source rocks. Int. J. Coal Geol. 46, 93–112. doi:10.1016/S0166-5162(01)00019-2

Adhikari, D.P., 2011. Paleolimnology of Lake Yamanaka as reflected on particle-size distribution. Bull. Dep. Geol. 14, 35–42.

AghaKouchak, A., Norouzi, H., Madani, K., Mirchi, A., Azarderakhsh, M., Nazemi, A., Nasrollahi, N., Farahmand, A., Mehran, A., Hasanzadeh, E., 2015. Aral Sea syndrome desiccates Lake Urmia: Call for action. J. Great Lakes Res. 41, 307–311. doi:10.1016/j.jglr.2014.12.007

Aguado, E., Burt, J.E., 2012. Understanding Weather and Climate, 6th ed. Prentice Hall.

Ahmadi, R., Mohebbi, F., Hagigi, P., Esmailly, L., Salmanzadeh, R., 2011. Macro-invertebrates in the wetlands of the Zarrineh estuary at the south of urmia lake (Iran). Int. J. Environ. Res. 5, 1047–1052.

Akagi, T., Fu, F.F., Yabuki, S., 2002. Absence of Ce anomaly in the REE patterns of peat moss and peat grass in the Ozegahara peatland. Geochem. J. 36, 113–118. doi:10.2343/geochemj.36.113

Albani, S., Mahowald, N.M., Perry, A.T., Scanza, R.A., Heavens, N.G., Zender, C.S., Maggi, V., Kok, J.F., Otto-Bliesner, B.L., 2014. Improved dust representation in the Community Atmosphere Model. J. Adv. Model. Earth Syst. 6, 541–570. doi:10.1002/2013MS000279

Albani, S., Mahowald, N.M., Winckler, G., Anderson, R.F., Bradtmiller, L.I., Delmonte, B., François, R., Goman, M., Heavens, N.G., Hesse, P.P., Hovan, S. a., Kang, S.G., Kohfeld, K.E., Lu, H., Maggi, V., Mason, J. a., Mayewski, P. a., McGee, D., Miao, X., Otto-Bliesner, B.L., Perry, a. T., Pourmand, a., Roberts, H.M., Rosenbloom, N., Stevens, T., Sun, J., 2015. Twelve thousand years of dust: the Holocene global dust cycle constrained by natural archives. Clim. Past 11, 869–903. doi:10.5194/cp-11-869-2015

Algeo, T.J., Maynard, J.B., 2004. Trace-element behavior and redox facies in core shales of Upper Pennsylvanian Kansas-type cyclothems. Chem. Geol. 206, 289–318. doi:10.1016/j.chemgeo.2003.12.009

Alijani, B., 2002. Variations of 500 hPa flow patterns over Iran and surrounding areas and their relationship with the climate of Iran. Theor. Appl. Climatol. 72, 41–54.

Alijani, B., Harman, J., 1985. Synoptic climatology of precipitation in Iran. Ann. Assoc. Am. Geogr. 75, 404–416.

Alizadeh-Choobari, O., Ahmadi-Givi, F., Mirzaei, N., Owlad, E., 2016. Climate change and anthropogenic impacts on the rapid shrinkage of Lake Urmia. Int. J. Climatol. n/a-n/a. doi:10.1002/joc.4630

Altabet, M. a, Higginson, M.J., Murray, D.W., 2002. The effect of millennial-scale changes in Arabian Sea denitrification on atmospheric CO2. Nature 415, 159–162. doi:10.1038/415159a

Andersson, R.A., Meyers, P., Hornibrook, E., Kuhry, P., Mörth, C.-M., 2012. Elemental and isotopic carbon and nitrogen records of organic matter accumulation in a Holocene permafrost peat sequence in the East European Russian Arctic. J. Quat. Sci. 27, 545–552. doi:10.1002/jqs.2541

Angert, A., Lee, J.E., Yakir, D., 2008. Seasonal variations in the isotopic composition of near-surface water vapour in the eastern Mediterranean. Tellus, Ser. B Chem. Phys. Meteorol. 60, 674–684. doi:10.1111/j.1600-0889.2008.00357.x

Arimoto, R., 2001. Eolian dust and climate: relationships to sources, tropospheric chemistry, transport and deposition. Earth-Science Rev. 54, 29–42. doi:10.1016/S0012-8252(01)00040-X

ARMC-Azarbaidjan Regional Mining Cooperation, 1995. Hydrochemistry of Urmia Lake.

Arnaud, F., Révillon, S., Debret, M., Revel, M., Chapron, E., Jacob, J., Giguet-Covex, C., Poulenard, J., Magny, M., 2012. Lake Bourget regional erosion patterns reconstruction reveals Holocene NW European Alps soil evolution and paleohydrology. Quat. Sci. Rev. 51, 81–92. doi:10.1016/j.quascirev.2012.07.025

Aubert, C., 2013. Changements environnementaux et climatiques en Iran à la transition Tardiglaciaire/Holocène: apport des assemblages fossiles de Chironomideae (Insectes, Diptères) de la séquence lacustre de Neor au nord-ouest de l'Iran (altitude 2480 m). Institut Méditerranéen de Biodiversité et d'Ecologie.

Aubert, D., Le Roux, G., Krachler, M., Cheburkin, A., Kober, B., Shotyk, W., Stille, P., 2006. Origin and fluxes of atmospheric REE entering an ombrotrophic peat bog in Black Forest (SW Germany): Evidence from snow, lichens and mosses. Geochim. Cosmochim. Acta 70, 2815–2826. doi:10.1016/j.gca.2006.02.020

Bąbel, M., Schreiber, B.C., 2013. Geochemistry of Evaporites and Evolution of Seawater, Treatise on Geochemistry: Second Edition. doi:10.1016/B978-0-08-095975-7.00718-X

Babu, C.A., Samah, A.A., Varikoden, H., 2011. Rainfall Climatology over Middle East Region and its Variability. Int. J. Water Resour. Arid Environ. 1, 180–192.

Bao, K., Xing, W., Yu, X., Zhao, H., McLaughlin, N., Lu, X., Wang, G., 2012. Recent atmospheric dust deposition in an ombrotrophic peat bog in Great Hinggan Mountain, Northeast China. Sci. Total Environ. 431, 33–45. doi:10.1016/j.scitotenv.2012.05.014

Bar-Matthews, M., Ayalon, a., 2011. Mid-Holocene climate variations revealed by high-resolution speleothem records from Soreq Cave, Israel and their correlation with cultural changes. The Holocene 21, 163–171. doi:10.1177/0959683610384165

Barber, K.E., Langdon, P.G., 2007. What drives the peat-based palaeoclimate record? A critical test using multi-proxy climate records from northern Britain. Quat. Sci. Rev. 26, 3318–3327. doi:10.1016/j.quascirev.2007.09.011

Bayon, G., Burton, K.W., Soulet, G., Vigier, N., Dennielou, B., Etoubleau, J., Ponzevera, E., German, C.R., Nesbitt, R.W., 2009. Hf and Nd isotopes in marine sediments: Constraints on global silicate weathering. Earth Planet. Sci. Lett. 277, 318–326. doi:10.1016/j.epsl.2008.10.028

Bengtsson, L., Hodges, K.I., Roeckner, E., 2006. Storm tracks and climate change. J. Clim. 19, 3518–3543. doi:10.1175/JCLI3815.1

Berberian, M., Arshadi, S., 1976. On the evidence of the youngest activity of the North Tabriz Fault and the seismicity of Tabriz city, Contribution to the seismotectonics of Iran (Part II).

Berke, M. a., Johnson, T.C., Werne, J.P., Grice, K., Schouten, S., Sinninghe Damsté, J.S., 2012. Molecular records of climate variability and vegetation response since the Late Pleistocene in the Lake Victoria basin, East Africa. Quat. Sci. Rev. 55, 59–74. doi:10.1016/j.quascirev.2012.08.014

Biscaye, P.E., Grousset, F.E., Revel, M., Van der Gaast, S., Zielinski, G. a., Vaars, a., Kukla, G., 1997. Asian provenance of glacial dust (stage 2) in the Greenland Ice Sheet Project 2 Ice Core, Summit, Greenland. J. Geophys. Res. 102, 26765. doi:10.1029/97JC01249

Bitz, C.M., Shell, K.M., Gent, P.R., Bailey, D.A., Danabasoglu, G., Armour, K.C., Holland, M.M., Kiehl, J.T., 2012. Climate sensitivity of the community climate system model, version 4. J. Clim. 25, 3053–3070. doi:10.1175/JCLI-D-11-00290.1

Black, E., 2009. The impact of climate change on daily precipitation statistics in Jordan and Israel. Atmos. Sci. Lett. 10, 192–200. doi:10.1002/asl.233

Black, E., Brayshaw, D.J., Rambeau, C.M.C., 2010. Past, present and future precipitation in the Middle East: insights from models and observations. Philos. Trans. A. Math. Phys. Eng. Sci. 368, 5173–5184. doi:10.1098/rsta.2010.0199

Bobek, H., 1963. Nature and implications of Quaternary climatic changes in Iran. Chang. Clim. 20, 403–413.

Boelter, D.H., 1966. Important Physical Properties of Peat Materials, in: Proceeding of the Third International Peat Congress. Quebec, pp. 150–154.

Bond, G., Kromer, B., Beer, J., Muscheler, R., Evans, M.N., Showers, W., Hoffmann, S., Lotti-Bond, R., Hajdas, I., Bonani, G., 2001. Persistent solar influence on North Atlantic climate during the Holocene. Science 294, 2130–6. doi:10.1126/science.1065680

Bond, G., Showers, W., Cheseby, M., Lotti, R., Almasi, P., Priore, P., Cullen, H., Hajdas, I., Bonani, G., 1997. A pervasive millennial-scale cycle in north atlantic holocene and glacial climates. Science (80-.). 278, 1257–1266.

Borg, L.E., Banner, J.L., 1996. Neodymium and strontium isotopic constraints on soil surfaces in Barbados, West Indies. Geochim. Cosmochim. Acta 60, 4193–4206.

Bottema, S., 1986. A late quaternary pollen diagram from Lake Urmia (Northwestern Iran). Rev. Palaeobot. Palynol. 47, 241–261. doi:10.1016/0034-6667(86)90039-4

Bourbonniere, R. a., Meyers, P. a., 1996. Sedimentary geolipid records of historical changes in the watersheds and productivities of Lakes Ontario and Erie. Limnol. Oceanogr. 41, 352–359. doi:10.4319/lo.1996.41.2.0352

Bouvier, A., Vervoort, J.D., Patchett, P.J., 2008. The Lu-Hf and Sm-Nd isotopic composition of CHUR: Constraints from unequilibrated chondrites and implications for the bulk composition of terrestrial planets. Earth Planet. Sci. Lett. 273, 48–57. doi:10.1016/j.epsl.2008.06.010

Braconnot, P., Otto-Bliesner, B., Harrison, S., Joussaume, S., Peterchmitt, J.-Y., Abe-Ouchi, a., Crucifix, M., Driesschaert, E., Fichefet, T., Hewitt, C.D., Kageyama, M., Kitoh, a., Loutre, M.-F., Marti, O., Merkel, U., Ramstein, G., Valdes, P., Weber, L., Yu, Y., Zhao, Y., 2007. Results of PMIP2 coupled simulations of the Mid-Holocene and Last Glacial Maximum – Part 2: feedbacks with emphasis on the location of the ITCZ and mid- and high latitudes heat budget. Clim. Past 3, 279–296. doi:10.5194/cp-3-279-2007

Brayshaw, D.J., Hoskins, B., Black, E., 2010. Some physical drivers of changes in the winter storm tracks over the North Atlantic and Mediterranean during the Holocene. Philos. Trans. A. Math. Phys. Eng. Sci. 368, 5185–5223. doi:10.1098/rsta.2010.0180

Brooks, N., 2006. Cultural responses to aridity in the Middle Holocene and increased social complexity. Quat. Int. 151, 29–49. doi:10.1016/j.quaint.2006.01.013

Brown, E.T., 2011. Lake Malawi's response to "megadrought" terminations : Sedimentary records of fl ooding , weathering and erosion. Palaeogeogr. Palaeoclimatol. Palaeoecol. 303, 120–125. doi:10.1016/j.palaeo.2010.01.038

Buurman, P., van Lagen, B., Velthorst, E.J. (Eds.), 1996. Manual for soil and water analysis. Backhuys Publishers, Leiden, The Netherlands.

Çağatay, M.N., Öğretmen, N., Damci, E., Stockhecke, M., Sancar, Eriş, K.K., Özeren, S., 2014. Lake level and climate records of the last 90ka from the Northern Basin of Lake Van, eastern Turkey. Quat. Sci. Rev. 104, 97–116. doi:10.1016/j.quascirev.2014.09.027

Calvert, S.E., Pedersen, T.F., 1993. Geochemistry of Recent oxic and anoxic marine sediments: Implications for the geological record. Mar. Geol. 113, 67–88. doi:10.1016/0025-3227(93)90150-T

Calvert, S.E., Pedersen, T.F., 2007. Elemental proxies for palaeoclimatic and palaeoceanographic variability in marine sediments: interpretation and application, in: Hillaire-Marcel, C., Vernal, A.D. (Eds.), Proxies in Late Cenozoic Paleoceanography. Elsevie, Amsterdam, pp. 567–644. doi:http://dx.doi.org/10.1016/S1572-5480(07)01019-6

Castañeda, I.S., Mulitza, S., Schefuss, E., dos Santos, R.A.L., Damste, J.S.S., Schouten, S., 2009. Wet phases in the Sahara/Sahel region and human migration patterns in North Africa. Proc. Natl. Acad. Sci. U. S. A. 106, 20159–20163. doi:Doi 10.1073/Pnas.0905771106

Chambers, F.M., Beilman, D.W., Yu, Z., 2011. Methods for determining peat humification and for quantifying peat bulk density , organic matter and carbon content for palaeostudies of climate and peatland carbon dynamics. Mires and Peats 7, 1–10.

Chambers, F.M., Charman, D.J., 2004. Holocene environmental change: contributions from the peatland archive. The Holocene 14, 1–6. doi:10.1191/0959683604hl684ed

Chen, J., Li, G., Yang, J., Rao, W., Lu, H., Balsam, W., Sun, Y., Ji, J., 2007. Nd and Sr isotopic characteristics of Chinese deserts: Implications for the provenances of Asian dust. Geochim. Cosmochim. Acta 71, 3904–3914. doi:10.1016/j.gca.2007.04.033

Chen, Z., Li, G., 2013. Evolving sources of eolian detritus on the Chinese Loess Plateau since early Miocene : Tectonic and climatic controls. Earth Planet. Sci. Lett. 371–372, 220–225. doi:10.1016/j.epsl.2013.03.044

Chiang, J.C.H., Fung, I.Y., Wu, C.H., Cai, Y., Edman, J.P., Liu, Y., Day, J.A., Bhattacharya, T., Mondal, Y., Labrousse, C.A., 2015. Role of seasonal transitions and westerly jets in East Asian paleoclimate. Quat. Sci. Rev. 108, 111–129. doi:10.1016/j.quascirev.2014.11.009

Childe, V.G., 1950. The Urban Revolution. Town Plan. Rev. 21, 3–17.

Choobari, O.A., Zawar-Reza, P., Sturman, a., 2014. The global distribution of mineral dust and its impacts on the climate system: A review. Atmos. Res. 138, 152–165. doi:10.1016/j.atmosres.2013.11.007

Clemens, S., Prell, W., Murray, D., Shimmield, G., Weedon, G., 1991. Forcing mechanisms of the Indian Ocean monsoon. Nature 353, 720–725. doi:10.1038/353720a0

Cohen, A.S., 2004. Paleolimnology: The History and Evolution of Lake Systems, Palaios. doi:10.1669/0883-1351(2004)019<0184:BR>2.0.CO;2

Cohen, A.S., Palacios-fest, M.R., Negrini, R.M., Wigand, P.E., Erbes, D.B., 2000. A paleoclimate record for the past 250 , 000 years from Summer Lake , Oregon , USA : II . Sedimentology , paleontology and geochemistry. J. Paleolimnol. 24, 151–182.

Cole, J.E., Rind, D., Webb, R.S., Jouzel, J., Healy, R., 1999. Climatic controls on interannual variability of precipitation δ 18 O: Simulated influence of temperature, precipitation amount, and vapor source region. J. Geophys. Res. 104, 14223–14235. doi:10.1029/1999JD900182

Connor, S.E., Kvavadze, E. V, 2008. Modelling late Quaternary changes in plant distribution , vegetation and climate using pollen data from Georgia , Caucasus. J. Biogeogr. 36, 529–545. doi:10.1111/j.1365-2699.2008.02019.x

Cooper, G.R.J., Cowan, D.R., 2008. Comparing time series using wavelet-based semblance analysis. Comput. Geosci. 34, 95–102. doi:10.1016/j.cageo.2007.03.009

Costa, K., Russell, J., Konecky, B., Lamb, H., 2014. Isotopic reconstruction of the African Humid Period and Congo Air Boundary migration at Lake Tana, Ethiopia. Quat. Sci. Rev. 83, 58–67. doi:10.1016/j.quascirev.2013.10.031

Cullen, H.M., 2000. North Atlantic influence on Tigris – Euphrates. Int. J. Climatol. 20, 853–863.

Cullen, H.M., deMenocal, P.B., Hemming, S., Hemming, G., Brown, F.H., Guilderson, T., Sirocko, F., 2000. Climate change and the collapse of the Akkadian empire: Evidence from the deep sea. Geology 28, 379. doi:10.1130/0091-7613(2000)28<379:CCATCO>2.0.CO;2

Cullen, M.H., Kaplan, A., Arkin, P.A., Demenocal, P.B., 2002. Impact of the North Atlantic oscillation on Middle Eastern climate and streamflow. Clim. Chang. 55, 315–338.

D'Haen, K., Verstraeten, G., Degryse, P., 2012. Fingerprinting historical fluvial sediment fluxes. Prog. Phys. Geogr. 36, 154–186. doi:10.1177/0309133311432581

Daryaee, T., 2011. The Oxford Handbook of Iranian History, 1st ed. Oxford University Press Inc., New York.

Das, B.K., AL-Mikhlafi, a. S., Kaur, P., 2006. Geochemistry of Mansar Lake sediments, Jammu, India: Implication for source-area weathering, provenance, and tectonic setting. J. Asian Earth Sci. 26, 649–668. doi:10.1016/j.jseaes.2005.01.005

Das, B.K., Haake, B.-G., 2003. Geochemistry of Rewalsar Lake sediment , Lesser Himalaya , India : implications for source-area weathering , provenance and tectonic setting. Geosci. J. 7, 299–312.

Degens, E.T., Wong, H.K., Kempe, S., Kurtman, F., 1984. A geological study of lake van, Eastern Turkey. Geol. Rundschau 73, 701–734. doi:10.1007/BF01824978

Delju, a. H., Ceylan, A., Piguet, E., Rebetez, M., 2013. Observed climate variability and change in Urmia Lake Basin, Iran. Theor. Appl. Climatol. 111, 285–296. doi:10.1007/s00704-012-0651-9

deMenocal, P., Ortiz, J., Guilderson, T., Adkins, J., Sarnthein, M., Baker, L., Yarusinsky, M., 2000. Abrupt onset and termination of the African Humid Period : rapid climate responses to gradual insolation forcing. Quat. Sci. Rev. 19, 347–361.

deMenocal, P.B., 2001. Cultural responses to climate change during the late holocene. Science (80-.). 292, 667–673. doi:10.1126/science.1059287

deMenocal, P.B., Tierney, J.E., 2012. Green Sahara: African Humid Periods Paced by Earth's Orbital Changes. Nat. Educ. Knowl. 3, 12.

Diester-Haass, L., 1973. Holocene climate in the Persian Gulf as deduced from grain-size and pteropod distribution. Mar. Geol. 14, 207–223. doi:10.1016/0025-3227(73)90029-7

Djamali, M., Akhani, H., Andrieu-Ponel, V., Braconnot, P., Brewer, S., de Beaulieu, J.-L., Fleitmann, D., Fleury, J., Gasse, F., Guibal, F., Jackson, S.T., Lezine, a.-M., Medail, F., Ponel, P., Roberts, N., Stevens, L., 2010. Indian Summer Monsoon variations could have affected the early-Holocene woodland expansion in the Near East. The Holocene 20, 813–820. doi:10.1177/0959683610362813

Djamali, M., Beaulieu, J.-L., Miller, N.F., Andrieu-Ponel, V., Ponel, P., Lak, R., Sadeddin, N., Akhani, H., Fazeli, H., 2009a. Vegetation history of the SE section of the Zagros Mountains during the last five millennia; a pollen record from the Maharlou Lake, Fars Province, Iran. Veg. Hist. Archaeobot. 18, 123–136. doi:10.1007/s00334-008-0178-2

Djamali, M., de Beaulieu, J.-L., Andrieu-Ponel, V., Berberian, M., Miller, N.F., Gandouin, E., Lahijani, H., Shah-Hosseini, M., Ponel, P., Salimian, M., Guiter, F., 2009b. A late Holocene pollen record from Lake Almalou in NW Iran: evidence for changing land-use in relation to some historical events during the last 3700 years. J. Archaeol. Sci. 36, 1364–1375. doi:10.1016/j.jas.2009.01.022

Djamali, M., de Beaulieu, J.-L., Shah-hosseini, M., Andrieu-Ponel, V., Ponel, P., Amini, A., Akhani, H., Leroy, S. a. G., Stevens, L., Lahijani, H., Brewer, S., 2008. A late Pleistocene long pollen record from Lake Urmia, NW Iran. Quat. Res. 69, 413–420. doi:10.1016/j.yqres.2008.03.004

Djamali, M., Ponel, P., Delille, T., Thiery, A., Asem, A., Andrieu-Ponel, V., de Beaulieu, J.-L., Lahijani, H., Shah-Hosseini, M., Amini, A., Stevens, L., 2010. A 200,000-year record of the brine shrimp Artemia (Crustacea: Anostraca) remains in Lake Urmia, NW Iran. Int. J. Aquat. Sci. 1, 14–18.

DOE, 2009. Urmia Lake Integrated Management Plan. Tehran.

Eastwood, W.J., Leng, M.J., Roberts, N., Davis, B., 2007. Holocene climate change in the eastern Mediterranean region : a comparison of stable isotope and pollen data from Lake Go southwest Turkey. J. Quarternary Sci. 22, 327–341. doi:10.1002/jqs

Eastwood, W.J., Roberts, N., Lamb, H.F., Tibby, J.C., 1999. Holocene environmental change in southwest Turkey: A palaeoecological record of lake and catchment-related changes. Quat. Sci. Rev. 18, 671–695. doi:10.1016/S0277-3791(98)00104-8

Eglinton, T.I., Eglinton, G., 2008. Molecular proxies for paleoclimatology. Earth Planet. Sci. Lett. 275, 1–16. doi:10.1016/j.epsl.2008.07.012

Eimanifar, A., Mohebbi, F., 2007. Urmia Lake (Northwest Iran): a brief review. Saline Systems 3, 5. doi:10.1186/1746-1448-3-5

Eiss, D.O.W., Hotyk, W.I.S., Ieley, J.A.C.K.R., Age, S.U.P., Loor, M.A.G., Eese, S.T.R., 2002. The geochemistry of major and selected trace elements in a forested peat bog , Kalimantan , SE Asia , and its implications for past atmospheric dust deposition. Geochim. Cosmochim. Acta 66, 2307–2323.

El-Moslimany, P., 1982. The late Quaternary vegetational history of the Zagros and Taurus Mountains in the regions of Lake Mirabad, Lake Zeribar, and Lake Van -a reappraisal., in: Bintliff, J.L., Zeist, W. Van (Eds.), Palaeoclimates, Palaeoenvironments and Human Communities in the Eastern Mediterranean Region in Later Prehistory. Part Ii. British Archaeological Reports,Oxford, pp. 275–540.

Esmeijer-Liu, A.J., Kürschner, W.M., Lotter, A.F., Verhoeven, J.T. a, Goslar, T., 2012. Stable carbon and nitrogen isotopes in a peat profile are influenced by early stage diagenesis and changes in atmospheric CO_2 and N deposition. Water. Air. Soil Pollut. 223, 2007–2022. doi:10.1007/s11270-011-1001-8

Eugster, H.P., Jones, B.F., 1979. Behavior of major solutes during closed basin- lakes brine evolution. Am. J. Sci. doi:10.2475/ajs.279.6.609

Evans, H.B., 1965. GRAPE - A device for continuous determination of material density and porosity. Trans. 6th Annu. SPWLA Logging Symp. II, B:1-25.

Evans, J.P., 2009. 21st century climate change in the Middle East. Clim. Change 92, 417–432. doi:10.1007/s10584-008-9438-5

Evans, J.P., 2010. Global warming impact on the dominant precipitation processes in the Middle East. Theor. Appl. Climatol. 99, 389–402. doi:10.1007/s00704-009-0151-8

Evans, J.P., Smith, R.B., 2006. Water Vapor Transport and the Production of Precipitation in the Eastern Fertile Crescent. J. Hydrometeorol. 7, 1295–1307. doi:10.1175/JHM550.1

Evans, J.P., Smith, R.B., Oglesby, R.J., 2004. Middle East climate simulation and dominant precipitation processes. Int. J. Climatol. 24, 1671–1694. doi:10.1002/joc.1084

Feng, J.L., Zhu, L.P., X.L., Z., Hu, Z.G., 2009. Grain size effect on Sr and Nd isotopic compositions in eolian dust : Geochem. J. 43, 123–131.

Ficken, K.J., Li, B., Swain, D.L., Eglinton, G., 2000. An n -alkane proxy for the sedimentary input of submerged / ¯ oating freshwater aquatic macrophytes. Org. Geochem. 31, 745–749.

Fleitmann, D., Burns, S.J., Mangini, A., Mudelsee, M., Kramers, J., Villa, I., Neff, U., Al-Subbary, A. a., Buettner, A., Hippler, D., Matter, A., 2007. Holocene ITCZ and Indian monsoon dynamics recorded in stalagmites from Oman and Yemen (Socotra). Quat. Sci. Rev. 26, 170–188. doi:10.1016/j.quascirev.2006.04.012

Fleitmann, D., Burns, S.J., Mudelsee, M., Neff, U., Kramers, J., Mangini, A., Matter, A., 2003. Holocene forcing of the Indian monsoon recorded in a stalagmite from southern Oman. Science 300, 1737–1739. doi:10.1126/science.1083130

Frankignoul, C., Gastineau, G., Kwon, Y.O., 2013. The influence of the amoc variability on the atmosphere in CCSM3. J. Clim. 26, 9774–9790. doi:10.1175/JCLI-D-12-00862.1

Frechen, M., Kehl, M., Rolf, C., Sarvati, R., Skowronek, A., 2009. Loess chronology of the Caspian Lowland in Northern Iran. Quat. Int. 198, 220–233. doi:10.1016/j.quaint.2008.12.012

Fritz, S., 1996. Paleolimnological records of climatic change in North America. Limnol. Oceanogr. 41, 882–889. doi:10.4319/lo.1996.41.5.0882

Frost, C.D., Barnes, C.G., Snoke, A.W., 2006. Nd and Sr isotopic data from argillaceous rocks of the Galice Formation and Rattlesnake Creek terrane, Klamath Mountains: Evidence for input of Precambrian sources. Geol. Soc. Am. Spec. Pap. 410 80301, 103–120. doi:10.1130/2006.2410(05).

Gasse, F., 2000. Hydrological changes in the African tropics since the Last Glacial Maximum. Quat. Sci. Rev. 19, 189–211. doi:10.1016/S0277-3791(99)00061-X

Gasse, F., Van Campo, E., 1994. Abrupt post-glacial climate events in West Asia and North Africa monsoon domains. Earth Planet. Sci. Lett. 126, 435–456.

Gent, P.R., Danabasoglu, G., Donner, L.J., Holland, M.M., Hunke, E.C., Jayne, S.R., Lawrence, D.M., Neale, R.B., Rasch, P.J., Vertenstein, M., Worley, P.H., Yang, Z.L., Zhang, M., 2011. The community climate system model version 4. J. Clim. 24, 4973–4991. doi:10.1175/2011JCLI4083.1

Geyh, M.A., Schittere, U., Grosjean, M., 1998. Temporal changes of the C-14 reservoir effect in lakes. Radiocarbon 40, 921–931.

Ghalibaf, M., Moussavi, Z., 2014. Development and environment in Urmia Lake of Iran. Eur. J. Sustain. Dev. 3, 219–226. doi:10.14207/ejsd.2014.v3n3p219

Gibbs, R.J., 1970. Mechanisms controlling world water chemistry. Science 170, 1088–1090.

Ginoux, P., Prospero, J.M., Gill, T.E., Hsu, N.C., Zhao, M., 2012. Global-scale attribution of anthropogenic and natural dust sources and their emission rates based on MODIS Deep Blue aerosol products. Rev. Geophys. 50, 1–36.

Golafshani, R., 1995. Geochemical and petrological investigations of high potassic rocks from Shahi peninsula- east of the Urumia Lake. University of Tehran.

Goldstein, S.L., Onions, R.K., Hamilton, P.J., 1984. A Sm-Nd isotopic study of atmospheric dusts and particulates from major river systems. Earth Planet. Sci. Lett. 70, 221–236. doi:10.1016/0012-821X(84)90007-4

Golian, S., Mazdiyasni, O., AghaKouchak, A., 2014. Trends in meteorological and agricultural droughts in Iran. Theor. Appl. Climatol. doi:10.1007/s00704-014-1139-6

Golubkov, S., Kemp, R., Golubkov, M., Balushkina, E., Litvinchuk, L., Gubelit, Y., 2007. Biodiversity and the functioning of hypersaline lake ecosystems from Crimea Peninsula (Black Sea). Fundam. Appl. Limnol. 169, 79–87. doi:10.1127/1863-9135/2007/0169-0079

Gong, D.-Y., Ho, C.-H., 2002. The Siberian High and climate change over middle to high latitude Asia. Theor. Appl. Climatol. 72, 1–9. doi:10.1007/s007040200008

Gong, D.Y., Wang, S.W., Zhu, J.H., 2001. East Asian winter monsoon and Arctic Oscillation. Geophys. Res. Lett. 28, 2073–2076. doi:10.1029/2000GL012311

Goudie, A.S., Middleton, N.J., 2006. Desert Dust in Global System. Springer-Verlag, N.

Govin, A., Holzwarth, U., Heslop, D., Ford Keeling, L., Zabel, M., Mulitza, S., Collins, J. a., Chiessi, C.M., 2012. Distribution of major elements in Atlantic surface sediments (36°N-49°S): Imprint of terrigenous input and continental weathering. Geochemistry, Geophys. Geosystems 13, 1–23. doi:10.1029/2011GC003785

Griffiths, H.I., Schwalb, a., Stevens, L.R., 2001. Environmental change in southwestern Iran: the Holocene ostracod fauna of Lake Mirabad. The Holocene 11, 757–764. doi:10.1191/09596830195771

Grootes, P.M., Stuiver, M., White, J.W.C., Johnsen, S., Jouzel, J., 1993. Comparison of oxygen isotope records from the GISP2 and GRIP Greenland ice cores. Nature 366, 552–554. doi:10.1038/366552a0

Grousset, F.E., Biscaye, P.E., 2005. Tracing dust sources and transport patterns using Sr, Nd and Pb isotopes. Chem. Geol. 222, 149–167. doi:10.1016/j.chemgeo.2005.05.006

Grousset, F.E., Biscaye, P.E., Zindler, A., Prospero, J., Chester, R., 1988a. Neodymium isotopes as tracers in marine sediments and aerosols: North Atlantic. Earth Planet. Sci. Lett. 87, 367–378. doi:10.1016/0012-821X(88)90001-5

Grousset, F.E., Buat-Menard, P., Boust, D., Tian, R.-C., Baudel, S., Pujol, C., Vergnaud-Grazzini, C., 1988b. Temporal changes of aeolian Saharan input in the Cape Verde abyssal plain since the last Glacial period. Oceanol. Acta 11, 177–185.

Håkanson, L., Jansson, M., 1983. Principles of Lake Sedimentology. Springer-Verlag, Berlin.

Hamidi, M., Kavianpour, M.R., Shao, Y., 2013. Synoptic analysis of dust storms in the Middle East. Asia-Pacific J. Atmos. Sci. 49, 279–286. doi:10.1007/s13143-013-0027-9

Han, Y., Fang, X., Kang, S., Wang, H., Kang, F., 2008. Shifts of dust source regions over central Asia and the Tibetan Plateau: Connections with the Arctic oscillation and the westerly jet. Atmos. Environ. 42, 2358–2368. doi:10.1016/j.atmosenv.2007.12.025

Harmon, R.S., Wörner, G., Goldsmith, S.T., Harmon, B.A., Gardner, C.B., Lyons, W.B., Ogden, F.L., Pribil, M.J., Long, D.T., Kern, Z., Fórizs, I., Corps, U.S.A., 2016. Linking silicate weathering to riverine geochemistry — A case study from a mountainous tropical setting in west-central Panama. Geol. Soc. Am. Bull. 128, 1780–1812. doi:10.1130/B31388.1

Harrison, S.P., Kohfeld, K.E., Roelandt, C., Claquin, T., 2001. The role of dust in climate changes today, at the last glacial maximum and in the future. Earth-Science Rev. 54, 43–80. doi:10.1016/S0012-8252(01)00041-1

Hassink, J., 1997. The capacity of soils to preserve organic C and N by their association with clay and silt particles. Plant Soil 191, 77–87. doi:10.1023/A:1004213929699

He, F., Shakun, J.D., Clark, P.U., Carlson, A.E., Liu, Z., Otto-Bliesner, B.L., Kutzbach, J.E., 2013. Northern Hemisphere forcing of Southern Hemisphere climate during the last deglaciation. Nature 494, 81–5. doi:10.1038/nature11822

Hedges, J., Stern, J., 1984. Carbon and nitrogen determinations of carbonate-containing solids. Limnol. Oceanogr. 29, 657–663.

Hoelzmann, P., Jolly, D., Harrison, S.P., Laarif, F., Bonnefille, R., Pachur, H.J., 1998. Mid-Holocene land-surface conditions in northern Africa and the Arabian peninsula: A data set for the analysis of biogeophysical feedbacks in the climate system. Global Biogeochem. Cycles 12, 35–51. doi:10.1029/97GB02733

Holtvoeth, J., Vogel, H., Wagner, B., Wolff, G. a., 2010. Lipid biomarkers in Holocene and glacial sediments from ancient Lake Ohrid (Macedonia, Albania). Biogeosciences 7, 3473–3489. doi:10.5194/bg-7-3473-2010

Hong, Y.T., Hong, B., Lin, Q.H., Zhu, Y.X., Shibata, Y., Hirota, M., Uchida, M., Leng, X.T., Jiang, H.B., Xu, H., Wang, H., Yi, L., 2003. Correlation between Indian Ocean summer monsoon and North Atlantic climate during the Holocene. Earth Planet. Sci. Lett. 211, 371–380. doi:10.1016/S0012-821X(03)00207-3

Hossenzadeh, S.R., 1997. One hundred and twenty days winds of Sistan, Iran. Iran. J. Reserch Geogr. 46, 103–127.

Hulseman, J., 1966. An inventory of marine carbonate materials. J. Sediment. Petrol. ASCE 36, 622–625.

Hurrell, J.W., 1995. Decadal trends in the north atlantic oscillation: regional temperatures and precipitation. Science 269, 676–679. doi:10.1126/science.269.5224.676

Hurrell, J.W., VanLoon, H., 1997. Decadal variation in climate associated with the North Atlantic oscilation. Clim. Chang. 36, 301–326.

Hutchinson, G.E., Cowgill, U.M., 1963. Chemical examination of a core from Lake Zeribar , Iran. Science (80-.). 140, 67–69.

Ingram, B.L., Conrad, M.E., Ingle, J.C., 1996. Stable isotope and salinity systematics in estuarine waters and carbonates: San Francisco Bay. Geochim. Cosmochim. Acta 60, 455–467. doi:10.1016/0016-7037(95)00398-3

Ingram, B.L., Sloan, D., 1992. Strontium isotopic composition of estuarine sediments as paleosalinity-paleoclimate indicator. Science 255, 68–72. doi:10.1126/science.255.5040.68

IPCC, 2014. IPCC Climate Change (2014) Synthesis Report. Contribution of Working Groups I, II and III to the Fifth Assessment Report of the Intergovernmental Panel on Climate Change. Intergovernmental Panel on Climate Change, Geneva, Switzerland.

Isfahani, F. and Sharifi, A., 1999. Geochemical characteristics of magmatic rocks of Iran,. Geological Survey of Iran, Treatise on Geology of Iran, Book No. 70, Tehran.

Jackson, M.L., Tyler, S.A., Willis, A.L., Bourbeau, G.A., Pennington, R.P., 1948. Weathering sequence of clay-size minerals in soils and sediments. I. Fundamental generalizations. J. Phys. Chem. 52, 1237–1260. doi:DOI: 10.1021/j150463a015

Jalili, S., Morid, S., Banakar, A., Namdar Qanbari, R., 2011. Assessing the effect of soi and NAO indices on Lake Urmia water level variations, application of spectral analysis. J. Water Soil 25, 140–149 (in Persian with English abstract).

Janssens, J.A., 1983. A quantitative method for stratigraphic analysis of bryophytes in holocene peat. J. Ecol. 71, 189–196.

Jiménez-Espejo, F.J., García-Alix, a., Jiménez-Moreno, G., Rodrigo-Gámiz, M., Anderson, R.S., Rodríguez-Tovar, F.J., Martínez-Ruiz, F., Giralt, S., Delgado Huertas, a., Pardo-Igúzquiza, E., 2014. Saharan aeolian input and effective humidity variations over western Europe during the Holocene from a high altitude record. Chem. Geol. 374–375, 1–12. doi:10.1016/j.chemgeo.2014.03.001

Jiménez-Moreno, G., Anderson, R.S., 2012. Holocene vegetation and climate change recorded in alpine bog sediments from the Borreguiles de la Virgen, Sierra Nevada, southern Spain. Quat. Res. 77, 44–53. doi:10.1016/j.yqres.2011.09.006

Jin, Z., Li, F., Cao, J., Wang, S., Yu, J., 2006. Geochemistry of Daihai Lake sediments, Inner Mongolia, north China: Implications for provenance, sedimentary sorting, and catchment weathering. Geomorphology 80, 147–163. doi:10.1016/j.geomorph.2006.02.006

Jin, Z., Wang, S., Shen, J., Wang, Y., 2003. Carbonate verse silicate Sr isotope in lake sediments and its response to Little Ice Age. Chinese Sci. Bull. 48, 95–100. doi:10.1007/BF03183343

Jin, Z., Wang, S., Shen, J., Zhang, E., Li, F., Ji, J., Lu, X., 2001. Chemical weathering since the little ice age recorded in lake sediments: A high-resolution proxy of past climate. Earth Surf. Process. Landforms 26, 775–782. doi:10.1002/esp.224

Jirsa, F., Gruber, M., Stojanovic, A., Omondi, S.O., Mader, D., Körner, W., Schagerl, M., 2013. Major and trace element geochemistry of Lake Bogoria and Lake Nakuru, Kenya, during extreme draught. Chemie der Erde - Geochemistry 73, 275–282. doi:10.1016/j.chemer.2012.09.001

Jolly, D., Harrison, S.., Damnati, B., Bonnefille, R., 1998. Simulated climate and biomes of Africa during the late quaternary. Quat. Sci. Rev. 17, 629–657. doi:10.1016/S0277-3791(98)00015-8

Jones, B.F., Naftz, D.L., Spencer, R.J., Oviatt, C.G., 2009. Geochemical evolution of Great Salt Lake, Utah, USA. Aquat. Geochemistry 15, 95–121. doi:10.1007/s10498-008-9047-y

Jones, M.D., Roberts, C.N., Leng, M.J., Türkeş, M., 2006. A high-resolution late Holocene lake isotope record from Turkey and links to North Atlantic and monsoon climate. Geology 34, 361–364. doi:10.1130/G22407.1

Kabiri, K., Pradhan, B., Sharifi, A., Ghobadi, Y., Pirasteh, S., 2012. Manifestation of Remotely Sensed Data Coupled With Field Measured Meteorological Data for an Assessment of Degradation of Urmia Lake, Iran, in: 2012 Asia Pacific Conference on Environmental Science and Technology (APEST 2012). pp. 395–401.

Kamenov, G.D., Brenner, M., Tucker, J.L., 2009. Anthropogenic versus natural control on trace element and Sr-Nd-Pb isotope stratigraphy in peat sediments of southeast Florida (USA), ???1500 AD to present. Geochim. Cosmochim. Acta 73, 3549–3567. doi:10.1016/j.gca.2009.03.017

Kaniewski, D., Paulissen, E., Van Campo, E., Weiss, H., Otto, T., Bretschneider, J., Van Lerberghe, K., 2010. Late second–early first millennium BC abrupt climate changes in coastal Syria and their possible significance for the history of the Eastern Mediterranean. Quat. Res. 74, 207–215. doi:10.1016/j.yqres.2010.07.010

Karbassi, A., Bidhendi, G.N., Pejman, A., Bidhendi, M.E., 2010. Environmental impacts of desalination on the ecology of Lake Urmia. J. Great Lakes Res. 36, 419–424. doi:10.1016/j.jglr.2010.06.004

Kehl, M., 2009. Quaternary climate change in Iran – the state of knowledge. Erdkunde 63, 1–17. doi:10.3112/erdkunde.2009.01.01

Kelts, K., Shahrabi, M., 1986. Holocene sedimentology of hypersaline Lake Urmia, Nothwestern Iran. Palaeogeogr. Palaeoclimatol. Palaeoecol. 54, 105–130.

Kemp, J., Radke, L.C., Olley, J., Juggins, S., De Deckker, P., 2012. Holocene lake salinity changes in the Wimmera, southeastern Australia, provide evidence for millennial-scale climate variability. Quat. Res. 77, 65–76. doi:10.1016/j.yqres.2011.09.013

Khan, M., 2013. Relation between sediment flux variation and land use patterns along the Swedish Baltic Sea coast Mansoor Khan. Lund University.

Kitoh, A., Yatagai, A., Alpert, P., 2008. First super-high-resolution model projection that the ancient "Fertile Crescent" will disappear in this century. Hydrol. Res. Lett. 2, 1–4. doi:10.3178/hrl.2.1

Kowalewska, A., Cohen, A.S., 1998. Reconstruction of paleoenvironments of the Great Salt Lake Basin during the late Cenozoic. J. Paleolimnol. 20, 381–407. doi:10.1023/A:1008053505320

Krachler, M., Mohl, C., Emons, H., Shotyk, W., 2003. Two thousand years of atmospheric rare earth element (REE) deposition as revealed by an ombrotrophic peat bog profile, Jura Mountains, Switzerland. J. Environ. Monit. 5, 111–121. doi:10.1039/b208355h

Kutiel, H., Furman, H., 2003. Dust storms in the Middle East: sources of origin and Their temporal characteristics. Indoor Built Environ. 12, 419–426. doi:10.1177/1420326X03037110

Kutzbach, J.E., Liu, Z., 1997. Response of the African monsoon to orbital forcing and ocean feedbacks in the middle Holocene. Science (80-.). 278, 440–443. doi:10.1126/science.278.5337.440

Kuzucuoglu, C., Dorfler, W., Kunesch, S., Goupille, F., 2011. Mid- to late-Holocene climate change in central Turkey: The Tecer Lake record. The Holocene 21, 173–188. doi:10.1177/0959683610384163

Kylander, M.E., Martínez-Cortizas, A., Bindler, R., Greenwood, S.L., Mörth, C.M., Rauch, S., 2016. Potentials and problems of building detailed dust records using peat archives: An example from Store Mosse (the "Great Bog"), Sweden. Geochim. Cosmochim. Acta 190, 156–174. doi:10.1016/j.gca.2016.06.028

Lambert, F., Delmonte, B., Petit, J.R., Bigler, M., Kaufmann, P.R., Hutterli, M. a, Stocker, T.F., Ruth, U., Steffensen, J.P., Maggi, V., 2008. Dust-climate couplings over the past 800,000 years from the EPICA Dome C ice core. Nature 452, 616–619. doi:10.1038/nature06763

Langbein, W.B., 1961. Salinity and hydrology of closed lakes, U.S. Geological Survey Professional Paper 412. Washington D.C.

Lawrence, D.M., Oleson, K.W., Flanner, M.G., Thornton, P.E., Swenson, S.C., Lawrence, P.J., Zeng, X., Yang, Z.-L., Levis, S., Sakaguchi, K., Bonan, G.B., Slater, A.G., 2011. Parameterization improvements and functional and structural advances in Version 4 of the Community Land Model. J. Adv. Model. Earth Syst. 3, 1–27. doi:10.1029/2011MS000045

Leick, G., 2010. Historical Dictionary of Mesopotamia, Second. ed. The Scarecrow Press, Inc., Lanham. Toronto. Plymouth, UK.

Levis, S., Bonan, G.B., Bonfils, C., 2004. Soil feedback drives the mid-Holocene North African monsoon northward in fully coupled CCSM2 simulations with a dynamic vegetation model. Clim. Dyn. 23, 791–802. doi:10.1007/s00382-004-0477-y

Littmann, T., 1991. Dust storm frequency in Asia: Climatic control and variability. Int. J. Climatol. 11, 393–412. doi:10.1002/joc.3370110405

Liu, X.-Y., Xiao, H.-Y., Liu, C.-Q., Li, Y.-Y., Xiao, H.-W., 2008. Stable carbon and nitrogen isotopes of the moss Haplocladium microphyllum in an urban and a background area (SW China): The role of environmental conditions and atmospheric nitrogen deposition. Atmos. Environ. 42, 5413–5423. doi:10.1016/j.atmosenv.2008.02.038

Liu, Y., Lo, L., Shi, Z., Wei, K.-Y., Chou, C.-J., Chen, Y.-C., Chuang, C.-K., Wu, C.-C., Mii, H.-S., Peng, Z., Amakawa, H., Burr, G.S., Lee, S.-Y., DeLong, K.L., Elderfield, H., Shen, C.-C., 2015. Obliquity pacing of the western Pacific Intertropical Convergence Zone over the past 282,000 years. Nat. Commun. 6, 10018. doi:10.1038/ncomms10018

Liu, Z., Otto-Bliesner, B.L., Brady, E.C., Tomas, R., Clark, P.U., Carlson, A.E., Lynch-Stieglitz, J., Curry, W., Brook, E., Jacob, R., Kutzbach, J., Cheng, J., 2009. Transient simulation of last deglaciation with a new mechanism for Bolling-Allerod warming. Science (80-.). 325, 310–314.

López-Días, V., Borrego, a G., Blanco, C.G., Arboleya, M., López-Sáez, J. a, López-Merino, L., 2010. Biomarkers in a peat deposit in Northern Spain (Huelga de Bayas, Asturias) as proxy for climate variation. J. Chromatogr. A 1217, 3538–46. doi:10.1016/j.chroma.2010.03.038

Lupker, M., Aciego, S.M., Bourdon, B., Schwander, J., Stocker, T.F., 2010. Isotopic tracing (Sr, Nd, U and Hf) of continental and marine aerosols in an 18th century section of the Dye-3 ice core (Greenland). Earth Planet. Sci. Lett. 295, 277–286. doi:10.1016/j.epsl.2010.04.010

M.Q.C.E., 2013. Updates on Integrated National Water Management Plan in Aras, Urmia, Talesh-Anzali, Sefir Ruod, Haraz, Haraz-Qarasou, Gorganruod and Atrak

Watersheds. Volume12: Environmental Investigations in Urmia Watershed Area. Tehran.

Madadi, A., Moghaddam, M.H.R., Rajaei, A.H., 2005. Study of the geomorphological evolution of the Neor Lake in Ardabil region, NW Iran. Quaterly J. Geogr. Res. 1–12 (in Persian).

Manaffar, R., Zare, S., Agh, N., Siyabgodsi, a., Soltanian, S., Mees, F., Sorgeloos, P., Bossier, P., van Stappen, G., 2011. Sediment cores from Lake Urmia (Iran) suggest the inhabitation by parthenogenetic Artemia around 5,000 years ago. Hydrobiologia 671, 65–74. doi:10.1007/s10750-011-0704-6

Martinez-Ruiz, F., Kastner, M., Gallego-Torres, D., Rodrigo-Gámiz, M., Nieto-Moreno, V., Ortega-Huertas, M., 2015. Paleoclimate and paleoceanography over the past 20,000yr in the Mediterranean Sea Basins as indicated by sediment elemental proxies. Quat. Sci. Rev. 107, 25–46. doi:10.1016/j.quascirev.2014.09.018

Mauquoy, D., Barber, K., 2002. Testing the sensitivity of the palaeoclimatic signal from ombrotrophic peat bogs in northern England and the Scottish Borders. Rev. Palaeobot. Palynol. 119, 219–240. doi:10.1016/S0034-6667(01)00099-9

Mauquoy, D., Yeloff, D., 2008. Raised peat bog development and possible responses to environmental changes during the mid- to late-Holocene. Can the palaeoecological record be used to predict the nature and response of raised peat bogs to future climate change? Biodivers. Conserv. 17, 2139–2151. doi:10.1007/s10531-007-9222-2

Mayer, L.M., 1994. Surface area control of organic carbon accumulation in continental shelf sediments. Geochim. Cosmochim. Acta 58, 1271–1284. doi:10.1016/0016-7037(94)90381-6

Mayewski, P.A., Meeker, L.D., Twickler, M.S., Lyons, W.B., Prentice, M., 1997. Major features and forcing of high-latitude northern hemisphere atmospheric circulation using a 110 , 000- year-long glaciochemical series. J. Geophys. Res. 102, 26,345-26,366.

Mayewski, P.A., Rohling, E.E., Stager, J.C., Maasch, K.A., Meeker, L.D., Meyerson, E.A., Gasse, F., Kreveld, S. Van, Holmgren, K., Lee-thorp, J., Rosqvist, G., Rack, F., Staubwasser, M., Schneider, R.R., Steig, E.J., 2004. Holocene climate variability. Quat. Res. 62, 243–255. doi:10.1016/j.yqres.2004.07.001

McCulloch, M.T., De Deckker, P., Chivas, A.R., 1989. Strontium isotope variations in single ostracod valves from the Gulf of Carpentaria, Australia: A palaeoenvironmental indicator. Geochim. Cosmochim. Acta 53, 1703–1710. doi:10.1016/0016-7037(89)90256-1

McGee, D., Donohoe, A., Marshall, J., Ferreira, D., 2014. Changes in ITCZ location and cross-equatorial heat transport at the Last Glacial Maximum, Heinrich Stadial 1, and the mid-Holocene. Earth Planet. Sci. Lett. 390, 69–79. doi:10.1016/j.epsl.2013.12.043

Mckenzie, D., 1972. Active tectonics of the Mediterranean region. Geophys. J. R. astr. Soc. 30, 109–186. doi:10.1111%2Fj.1365-246x.1972.tb02351.x

Mckenzie, D., 1976. The East Anatolian Fault: A major structure in Eastern Turkey. Earth Planet. Sci. Lett. 29, 189–193. doi:10.1136/bmj.2.3908.1076

Mehterian, S., Pourmand, A., Sharifi, A., Lahijani, H.A.K., Naderi, M., Swart, P.K., 2017. Speleothem records of glacial/interglacial climate from Iran forewarn of future Water Availability in the interior of the Middle East. Quat. Sci. Rev. 164, 187–198. doi:10.1016/j.quascirev.2017.03.028

Mellaart, J., 1975. The Neolithic of the Near East. Charles Scribner's Sons, New York.

Meyers, P. a., 2003. Applications of organic geochemistry to paleolimnological reconstructions: A summary of examples from the Laurentian Great Lakes. Org. Geochem. 34, 261–289. doi:10.1016/S0146-6380(02)00168-7

Meyers, P. a., Ishiwatari, R., 1993. Lacustrine organic geochemistry—an overview of indicators of organic matter sources and diagenesis in lake sediments. Org. Geochem. 20, 867–900. doi:10.1016/0146-6380(93)90100-P

Middleton, N.J., 1986. A geography of dust storms in South-West Asia. Int. J. Climatol. 6, 183–196. doi:10.1002/joc.3370060207

Migowski, C., Stein, M., Prasad, S., Negendank, J.F.W., Agnon, A., 2006. Holocene climate variability and cultural evolution in the Near East from the Dead Sea sedimentary record. Quat. Res. 66, 421–431. doi:10.1016/j.yqres.2006.06.010

Miller, R.L., Tegen, I., 1998. Climate response to soil dust aerosols. J. Clim. 11, 3247–3267. doi:10.1175/1520-0442(1998)011<3247:CRTSDA>2.0.CO;2

Miot, J., Jézéquel, D., Benzerara, K., Cordier, L., Rivas-Lamelo, S., Skouri-Panet, F., Férard, C., Poinsot, M., Duprat, E., 2016. Mineralogical diversity in Lake Pavin: connections with water column chemistry and biomineralization processes. Minerals 6, 24. doi:10.3390/min6020024

Mischke, S., Herzschuh, U., Zhang, C., Bloemendal, J., Riedel, F., 2005. A Late Quaternary lake record from the Qilian Mountains (NW China): Lake level and salinity changes inferred from sediment properties and ostracod assemblages. Glob. Planet. Change 46, 337–359. doi:10.1016/j.gloplacha.2004.09.023

Mohajer Bavaghar, N., 1997. Sedimentolocical and geochemical study of Urmia Lake with emphasis on the origin of salt. University of Tehran.

Mohtadi, M., Prange, M., Oppo, D.W., De Pol-Holz, R., Merkel, U., Zhang, X., Steinke, S., Lückge, A., 2014. North Atlantic forcing of tropical Indian Ocean climate. Nature 509, 76–80. doi:10.1038/nature13196

Moore, J.K., Doney, S.C., Glover, D.M., Fung, I.Y., 2002. Iron cycling and nutrient-limitation patterns in surface waters of the world ocean. Deep. Res. Part II Top. Stud. Oceanogr. 49, 463–507. doi:10.1016/S0967-0645(01)00109-6

Mügler, I., Sachse, D., Werner, M., Xu, B., Wu, G., Yao, T., Gleixner, G., 2008. Effect of lake evaporation on δD values of lacustrine n-alkanes: A comparison of Nam Co (Tibetan Plateau) and Holzmaar (Germany). Org. Geochem. 39, 711–729. doi:10.1016/j.orggeochem.2008.02.008

Muhs, D.R., Bettis, E. a., Been, J., McGeehin, J.P., 2001. Impact of climate and parent material on chemical weathering in loess-derived soils of the Mississippi River Valley. Soil Sci. Soc. Am. J. 65, 1761. doi:10.2136/sssaj2001.1761

Muhs, D.R., Prospero, J.M., Baddock, M.C., Gill, T.E., 2014. Identifying sources of aeolian mineral dust: Present and Past, in: Stuut, J.B., Knippertz, P. (Eds.), Mineral Dust: A Key Player in the Earth System. Springer, pp. 1–509. doi:10.1007/978-94-017-8978-3

Muller, J., Kylander, M., Martinez-Cortizas, A., Wüst, R. a. J., Weiss, D., Blake, K., Coles, B., Garcia-Sanchez, R., 2008. The use of principle component analyses in characterising trace and major elemental distribution in a 55kyr peat deposit in tropical Australia: Implications to paleoclimate. Geochim. Cosmochim. Acta 72, 449–463. doi:10.1016/j.gca.2007.09.028

Muri, G., Wakeham, S.G., 2006. Organic matter and lipids in sediments of Lake Bled (NW Slovenia): Source and effect of anoxic and oxic depositional regimes. Org. Geochem. 37, 1664–1679. doi:10.1016/j.orggeochem.2006.07.016

Myers, T.S., Tabor, N.J., Rosenau, N. a., 2014. Multiproxy approach reveals evidence of highly variable paleoprecipitation in the Upper Jurassic Morrison Formation (western United States). Bull. Geol. Soc. Am. 126, 1105–1116. doi:10.1130/B30941.1

Nagashima, K., Tada, R., Tani, A., Sun, Y., Isozaki, Y., Toyoda, S., Hasegawa, H., 2011. Millennial-scale oscillations of the westerly jet path during the last glacial period. J. Asian Earth Sci. 40, 1214–1220. doi:10.1016/j.jseaes.2010.08.010

Nazemosadat, M.J., Cordery, I., 2000. On the relationships between ENSO and autumn rainfall in Iran. Int. J. Climatol. 20, 47–61. doi:10.1002/(SICI)1097-0088(200001)20:1<47::AID-JOC461>3.3.CO;2-G

Nazemosadat, M.J., Samani, N., Barry, D.A., Niko, M.M., 2006. ENSO forcing on climate change in Iran : precipitation analysis. Iran. J. Sci. Technol. 30, 555–565.

Neff, U., Burns, S.J., Mangini, a, Mudelsee, M., Fleitmann, D., Matter, a, 2001. Strong coherence between solar variability and the monsoon in Oman between 9 and 6 kyr ago. Nature 411, 290–3. doi:10.1038/35077048

Nesbitt, H.W., Markovics, G., Price, R.G., 1980. Chemical processes affecting alkalis and alkaline earths during continental weathering. Geochim. Cosmochim. Acta 44, 1659–1666. doi:10.1016/0016-7037(80)90218-5

Nesbitt, H.W., Young, G.M., 1982. Early Proterozoic climate and plate motions inferred from major element chamistry of lutites. Nature. doi:10.1007/s12594-012-0045-8

Nesbitt, H.W., Young, G.M., 1989. Formation and diagenesis of weathering profiles. J. Geol. 97, 129–146.

Nesbitt, H.W., Young, G.M., Mclennan, S.M., Keays, R.R., 1996. Effects of chemical weathering and sorting on the petrogenesis of siliciclastic sediments with implications for provenance studies. J. Geol. 104, 525–542.

Nicoll, K., Küçükuysal, C., 2013. Emerging multi-proxy records of Late Quaternary Palaeoclimate dynamics in Turkey and the surrounding region. Turkish J. Earth Sci. 22, 126–142. doi:10.3906/yer-1109-7

Nieto-Moreno, V., Martínez-Ruiz, F., Giralt, S., Jiménez-Espejo, F., Gallego-Torres, D., Rodrigo-Gámiz, M., García-Orellana, J., Ortega-Huertas, M., de Lange, G.J., 2011. Tracking climate variability in the western Mediterranean during the Late Holocene: a multiproxy approach. Clim. Past 7, 1395–1414. doi:10.5194/cp-7-1395-2011

Nordt, L.C., Driese, S.D., 2010. New weathering index improves paleorainfall estimates from Vertisols. Geology 38, 407–410. doi:10.1130/G30689.1

Nott, C.J., Xie, S., Avsejs, L.A., Maddy, D., Chambers, F.M., Evershed, R.P., 2000. n - Alkane distributions in ombrotrophic mires as indicators of vegetation change related to climatic variation. Org. Geochem. 31, 231–235.

Novak, M., Buzek, F., Adamova, M., 1999. Vertical trends in d 13 C , d 15 N and d 34 S ratios in bulk Sphagnum peat. Soil Biol. Biochem. 31, 1343–1346.

Novak, M., Pacherova, P., 2008. Mobility of trace metals in pore waters of two Central European peat bogs. Sci. Total Environ. 394, 331–337. doi:10.1016/j.scitotenv.2008.01.036

Oren, A., 2009. Saline lakes around the world: Unique systems with unique values , 10th ISSLR conference and 2008 FRIENDS of Great Salt Lake forum , May 11-16 , 2008 , University of Utah , Salt Lake CIty. Nat. Resour. Environ. Issues 15.

Orru, H., Orru, M., 2006. Sources and distribution of trace elements in Estonian peat. Glob. Planet. Change 53, 249–258. doi:10.1016/j.gloplacha.2006.03.007

Otto-Bliesner, B.L., Schneider, R., Brady, E.C., Kucera, M., Abe-Ouchi, A., Bard, E., Braconnot, P., Crucifix, M., Hewitt, C.D., Kageyama, M., Marti, O., Paul, A., Rosell-Melé, A., Waelbroeck, C., Weber, S.L., Weinelt, M., Yu, Y., 2009. A comparison of PMIP2 model simulations and the MARGO proxy reconstruction for tropical sea surface temperatures at last glacial maximum. Clim. Dyn. 32, 799–815. doi:10.1007/s00382-008-0509-0

Page, S.E., Wűst, R. a. J., Weiss, D., Rieley, J.O., Shotyk, W., Limin, S.H., 2004. A record of Late Pleistocene and Holocene carbon accumulation and climate change from an equatorial peat bog(Kalimantan, Indonesia): implications for past, present and future carbon dynamics. J. Quat. Sci. 19, 625–635. doi:10.1002/jqs.884

Pancost, R.D., Baas, M., Van Geel, B., Sinninghe Damsté, J.S., 2002. Biomarkers as proxies for plant inputs to peats: An example from a sub-boreal ombrotrophic bog. Org. Geochem. 33, 675–690. doi:10.1016/S0146-6380(02)00048-7

Ponel, P., Andrieu-ponel, V., Djamali, M., Lahijani, H., Leydet, M., Mashkour, M., 2013. Fossil beetles as possible evidence for transhumance during the middle and late Holocene in the high mountains of Talysch (Talesh) in NW Iran ? J. Environ. Archeol. 18, 201–210.

Pourasghar, F., Tozuka, T., Jahanbakhsh, S., Sari Sarraf, B., Ghaemi, H., Yamagata, T., 2012. The interannual precipitation variability in the southern part of Iran as linked to large-scale climate modes. Clim. Dyn. 39, 2329–2341. doi:10.1007/s00382-012-1357-5

Pourmand, A., Dauphas, N., 2010. Distribution coefficients of 60 elements on TODGA resin: Application to Ca, Lu, Hf, U and Th isotope geochemistry. Talanta 81, 741–753. doi:10.1016/j.talanta.2010.01.008

Pourmand, A., Dauphas, N., Ireland, T.J., 2012. A novel extraction chromatography and MC-ICP-MS technique for rapid analysis of REE, Sc and Y: Revising CI-chondrite and Post-Archean Australian Shale (PAAS) abundances. Chem. Geol. 291, 38–54. doi:10.1016/j.chemgeo.2011.08.011

Pourmand, A., Marcantonio, F., Bianchi, T.S., Canuel, E. a., Waterson, E.J., 2007a. A 28-ka history of sea surface temperature, primary productivity and planktonic community variability in the western Arabian Sea. Paleoceanography 22, PA4208 1-14. doi:10.1029/2007PA001502

Pourmand, A., Marcantonio, F., Bianchi, T.S., Canuel, E. a., Waterson, E.J., 2007b. A 28-ka history of sea surface temperature, primary productivity and planktonic community variability in the western Arabian Sea. Paleoceanography 22, PA4208. doi:10.1029/2007PA001502

Pourmand, A., Marcantonio, F., Schulz, H., 2004. Variations in productivity and eolian fluxes in the northeastern Arabian Sea during the past 110 ka. Earth Planet. Sci. Lett. 221, 39–54. doi:10.1016/S0012-821X(04)00109-8

Pourmand, A., Prospero, J.M., Sharifi, A., 2014. Geochemical fingerprinting of trans-Atlantic African dust based on radiogenic Sr-Nd-Hf isotopes and rare earth element anomalies. Geology 42, 675–678. doi:10.1130/G35624.1

Pourmand, a., Marcantonio, F., Bianchi, T.S., Canuel, E. a., Waterson, E.J., 2005. Radionuclide and biomarker proxies of past ocean circulation and productivity in the Arabian Sea. Geophys. Res. Lett. 32, 1–4. doi:10.1029/2005GL022612

Price, J.R., Velbel, M. a., 2003. Chemical weathering indices applied to weathering profiles developed on heterogeneous felsic metamorphic parent rocks. Chem. Geol. 202, 397–416. doi:10.1016/j.chemgeo.2002.11.001

Prospero, J.M., Ginoux, P., Torres, O., Nicholson, S.E., Gill, T.E., 2002. Environmental characterization of global sources of atmospheric soil dust identified with the NIMBUS 7 Total Ozone Mapping Spectrometer (TOMS) absorbing aerosol product. Rev. Geophys. 40, 1–31. doi:10.1029/2000RG000095

Psomiadis, D., Ghilardi, M., Demory, F., Delanghe-Sabatier, D., Bloemendal, J., Yiu, C., 2014. Late Pleistocene to Mid-Holocene landscape reconstruction in the western part of the Thessaloniki Plain, Greece: evidence for environmental changes, and implications for human occupation. Zeitschrift für Geomorphol. Suppl. Issues 58, 67–87. doi:10.1127/0372-8854/2013/S-00137

Rahaman, A.A., Ambikadevi, M., 2000. Variations in hatching characteristics of Artemia cysts of Indian saline ponds in relation to salinity The studies on ecology and distribution of Artemia salt operations are seasonal ; the production period is, in: 8th World Salt Symposium. The Hague, Netherlands, pp. 909–913.

Ramezani, E., Marvie Mohadjer, M.R., Knapp, H.-D., Ahmadi, H., Joosten, H., 2008. The late-Holocene vegetation history of the Central Caspian (Hyrcanian) forests of northern Iran. The Holocene 18, 307–321. doi:10.1177/0959683607086768

Rausch, N., Nieminen, T., Ukonmaanaho, L., Le Roux, G., Krachler, M., Cheburkin, A.K., Bonani, G., Shotyk, W., 2005. Comparison of atmospheric deposition of copper, nickel, cobalt, zinc, and cadmium recorded by Finnish peat cores with monitoring data and emission records. Environ. Sci. Technol. 39, 5989–5998. doi:10.1021/es050260m

Raziei, T., Bordi, I., Santos, J. a., Mofidi, A., 2013a. Atmospheric circulation types and winter daily precipitation in Iran. Int. J. Climatol. 33, 2232–2246. doi:10.1002/joc.3596

Raziei, T., Daryabari, J., Bordi, I., Pereira, L.S., 2013b. Spatial patterns and temporal trends of precipitation in Iran. Theor. Appl. Climatol. 115, 531–540. doi:10.1007/s00704-013-0919-8

Raziei, T., Mofidi, A., Santos, J. a., Bordi, I., 2012. Spatial patterns and regimes of daily precipitation in Iran in relation to large-scale atmospheric circulation. Int. J. Climatol. 32, 1226–1237. doi:10.1002/joc.2347

Redman, C.L., 1978. The Rise of Civilization. W. H. Freeman and Company, San Francisco.

Regard, V., Bellier, O., Braucher, R., Gasse, F., Bourlès, D., Mercier, J., Thomas, J.C., Abbassi, M.R., Shabanian, E., Soleymani, S., 2006. 10Be dating of alluvial deposits from Southeastern Iran (the Hormoz Strait area). Palaeogeogr. Palaeoclimatol. Palaeoecol. 242, 36–53. doi:10.1016/j.palaeo.2006.05.012

Reimer, P., Bard, E., Bayliss, A., 2013. IntCal13 and Marine13 radiocarbon age calibration curves 0–50,000 years cal BP. Radiocarbon 55, 1869–1887.

Reinhardt, E.G., Stanley, D.J., Patterson, R.T., 1998. Strontium isotopic-paleontological method as a high-resolution paleosalinity tool for lagoonal environments. Geology 26, 1003–1006. doi:10.1130/0091-7613(1998)026<1003:SIPMAA>2.3.CO;2

Revel-Rolland, M., Arnaud, F., Chapron, E., Desmet, M., Givelet, N., Alibert, C., McCulloch, M., 2005. Sr and Nd isotopes as tracers of clastic sources in Lake Le Bourget sediment (NW Alps, France) during the Little Ice Age: Palaeohydrology implications. Chem. Geol. 224, 183–200. doi:10.1016/j.chemgeo.2005.04.014

Revel, M., Colin, C., Bernasconi, S., Combourieu-Nebout, N., Ducassou, E., Grousset, F.E., Rolland, Y., Migeon, S., Bosch, D., Brunet, P., Zhao, Y., Mascle, J., 2014. 21,000 Years of Ethiopian African monsoon variability recorded in sediments of the western Nile deep-sea fan. Reg. Environ. Chang. 1–12. doi:10.1007/s10113-014-0588-x

Riehl, S., 2009. Archaeobotanical evidence for the interrelationship of agricultural decision-making and climate change in the ancient Near East. Quat. Int. 197, 93–114. doi:10.1016/j.quaint.2007.08.005

Riehl, S., Zeidi, M., Conard, N.J., 2013. Emergence of agriculture in the foothills of the Zagros Mountains of Iran. Science 341, 65–7. doi:10.1126/science.1236743

Rivas-Martinez, S., Sánchez-Mata, D., Costa, M., 1999. North American boreal and western temperate forest vegetation (syntaxonomical synopsis of the potential natural plant communities of North America II). Itinera Geobot. 12, 5–316.

Roberts, N., 2002. Did prehistoric landscape management retard the post-glacial spread of woodland in Southwest Asia? Ant 76, 1002–1010.

Roberts, N., Brayshaw, D., Kuzucuoglu, C., Perez, R., Sadori, L., 2011. The mid-Holocene climatic transition in the Mediterranean: Causes and consequences. The Holocene 21, 3–13. doi:10.1177/0959683610388058

Roberts, N., Jones, M.D., Benkaddour, A., Eastwood, W.J., Filippi, M.L., Frogley, M.R., Lamb, H.F., Leng, M.J., Reed, J.M., Stein, M., Stevens, L., Valero-Garcés, B., Zanchetta, G., 2008. Stable isotope records of Late Quaternary climate and hydrology from Mediterranean lakes: the ISOMED synthesis. Quat. Sci. Rev. 27, 2426–2441. doi:10.1016/j.quascirev.2008.09.005

Roberts, N., Reed, J.M., Leng, M.J., Kuzucuoglu, C., Fontugne, M., Bertaux, J., Woldring, H., Bottema, S., Black, S., Hunt, E., Karabiyikoglu, M., 2001. The tempo of Holocene climatic change in the eastern Mediterranean region: new high-resolution crater-lake sediment data from central Turkey. The Holocene 11, 721–736. doi:10.1191/09596830195744

Roberts, N., Wright, H.E.J., 1993. Vegetational, lake-level and climatic history of the Neat-East and Southwest Asia., in: Wright, H.E.J., Kutzbach, J.E., Webb, T. lll., Ruddiman, W.F., Stieet-Perrott, F.A., Bartleini, P.J. (Eds.), Global Climates since the Last Glacial Maximum. University of Minnesota Press, pp. 194–220.

Rodrigo-Gámiz, M., Martínez-Ruiz, F., Rodríguez-Tovar, F.J., Jiménez-Espejo, F.J., Pardo-Igúzquiza, E., 2014. Millennial- to centennial-scale climate periodicities and forcing mechanisms in the westernmost Mediterranean for the past 20,000 yr. Quat. Res. (United States) 81, 78–93. doi:10.1016/j.yqres.2013.10.009

Rossignol-Strick, M., 1995. Sea-land correlation of pollen records in the Eastern Mediterranean for the glacial-interglacial transitions: Biostratigraphy versus radiometric time-scale. Quat. Sci. Rev. 14, 893–915.

Rossignol-Strick, M., 1999. The Holocene climatic optimum and pollen records of sapropel 1 in the eastern Mediterranean , 9000 — 6000 BP. Quat. Sci. Rev. 18, 515–530.

Rutberg, R.L., Goldstein, S.L., Hemming, S.R., Anderson, R.F., 2005. Sr isotope evidence for sources of terrigenous sediment in the southeast Atlantic Ocean: Is there increased available Fe for enhanced glacial productivity? Paleoceanography 20, 1–10. doi:10.1029/2003PA000999

Sabziparvar, a. a., Mirmasoudi, S.H., Tabari, H., Nazemosadat, M.J., Maryanaji, Z., 2010. ENSO teleconnection impacts on reference evapotranspiration variability in some warm climates of Iran. Int. J. Climatol. 31, 1710–1723. doi:10.1002/joc.2187

Sachse, D., Radke, J., Gleixner, G., 2006. δD values of individual n-alkanes from terrestrial plants along a climatic gradient - Implications for the sedimentary biomarker record. Org. Geochem. 37, 469–483. doi:10.1016/j.orggeochem.2005.12.003

Saito, S., 1998. Major and trace element geochemistry of sediments from Esat Greenland continental rise: an implication for sediment provenance and source area weathering. Proc. Ocean Drill. Program, Sci. Results 152, 19–28.

Schellekens, J., Buurman, P., 2011. n-Alkane distributions as palaeoclimatic proxies in ombrotrophic peat: The role of decomposition and dominant vegetation. Geoderma 164, 112–121. doi:10.1016/j.geoderma.2011.05.012

Scheuvens, D., Schütz, L., Kandler, K., Ebert, M., Weinbruch, S., 2013. Bulk composition of northern African dust and its source sediments - A compilation. Earth-Science Rev. 116, 170–194. doi:10.1016/j.earscirev.2012.08.005

Schiemann, R., Lüthi, D., Schär, C., 2009. Seasonality and interannual variability of the westerly jet in the Tibetan Plateau region. J. Clim. 22, 2940–2957. doi:10.1175/2008JCLI2625.1

Schilman, B., Bar-Matthews, M., Almogi-labin, A., Luz, B., 2001. Global climate instability reflected by Eastern Mediterranean marine records during the late Holocene. Palaeogeogr. Palaeoclimatol. Palaeoecol. 176, 157–176.

Schilman, B.Y., Bar-Matthews, M., Almogi-labin, A., 2001. Global climate instability reflected by Eastern Mediterranean marine records during the late Holocene. Palaeogeogr. Palaeoclimatol. Palaeoecol. 176, 157–176.

Schulz, H., von Rad, U., Erlenkeuser, H., 1998. Correlation between Arabian Sea and Greenland climate oscillations of the past 110,000 years: Nature. Nature 393, 54–62.

Scott, D.A., 1995. A directory of wetlands in the Middle East. IUCN; IWRB, Gland, Switzerland andSlimbridge, U.K.

Seki, O., Meyers, P. a., Kawamura, K., Zheng, Y., Zhou, W., 2009. Hydrogen isotopic ratios of plant wax n-alkanes in a peat bog deposited in northeast China during the last 16kyr. Org. Geochem. 40, 671–677. doi:10.1016/j.orggeochem.2009.03.007

Shah-Hosseini, M., 2003. Sedimentology of hypersaline Lake Urmia in central part of Shahid Kalantari highway with special reference to their origin. University of Tehran.

Shahabfar, A., Eitzinger, J., 2013. Spatio-temporal analysis of droughts in semi-arid regions by using meteorological drought indices. Atmosphere (Basel). 4, 94–112. doi:10.3390/atmos4020094

Shahabfar, A., Ghulam, A., Eitzinger, J., 2012. Drought monitoring in Iran using the perpendicular drought indices. Int. J. Appl. Earth Obs. Geoinf. 18, 119–127. doi:10.1016/j.jag.2012.01.011

Shahrabi, M., 1994. Seas and Lakes of Iran. Geologiacal Survey of Iran, Treatise on Geology of Iran, Book No. 10, Tehran.

Shao, Y., Wyrwoll, K.-H., Chappell, A., Huang, J., Lin, Z., McTainsh, G.H., Mikami, M., Tanaka, T.Y., Wang, X., Yoon, S., 2011. Dust cycle: An emerging core theme in Earth system science. Aeolian Res. 2, 181–204. doi:10.1016/j.aeolia.2011.02.001

Sharifi, A., 2002. Factors controlling the sedimentological and geochemical characteristics of the Lake Urmia. Iranian National Institute for Oceanography and Atmospheric Science, Report No. 381-2-04, 131 p. (in Persian with English abstract)

Sharifi, A., Pourmand, A., Canuel, E.A., Ferer-Tyler, E., Peterson, L.C., Aichner, B., Feakins, S.J., Daryaee, T., Djamali, M., Beni, A.N., Lahijani, H.A.K., Swart, P.K., 2015. Abrupt climate variability since the last deglaciation based on a high-resolution, multi-proxy peat record from NW Iran: The hand that rocked the Cradle of Civilization? Quat. Sci. Rev. 123, 215–230. doi:10.1016/j.quascirev.2015.07.006

Sheldon, N.D., Retallack, G.J., Tanaka, S., 2002. Geochemical climofunctions from north american soils and application to paleosols across the Eocene-Oligocene boundary in Oregon. J. Geol. 110, 687–696. doi:10.1086/342865

Shotyk, W., Krachler, M., Martinez-Cortizas, A., Cheburkin, A.K., Emons, H., 2002. A peat bog record of natural, pre-anthropogenic enrichments of trace elements in atmospheric aerosols since 12 370 14C yr BP, and their variation with Holocene climate change. Earth Planet. Sci. Lett. 199, 21–37. doi:10.1016/S0012-821X(02)00553-8

Shotyk, W., Weiss, D., Kramers, J.D., Frei, R., Cheburkin, A.K., Gloor, M., Reese, S., 2001. Geochemistry of the peat bog at Etang de la Grue ` re , Jura Mountains , Switzerland , and its record of atmospheric Pb and lithogenic trace metals (Sc , Ti , Y , Zr , and REE) since 12 , 370 C yr BP. Geochim. Cosmochim. Acta 65, 2337–2360.

Shvartsev, S.L., Kolpakova, M.N., Isupov, V.P., Vladimirov, a. G., Ariunbileg, S., 2014. Geochemistry and chemical evolution of saline lakes of Western Mongolia. Geochemistry Int. 52, 388–403. doi:10.1134/S0016702914030070

Sima, S., Ahmadalipour, A., Shafiee Jood, M., Tajrishy, M., Abrishamchi, A., 2012. Monitoring Urmia Lake Area Variation Using MODIS Satellite Data, in: World Environmental and Water Resources Congress 2012: Crossing Boundaries © ASCE 2012. pp. 1917–1926.

Sima, S., Ahmadalipour, a., Tajrishy, M., 2013. Mapping surface temperature in a hyper-saline lake and investigating the effect of temperature distribution on the lake evaporation. Remote Sens. Environ. 136, 374–385. doi:10.1016/j.rse.2013.05.014

Singh, A.K., Hasnain, S.I., 1999. Environmental geochemistry of Damodar river basin, east coast of India. Environ. Earth Sci. 37, 124–136.

Sirocko, F., Garbe-Schönberg, D., Devey, C., 2000. Processes controlling trace element geochemistry of Arabian Sea sediments during the last 25,000 years. Glob. Planet. Change 26, 217–303. doi:Doi: 10.1016/s0921-8181(00)00046-1

Sly, P.G., 1978. Sedimentary proccesses in lakes, in: Lerman, A. (Ed.), Lakes: Chemistry, Geology, Physics. Springer, New York, pp. 65–89.

Sly, P.G., 1989a. Sediment dispersion : part 1 , fine sediments and significance of the silt / clay ratio. Hydrobiologia 176/177, 99–110.

Sly, P.G., 1989b. Sediment dispersion : part 2 , characterisation by size of sand fraction and percent mud. Hydrobiologia 176/177, 111–124.

Snyder, J. a., Wasylik, K., Fritz, S.C., Wright Jr, H.E., 2001. Diatom-based conductivity reconstruction and palaeoclimatic interpretation of a 40-ka record from Lake Zeribar, Iran. The Holocene 11, 737–745. doi:10.1191/09596830195753

Solanki, S.K., Usoskin, I.G., Kromer, B., Schüssler, M., Beer, J., 2004. Unusual activity of the Sun during recent decades compared to the previous 11,000 years. Nature 431, 1084–7. doi:10.1038/nature02995

Stallard, R.F., 1985. River chemistry, geology , geomorphology and soils in the Amazon and Orinoco Basins, in: Drever, J.I. (Ed.), The Chemistry of Weathering. N.A.T.O. Advanced Science Institutes Series. D. Reidel, Dordrecht, pp. 324–345.

Staubwasser, M., Weiss, H., 2006. Holocene climate and cultural evolution in late prehistoric–early historic West Asia. Quat. Res. 66, 372–387. doi:10.1016/j.yqres.2006.09.001

Stein, A.F., Draxler, R.., Rolph, G.D., Stunder, B.J.B., Cohen, M.D., Ngan, F., 2016. NOAA's HYSPLIT atmospheric transport and dispersion modeling system. Bull. Am. Meteorol. Soc. 96, 2059–2077. doi:10.1175/BAMS-D-14-00110.1

Steinhilber, F., Abreu, J. a, Beer, J., Brunner, I., Christl, M., Fischer, H., Heikkilä, U., Kubik, P.W., Mann, M., McCracken, K.G., Miller, H., Miyahara, H., Oerter, H., Wilhelms, F., 2012. 9,400 Years of Cosmic Radiation and Solar Activity From Ice Cores and Tree Rings. Proc. Natl. Acad. Sci. U. S. A. 109, 5967–71. doi:10.1073/pnas.1118965109

Steinmann, P., Huon, S., Roos-Barraclough, F., Föllmi, K., 2006. A peat core based estimate of Late-glacial and Holocene methane emissions from northern peatlands. Glob. Planet. Change 53, 233–239. doi:10.1016/j.gloplacha.2006.03.005

Stevens, L.R., Djamali, M., Andrieu-Ponel, V., Beaulieu, J.-L., 2012. Hydroclimatic variations over the last two glacial/interglacial cycles at Lake Urmia, Iran. J. Paleolimnol. 47, 645–660. doi:10.1007/s10933-012-9588-3

Stevens, L.R., Ito, E., Schwalb, A., Wright, H.E., 2006. Timing of atmospheric precipitation in the Zagros Mountains inferred from a multi-proxy record from Lake Mirabad, Iran. Quat. Res. 66, 494–500. doi:10.1016/j.yqres.2006.06.008

Stevens, L.R., Wright Jr, H.E., Ito, E., 2001. Proposed changes in seasonality of climate during the Lateglacial and Holocene at Lake Zeribar, Iran. The Holocene 11, 747–755. doi:10.1191/09596830195762

Stichel, T., Frank, M., Rickli, J., Hathorne, E.C., Haley, B. a., Jeandel, C., Pradoux, C., 2012. Sources and input mechanisms of hafnium and neodymium in surface waters of the Atlantic sector of the Southern Ocean. Geochim. Cosmochim. Acta 94, 22–37. doi:10.1016/j.gca.2012.07.005

Street-Perrott, F.A., Roberts, N., 1983. Fluctuations in closed basin lakes as an indicator of past atmospheric circulation patterns, in: Street-Perrott, A., Beran, M., Robert, R. (Eds.), Variations in the Global Water Budget. Springer Netherlands, pp. 331–345. doi:10.1007/978-94-009-6954-4_26

Stuiver, M., Braziunas, T.F., 1991. Climatic , Solar , Oceanic , and Geomagnetic influences on Late-Glacial and Holocene Atmospheric ^{14}C / ^{12}C Change. Quat. Res. 35, 1–24.

Stuiver, M., Reimer, P.. J., Bard, E.., Beck, J.. W., Burr, G.. S., Hughen, K.A., Kromer, B., McCormac, G., van der Plicht, J., Spurk, M., 1998. INTCAL98 radiocarbon age calibration, 24,000-0 cal BP. Radiocarbon 40, 1041–1083.

Taboada, T., Cortizas, A.M., García, C., García-Rodeja, E., 2006. Particle-size fractionation of titanium and zirconium during weathering and pedogenesis of granitic rocks in NW Spain. Geoderma 131, 218–236. doi:10.1016/j.geoderma.2005.03.025

Talebi, T., Ramezani, E., Djamali, M., Lahijani, H.A.K., Naqinezhad, A., Alizadeh, K., Andrieu-Ponel, V., 2016. The Late-Holocene climate change, vegetation dynamics, lake-level changes and anthropogenic impacts in the Lake Urmia region, NW Iran. Quat. Int. 408, 40–51. doi:10.1016/j.quaint.2015.11.070

Tegen, I., Lacis, A., 1996. Modeling of particle size distribution and its influence on the radiative properties of mineral dust aerosol. J. Geophys. Res. 101, 19237–19244.

Thomas, D.S.G., Bateman, M.D., Mehrshahi, D., O'hara, S.L., 1997. Development and environmental significance of an eolian sand ramp of Last-Glacial Age, Central Iran. Quat. Res. 48, 155–161. doi:10.1006/qres.1997.1923

Tierney, J.E., Russell, J.M., Huang, Y., Damsté, J.S.S., Hopmans, E.C., Cohen, A.S., 2008. Northern hemisphere controls on tropical southeast African climate during the past 60,000 years. Science 322, 252–5. doi:10.1126/science.1160485

Tolonen, K., Turunen, J., 1996. Accumulation rates of carbon in mires in Finland and implications for climate change. The Holocene 6, 171–178.

Tolouei, J., 1995. Geochemical and hydrochemical investigations of chemical percipitated pahses in Urmia Lake evaporative basin. University of Tehran.

Torrence, C., Compo, G.P., 1995. A Practical Guide to Wavelet Analysis. Bull. Am. Meteorol. Soc. 79, 61–78.

Torres, E., Colominas, M.A., Schlotthauer, G., Flandrin, P., 2011. A complete ensemble empirical mode decomposition with adaptive noise, in: IEEE Int. Conf. on Acoust., Speech and Signal Proc. ICASSP-11, Prague (CZ). IEEE, Prague, pp. 4144–4147. doi:CFP11ICA-ART

Turner, R., Roberts, N., Jones, M.D., 2008. Climatic pacing of Mediterranean fire histories from lake sedimentary microcharcoal. Glob. Planet. Change 63, 317–324. doi:10.1016/j.gloplacha.2008.07.002

UNEP, 2012. The Drying of Iran's Lake Urmia and its environmental consequences. Environ. Dev. 2, 128–137. doi:10.1016/j.envdev.2012.03.011

Vahed, S.Z., Forouhandeh, H., Hassanzadeh, S., Klenk, H.P., Hejazi, M.A., Hejazi, M.S., 2011. Isolation and identification of halophilic bacteria from Urmia Lake in Iran. Microbiology 80, 834–841. doi:10.1134/S0026261711060191

Van Zeist, W., Bottema, S., 1977. Palynological investigations in western Iran. Palaeohistoria XIX.

Van Zeist, W., H . E . Wright, J.., 1963. Preliminary Pollen Studies at Lake Zeribar , Zagros Mountains , Southwestern Iran. Science (80-.). 140, 65–67.

Vandenberghe, J., Renssen, H., van Huissteden, K., Nugteren, G., Konert, M., Lu, H., Dodonov, A., Buylaert, J.P., 2006. Penetration of Atlantic westerly winds into Central and East Asia. Quat. Sci. Rev. 25, 2380–2389. doi:10.1016/j.quascirev.2006.02.017

Vengosh, a., 2013. Salinization and Saline Environments. Treatise Geochemistry Second Ed. 11, 325–378. doi:10.1016/B978-0-08-095975-7.00909-8

Vermoere, M., Bottema, S., Vanhecke, L., Waelkens, M., Paulissen, E., Smets, E., 2002. Palynological evidence for late-Holocene human occupation recorded in two wetlands in SW Turkey. The Holocene 12, 569–584. doi:10.1191/0959683602hl568rp

Vita-Finzi, C., 1968. Late quaternary alluvial chronology of Iran. Geol. Rundschau 58, 91–973.

Wang, Y., Cheng, H., Edwards, R.L., He, Y., Kong, X., Science, S., Series, N., May, N., 2005. The Holocene Asian monsoon : links to solar changes and North Atlantic Climate. Science (80-.). 308, 854–857.

Wasylikowa, E.K., Witkowski, A. (Eds.), 2008. Diatom Monographs Vol.8 The palaeoecology of Lake Zeribar and surrounding areas , Western Iran , during the last 48000 years. A.R.G.Gantner Verlag K.G.

Wasylikowa, K., 2005. Palaeoecology of Lake Zeribar, Iran, in the Pleniglacial, Lateglacial and Holocene, reconstructed from plant macrofossils. The Holocene 15, 720–735. doi:10.1191/0959683605hl846rp

Wasylikowa, K., Witkowski, A., Walanus, A., Hutorowicz, A., Alexandrowicz, S.W., Langer, J.J., 2006. Palaeolimnology of Lake Zeribar, Iran, and its climatic implications. Quat. Res. 66, 477–493. doi:10.1016/j.yqres.2006.06.006

Waterson, E.J., Canuel, E. a., 2008. Sources of sedimentary organic matter in the Mississippi River and adjacent Gulf of Mexico as revealed by lipid biomarker and ??13CTOC analyses. Org. Geochem. 39, 422–439. doi:10.1016/j.orggeochem.2008.01.011

Wedepohl, K.H., 1995. The composition of the continental crust. Geochim. Cosmochim. Acta 59, 1217–1232.

Weiguo, L., Xiahong, F., Youfeng, N., Qingle, Z., Yunning, C., Zhisheng, a N., 2005. delta13C variation of C3 and C4 plants across an Asian monsoon rainfall gradient in arid northwestern China. Glob. Chang. Biol. 11, 1094–1100. doi:10.1111/j.1365-2486.2005.00969.x

Wick, L., Lemcke, G., Sturm, M., 2003. Evidence of Lateglacial and Holocene climatic change and human impact in eastern Anatolia: high-resolution pollen, charcoal, isotopic and geochemical records from the laminated sediments of Lake Van, Turkey. The Holocene 13, 665–675. doi:10.1191/0959683603hl653rp

Williams, W.D., 1998. Salinity as a determinant of the structure of biological communities in salt lakes. Hydrobiologia 381, 191–201. doi:10.1023/A:1003287826503

Williams, W.D., Boulton, a. J., Taaffe, R.G., 1990. Salinity as a determinant of salt lake fauna: a question of scale. Hydrobiologia 197, 257–266. doi:10.1007/BF00026955

Wu, B., Wang, J., 2002. Winter Arctic Oscillation, Siberian High and East Asian Winter Monsoon. Geophys. Res. Lett. 29, 3–6. doi:10.1029/2002GL015373

Wurtsbaugh, W.A., 1992. Ecology food-web modification by an invertebrate predator in the Great Salt Lake (USA). Oecologia 89, 168–175. doi:10.1007/s00442-007

Wurtsbaugh, W., Gliwicz, M., 2001. Limnological control of brine shrimp population dynamics and cyst production in the Great Salt Lake, Utah. Hydrobiologia 466, 119–132.

Xiao, J., Chang, Z., Si, B., Qin, X., Itoh, S., Lomtatidze, Z., 2009. Partitioning of the grain-size components of Dali Lake core sediments : evidence for lake-level changes during the Holocene. J. Paleolimnol. 42, 249–260. doi:10.1007/s10933-008-9274-7

Yang, T., Han, G., Wu, Q., Xu, Z., 2013. Use of rare earth element patterns to trace the provenance of the atmospheric dust near Beijing, China. Environ. Earth Sci. 68, 871–879. doi:10.1007/s12665-012-1791-z

Yeloff, D., Mauquoy, D., 2006. The influence of vegetation composition on peat humification: implications for palaeoclimatic studies. Boreas 35, 662–673. doi:10.1111/j.1502-3885.2006.tb01172.x

Zaccone, C., Cocozza, C., Cheburkin, a. K., Shotyk, W., Miano, T.M., 2008. Distribution of As, Cr, Ni, Rb, Ti and Zr between peat and its humic fraction along an undisturbed ombrotrophic bog profile (NW Switzerland). Appl. Geochemistry 23, 25–33. doi:10.1016/j.apgeochem.2007.09.002

Zaccone, C., Shotyk, W., Cocozza, C., Miano, T.M., 2010. Major and trace elements biogeochemistry and C sequestration in bog soils, in: 19th World Congress of Soil Science, Soil Solutions for a Changing World. Brisbane, pp. 33–36.

Zdanowicz, C., Hall, G., Vaive, J., Amelin, Y., Percival, J., Girard, I., Biscaye, P., Bory, A., 2006. Asian dustfall in the St. Elias Mountains, Yukon, Canada. Geochim. Cosmochim. Acta 70, 3493–3507. doi:10.1016/j.gca.2006.05.005

Zeinoddini, M., Tofighi, M.A., Vafaee, F., 2009. Evaluation of dike-type causeway impacts on the flow and salinity regimes in Urmia Lake, Iran. J. Great Lakes Res. 35, 13–22. doi:10.1016/j.jglr.2008.08.001

Zhang, Z., Zhao, M., Lu, H., Faiia, A.M., 2003. Lower temperature as the main cause of C4 plant declines during the glacial periods on the Chinese Loess Plateau. Earth Planet. Sci. Lett. 214, 467–481. doi:10.1016/S0012-821X(03)00387-X

Zhao, W., Sun, Y., Balsam, W., Lu, H., Liu, L., Chen, J., Ji, J., 2014. Hf-Nd isotopic variability in mineral dust from Chinese and Mongolian deserts: implications for sources and dispersal. Sci. Rep. 4, 5837, 1–6. doi:10.1038/srep05837

Zhao, Y., Yu, Z., Zhao, W., 2011. Holocene vegetation and climate histories in the eastern Tibetan Plateau: Controls by insolation-driven temperature or monsoon-derived precipitation changes? Quat. Sci. Rev. 30, 1173–1184. doi:10.1016/j.quascirev.2011.02.006

Zheng, Y., Zhou, W., Meyers, P. a., Xie, S., 2007. Lipid biomarkers in the Zoigê-Hongyuan peat deposit: Indicators of Holocene climate changes in West China. Org. Geochem. 38, 1927–1940. doi:10.1016/j.orggeochem.2007.06.012

Zhou, W., Lu, X., Wu, Z., Deng, L., Jull, A.J.T., Donahue, D., Beck, W., 2002. Peat record reflecting Holo- cene climatic change in the Zoigê Plateau and AMS radiocarbon dating. Chinese Sci. Bull. 74, 66–70.

Zhou, W., Xie, S., Meyers, P. a., Zheng, Y., 2005. Reconstruction of late glacial and Holocene climate evolution in southern China from geolipids and pollen in the Dingnan peat sequence. Org. Geochem. 36, 1272–1284. doi:10.1016/j.orggeochem.2005.04.005

Zohary, D., Hopf, M., 2000. Domestication of Plants in the Old World. The origin and spread of cultivated plants in West Asia, Europe and the Nile Valley. 3, 3rd ed. Oxford University Press Inc., New York.

Zoljoodi, M., Didevarasl, A., 2014. Water-level fluctuations of Urmia Lake: relationship with the long-term changes of meteorological variables (solutions for water-crisis management in urmia lake basin). Atmos. Clim. Sci. 4, 358–368. doi:10.4236/acs.2014.43036

Zonneveld, K. A. F., Ganssen, G., Troelstra, S., Versteegh, G.J.M., Visscher, H., 1997. Mechanisms forcing abrupt fluctuations of the indian ocean summer monsoon during the last deglaciation. Quat. Sci. Rev. 16, 187–201. doi:10.1016/S0277-3791(96)00049-2

APPENDIX A

CORE LOGS OF PEAT AND LAKE SEDIMENT CORE SAMPLES FROM NW IRAN

Core No.:NES3-1

Location: Neor Lake-IRAN
Date:02-24-2011
Analyzed by: Arash Sharifi

End of the Core @ 99.5 cm
Length @ 04-06-2011=97.5 cm
Length @ = cm

cm	^{14}C	Organic	Inorganic	
5				Dark brown peat
10				Light brown peat with fine grain sediments
15				Dark brown to black peat
20				Light brown peat, coarsely laminated with intervals of brown layers. Contains fine sediments.
25				Brown to dark brown peat with dark brown to black brown layers (1.5-2.0 cm thick). Some holes and pockets.
30				
35				Dark brown peat with lot of holes and pockets.
40				
45				
50				Brown to light brown peat with fine grain sediments. Lot of holes and pockets.
55				Brown peat with lot of holes and pockets.
60				Brown to gray peat with fine sediments.
65				Dark brown to dark gray-brwon peat with fine sediments. Unclear layering of gray-brown material.
70				
75				
80				Dark brown peat with holes and pockets.
85				
90				
95				Dark brown to black brown peat.
100				

Core No.:NES3-2

Location: Neor Lake-IRAN
Date:02-24-2011
Analyzed by: Arash Sharifi

End of the Core @ 100 cm
Length @ 04-06-2011= 96.5 cm
Length @ = cm

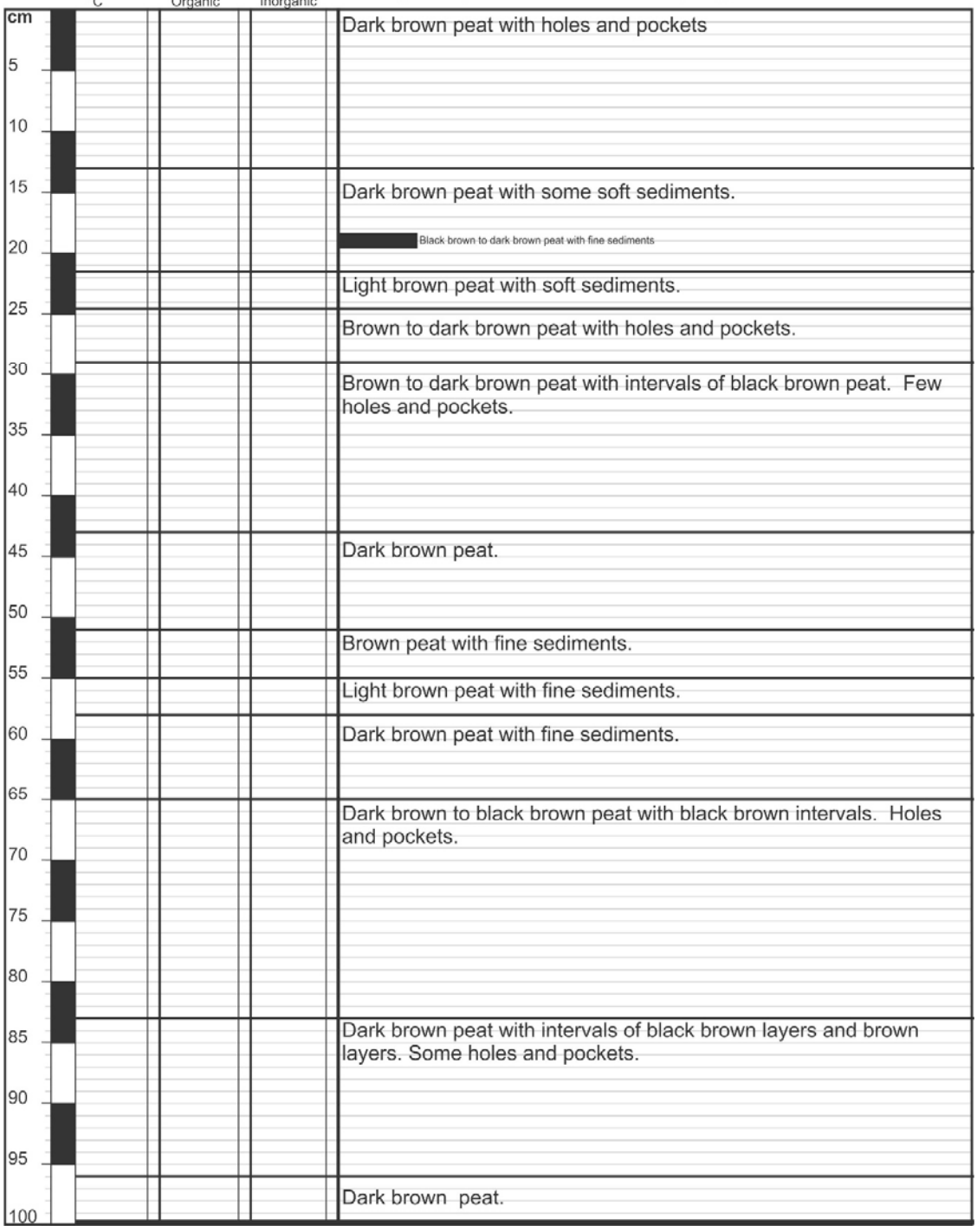

Core No.:NES3-3

Location: Neor Lake-IRAN
Date:02-25-2011
Analyzed by: Arash Sharifi

End of the Core @ 99.5 cm
Length @ 04-06-2011=98.6 cm
Length @ = cm

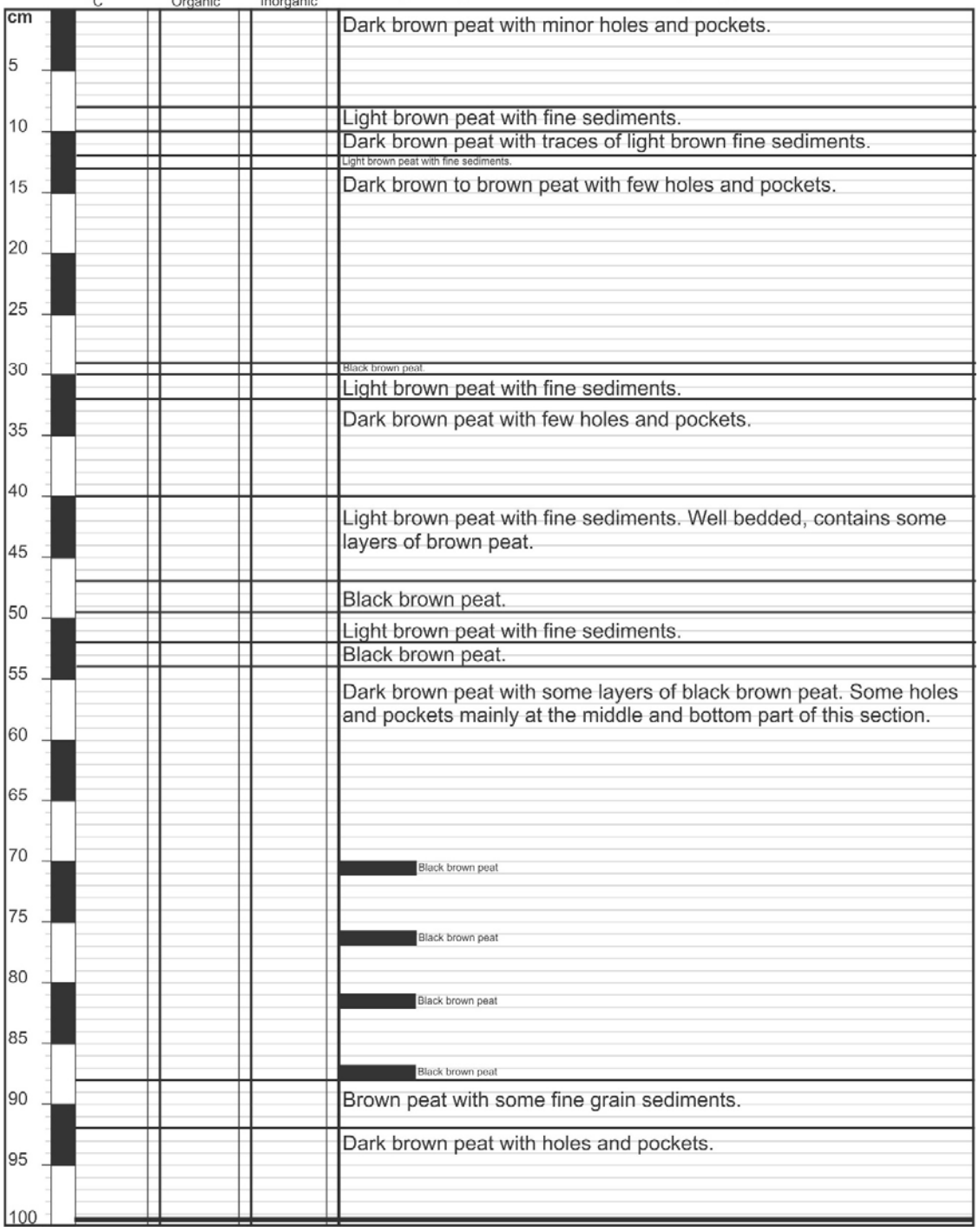

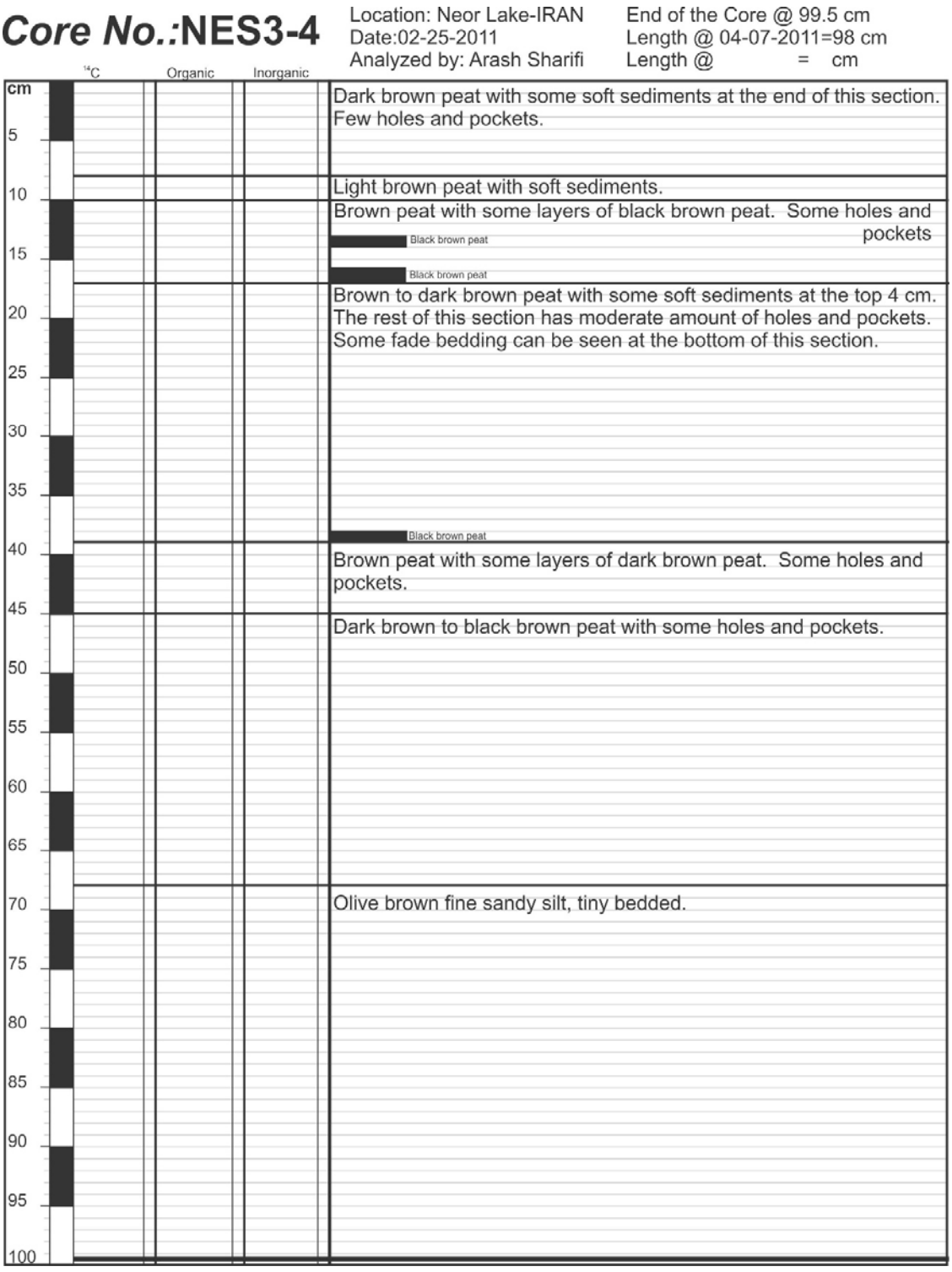
Core No.:NES3-4
Location: Neor Lake-IRAN
Date:02-25-2011
Analyzed by: Arash Sharifi
End of the Core @ 99.5 cm
Length @ 04-07-2011=98 cm
Length @ = cm
14C
Organic
Inorganic
cm
5
10
15
20
25
30
35
40
45
50
55
60
65
70
75
80
85
90
95
100
Dark brown peat with some soft sediments at the end of this section. Few holes and pockets.
Light brown peat with soft sediments.
Brown peat with some layers of black brown peat. Some holes and pockets
Black brown peat
Black brown peat
Brown to dark brown peat with some soft sediments at the top 4 cm. The rest of this section has moderate amount of holes and pockets. Some fade bedding can be seen at the bottom of this section.
Black brown peat
Brown peat with some layers of dark brown peat. Some holes and pockets.
Dark brown to black brown peat with some holes and pockets.
Olive brown fine sandy silt, tiny bedded.

Core No.:NES3-5

Location: Neor Lake-IRAN
Date:02-28-2011
Analyzed by: Arash Sharifi

End of the Core @ 99 cm
Length @ 04-07-2011=97.5 cm
Length @ = cm

Core No.:NES3-6

Location: Neor Lake-IRAN
Date:02-28-2011
Analyzed by: Arash Sharifi

End of the Core @ 100 cm
Length @ 04-08-2011=98.5 cm
Length @ = cm

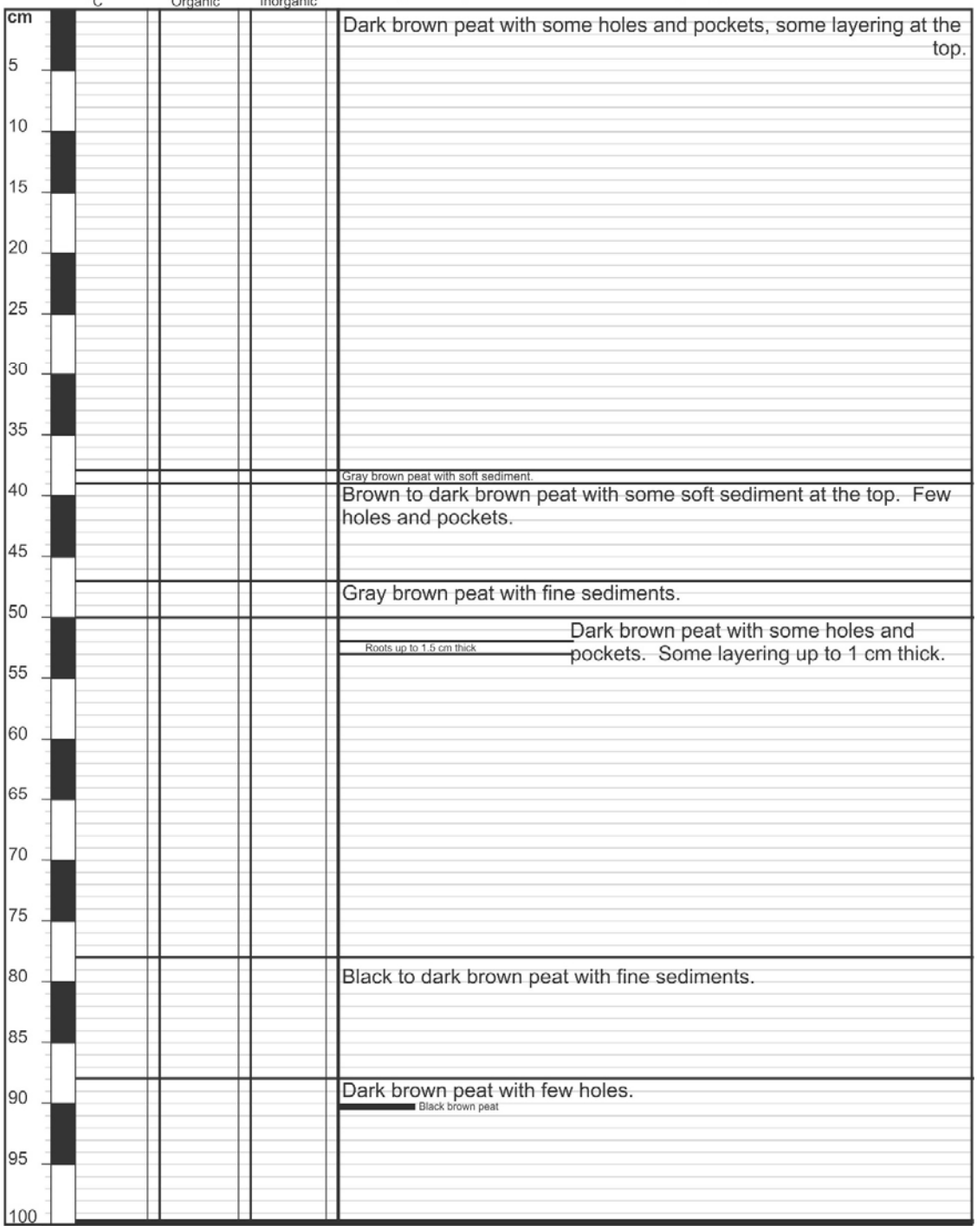

Core No.:NES3-7

Location: Neor Lake-IRAN
Date:02-28-2011
Analyzed by: Arash Sharifi

End of the Core @ 100 cm
Length @ 04-08-2011=98.3 cm
Length @ = cm

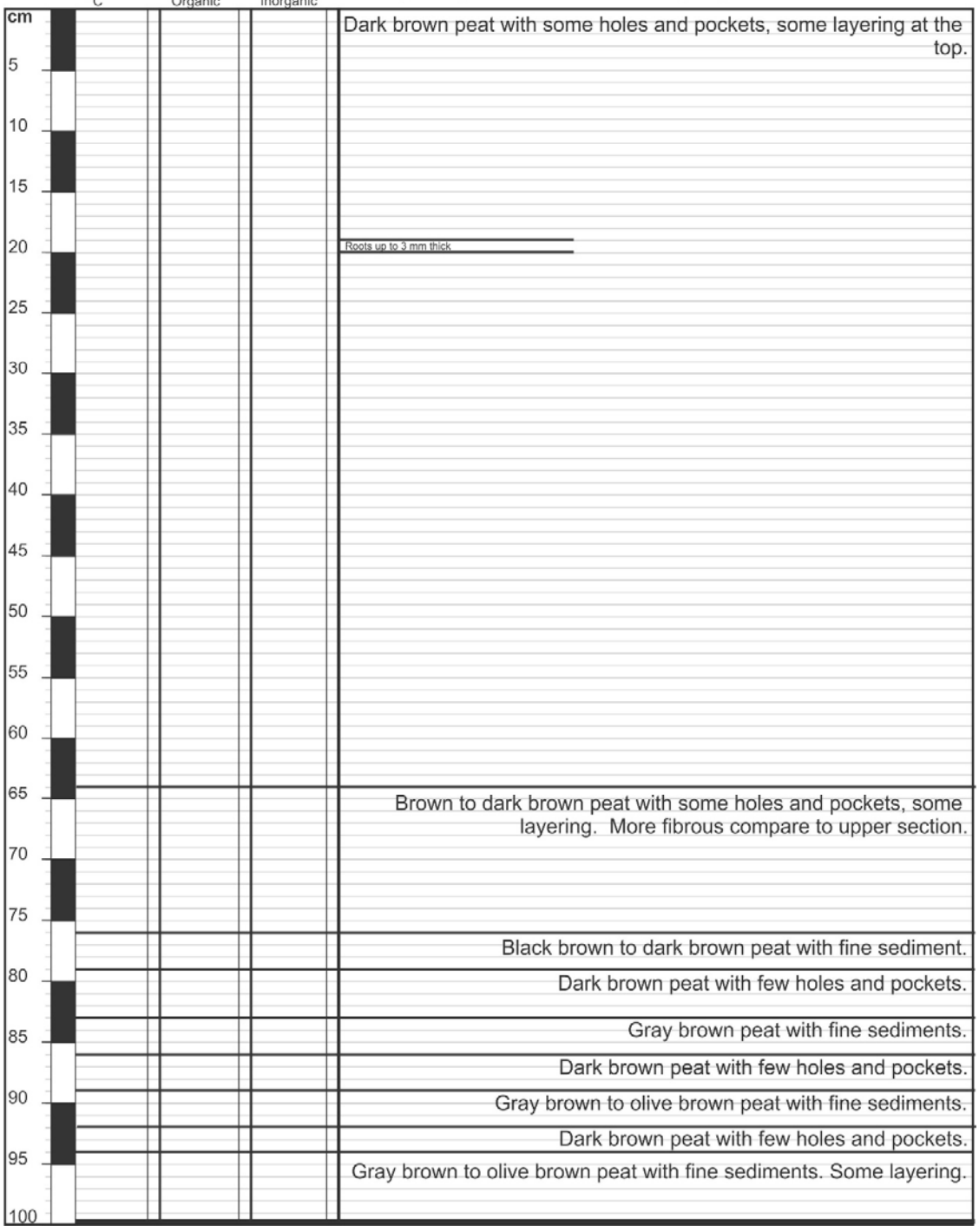


Core No.:NES3-8
Location: Neor Lake-IRAN
Date:02-28-2011
Analyzed by: Arash Sharifi
End of the Core @ 101 cm
Length @ 04-08-2011=99.5 cm
Length @ = cm
14C
Organic
Inorganic
cm
5
10
15
20
25
30
35
40
45
50
55
60
65
70
75
80
85
90
95
100
Dark brown peat with some soft sediments and few holes.
Dark brown peat with soft sediments.
Black brown peat with some soft sediments.
Brown to dark brown to olive-brown soft sediments (fine sandy silt) showing some lamination.
Roots up to 3 mm thick
Roots up to 3 mm thick
Light gray to yellow-gray to olive-brown soft sediments (fine sandy silt) with some yellow patches.
Light brown sandy silt.

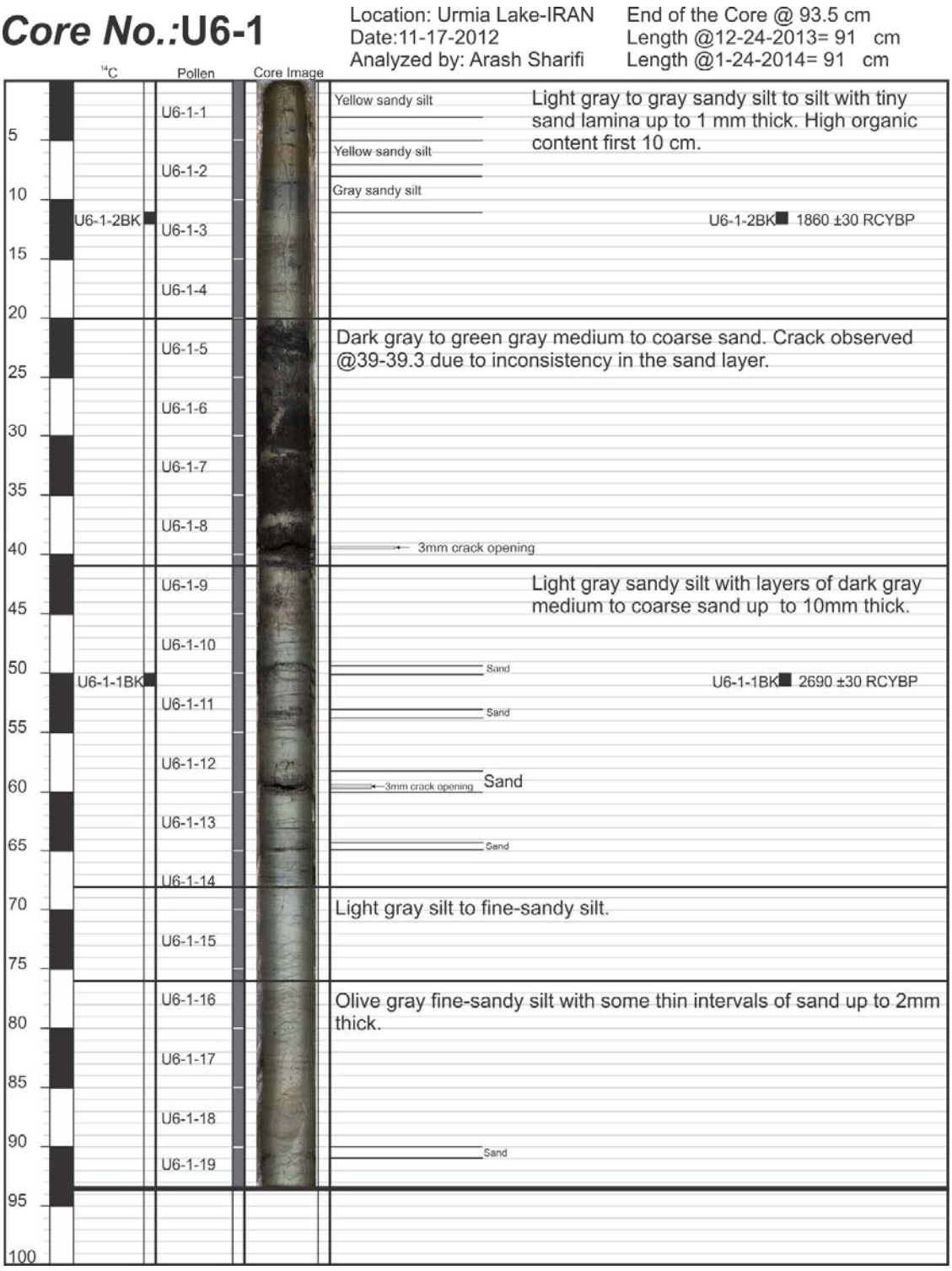
Core No.:U6-1
Location: Urmia Lake-IRAN
Date:11-17-2012
Analyzed by: Arash Sharifi
End of the Core @ 93.5 cm
Length @12-24-2013= 91 cm
Length @1-24-2014= 91 cm
14C
Pollen
Core Image
U6-1-1
U6-1-2
U6-1-3
U6-1-4
U6-1-5
U6-1-6
U6-1-7
U6-1-8
U6-1-9
U6-1-10
U6-1-11
U6-1-12
U6-1-13
U6-1-14
U6-1-15
U6-1-16
U6-1-17
U6-1-18
U6-1-19
U6-1-2BK
U6-1-1BK
5
10
15
20
25
30
35
40
45
50
55
60
65
70
75
80
85
90
95
100
Yellow sandy silt
Yellow sandy silt
Gray sandy silt
Light gray to gray sandy silt to silt with tiny sand lamina up to 1 mm thick. High organic content first 10 cm.
U6-1-2BK 1860 ±30 RCYBP
Dark gray to green gray medium to coarse sand. Crack observed @39-39.3 due to inconsistency in the sand layer.
3mm crack opening
Light gray sandy silt with layers of dark gray medium to coarse sand up to 10mm thick.
Sand
Sand
3mm crack opening
Sand
Sand
U6-1-1BK 2690 ±30 RCYBP
Light gray silt to fine-sandy silt.
Olive gray fine-sandy silt with some thin intervals of sand up to 2mm thick.
Sand

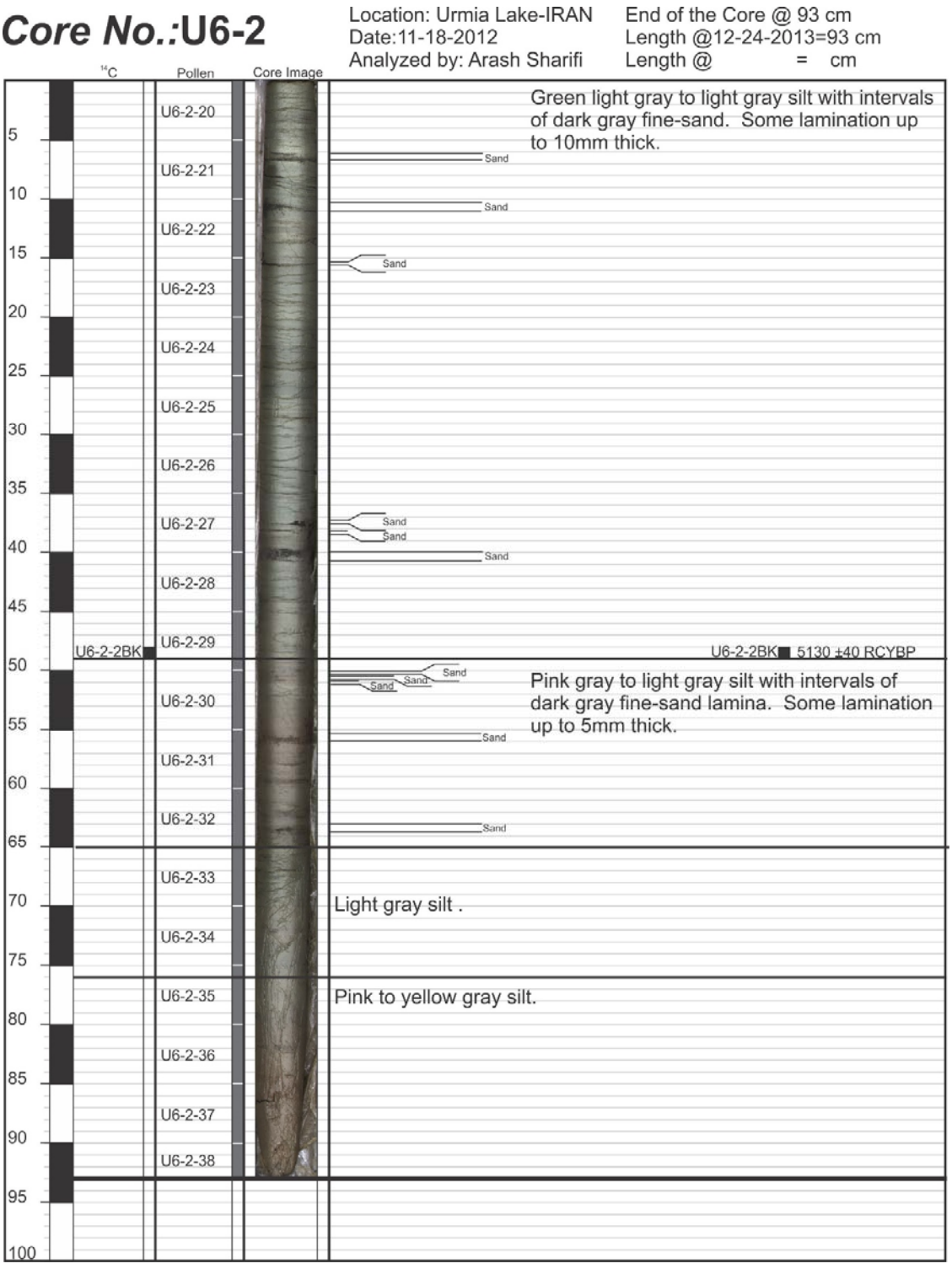
Core No.:U6-2
Location: Urmia Lake-IRAN
Date:11-18-2012
Analyzed by: Arash Sharifi
End of the Core @ 93 cm
Length @12-24-2013=93 cm
Length @ = cm
14C
Pollen
Core Image
U6-2-20
U6-2-21
U6-2-22
U6-2-23
U6-2-24
U6-2-25
U6-2-26
U6-2-27
U6-2-28
U6-2-29
U6-2-30
U6-2-31
U6-2-32
U6-2-33
U6-2-34
U6-2-35
U6-2-36
U6-2-37
U6-2-38
U6-2-2BK
U6-2-2BK 5130 ±40 RCYBP
Green light gray to light gray silt with intervals of dark gray fine-sand. Some lamination up to 10mm thick.
Pink gray to light gray silt with intervals of dark gray fine-sand lamina. Some lamination up to 5mm thick.
Light gray silt .
Pink to yellow gray silt.
Sand
5
10
15
20
25
30
35
40
45
50
55
60
65
70
75
80
85
90
95
100

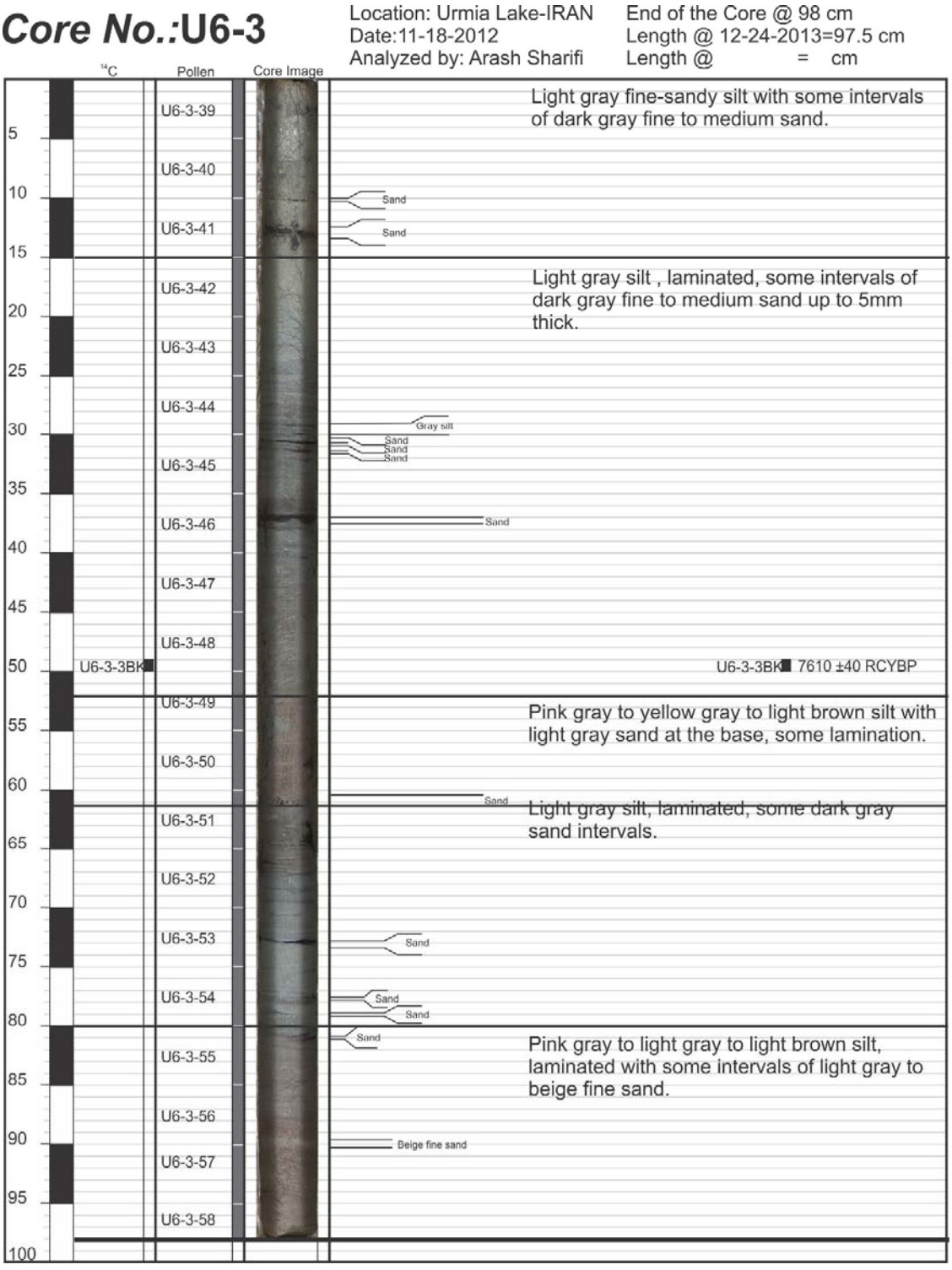
Core No.:U6-3
Location: Urmia Lake-IRAN
Date:11-18-2012
Analyzed by: Arash Sharifi
End of the Core @ 98 cm
Length @ 12-24-2013=97.5 cm
Length @ = cm
14C
Pollen
Core Image
U6-3-39
U6-3-40
U6-3-41
U6-3-42
U6-3-43
U6-3-44
U6-3-45
U6-3-46
U6-3-47
U6-3-48
U6-3-49
U6-3-50
U6-3-51
U6-3-52
U6-3-53
U6-3-54
U6-3-55
U6-3-56
U6-3-57
U6-3-58
U6-3-3BK
U6-3-3BK 7610 ±40 RCYBP
Sand
Gray silt
Beige fine sand
Light gray fine-sandy silt with some intervals of dark gray fine to medium sand.
Light gray silt , laminated, some intervals of dark gray fine to medium sand up to 5mm thick.
Pink gray to yellow gray to light brown silt with light gray sand at the base, some lamination.
Light gray silt, laminated, some dark gray sand intervals.
Pink gray to light gray to light brown silt, laminated with some intervals of light gray to beige fine sand.

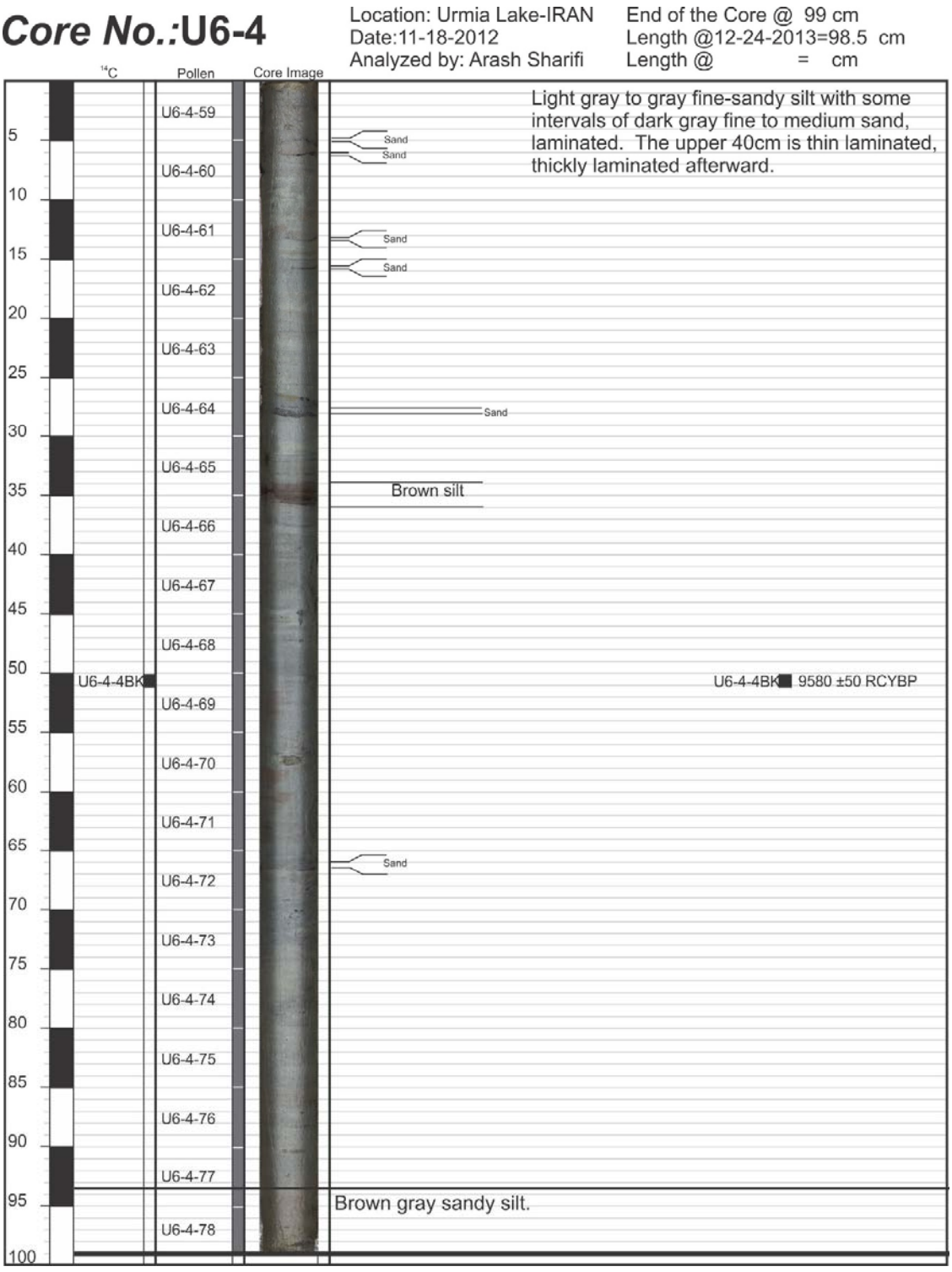
Core No.:U6-4
Location: Urmia Lake-IRAN
Date:11-18-2012
Analyzed by: Arash Sharifi
End of the Core @ 99 cm
Length @12-24-2013=98.5 cm
Length @ = cm
14C
Pollen
Core Image
Light gray to gray fine-sandy silt with some intervals of dark gray fine to medium sand, laminated. The upper 40cm is thin laminated, thickly laminated afterward.
Sand
Sand
Sand
Sand
Sand
Brown silt
U6-4-4BK
U6-4-4BK 9580 ±50 RCYBP
Brown gray sandy silt.
U6-4-59
U6-4-60
U6-4-61
U6-4-62
U6-4-63
U6-4-64
U6-4-65
U6-4-66
U6-4-67
U6-4-68
U6-4-69
U6-4-70
U6-4-71
U6-4-72
U6-4-73
U6-4-74
U6-4-75
U6-4-76
U6-4-77
U6-4-78
5
10
15
20
25
30
35
40
45
50
55
60
65
70
75
80
85
90
95
100

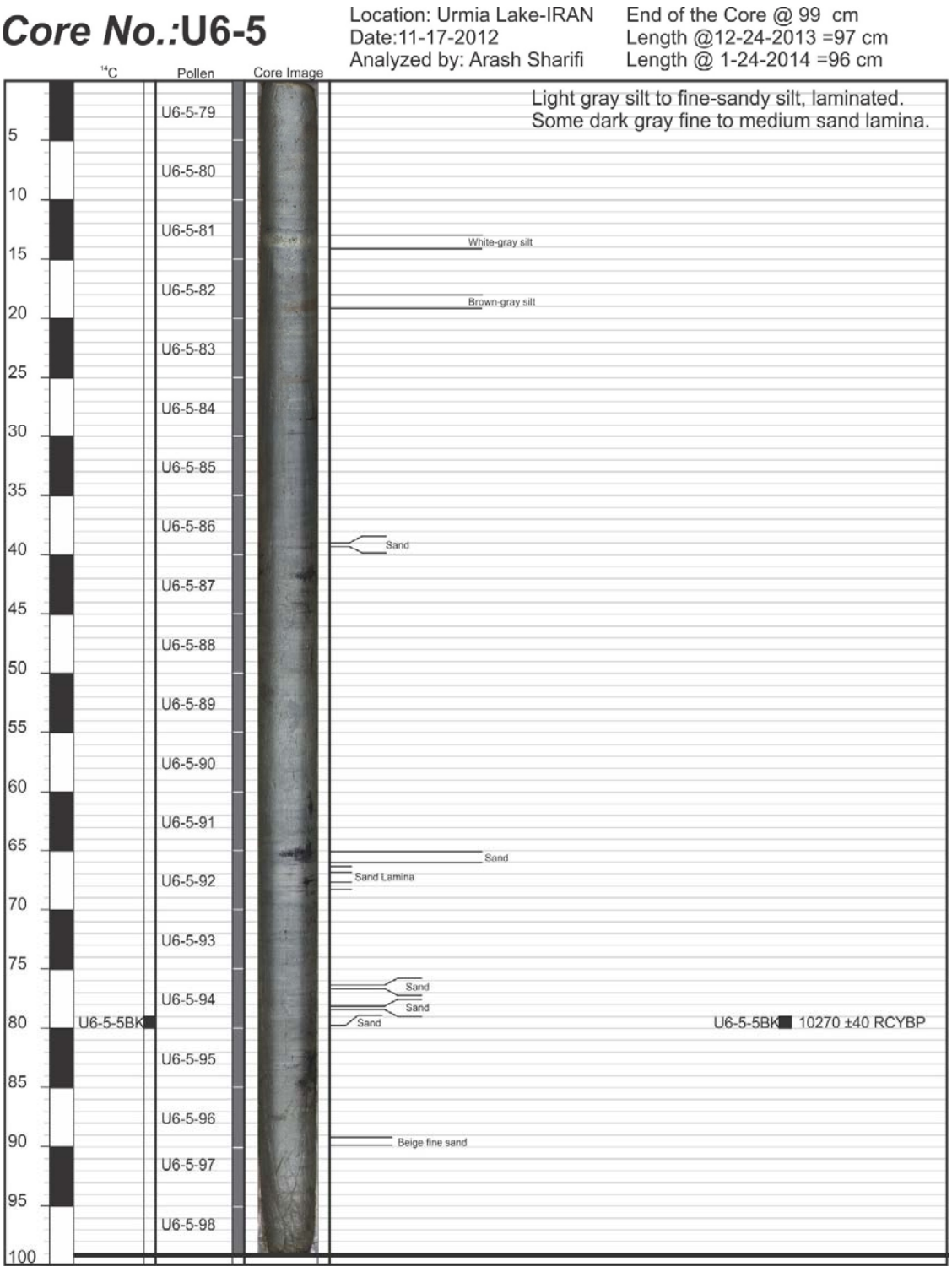
Core No.:U6-5
Location: Urmia Lake-IRAN
Date:11-17-2012
Analyzed by: Arash Sharifi
End of the Core @ 99 cm
Length @12-24-2013 =97 cm
Length @ 1-24-2014 =96 cm
14C
Pollen
Core Image
Light gray silt to fine-sandy silt, laminated.
Some dark gray fine to medium sand lamina.
U6-5-79
U6-5-80
U6-5-81
U6-5-82
U6-5-83
U6-5-84
U6-5-85
U6-5-86
U6-5-87
U6-5-88
U6-5-89
U6-5-90
U6-5-91
U6-5-92
U6-5-93
U6-5-94
U6-5-95
U6-5-96
U6-5-97
U6-5-98
White-gray silt
Brown-gray silt
Sand
Sand
Sand Lamina
Sand
Sand
Sand
Beige fine sand
U6-5-5BK
U6-5-5BK 10270 ±40 RCYBP
5
10
15
20
25
30
35
40
45
50
55
60
65
70
75
80
85
90
95
100

APPENDIX B

COMPILATION OF THE URMIA LAKE'S HYDROCHEMICAL DATA

Supplementary Data File

Description:

The accompanying Excel spreadsheet available hydrochemical data from Urmia Lake, its peripheral ponds and major tributaries from 1977 to 2010.

Filename:

Table SI-1.xlsx

APPENDIX C

EXTRACTION CHROMATOGRAPHY SCHEME FOR AEROSOL ANALYSIS AND INSTRUMENTAL SETTING FOR ISOTOPE MEASUREMENTS*[3]

Sample digestion

In order to ensure complete dissolution of refractory minerals for accurate elemental and isotope analysis, we preferred high-temperature flux fusion of the aerosol samples with high-purity lithium metaborate ($LiBO_2$) over conventional hot-plate or Parr bomb acid digestion methods. While commercially available flux must be additionally purified to ensure low background levels for processing extra-terrestrial material, the relatively higher concentrations of Sr, Hf and the REE in terrestrial aerosols allow for the direct use of Puratronic $LiBO_2$ (Alfa Aesar, part # 10739) without the need for further purification of the flux. A brief description of alkali fusion is included in the following. Extensive details regarding the fusion technique can be found in Pourmand and Dauphas (2010) and Pourmand et al. (2012).

Approximately 250 mg of $LiBO_2$ was transferred to an 8-mL high-purity graphite crucible (Spex Certiprep part # 7152HP). The ashed aerosol sample (15-30 mg) was weighed onto a depression at the center of the flux and approximately 150 mg of ultra-pure grade lithium bromide (Spex Certiprep part # FFB-103-03) was added to the mix as non-wetting agent to ensure complete recovery of the melt. The sample-flux mixture was capped with a second crucible and fused in a furnace at 1070 °C for 12 minutes. The melt was directly transferred to 25 mL of 6 mol L^{-1} HNO_3 in a PFA savillex vial and the shattered glass was dissolved within minutes on a Vortex mixer. Procedural blanks were prepared similarly without the addition of sample powder.

Extraction chromatography

Concentrated nitric (HNO_3) and hydrochloric (HCl) acids were distilled once from ACS grade using Savillex DST-1000 sub-boiling stills. The distilled acids were titrated against certified 0.1 and 1 mol L^{-1} NaOH solutions to determine the concentrations accurately. High-purity (Optima grade) Hydrofluoric acid (HF) was used directly without distillation. 30-mL Savillex vials (part # 200-030-30) were cleaned first in a solution of 50% HNO_3 followed by boiling in a mixture of 1:3 HNO_3: HCl (Aqua regia) and dried in class-100 laminar flow hoods. Extraction chromatography procedures were conducted inside a class-100 Microzone trace-metal workstation at the Neptune Isotope Lab (NIL). In order to separate Sr, Hf, Nd and the REE from matrix elements, we developed a novel, 3-stage extraction chromatography scheme based on the studies of Horwitz et al. (1992)

[3] This methodology has been published as part of supplementary information to the following manuscript: Pourmand, A., Prospero, J.M., Sharifi, A., 2014. Geochemical fingerprinting of trans-Atlantic African dust based on radiogenic Sr-Nd-Hf isotopes and rare earth element anomalies. Geology 42, 675–678. doi:10.1130/G35624.1.

for Sr and Horwitz et al. (2005), Pourmand et al. (2010) and Pourmand et al. (2012) for Hf, Nd and the REE.

The first and second steps of elemental separation involved two pre-packed, 1-mL cartridges containing Sr (4,4'(5')-di-t-butylcyclohexano 18-crown-6 (crown ether) in 1-octanol, part #SR1ML-R50-S) and TODGA (N,N,N',N'-tetra-n-octyldiglycolamide, part# DN1ML-R200-S) extraction chromatography resins from Eichrom Inc. A third step was necessary to separate Nd from other REE, particularly Sm. According to Fig. 1 of Horwitz et al. (1992), the affinity (k') of the extraction resin is highest for Sr in HNO3 concentrations that exceed 6 mol L^{-1}. The resin shows no affinity for interfering cations such as Ca, Mg and other trace elements (including the REE) in this acid concentration. In contrast, the resin affinity for Sr drops significantly below 1 in 0.01 mol L^{-1} HNO_3, allowing for quantitative separation of Sr from matrix elements. In comparison, the TODGA resin shows exceptionally high affinity for Hf and the REE in 6 mol L^{-1} HNO_3 (Fig. 1 in Pourmand and Dauphas 2010).

Following these observations and the elution curves developed for Sr, Hf and the REE in the above-mentioned studies, the first purification stage was devised with Sr and TODGA cartridges mounted in tandem on a 12-slot vacuum box (Eichrom part # AC-12-LINER) equipped with a pneumatic pressure regulator. The cartridge assembly was conditioned with 10 mL of 0.01 mol L^{-1} HCl to remove resin background elements, followed by 5 mL of 6 mol L^{-1} HNO_3 to convert the resin medium to the sample load solution. The dissolved samples were subsequently loaded onto the Sr + TODGA array and the eluent, which contained the matrix elements, was collected in a 50 mL polypropylene centrifuge tube. The cartridges were conditioned with an additional 15 mL of 6 mol L^{-1} HNO_3 to elute residual matrix elements. In the second step, the Sr and TODGA cartridges were detached and treated separately for the remainder of the chromatography procedure. The flow rates for sample load and elemental elution were kept below 1 mL min^{-1} to ensure quantitative elution and reproducibility.

Prior to Sr elution, an additional 20 mL of 6 mol L^{-1} HNO_3 was loaded to the Sr cartridge to eliminate residual matrix elements. Quantitative elution of Sr was achieved in 10 mL of 0.01 mol L-1 HNO_3 and the eluent was directly analyzed on the mass spectrometer for Sr isotopes.

Prior to Hf elution, an additional 5 mL of 6 mol L^{-1} HNO_3 was loaded to remove residual matrix elements from the TODGA resin. Hafnium was subsequently eluted using 3 × 2 mL (6 mL total) of 1 mol L^{-1} HNO_3 + 0.2 mol L^{-1} HF that was kept at an ambient temperature of 90 °C. Pourmand et al. (2010) showed near-quantitative elution of Hf can be achieved in 20 mL of this solution at 70 °C on a 2-mL TODGA cartridge without any loss of the REE from the resin. Using a 1-mL cartridge and increasing the acid temperature allowed for elution of > 70 % of Hf in 6 mL of 1 mol L^{-1} HNO_3 + 0.2 mol L^{-1} HF. The Hf content was sufficient for direct analysis of Hf isotopes. The REE (La-Lu) were subsequently eluted quantitatively from the TODGA resin in 25 mL of 0.01 mol L^{-1} HCl onto a 50 mL centrifuge tube, and the sample was analyzed directly for REE abundances.

In order to minimize the effect of isobaric interferences and allow for high-precision Nd isotope ratio analysis, it was necessary to separate Sm from Nd in the samples. We conducted elution experiments to test the possibility of separating Nd from Sm using the TODGA resin. Small but resolvable differential between the affinity of TODGA resin for light REE (LREE, La-Gd, see Fig. 7 in Horwitz et al., 2005) in low concentrations of HNO3 can be exploited to separate Nd from Sm. The extraction procedure was calibrated by a multi-element standard solution with elemental concentrations of 500 ng g^{-1} using a mixture of La, Ce, Pr, Nd and Sm from mono-elemental standard solutions (1000 ppm, Spex Certiprep) prepared in 3 mol L^{-1} HCl. The multi-element solution was loaded to a 1-mL TODGA and the LREE were eluted in 1 mL increments in 0.0075 mol L^{-1} HNO3. The results (Fig SI1) show that after removing > 80% La-Ce and > 40% of Pr in 4 mL of 0.0075 mol L^{-1} HNO_3, more than 70% of Nd can be eluted in 5 mL of the same acid. The Sm content of the Nd fraction did not exceed 2 %. The residual isobaric interference from ^{144}Sm on ^{144}Nd was accounted for by simultaneous measurement of Sm and Nd isotopes (see the next section below). The elution volume of Sm-free Nd is highly dependent on the accurate calibration of the eluting acid solution. Two liters of 0.0075 mol L^{-1} HNO_3 prepared from concentrated HNO_3 and titrated against certified NaOH solutions was subsequently used for Nd purification of all samples.

For the final step of Nd purification, a new TODGA cartridge was conditioned with 10 mL of 0.01 HCl to remove background contribution from the resin, followed by 5 mL of 3 mol L^{-1} HCl to convert the resin to the load solution. A 10-mL aliquot of 0.01 mol L^{-1} HCl from stage 1 that contained the REE was mixed with concentrated HCl to adjust the load acid concentration to 3 mol L^{-1} HCl. Lanthanum, Ce and Pr were eluted in 4 mL of 0.0075 mol L^{-1} HNO_3 followed by Nd in 5 mL of 0.0075 mol L^{-1} HNO_3. The fraction containing Nd was directly analyzed on the mass spectrometer without further processing. The extraction chromatography procedure is summarized in table SI-1 and Fig. SI-2.

Mass spectrometry

The radiogenic isotopes of Sr ($^{87}Sr/^{86}Sr$), Hf ($^{176}Hf/^{177}Hf$), Nd ($^{143}Nd/^{144}Nd$) and the REE (La-Lu) abundances were measured on a Thermofisher Scientific Neptune Plus multi-collection inductively coupled plasma mass spectrometer (MC-ICP-MS) at the Neptune Isotope Lab (NIL), the University of Miami. The instrument at NIL is equipped with 9 Faraday collectors that can be associated to eight 1011 Ω, and two 1010 Ω and 1012 Ω amplifies to extend the dynamical range of the measurements. Additional details regarding the Neptune instrument at NIL can be found in Pourmand et al. (2014). The collector configuration for Sr, Nd, Hf isotope measurements and the REE are shown in table SI-2. Details of REE analysis are extensively discussed elsewhere (Pourmand et al., 2012). The sample introduction system for Sr isotope measurements involved a high-volume nebulizer at a nominal flow rate of 400 µL min-1 paired with a quartz stable sample introduction (SSI) system. Neodymium and Hf isotopes and the REE abundances were measured using an Apex-Q desolvation nebulizer paired with a 92 µL min-1 nebulizer and high-purity nitrogen gas. High-performance Jet sampler and X-series skimmer cones were used for all measurements.

The cup configuration for each systematic was loaded at the beginning of each analytical session followed by an automatic gain calibration of the Faraday collectors through the Neptune software. The signal sensitivity and stability were optimized using the Neptune's Tune solution, which contains 200 ng g^{-1} Sr, Nd and Hf. Peak optimization for other REE was achieved using a certified multi-element solution from Spex Certiprep, which was also used for quantification of elemental abundances by standard-sample bracketing technique (Pourmand et al., 2012).

Data acquisition for Sr, Nd and Hf isotopes involved five blocks of ten cycles each at 8.389 s integration time and 3 s magnet settling time. Sample uptake for Sr measurements was 70 seconds; higher uptake time of 110 seconds was needed for other systematics due to lower nebulizer flow rate. Baseline calibration was performed prior to each measurement through the Neptune software. The analytical precision reported on all isotope ratios from this study are based on 95% confidence interval (2σ mean) of individual measurements.

Mass-dependent fractionation of heavy versus light isotopes of Sr, Nd and Hf that occurs in the plasma was accounted for by internal normalization using the exponential law and the following relationship (Russell et al., 1978):

$$R_{true} = R_{meas.}\left(\frac{M_2}{M_1}\right)^{\beta} \qquad \text{(eq. 1)}$$

where Rtrue and Rmeas. are the accepted and measured isotopic ratios of masses M2 and M1, respectively. The mass bias coefficient, β , is a free parameter determined experimentally and applied to other measured isotope ratios for mass bias correction. Data reduction and adjustments for isobaric interferences were performed directly through the Neptune Method Editor software.

During the Sr isotope measurements (table SI-2), we also monitored the abundances of ^{82}Kr, ^{83}Kr and ^{85}Rb isotopes. ^{82}Kr served as a good indicator of how well bromine from the non-wetting agent was removed from the sample matrix during extraction chromatography; high levels of ^{81}Br manifest as a tail on ^{82}Kr peak. The contributions of ^{84}Kr and ^{86}Kr on ^{84}Sr and ^{86}Sr beams, respectively, are accounted for by measuring ^{83}Kr and allowing for abundance ratios of ^{83}Kr/^{84}Kr=0.2017 and ^{83}Kr/^{86}Kr=0.6647. We performed on-peak zero (OPZ) subtraction of Kr isotope abundances at the beginning of each measurement sequence, which rendered Kr contribution to Sr isotopes negligible. All measured Sr isotope ratios were normalized to ^{88}Sr/^{86}Sr = 8.375209 to correct for instrumental mass bias using equation 1.

Every 1-2 sample measurements were bracketed with measurements of two SRM987 standard solutions at 600 ng g^{-1}. Strontium concentrations in aerosol samples were measured against the concentration of Sr in SRM987, which was also calibrated against a certified mono-elemental standard solution (± 5‰). The mean of ^{87}Sr/^{86}Sr ratio in SRM987 measured during the course of this study was 0.710256 ± 12 (95% CI uncertainty on the last digits, n=24), which deviated from the accepted value of 0.710248 (Weis et al., 2006) by 12 ppm. The measured ^{87}Sr/^{86}Sr ratios were corrected for mass bias and isobaric interferences and the final ratio was further adjusted relative to the accepted value of

0.710248 for SRM987 to allow comparison with literature measurements of radiogenic Sr isotopes.

During the Nd isotope measurements (table SI-2), ^{147}Sm and ^{179}Sm isotopes were also monitored to determine effective elemental separation between Nd and Sm in the second extraction chromatography stage (Fig. SI-2). The mean of Sm/Nd ratio from all samples processed in this study was 0.03 ± 0.01, too low to have any detectable effect on Nd isotope ratios. Nevertheless, the residual isobaric influence of ^{144}Sm on ^{144}Nd was accounted for by allowing $^{147}Sm/^{144}Sm = 4.8387$. All measured Nd isotope ratios were normalized to $^{146}Nd/^{147}Nd = 0.7219$ to correct for instrumental mass bias using equation 1. Every 1-2 sample measurements were bracketed with measurements of two JNdi-1 standard solutions at 25 ng g^{-1} (courtesy of Franco Marcantonio, Texas A&M University). The mean of $^{143}Nd/^{144}Nd$ ratio in JNdi-1 was 0.512090 ± 3 (n=29), which deviated from the accepted value of 0.512115 ± 5 by 49 ppm. The sample $^{176}Hf/^{177}Hf$ ratios, corrected for mass bias and isobaric interferences, were adjusted to 0.512115 based on the mean of JNdi-1 bracketing standards.

During Hf isotope measurements (table SI-2), ^{172}Yb and ^{175}Lu were also monitored to determine elemental separation between Hf, Yb and Lu (Fig. SI-2). The isobaric interferences from ^{174}Yb and ^{176}Yb on ^{174}Hf and ^{176}Hf, respectively, were accounted for by allowing for the abundance ratios of $^{172}Yb/^{174}Yb = 0.6858$ and $^{172}Yb/^{176}Yb = 1.7108$. Similarly, the contribution of ^{176}Lu to ^{176}Hf beam was assessed by allowing for $^{175}Lu/^{176}Lu = 37.61$. Given the effective separation of these elements from Hf (Pourmand and Dauphas 2010), interference contributions from Yb and Lu on Hf isotopes were negligible. Measured Hf isotope ratios were normalized to $^{179}Hf/^{177}Hf = 0.7325$ to correct for instrumental mass bias using equation 1. Every two sample measurements were bracketed with measurements of two JMC475 standard solutions at 25 ng g^{-1} (courtesy of Nicolas Dauphas, University of Chicago and Jonathan Patchett, University of Arizona). The mean of $^{176}Hf/^{177}Hf$ ratio in JMC475 was 0.282146 ± 4 (n=18), which deviated from the accepted value of 0.282160 by 48 ppm, but was in better agreement with the value of 0.282154 ± 6, n=24, reported by Bouvier et al. (2008). The sample $^{176}Hf/^{177}Hf$ ratios, corrected for mass bias and isobaric interferences, were adjusted to 0.282160 based on the mean of bracketing JMC475 standards.

The measured $^{143}Nd/^{144}Nd$ and $^{176}Hf/^{177}Hf$ ratios are reported in " ε " notation relative to the Chondritic Uniform Reservoir (CHUR) values of 0.512638 ± 25 and 0.282785 ± 11, respectively (Jacobsen and Wasserburg, 1980, Bouvier et al. 2008), and are expressed in parts per ten thousand. The uncertainties on εNd and εHf values reported in this study do not propagate the uncertainty on CHUR.

In order to examine the external reproducibility of our analytical procedure for Sr, Hf and Nd isotopes, we processed duplicate aliquots of BCR-2 and BHVO-2 CRMs from the USGS. Approximately 20 mg of the CRM was processed similarly to the samples and the results were compared with the mean of literature compilations from tables DR3-5 (GEOREM: http://georem.mpch-mainz.gwdg.de/). As shown in in Fig. SI-3, all isotope ratios measured in these CRMs agree with the mean of literature values measured by MC-ICP-MS and thermal ionization mass spectrometry (TIMS) within analytical and literature

uncertainties. The analytical precisions (relative standard deviation of the mean, RSDm) on Eu/Eu* (EuN/√(SmN × GdN, normalized to mean of CI-Chondrites), Ce/Ce* (CeN/√(PrN × LaN), LaN/LuN and the mean of REE abundances were better than 0.24 %, 0.07 %, 0.64 %, and 0.86 %, respectively. These uncertainties are based on five independent replicates of G-3 CRM. The results of REE abundances from replicates of USGS CRMs BCR-2, BHVO-1, BIR-1, PCC-1, W-2, and G-2 agreed well with literature compilations (Pourmand et al., 2012).

Contribution from procedural blanks (n =3) for Sr, Nd and Hf were 800, 21 and 18 and picogram. These blank levels were negligible relative to the concentration of these elements in the running solutions, and no corrections were applied on isotope ratios measured in the samples and CRMs. Procedural blank adjustments affected the REE abundances by an average of 0.2 % for La-Lu, with the highest average correction of 1.4% on Yb. The overall agreement between isotope ratios and elemental abundances of CRMs and the literature gives us confidence in the fidelity of our analytical technique.

The procedure presented here is highly advantageous as it utilizes flux fusion for fast and effective sample dissolution. In contrast to the most common protocols in the literature, the eluted fractions containing Sr, Nf, Hf and the REE can be directly analyzed for isotope ratios and elemental abundances without the need for additional dry-down and acid conversion steps, which are time-consuming and can potentially result in higher blank contributions.

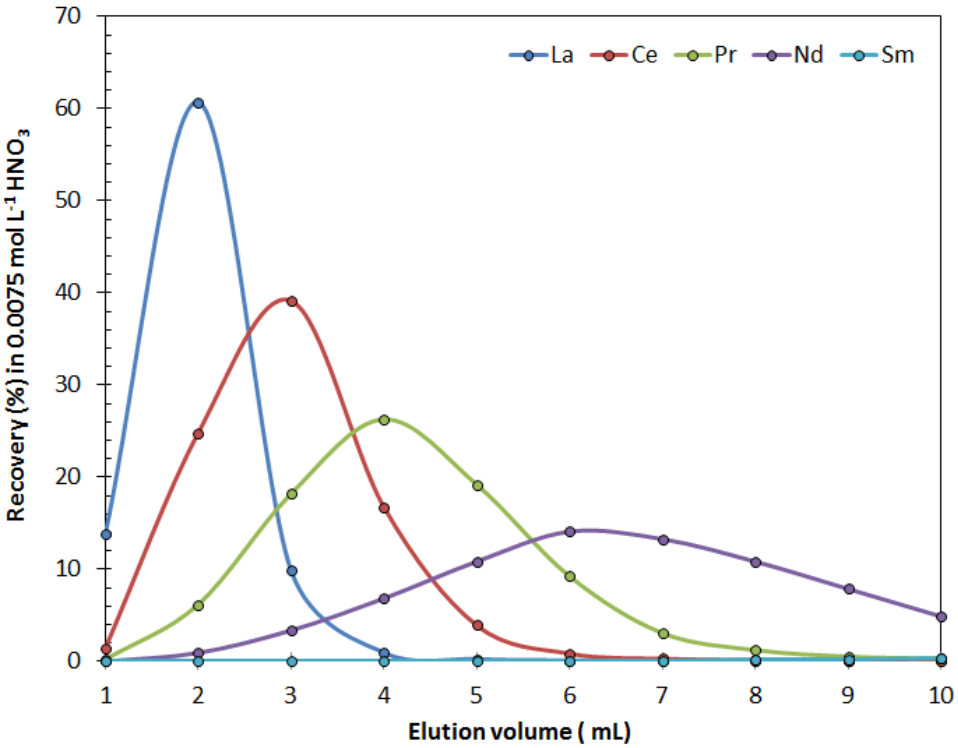

Fig. SI1. Elution curves for light REE. More than 80% of La and Ce and 40% of Pr are removed in 4 mL of 0.0075 mol L-1 HNO_3. At least 70 % of Sm-free Nd can be eluted in 5 mL of 0.0075 mol L-1 HNO_3.

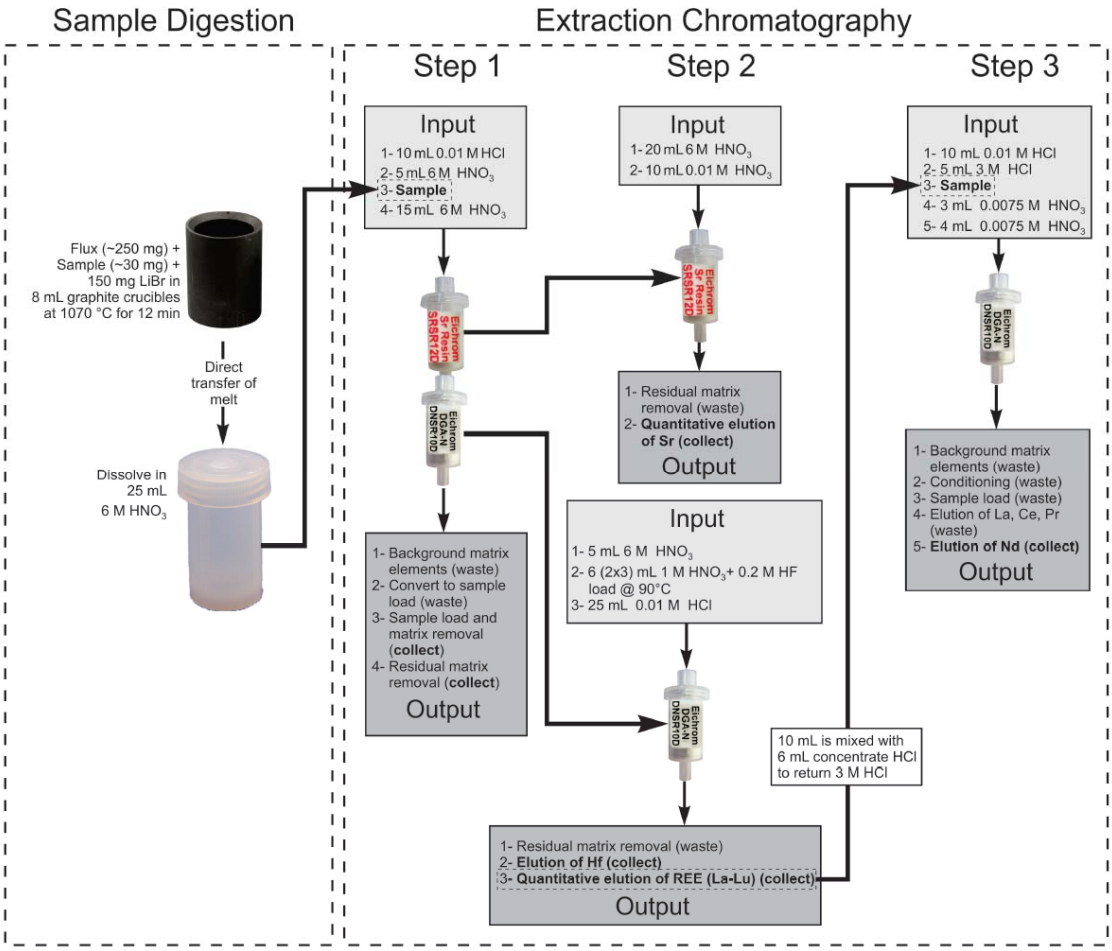

Fig. SI2. Summary of flux fusion and extraction chromatography for separating Sr, Nd, Hf and the REE from matrix elements for high-precision isotope ratio measurements and elemental abundances by MC-ICP-MS.

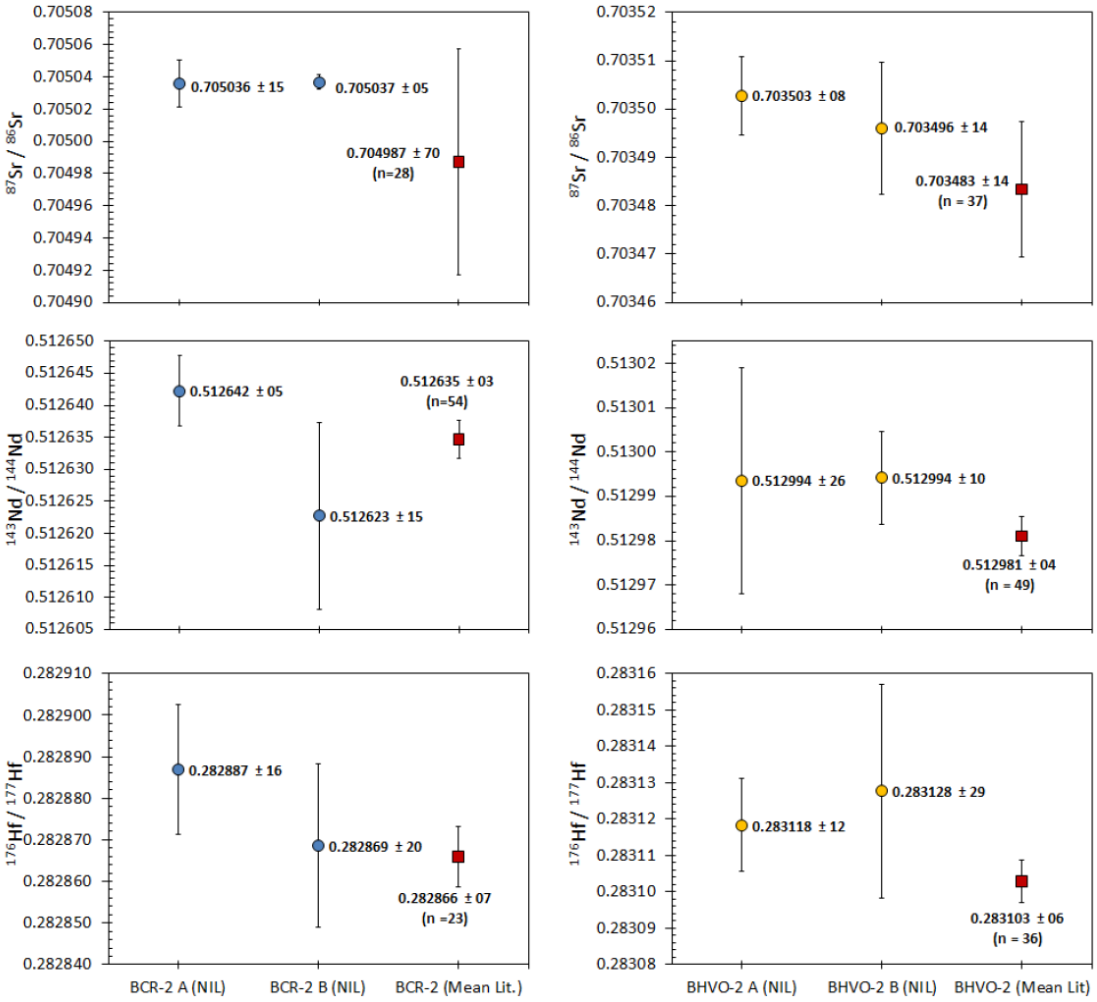

Fig. SI3. $^{87}Sr/^{86}Sr$, $^{143}Nd/^{144}Nd$ and $^{176}Hf/^{177}Hf$ isotope ratios measured in replicates of BCR-2 and BHVO-2 CRM powder from USGS in this study agree with literature compilations. The uncertainties in this study and the literature are calculated at 95% CI (2SD mean).

Table SI-1. Extraction chromotography procedure for separation of Sr, Nd, Hf and the REE from matrix.

Step	Resin (1 mL cartridge)	Input solution			Output solution	Elution
		Volume (mL)	Concentration (mol L^{-1})	Acid type		
1	**Separation of Sr, Hf and REE from matrix elements**					
1.1	SR + TODGA	10	0.01	HCl	Background matrix elements	waste
1.2	SR + TODGA	5	6	HNO_3	Convert to sample load	waste
1.3	SR + TODGA	20	6	HNO_3	Sample load and matrix removal	collect
1.4	SR + TODGA	15	6	HNO3	Residual matrix removal	collect
1.5	Separation of SR and TODGA cartridges					
2	**Separation of Sr and Hf from REE (from step 1.5)**					
2.1	SR	20	6	HNO_3	Residual matrix removal	collect
2.2	SR	10	0.01	HNO_3	**Quantitaive elution of Sr**	collect
2.3	TODGA	5	6	HNO_3	Residual matrix removal	waste
2.4	TODGA	6 (2x3)	1 + 0.2	HNO_3+ HF*	**Elution of Hf**	collect
2.5	TODGA	25	0.01	HCl	**Quantitative elution of REE (La-Lu)****	collect
3	**Separation of Nd from Sm**					
3.1	TODGA	10	0.01	HCl	Background matrix elements	waste
3.2	TODGA	16	3	HCl	Sample load from step 2.4	waste
3.3	TODGA	3	0.0075	HNO_3	Elution of La, Ce, Pr	Waste
3.4	TODGA	4	0.0075	HNO_3	**Elution of Nd**	collect

* Acid mixture is loaded at 90 °C.

** 10 mL is mixed with concentrated HCl to return 3 M HCl for step 3.2.

Table SI-2. Collector configuration for Sr, Nd, Hf and REE analysis.

	Faraday detectors and corresponding isotopes											
Element	L4	L3	L2	L1	C	H1	H2	H3	H4	Integration time (s)	Block	Cycle
Strontium	^{82}Kr	^{83}Kr	^{84}Sr	^{85}Rb	^{86}Sr	^{87}Sr	^{88}Sr	-	-	8.389	5	10
Neodymium	^{142}Nd	^{143}Nd	^{144}Nd	^{145}Nd	^{146}Nd	^{147}Sm	^{148}Nd	^{149}Sm	^{150}Nd	8.389	5	10
Hafnium	^{172}Yb	^{174}Hf	^{175}Lu	^{176}Hf	^{177}Hf	^{178}Hf	^{179}Hf	^{180}Hf	-	8.389	5	10
REE main	^{149}Sm	^{151}Eu	^{157}Gd	-	^{159}Tb	^{163}Dy	-	^{165}Ho	^{167}Er	4.2	1	3
REE Sub-config. 1	-	-	^{139}La	^{140}Ce	^{141}Pr	-	^{146}Nd	-	^{149}Sm	4.2	1	3
REE Sub-config. 2	-	-	^{167}Er	-	^{169}Tm	^{173}Yb	-	^{175}Lu	-	4.2	1	3

References

Abed, A. M., Al Kuisi, M., and Khair, H. A., 2009, Characterization of the Khamaseen (spring) dust in Jordan: Atmospheric Environment, v. 43, no. 18, p. 2868-2876.

Abouchami, W., Näthe, K., Kumar, A., Galer, S.J.G., Jochum, K.P., Williams, E., Horbe, A.M.C., Rosa, J.W.C., Balsam, W., Adams, D., Mezger, K., Andreae, M.O., 2013. Geochemical and isotopic characterization of the Bodélé Depression dust source and implications for transatlantic dust transport to the Amazon Basin. Earth and Planetary Science Letters 380, 112-123.

Bouvier, A., Vervoort, J.D., Patchett, P.J., 2008. The Lu–Hf and Sm–Nd isotopic composition of CHUR: Constraints from unequilibrated chondrites and implications for the bulk composition of terrestrial planets. Earth and Planetary Science Letters 273, 48-57.

Horwitz, E.P., Chiarizia, R., Dietz, M.L., 1992. A novel strontium-selective extraction chromatographic resin . Solvent Extraction and Ion Exchange 10, 313-336.

Horwitz, E.P., McAlister, D.R., Bond, A.H., Barrans, R.E., 2005. Novel Extraction of Chromatographic Resins Based on Tetraalkyldiglycolamides: Characterization and Potential Applications. Solvent Extraction and Ion Exchange 23, 319-344.

Jacobsen, S. B., and Wasserburg, G. J., 1980, Sm-Nd isotopic evolution of chondrites: Earth and Planetary Science Letters, v. 50, no. 1, p. 139-155.

Muhs, D.R., Budahn, J.R., Prospero, J.M., Carey, S.N., 2007. Geochemical evidence for African dust inputs to soils of western Atlantic islands: Barbados, the Bahamas, and Florida. Journal of Geophysical Research: Earth Surface 112, F02009.

Pourmand, A., Dauphas, N., 2010. Distribution coefficients of 60 elements on TODGA resin: Application to Ca, Lu, Hf, U and Th isotope geochemistry. Talanta 81, 741-753

Pourmand, A., Dauphas, N., Ireland, T.J., 2012. A novel extraction chromatography and MC-ICP-MS technique for rapid analysis of REE, Sc and Y: Revising CI-chondrite and Post-Archean Australian Shale (PAAS) abundances. Chemical Geology 291, 38-54.

Pourmand, A., Tissot, F. L. H., Arienzo, M., and Sharifi, A., 2014, Introducing a Comprehensive Data Reduction and Uncertainty Propagation Algorithm for U-Th Geochronometry with Extraction Chromatography and Isotope Dilution MC-ICP-MS: Geostandards and Geoanalytical Research, DOI: 10.1111/j.1751-908X.2013.00266.x

Prospero, J.M., Lamb, P.J., 2003. African Droughts and Dust Transport to the Caribbean: Climate Change Implications. Science 302, 1024-1027.

Russell, W.A., Papanastassiou, D.A., Tombrello, T.A., 1978. Ca isotope fractionation on the Earth and other solar system materials. Geochimica et Cosmochimica Acta 42, 1075-1090.

Trapp, J.M., Millero, F.J., Prospero, J.M., 2010. Temporal variability of the elemental composition of African dust measured in trade wind aerosols at Barbados and Miami. Marine Chemistry 120, 71-82.

Weis, D., Kieffer, B., Maerschalk, C., Barling, J., de Jong, J., Williams, G.A., Hanano, D., Pretorius, W., Mattielli, N., Scoates, J.S., Goolaerts, A., Friedman, R.M., Mahoney, J.B., 2006. High-precision isotopic characterization of USGS reference materials by TIMS and MC-ICP-MS. Geochemistry, Geophysics, Geosystems 7, Q08006.

APPENDIX D

INORGANIC AND ORGANIC GEOCHEMICAL DATA FROM NEOR LAKE

Supplementary Data File

Description:

The accompanying Excel spreadsheet consist of multiple tabs, where each tab provides inorganic and organic data for a 775-cm long peat core from Neor Lake. Description of individual tabs are as follow:

- Table SI-2a: XRF data
- Table SI-2b: TOC, TN, $\delta^{13}C_{TOC}$, $\delta^{15}N_{TOC}$ and water content
- Table SI-2c: Density, Flux and LORCA
- Table SI-2d: δD
- Table SI-2e: P_{aq} Biomarker

Filename:

Table SI-2.xlsx

APPENDIX E

ISOTOPIC AND RARE EARTH ELEMENT COMPOSITION OF PALEODUST FROM NEOR LAKE

Supplementary Data File

Description:

The accompanying Excel spreadsheet consist of three tabs for Sr-Nd-Hf isotopic composition, rare earth element (REE) concentrations of paleodust samples and grain size analysis of paleo-dust in a 775-cm long peat core from Neor Lake.

Filename:

Table SI-3.xlsx

APPENDIX F

GEOCHEMICAL DATA FROM URMIA LAKE

Supplementary Data File

Description:

The accompanying Excel spreadsheet consist of multiple tabs, where each tab provides geochemical data for a 500-cm long sediment core from Urmia Lake. Description of individual tabs are as follow:

- Table SI-4a: XRF data of 5-m long core
- Table SI-4b: Major and trace element Geochemical data and grain size data for short cores
- Table SI-4c: Geochemical data for 5-m long core
- Table SI-4d: $\delta^{13}C$ and $\delta^{18}O$ data
- Table SI-4e: Sr isotope data

Filename:

Table SI-4.xlsx